CONF-950198--

UCRL-ID-121571

Physics with the Collider Detectors at RHIC and the LHC

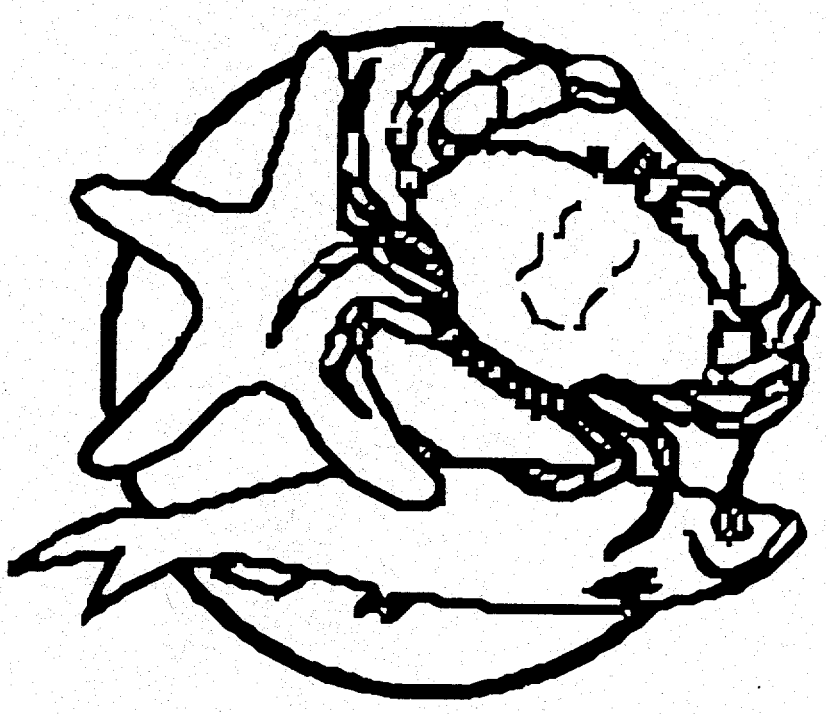

Proceedings of the Pre-Conference Workshop
Edited by Jim Thomas and Tim Hallman

Quark Matter '95
Monterey, California, USA

Work performed under the auspices of the U.S. Department of Energy by Lawrence Livermore National Laboratory under Contract W-7405-ENG-48.

PREFACE

On January 8th, 1995, over 180 participants gathered to hear the QM95 pre-conference workshop on "Physics with the Collider Detectors at RHIC and the LHC". Our goal was to bring together the experimentalists from a wide community of hadron and heavy ion collider detector collaborations. The speakers were encouraged to present the current status of their detectors, with all the blemishes, and the audience was encouraged to share their successes and failures in approaching similar detector design issues. The presentations were excellent and the discussions were lively and stimulating. We hope that you will find these proceedings to be equally stimulating.

We would like to thank all of the workshop speakers for their carefully prepared presentations. We would also like to thank the workshop summary speakers; Hans Gutbrod and Bill Willis.

July 15, 1995
Livermore, California — Jim Thomas
Berkeley, California — Tim Hallman

Contents

Leptons and Photons

New Technology

Fixed Target Operation Beyond RHIC Startup

Speakers and Participants

The RHIC Status Update

S. Ozaki[a*]

[a]RHIC Project
Brookhaven National Laboratory
Upton, New York 11713

The construction of the Relativistic Heavy Ion Collider (RHIC) began in 1991, with the completion date originally scheduled for 1997. Significant reduction of the funding levels in FY 1993 and 1994, and the funding level cap for FY 1995 and later years caused a 19-month stretchout of the construction period to the second quarter of FY 1999, and an increase of the total estimated cost (TEC) to $475 M. The Project, therefore, is now at the halfway mark of the construction period with actual cost and schedule performance tracking close to the DOE-approved baseline. Construction funding through FY 1995 reached close to 60% of the TEC. Incidentally, if you add the current value of preexisting facilities which will be incorporated into RHIC, such as the injection system (Tandem Van de Graaff - the Booster - the AGS), the existing 3.8 km tunnel, the 24 kW helium refrigerator, etc., the total value of the RHIC facility, when completed, will reach one billion dollars, if not more. I am pleased to note that there has been significant, tangible progress made during the past four years.

The accelerator lattice design was finalized in 1992 after an intensive study was made to optimize the collider design for performance, operational flexibility, and value engineering. This lattice design has been stable since then and has been the basis for the detailed design of accelerator hardware.

The civil construction, including the collider enclosure, magnet access ports to the ring tunnel, and six service buildings for accelerator power supplies and cryogenic control boxes was completed. The recent aerial photograph of the RHIC site is shown in Fig. 1. For most of the collider technical components, the detailed design is complete and the fabrication, either by industry or at BNL, is well underway; the fabrication rate is limited only by the availability of funding.

Big events took place on August 5, 1994 and on January 26, 1995 when the first Grumman-built dipole magnet and the first CQS magnet unit, respectively, were brought into the RHIC tunnel near the 6 o'clock hall. Since then, the activities in the tunnel have been mounting at a steady pace. To date, more than 100 dipole magnets and scores of CQS magnet units have been placed on their respective stands in the 5 o'clock and 3 o'clock sextants of the tunnel. Figure 2 shows two lines of arc dipole magnets installed in the 5 o'clock sextant.

Looking at the 600 m long beam injection line that connects the AGS and RHIC, all

*Work performed under the auspices of the U.S. Department of Energy.

of the beam transport magnets (room temperature) and virtually all of the vacuum gear are in place and are being connected. Figure 3 shows a view from the split point of the injection line—the right-hand arc for the counter clockwise beam and the left-hand arc for the clockwise beam. The construction of the beam line to this split point is virtually complete, and the beam duct from the AGS shielding wall to this point is already under vacuum. Presently, power supplies for this section, as well as the control system, are being exercised using the actual magnets as the load, in preparation of the injection line test scheduled in the fall of 1995.

Production of superconducting magnets, which is the most significant undertaking in the RHIC Project, is proceeding very well at industry and at the RHIC magnet facility (Fig. 4). Of the 1740 superconducting magnets required for RHIC, approximately 1100 are being produced by industry. They include 360 dipoles, 412 quadrupoles, 288 sextupoles, and 72 trim-quadrupoles, all with 80 mm coil bore diameters. The large bore magnets [i.e., 72 final focus triplet quadrupoles (Q1-Q3), 24 D0's, 12 DX's], and corrector assemblies that require special technology developed by BNL are being built at the RHIC magnet facility.

Another big event in this regard was the successful completion of the Phase I portion of the dipole magnet contract with Grumman Aerospace Corporation (now Northrop Grumman) on September 30, 1994 as scheduled. The Phase I was a cost-plus-fixed-fee type contract and covered technology transfer to industry, tooling setup, and the initial production of 30 magnets. Since October 1, Northrop Grumman has begun the routine production of one dipole magnet per day at their Bethpage, Long Island plant. To date, 118 dipole magnets, or about one third of the total number required, have been delivered. The quench performance of all magnets tested at the cryogenic temperature of 4.6 K is excellent (see Fig. 5). The excitation current at the quench-plateau comfortably exceeds 6500 A, 30% above the operating current of 5000 A. The magnetic field quality of all magnets is good and quite uniform from magnet to magnet, virtually eliminating a need to shuffle magnets to meet the collider lattice requirement. The target date of the completion of the dipole magnet manufacturing remains in mid-1996, well ahead of the final need date.

The production of arc quadrupole magnet cold mass units at Northrop Grumman has increased to the full production rate of two units per day in recent months. To date, 146 units, also about one third of the total number required, have been delivered. The magnetic field quality of all magnets is good and quite uniform from magnet to magnet. The quench performance of all magnets tested at the cryogenic temperature of 4.6 K (52 units) is also excellent as shown in Fig. 6. The excitation current at the quench-plateau comfortably exceeds 6500 A, 30% above the operating current of 5000 A. Northrop-Grumman plans to complete the production of the quadrupole cold masses before the end of 1995, well ahead of the need date for CQS magnet unit assembly. Everson Electric Co. of Allentown, Pennsylvania, has completed the delivery of 288 quality sextupole magnet cold masses. Manufacturing of corrector assemblies by BNL, again of good quality, is on schedule.

One each corrector coil assembly, quadrupole magnet cold mass, sextupole magnet cold mass, and the beam position monitor (supplied by the RHIC Instrumentation Group) is combined into one cold mass unit, and then inserted into a cryostat. The main thrust

of activity in the RHIC magnet facility is now directed toward the assembly of this combined element unit, the so-called "CQS" magnet unit. Just as good quality and good alignment of lenses define the quality of an optical system, the quality and alignment of magnets in the CQS unit, for that matter throughout the ring, define the quality of the colliding beam optics. In spite of tight tolerances imposed on this assembly, the tooling specifically designed for this task and the newly developed and automated colloidal cell survey technology make it possible to assemble the CQS magnet unit that meets the stringent collider specifications at the rate of one unit per day.

Another major undertaking in the collider construction is the establishment of a cryogen (liquid helium) distribution and control system. Two of the 12 cryogenic control valve boxes have been delivered and installed in the 6 o'clock service building. The delivery of the remaining boxes will follow within 1995. The delivery of vacuum jacketed piping to connect the existing 24 kW (at 4.2 K) helium refrigerator to the ring has begun. The manufacturing of vacuum jacketed piping to connect across the room temperature sections of the ring will follow, delivery scheduled in time for the beam test of the 5 o'clock sextant planned in the fall of 1996. In the meantime, work is in progress to refurbish and modify the refrigerator, which has not been operated since its acceptance test in 1986.

Progress is also seen in other technical areas of the collider construction. These include the magnet power supply system, rf system, vacuum system, beam instrumentation system, control system, and personnel safety system. The main power supplies for the collider ring are in place in the 4 o'clock service building. The acquisition of a total of 10 units of 200 MHz CERN SPS rf cavities was completed just before the exchange rate between the US dollar and the Swiss franc plummeted to a record low. These cavities will be retuned to 196 MHz and used as the storage rf cavities.

There are a number of signatures which are predicted to signify the formation of quark-gluon plasma. Typically, an observation of the global feature of hadron production from the heavy ion collisions, such as multiplicity, spatial and energy distributions of emerging hadrons, and the production of specific types of particles can reveal the plasma formation. Contrary to hadrons which are strongly absorbed by the nuclear matter and thus convey information only of the surface of the plasma, leptons and photons are penetrating probes and can give an insight to the inner making of the plasma. A change in the global feature as a function of energy can signify an onset of the plasma formation. The RHIC detector program consists of two complementary major detector systems (PHENIX and STAR) and two smaller-scale experiments (PHOBOS and BRAHMS).

These detectors as designed in the base-line configuration are adequate for the first round of the RHIC physics program. These detectors also collectively cover all of the predicted signatures. Significant progress was made in the RHIC detector program. The two major detector systems (PHENIX and STAR), which will occupy two large experimental halls, are well underway in the construction phase, after the Technical/Cost/Schedule baseline review of STAR in January 1993, and PHENIX in March 1994. The annual Technical/Cost/Schedule reviews of these detectors were made in October 1994 and March 1995, respectively, with satisfactory findings. PHOBOS, one of two smaller-scale experiments, received scientific approval and was reviewed for the construction approval, and is awaiting funding decisions to begin construction. The other, BRAHMS (Broad Range Hadron Spectrometer) has received scientific approval and is proceeding with technical de-

signs. At present, more than 700 physicists from 80 institutions nationwide and worldwide are involved in this program.

The RHIC Project is making excellent progress toward its completion in 1999. Most of the technical issues associated with the collider are resolved, procurement of magnets and other accelerator components are well underway, and a realistic picture of the experimental program is taking shape.

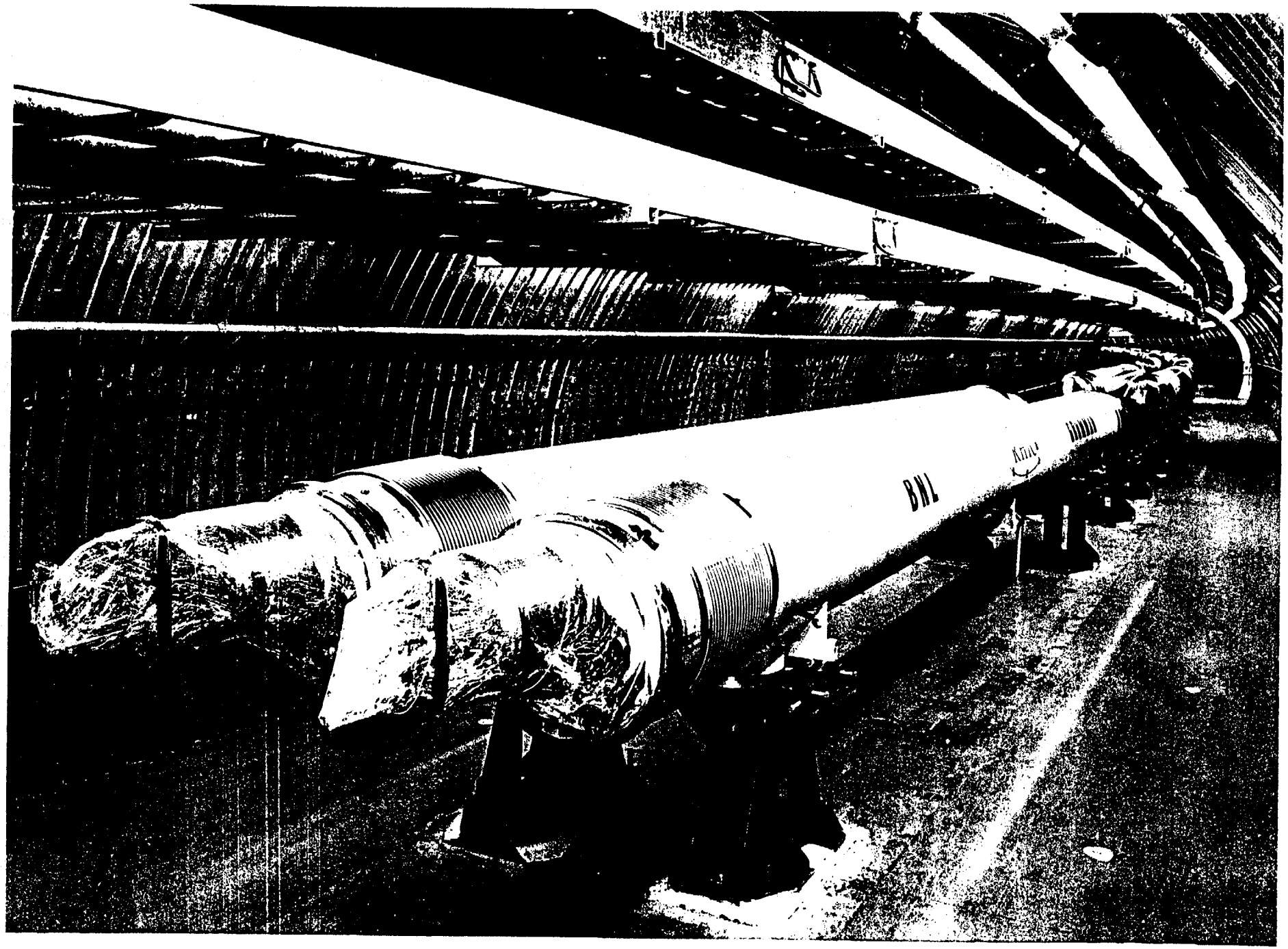
BNL

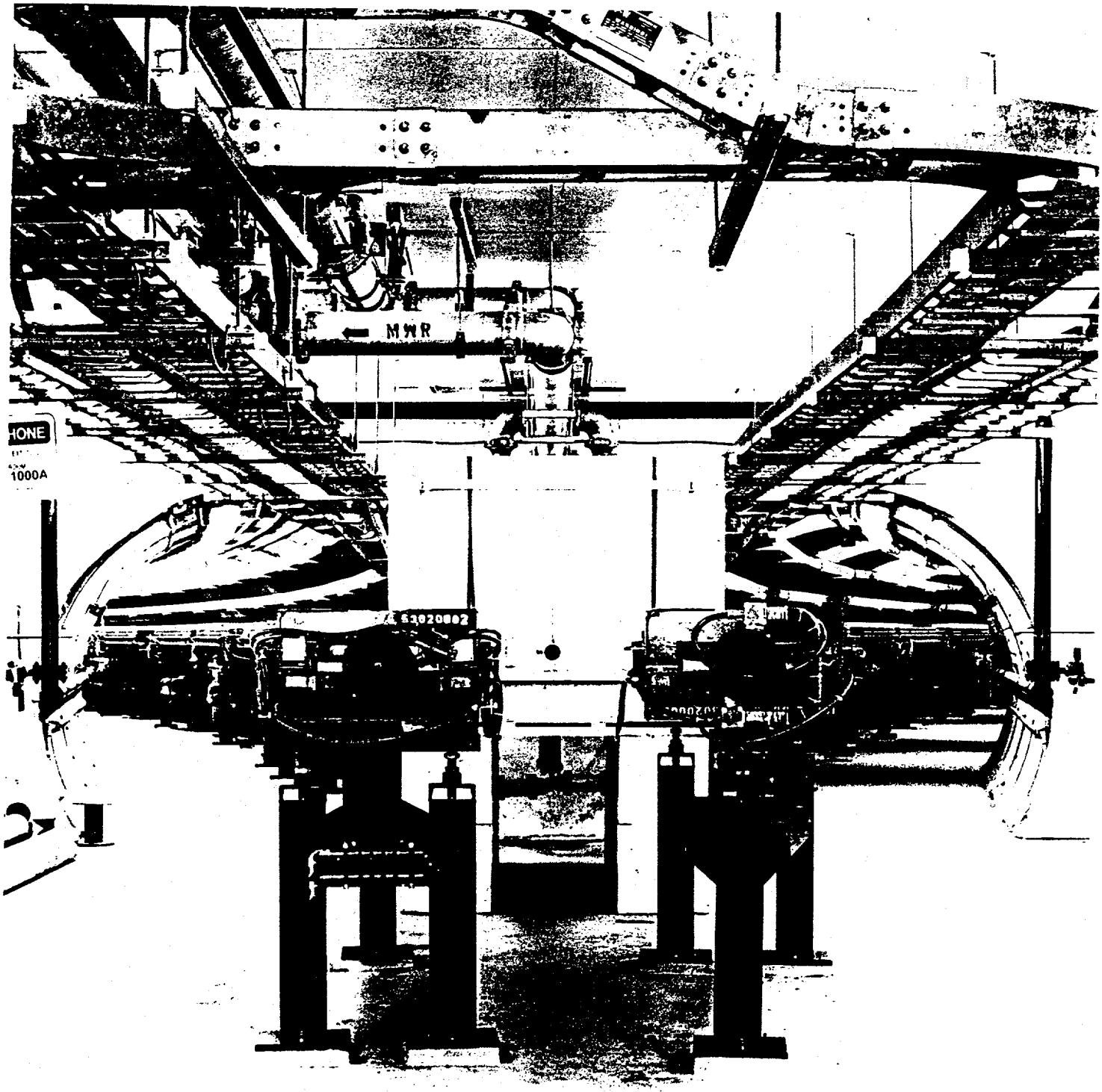
MWR
HONE
1000A

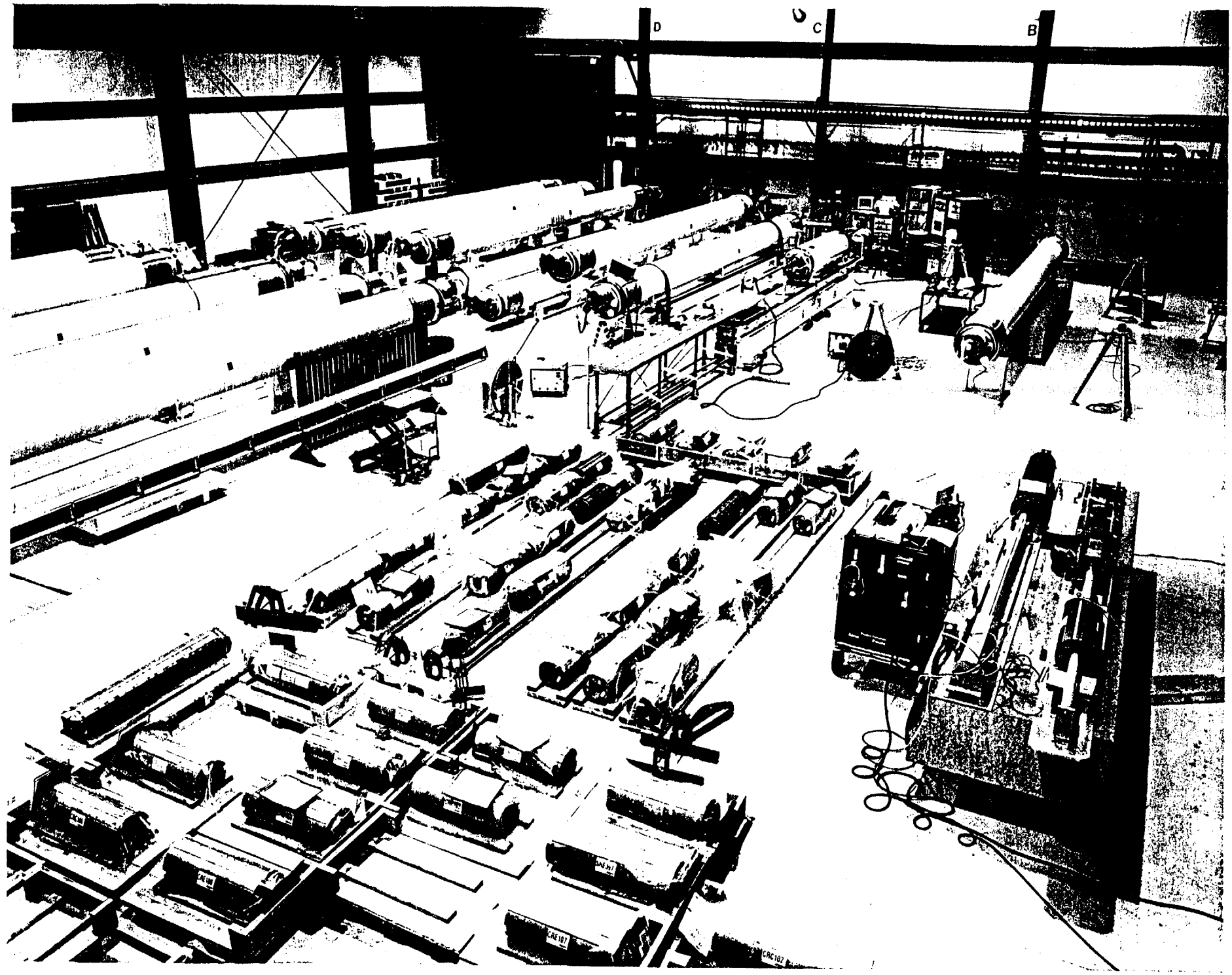
D
C
B
CRE107
CRC102

RHIC PRODUCTION DIPOLE QUENCH TESTS

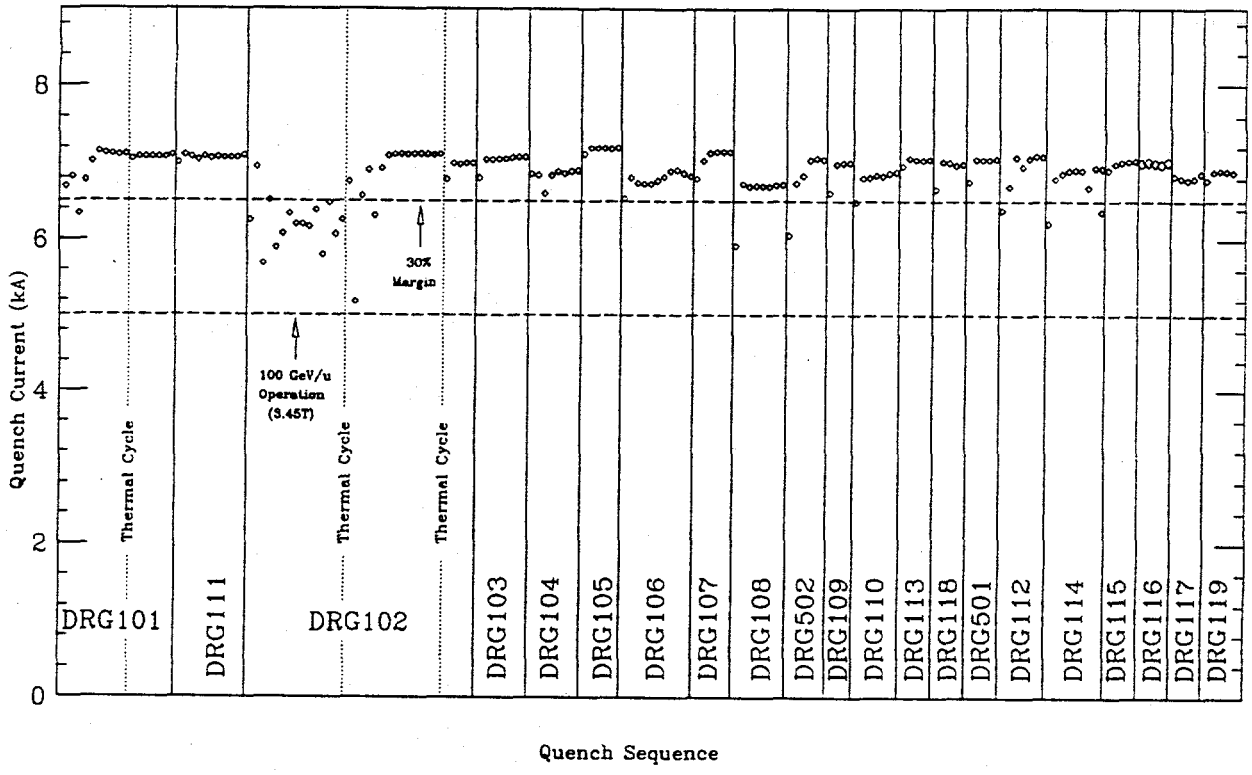

RHIC PRODUCTION DIPOLE QUENCH TESTS

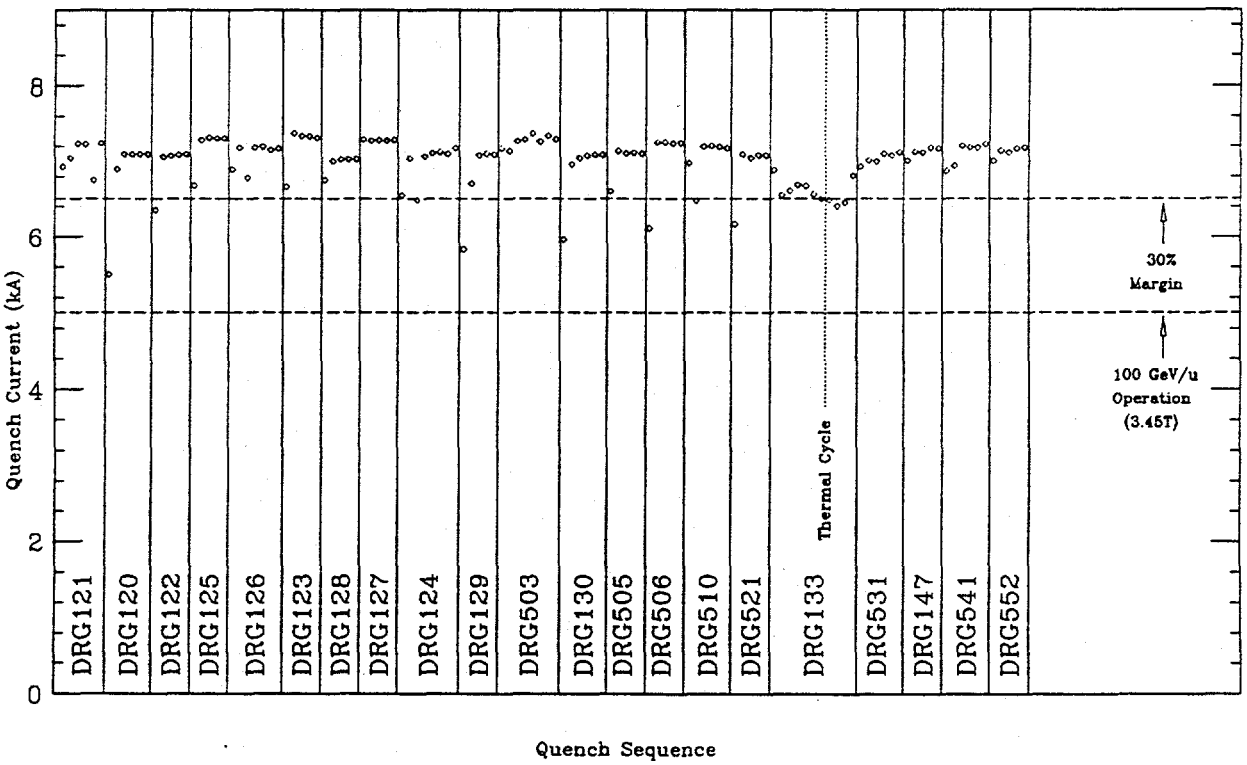

Note: Test temperature was 4.5K (nom).
Quenches with the warm bore are not included in this plot.

J. Muratore

RHIC PRODUCTION QUADRUPOLE QUENCH TESTS

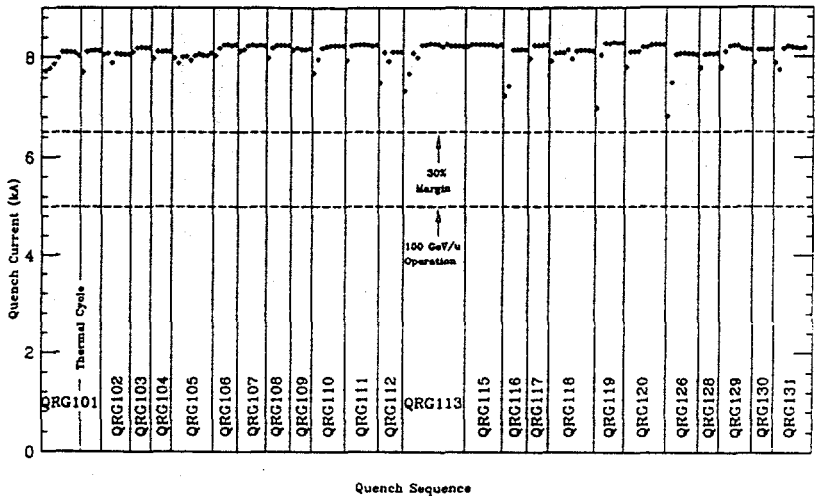

RHIC PRODUCTION QUADRUPOLE QUENCH TESTS

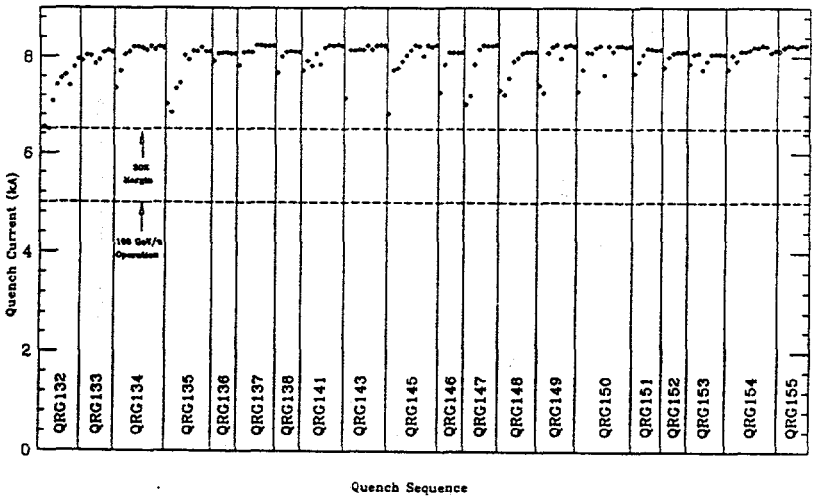

RHIC PRODUCTION QUADRUPOLE QUENCH TESTS

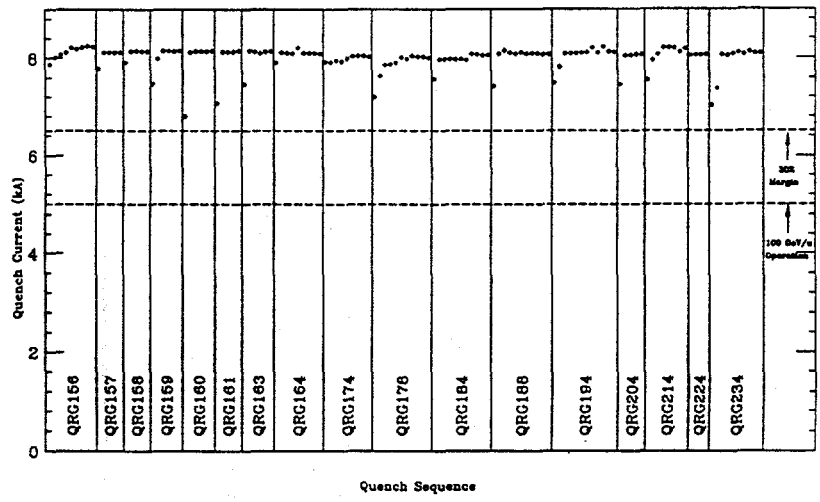

NOTE: The test temperature was 4.35K (nom).
The ramp rate for quenches was 63A/s.

J. Muratore

Midrapidity Measurements with the BRAHMS Spectrometer

D. Beavis[a] *
for the BRAHMS Collaboration[b]

[a]Physics Department, Brookhaven National Laboratory,
Upton, New York 11973, U.S.A.

[b]BNL, CRN-Strasbourg, NBI-Copenhagen, CIAE-Beijing, NYU, Texas A&M,
UCSSL-Berkeley

The forward- and midrapidity-arms of the BRAHMS experiment are designed to measure charged particle production over a wide range of transverse momentum for rapidities, $0 \leq y \leq 4$. Details of the midrapidity spectrometer, which provides coverage for $0 \leq \eta \leq 1.3$, are presented here. The capabilities for inclusive $\pi^{\pm}$, $K^{\pm}$, and $p^{\pm}$ measurements and boson pair correlations are discussed.

1. INTRODUCTION

High energy heavy ion collisions provide an opportunity to study properties of hot dense matter in extended volumes considerably larger than that of the initial hadronic constituents. The RHIC collider will enable the measurement of Au+Au collisions at $\sqrt{s}$=200 GeV per nucleon pair, where it is anticipated that the energy density achieved in central collisions will be sufficiently high to create the quark-gluon plasma (QGP). Unfortunately, predictions based solely on the underlying theory of strong interactions, Quantum Chromodynamics (QCD), can not be made. However, many interesting suggestions have been made on possible experimental signatures which may provide evidence for the creation of the QGP in relativistic heavy ion collisions. Each of the RHIC experiments, STAR[1], PHENIX[2], PHOBOS[3], and BRAHMS[4] have unique capabilities for investigating the conditions created in the heavy ion collisions at RHIC.

Measurements of particle yields and p_t spectra can certainly be expected to provide important basic information for understanding the processes that occur in heavy ion collisions. Several models have been developed based on aspects of QCD and data from p+p collisions. These models can be used for guidance in understanding the y-p_t coverage appropriate for experiments to investigate the physics of Au+Au collisions at RHIC. The predictions of VENUS[5], FRITIOF[6], and RQMD[7] for the rapidity distribution of net baryons and mesons are shown in Fig. 1. These models have considerably different expectations for the net baryon yield and resultant meson densities as a function of rapidity. FRITIOF predicts a "central plateau" region with nearly zero net baryon number. In contrast, VENUS has no "central plateau" and considerable net baryon density at

*This research was supported by the U.S. Department of Energy under contract no. DE-AC02-76CH00016.

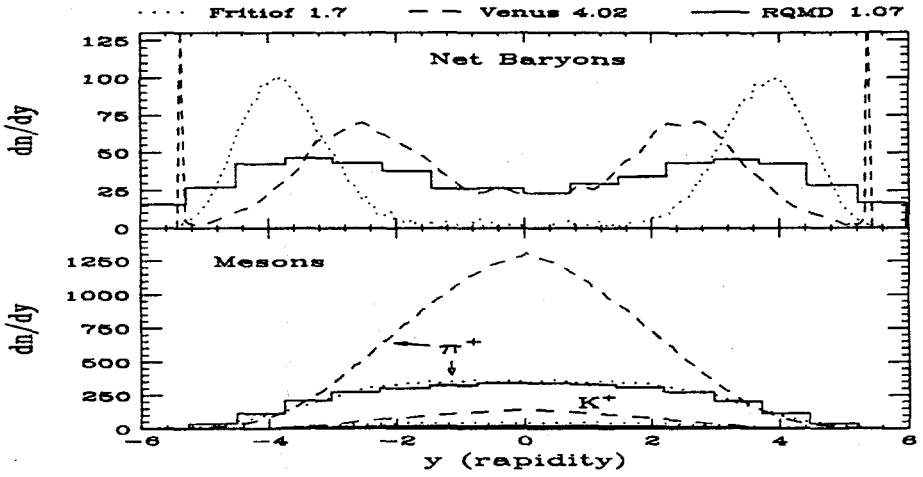

Figure 1. Predicitions of the rapidity distributions for net baryons (top) and mesons (bottom).

midrapidity. These model calculations demonstrate the uncertainty in the expectations for the environment created during heavy ion collisions at RHIC. The initial conditions and subsequent evolution of the hot dense matter may vary substantially with rapidity.

The *BRoad Range Hadron Magnetic Spectrometers* (BRAHMS) Experiment will measure inclusive and semi-inclusive $\pi^{\pm}$, $K^{\pm}$, and $p^{\pm}$ spectra for $0 \leq \eta \leq 4$. Typically the p_t coverage will range from 0.2 GeV/c to 3 GeV/c. This extensive y-p_T coverage for charged particle measurements is a unique feature of the BRAHMS experiment.The p_t spectra and rapidity distributions will be measured as a function of event centrality. Details of the midrapidity spectrometer, which provides coverage for $0 \leq \eta \leq 1.3$, are given below. The capabilities for single particle measurement and boson correlations are illustrated in the context of simple examples.

2. THE MIDRAPIDITY SPECTROMETER

As shown in the schematic layout of Fig. 2, BRAHMS has two movable magnetic spectrometers for charged particle measurements. A set of global/trigger detectors provide triggering and event-centrality characterization. The characteristics of the forward spectrometer, which measures charged particles for $1.3 \leq \eta \leq 4$, have been presented at this workshop by B. Moskowitz[8], and will not be discussed further here. In this section a brief description of the global/trigger detectors and the midrapidity spectrometer will be presented.

A set of beam-beam counters and a silicon multiplicity array provide the experiment with initial trigger information and vertex determination. The beam-beam counters (not shown in Fig. 2) are similar in concept to systems in other RHIC experiments. Two arrays, each of roughly 40 PMT's with Čerenkov radiators, will be placed on the left and right

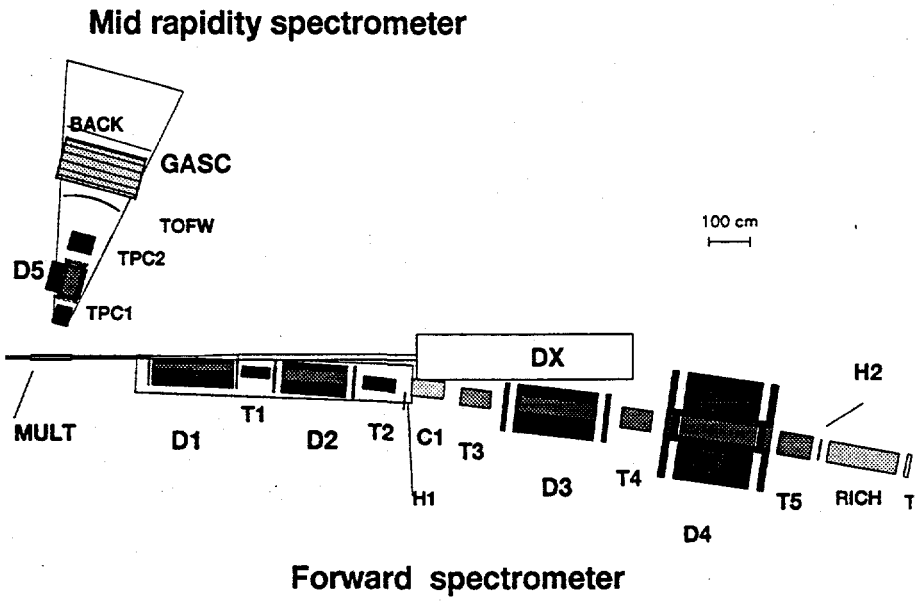

Figure 2. Layout of the BRAHMS spectrometers and the RHIC dipole DX.

sides of the intersection region, 200-250 cm from the crossing point. The detected light from $\beta \approx 1$ particles will provide the timing start for time-of-flight measurements, initial vertex determination via timing differences, and a sampling of $dn/d\eta$ for $3 \leq |\eta| \leq 4.5$. Event centrality will be characterized by a multiplicity array consisting of $\approx$3500 channels using silicon strip detectors of the type being developed by PHOBOS[3]. The array measures the charged particle multiplicity in the region $|\eta| \leq 2.5$ and will enable the experiment to selectively trigger on central collisions. The addition of a partial second layer of silicon detectors may be employed to provide more precise vertex information than determined by the beam-beam counters. The initial interaction time, collision vertex, and centrality are determined by the beam-beam counters and multiplicity array for triggering purposes and offline analysis.

The midrapidity spectrometer has been designed for charged particle measurements for $p \leq 5$GeV/c and $0 \leq \eta \leq 1.3$. The spectrometer has two TPCs (TPC1 and TPC2) for tracking, a magnet (D5) for momentum measurements, and a time-of-flight wall (TOFW) and segmented gas Čerenkov (GASC) for particle identification. The entire detector system is mounted on a rotatable platform allowing polar angle coverage from $30° \leq \theta \leq 90°$ in 9° increments. The spectrometer has a solid angle acceptance of 7 mstr which is sufficient to minimize systematics and yet provide sufficient data rates. The detectors have been dimensioned to match the acceptance of the D5 magnet aperture taking into account the interaction diamond size. The integrated magnetic field (Bdl) is adjustable to a maximum of 0.8T-m allowing optimization of the acceptance and resolution for the desired physics measurement. Typically, the spectrometer will provide $dp/p \approx 0.01p$ (p in GeV/c), which is sufficient for the intended measurements.

	primary	secondary	total	particles/cm^2
34°				
TPC1	101	12	113	0.19
TPC2	7	2	9	0.01
TOFW	7	5	12	
90°				
TPC1	30	5	35	0.05
TPC2	2	1	3	0.003
TOFW	2	1.4	3.4	

Table 1
Average charged particle multiplicities in the midrapidity spectrometer.

The detector segmentation requirements have been studied for central collisions of Au+Au at $\sqrt{s}$=200 GeV per nucleon pair. The event generator VENUS was chosen since typically it has charged particle rapidity densities 2-3 times that of FRITIOF in the region $0 \leq \eta \leq 1.3$, which provides a conservative design basis for measurements in central collisions. The simulated events were input into GEANT so that effects of particle interactions, gamma conversions, decay, and multiple scattering were considered in the segmentation of the detectors. The average charged particle multiplicities in the TPC's and the time-of-flight wall (TOFW) are given in Table 1 for the spectrometer at 90° and 34°. The hits for the TPC's are calculated at the front surface of the detectors where the density is highest. Although the hit density on the detectors is largest for regions of high η, the calculated densities are not expected to pose a difficult problem for the detectors. Tracking algorithms and a prototype TPC have been tested. The tracking algorithms begin searching for track segments at their exit from the TPC so even in TPC1 at 34° the density where track finding starts is typically less than 0.1 particles per cm^2. The small densities in TPC2 are easily accommodated.

Particle identification at low momentum is achieved with TOFW which has 225 slats. The 75 pico-second resolution will provide 4σ separation of k-π to 2.2 GeV/c and k-p to 3.7 GeV/c. At higher momentum, the separation is achieved with the GASC which is segmented into 20 cells. Operating with Freon-12 at four atmospheres, pions will be above the discriminator threshold at 1.8 GeV/c, kaons at 5 GeV/c, and protons at 11 GeV/c. The y-p_t coverage of the spectrometer for pions (kaons) is shown in the left (right) frame of Fig. 3 . The shaded areas display which detector system performs the particle identification.

3. SINGLE PARTICLE ACCEPTANCE and RATES

The capability of the spectrometer for measuring single particle spectra will be illustrated with a simple example. A simulation of the spectrometer performance has been conducted using GEANT to calculate the geometrical acceptance and effects due to multiple scattering, secondary interactions, and particle decay. The particle spectra are as-

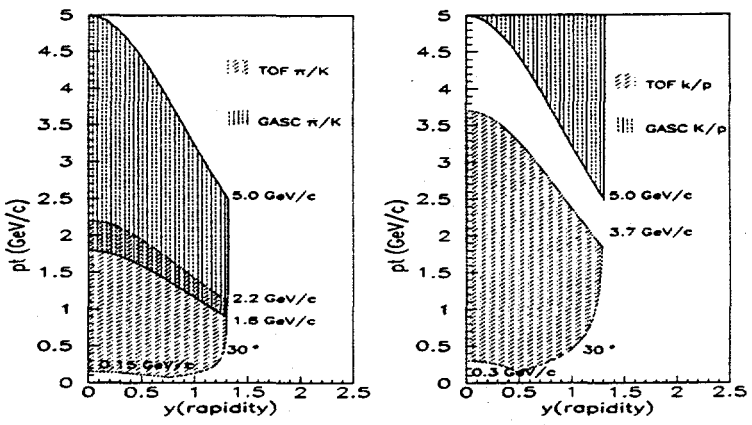

Figure 3. Coverage for the pions (left) and kaons (right) for the midrapidity spectrometer. The shaded areas indicate which device performs the particle identification.

sumed to be described by an exponential in transverse mass, $m_t=\sqrt{m^2+p_t^2}$. An inverse slope of 170 MeV/c was used in the simulations.

The y-p_t coverage for K^+ for two distinct settings of the spectrometer angle is shown in Fig. 4. The distributions are characteristic of modest-aperture spectrometers. The 4kG field used in the simulation would provide momentum resolution of approximately 1% for kaons at 1 GeV/c with some loss of low p_t acceptance due to dispersion. At low p_t the acceptance is slightly shifted to lower rapidities for this choice of magnetic field polarity. A systematic measurement of $K^{\pm}$ from 30°-90° would require 40 settings of the spectrometer incorporating 10 angular positions each with two magnetic field strengths and both field polarities.

Th p_t distribution of K^+ for the 34° setting shown in Fig. 4 includes the effects of decay, geometrical acceptance, etc. The statistics are sufficient to determine the inverse slope to an uncertainty of ±10 MeV in the region of $p_t = 1.5$ GeV/c. The required beam time to obtain such a distribution can be estimated from the acceptance, the assumed rapidity density of the K^+, and the trigger rate. The spectrometer accepts 0.07 K^+ per central Au+Au event assuming a rapidity density of 50 K^+ per central collision near $y = 1.2$. With a conservative estimate of 20 central events/sec. written to tape, the distribution shown in Fig. 4 could be obtained in 6 hours. Estimates for other particle species and rapidities can be obtained by scaling by $1/\sin^2\theta$ and the appropriate rapidity density. Typically, a minimum-bias data sample of comparable statistics will require a run several times longer.

The goal of providing a systematic measurement of inclusive $p^{\pm}$,$\pi^{\pm}$, and $K^{\pm}$ in the pseudorapidity interval $0 \leq \eta \leq 1.3$ with the BRAHMS midrapidity spectrometer is achievable with the spectrometer as designed. Based on the example given above for kaons, a systematic measurement of the p_t spectrum to $\approx$ 2 GeV/c could be accomplished with

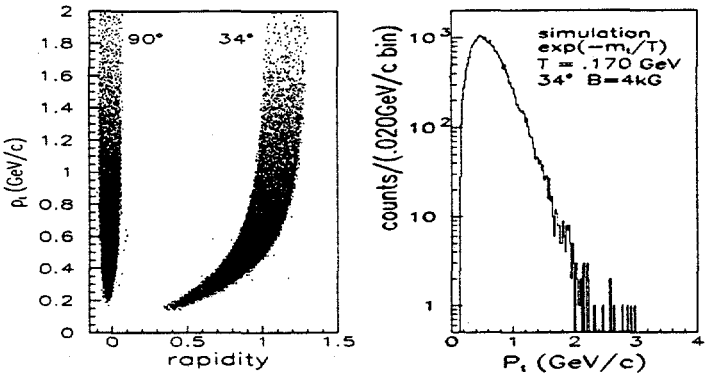

Figure 4. The K^+ y-p_t coverage for the spectrometer at two angle setting (left). The p_t distribtuion for the accepted K^+ for the 34° setting (right). See text for details.

about 1500 hours of beam time. Although it appears that this could be accomplished in the first few months of RHIC operations it must be realized that the accelerator is likely to achieve 10% of the design luminosity , $2x10^{26}$ $cm^{-2}sec^{-1}$, only after the first year of operation. Realistically, considering accelerator and experimental shakedown, this systematic program should be completed within the first two years of RHIC operation. At several selected regions of η, the midrapidity spectrometer will acquire high statistics data samples for measuring the p_t spectrum well beyond 2 GeV/c into the region where hard processes are expected to contribute substantially. The inclusive measurement of other particles such as the ϕ meson will also be undertaken.

The midrapidity spectrometer has sufficient solid angle to allow a modest measurement of ϕ meson production via the K^+K^- decay mode. The event generator VENUS has been used to explore the spectrometer's ability to reconstruct the ϕ meson from the K^+K^- invariant mass distribution . It has been assumed that 20% of the kaons arise from ϕ decay. The invariant K^+K^- mass distributions obtained at 34° (10^6 central events) and 90° (4x10^6 central events) are shown in Fig. 5. The inset shows a background-subtracted ϕ peak with a slight broadening of the width from 4.4 to 6 MeV caused by the momentum resolution. The average p_t of the reconstructed ϕ mesons is about 1 GeV/c. Thus, a measurement obtaining $\approx$1000 ϕ's at y$\approx$1 would complement the results obtained by other experiments at smaller rapidity and be achieved during a run for high statistics semi-inclusive measurements at large p_t.

4. BOSON PAIR CORRELATIONS (HBT)

The correlation of like-bosons as a function of the relative momentum can provide a measure of the space-time extent of the emission source[9–11]. However, the interpretation

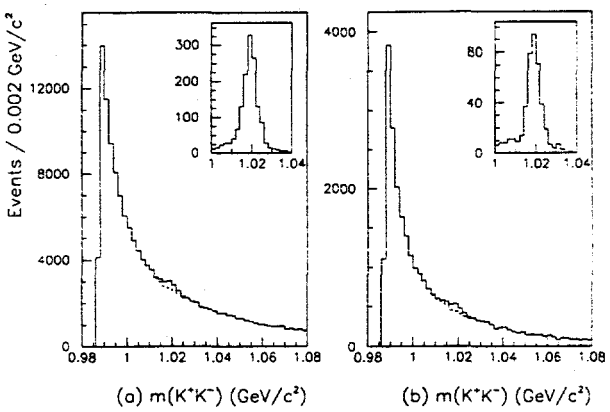

Figure 5. Simulated invariant K^+K^- invariant mass distributions for the midrapidity spectrometer at (a) 34° and (b) 90°. The solid curve represents all pairs and the dashed curves are for combinatorial background. The background-subtracted distributions are shown in the insets.

of such measured correlations can be affected by possible correlations of the emission coordinates and momenta[12], e.g. caused by transverse and longitudinal expansion of the source. Pair correlations coupled with single-particle measurements will help to provide a more complete understanding of the dynamics which controlled the evolution from an initial hot dense phase to the final hadronized state. In this section the ability to measure pion pair correlations will be discussed.

Pion pair correlations have been simulated in a fashion similar to that used for the single particle investigation. The pions are assumed to have exponential distributions in m_t with an inverse slope of 170 MeV. Pairs of pions are accepted through the spectrometer using GEANT to describe the geometrical acceptance, decays, etc. The simulation used a simple Gaussian correlation function given by

$$C(q) = 1 + \lambda e^{-(q^2R^2+q_0^2\tau^2)} \tag{1}$$

where q is the magnitude of the relative three-momentum, q_o is the relative energy, R is the source radius, τ is the source lifetime, and λ is the intercept parameter. All simulations presented here have the lifetime, τ, explicitly set to zero which allows for a simplified one-dimensional analysis.

The extracted correlation function for 100,000 π^+ pairs is shown in Fig. 6 for two representative examples. Fits to the correlation functions are also shown . The sensitivity to the radius and intercept parameters is shown in Fig. 7 for radii ranging from 2fm to 10fm. For 100,000 pairs the errors are typically less than 10% . It should be emphasized that there are no systematic errors allowed for in this simplistic analysis: a more realistic correlation function would cause a decrease in the sensitivity to the parameters. However,

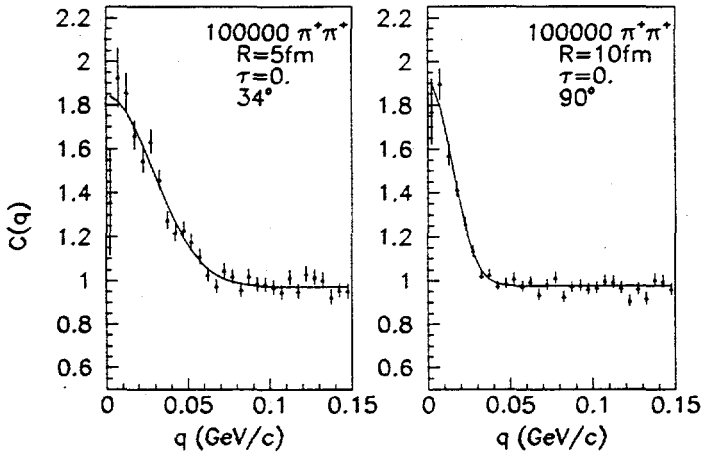

Figure 6. The two-pion correlations as a function of the relative momentum. The left panel is for the spectrometer at 34° and a 5 fm source and the right panel for the spectrometer at 90° and a 10 fm source. The solid lines are fits to the correlation function.

this simulation does serve to illustrate that the spectrometer has sufficient acceptance to make modest measurements of the pion-pair correlation function.

The pair density in q-q_o space is shown in the left panel of Fig. 8. This density distribution is typical for small-aperture spectrometers. The $\vec{q}$ of the accepted pairs is nearly always parallel to $\vec{\beta}^*$, the center of mass velocity of the pion pair, which is a direct result of the small aperture. Therefore, the analysis will be sensitive to distances along the " line-of-sight". The spectrometer does not have sensitivity to the cylindrical coordinate Q_{side}[13] because of the small vertical aperture.

The pion correlation analysis requires good two-track spatial resolution . The right panel of Fig. 8 shows the correlation between the separation distance at the back of TPC1 verses the relative momentum, $|\vec{q}|$ for pion pairs. The present design goal for the TPC is for two tracks to be resolved at a separation distance of 1-1.5 cm. Fig. 8 demonstrates that most pairs with $|\vec{q}| > 10$ MeV/c should be resolved. The interferometry analysis was repeated in which all pairs with distances of separation less than 2 cm at the exit of TPC1 were removed. The fitting results are shown in Fig. 7 for sources of radii 7fm and 10fm for the spectrometer at 34°. Only a modest decrease in sensitivity with no systematic distortion is found for these source sizes.

The spectrometer acquires 0.2 $\pi^+\pi^+$ pairs per central collision event when operating at 34°,y≈1.2 . Assuming a π^+ rapidity density of 350, see Fig. 1, about 7 hours of data taking are required to accumulate 100,000 $\pi^+\pi^+$. A similar number of π^- pairs would be obtained simultaneously. The running time at 90° to accumulate comparable statistics is an order of magnitude longer. Kaons pairs are acquired at a substantially lower rate and

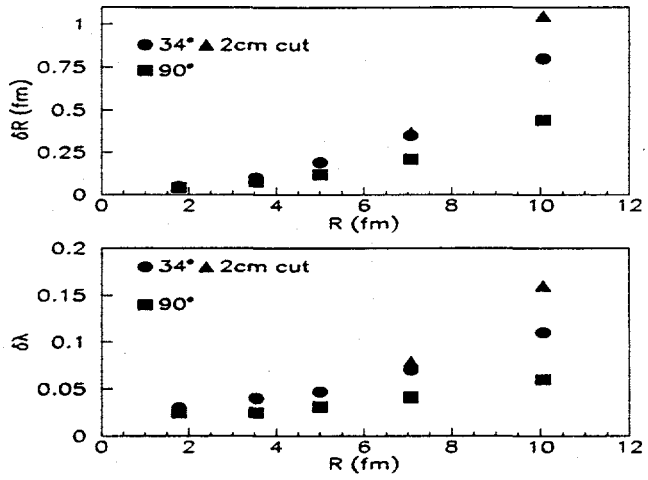

Figure 7. Sensitivity to the radius and intercept parameters presented as a function of radius for the 100,000 accepted pion pairs. See text for details.

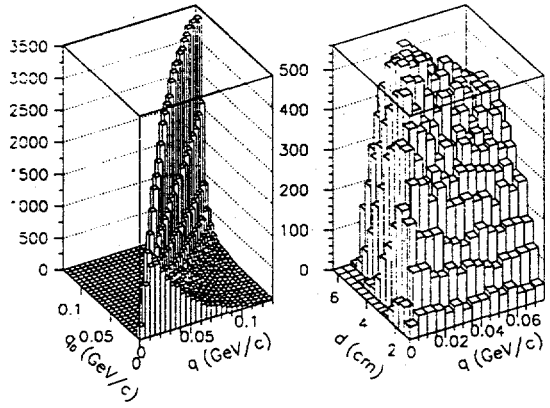

Figure 8. The pair densities given in counts per bin are shown for q-q_o (left) and q-d (right) spaces, as described in the text.

only limited statistics are expected to be achieved for kaon interferometry analysis. The pion correlation analysis achieved with the BRAHMS midrapidity spectrometer should complement the studies of the larger aperture experiments, which will typically be at lower y and p_t.

5. SUMMARY

The present models exhibit substantial differences in the predicted rapidity distributions as demonstrated in Fig. 1. Measurements of the particle yields and p_t spectra over the widest possible range of rapidity will be important in understanding the dynamics of the hot dense phase of nuclear matter created by relativistic heavy ion collisions at RHIC.

6. ACKNOWLEDGEMENTS

I would like to thank J.H. Lee, B. Moskowitz,J. Olness, and F. Videbæk for useful discussions. Finally, it is a pleasure to thank the workshop organizers, T. Hallman and J. Thomas, for their efforts in making this workshop proceedings possible.

REFERENCES

1. Conceptual Design Report for the Solenoidal Tracker at RHIC, The STAR collaboration, PUB-5347 (1992).
2. The PHENIX Conceptual Design Report, The Phenix Collaboration, BNL-48922 (1993).
3. D. Barton *et al.*, PHOBOS Conceptual Design Report, Brookhaven national Laboratory (1993).
4. K. Ashktorab *et al.*, BRAHMS Conceptual Design Report, Brookhaven National Laboratory (1994)
5. K. Werner, Z. Physics **C42** (1989) 85.
6. B. Anderson, G. Gustafson, and B. Nielsson-Almqvist, Nucl. Phys. **B281** (1987) 289.
7. Th. Schönfeld *et al.*, Mod. Phys. Lett **A8** (1993) 2631; Th Schönfeld *et al.*, Nucl. Phys. **A544** (1992) 439c; H. Sorge, private communication (1995).
8. B. Moskowitz, contribution to this volume.
9. R. Hanbury Brown and R. Q. Twiss, Nature **178** (1956) 1046.
10. G. Goldhaber *et al.*, Phys. Rev. **120** (1960) 300.
11. F. B. Yano and S. E. Koonin, Phys. Lett. **78B** (1978) 556.
12. Scott Pratt, Phys. Rev. Lett. **53** (1984) 1219.
13. G. Bertsch, Nuclear Physics **A498** (1989) 173c.

Hadron Distributions at Higher Rapidity Using the BRAHMS Forward Spectrometer

Bruce Moskowitz[a] *
for the BRAHMS Collaboration[b]

[a]Physics Department, Brookhaven National Laboratory,
Upton, New York 11973, U.S.A.

[b]BNL, CRN-Strasbourg, NBI-Copenhagen, CIAE-Beijing, NYU, Texas A&M,
UCSSL-Berkeley

Different conditions, and therefore different physics, are expected to exist over the range of rapidities at RHIC. The BRAHMS Forward Spectrometer will measure identified hadron distributions up to y=4, giving it a unique place in the RHIC experimental program.

1. WHY MAKE MEASUREMENTS AT HIGHER RAPIDITY?

The primary motivation for performing experiments at RHIC is to search for signs of the formation of a quark-gluon plasma. Regardless of whether such a state of matter is convincingly discovered or not, it is important that the basic conditions existing in RHIC collisions be well described in terms of energy and baryon density, thermodynamic and hydrodynamic properties, hadronization, etc. Since different conditions will certainly exist at different rapidities, experiments should investigate the regions of higher rapidity as well midrapidity.

2. SOFT PARTICLE SPECTRA

The dominant region of particle distributions from RHIC collisions is expected to be the "soft" part with transverse momentum $p_T < 2$ GeV/c. The QCD theory is highly non-perturbative in this regime of relatively large distances, but string models may be used to characterize particle production. Three popular models for nucleus-nucleus collisions, all of which are based in part on string theory and in part on scaling from p+p data, particularly from the CERN ISR ($\sqrt{s}$=24–63 GeV), are compared in Fig. 1. Plotted are the predictions of Fritiof[1], Venus[2] and RQMD[3] for the rapidity distributions of net baryons and of mesons from central Au+Au collisions at $\sqrt{s}$=200 GeV per nucleon pair. Note that the RQMD predictions for the net baryon distribution differ from those presented at Quark Matter '91[4] due to the correction of a computational error[5].

*This research was supported by the U.S. Department of Energy under contract no. DE-AC02-76CH00016.

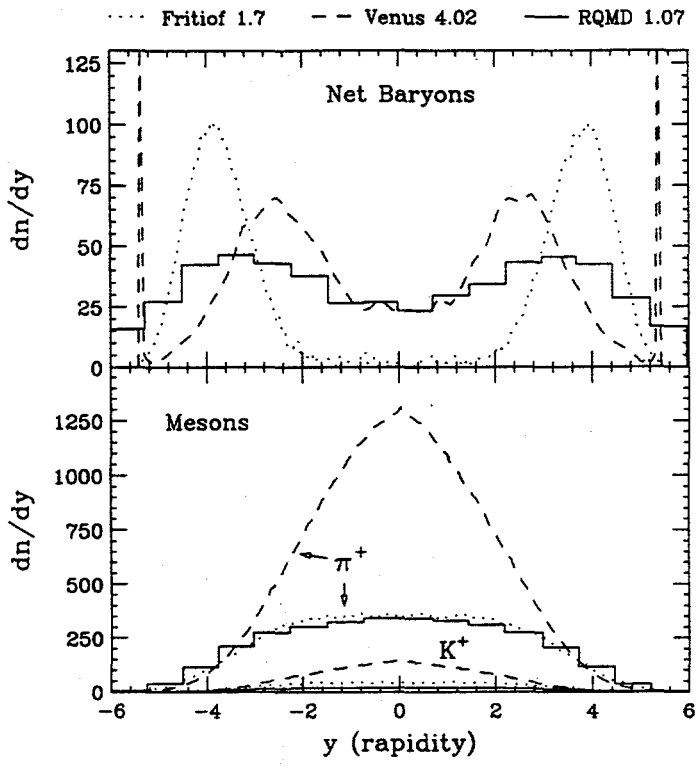

Figure 1. Rapidity distributions for net baryons (top panel) and mesons (bottom panel) from central Au+Au collisions at 200 GeV per nucleon pair as predicted by Fritiof 1.7 (dotted curves), Venus 4.02 (dashed) and RQMD 1.07 (solid, from Ref. [3]).

2.1. Baryon stopping

One of the most basic questions concerning RHIC is how high the net baryon density (i.e., the difference between baryons and antibaryons) will be in the central regions of Au+Au collisions. As seen in the top panel of Fig. 1, the net baryon dn/dy at midrapidity vanishes for Fritiof. Furthermore, Fritiof predicts the baryon "stopping power", i.e., the mean rapidity shift per projectile baryon, to be $<\Delta y>=1.9$ units. (Recall that the beam rapidity is ± 5.6.) By comparison, an analysis of fixed target data at $\sqrt{s}$=14 GeV yields $<\Delta y>=0.95\pm0.15$ for p+p and $<\Delta y>=1.9\pm0.3$ for p+Pb[6]. A new, improved compilation of p+p data from $\sqrt{s}$=5–27 GeV gives the value of $<\Delta y>=0.7$, independent of the beam energy[7].

For both Venus and RQMD, the net baryon dn/dy at midrapidity is approximately 25, but Venus displays a higher stopping power: $<\Delta y>=3.1$ units, versus 2.6 units for RQMD. The authors of RQMD emphasize the importance of baryon-meson rescattering (responsible for 25% of the stopping in RQMD) and note, " ... different y bins exhibit different physics (both in the baryon and meson sectors). It will be important to study experimentally a broad range of rapidities, not only the central rapidity slice."[3]

2.2. Meson distributions

The predictions for meson production are given in the bottom panel of Fig. 1. At issue is whether there will be in Au+Au the more or less flat "boost-invariant" plateau at midrapidity (± 2 units wide) that has been observed for p+p (p+$\bar{\text{p}}$) reactions over the range $\sqrt{s}$=24–900 GeV[8,9]. Also to be addressed is the question of strangeness production and the K/π ratio.

3. MINIJETS

Hard scatterings which produce "minijet" particles with $p_T > 2$ GeV/c are a probe of dense matter. Much can be learned about nuclear effects such as jet quenching and gluon shadowing from the inclusive minijet distributions[10,11]. The Hijing model[10] combines the Pythia[12] implementation of perturbative QCD for hard processes with elements of the Dual Parton Model[13] and Fritiof[1] for the soft processes. An alternative calculation is the Parton Cascade Model[14] with a cluster hadronization scheme[15]. Both of these models reproduce well the data from p+p and p+$\bar{\text{p}}$ reactions at collider energies[15,16].

The predicted charged particle $dn/d\eta$ of the two models is shown in Fig. 2, with the various physical processes turned on successively, as indicated. The parton shadowing is mainly determined from the gluon nuclear structure function, about which little is presently known; the model calculations are based on quark nuclear structure functions. The STAR Experiment at RHIC plans to measure the gluon nuclear structure function via the reaction p+Au $\rightarrow \gamma$+jet [17]; after those data are obtained the model calculations may be improved. The quenching processes, too, are determined to a large extent by gluon physics, namely the induced gluon bremsstrahlung energy loss. As seen in Fig. 2, Hijing shows no effects of quenching for $\eta \geq 2$, whereas the Parton Cascade-Cluster Hadronization Model shows quenching effects to be still important for $2 \leq \eta \leq 3$.

Figure 3 shows the invariant cross-section ratio

$$R^{\text{Au/p}} = \frac{\left[dn/d(p_T^2)\right]_{\text{Au+Au}}}{\left[dn/d(p_T^2)\right]_{\text{p+p}}} \qquad (1)$$

at midrapidity versus the transverse momentum, p_T, where Au+Au and p+p are at the same beam energy per nucleon. The model dependence of this ratio is striking, and the need to measure out to, say, p_T=6 GeV/c is evident. Furthermore, the rapidity dependence of these distributions is a means of constraining the models.

4. THE BRAHMS EXPERIMENT

The BRoad Range Hadron Magnetic Spectrometers (BRAHMS) Experiment[18,19] is designed to measure identified charged hadrons ($\pi^{\pm}$, $\text{K}^{\pm}$, $\text{p}^{\pm}$) over a wide range of rapidity and transverse momentum for all beams and energies available at RHIC. Due to the different conditions at midrapidity and at more forward angles, the experiment uses two movable spectrometers for the two regions. As the layout in Fig. 4 shows, there is a Midrapidity Spectrometer to cover the laboratory polar angles $30° \leq \theta \leq 90°$ ($0 \leq \eta \leq 1.3$) and a Forward Spectrometer to cover the angles $2° \leq \theta \leq 30°$ ($1.3 \leq \eta \leq 4.0$). The Midrapidity

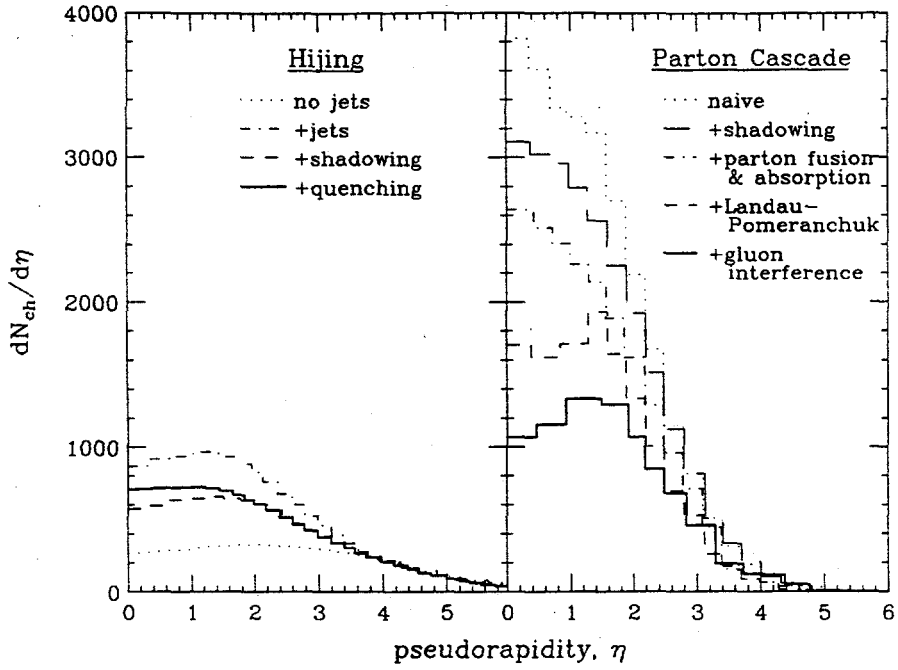

Figure 2. The charged particle distribution, $dN_{ch}/d\eta$, for central Au+Au collisions at RHIC as predicted by Hijing (left panel, from Ref. [11]) and the Parton Cascade Model (right panel, from Ref. [15]). The different curves show the effects of successively turning on various physical processes, with the full calculation given by the dark, solid histogram.

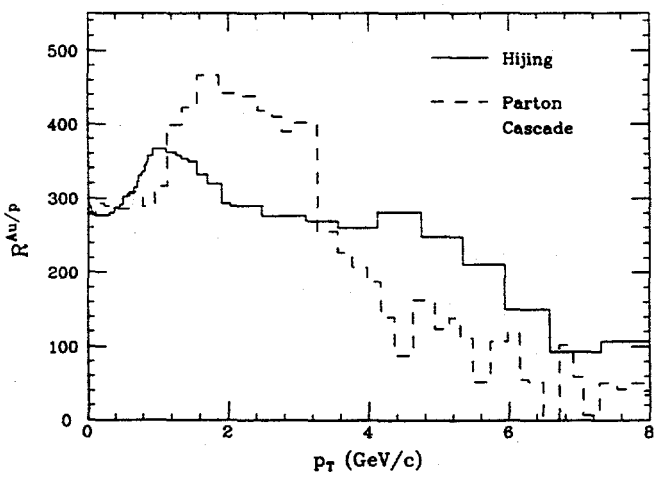

Figure 3. The ratio of the invariant cross-section from central Au+Au to that of p+p, as a function of p_T, from Hijing (Ref. [11]) and the Parton Cascade Model (Ref. [15]). Both reactions are at a c.m. energy of 200 GeV per nucleon pair.

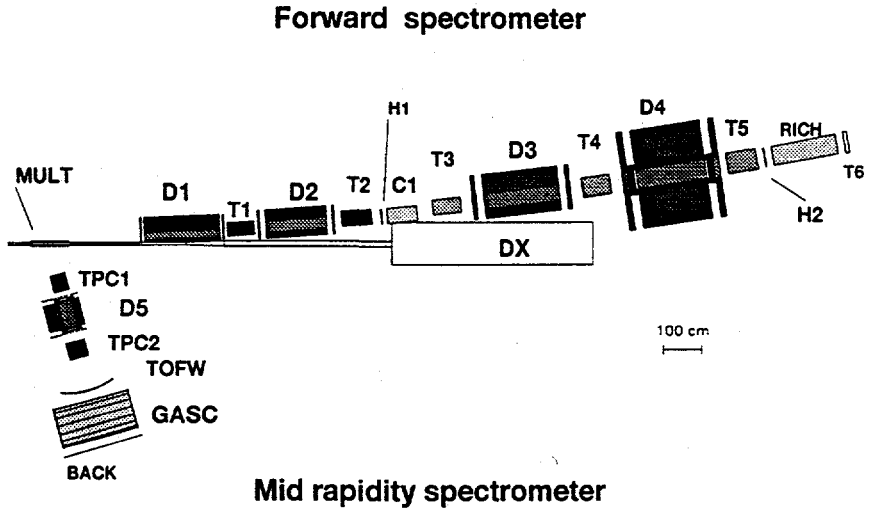

Figure 4. Plan view of the BRAHMS spectrometers. Both spectrometers are freely rotating: the forward arm is shown at θ=2° and the midrapidity arm at 75°. DX is the RHIC final focusing beam magnet.

Spectrometer is described in the contribution to these proceedings by D. Beavis[20], and is not discussed further here. Greater detail on all aspects of BRAHMS may be found in the Conceptual Design Report[19].

The Forward Spectrometer employs four dipole magnets, D1–D4, each of which has a maximum bending power of 2.4 T-m. D1 has a septum design, in order to allow positioning as close as possible to the beampipe, and has a fringe field on the collider beam of only 7 gauss. Tracking is performed by time projection chambers T1, T2 and T3, followed by drift chambers T4 and T5. Particle identification is achieved with time-of-flight hodoscopes H1 (at 9 m from the vertex) and H2 (at 20 m from the vertex), threshold Čerenkov counter C1 and ring-imaging Čerenkov counter RICH. The Forward Spectrometer moves in two pieces: the front arm consisting of D1–C1 can rotate over the range $2° \leq \theta \leq 30°$ ($1.3 \leq \eta \leq 4.0$), whereas the full spectrometer D1–T6 is restricted to $2° \leq \theta \leq 15°$ ($2.0 \leq \eta \leq 4.0$). The solid angle acceptance of the spectrometer is 0.8 msr.

BRAHMS also has a silicon strip multiplicity detector, MULT, which is based on the design of the PHOBOS vertex detector[21]. MULT covers the region $|\eta| \leq 2.5$ and provides the first-level centrality trigger for the experiment. The start signal for the time-of-flight system will come from beam-beam counters (not shown in Fig. 4) which will also perform a crude vertex position determination.

4.1. Acceptance of BRAHMS

The overall acceptance in (y, p_T) space of pions, kaons and protons for BRAHMS is shown in Fig. 5. The total BRAHMS rapidity coverage is $0 \leq y \leq 3.5$ for protons and $0 \leq y \leq 4.0$ for mesons (c.f. Fig. 1). To emphasize how the broad coverage of BRAHMS contributes to the RHIC program, the single pion acceptances of the four baseline RHIC

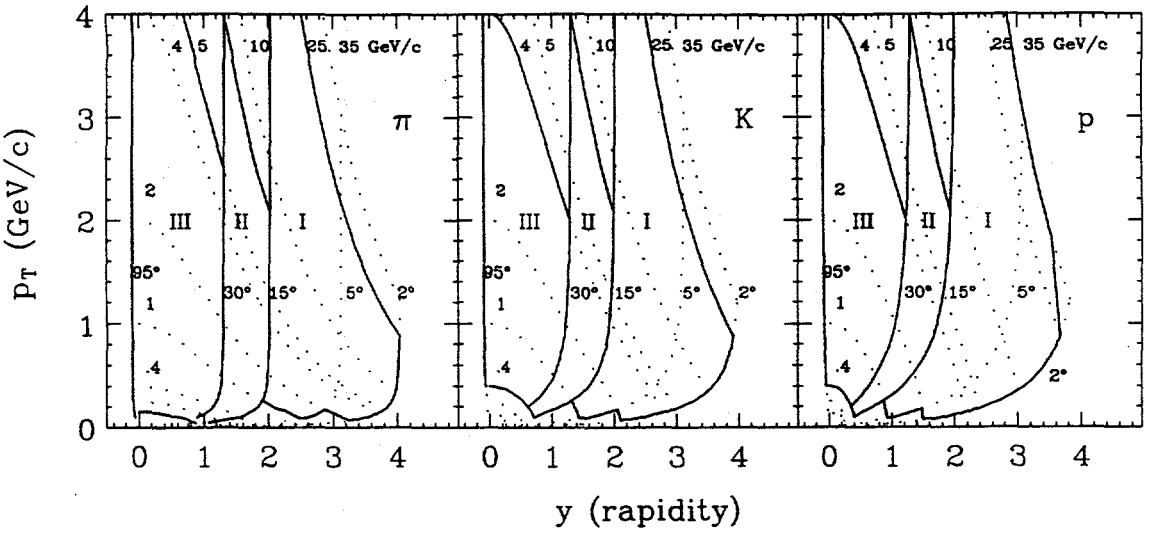

Figure 5. The acceptance of BRAHMS in (y, p_T) space for pions (left frame), kaons (middle frame) and protons (right frame). Region I is with the full Forward Arm, Region II is for the D1–C1 section of the Forward Arm alone, and Region III is with the Midrapidity Arm.

experiments are compared in Fig. 6.

4.2. Expected track density

The expected charged particle multiplicities in the Forward Spectrometer tracking chambers for different momentum settings are given in Table 1. The worst case of θ=2° and the model Venus is taken, yet the particle densities of $\leq$0.04 cm^{-2} do not present a major experimental difficulty.

4.3. Particle identification

The regions of π/K and K/p separation for the various particle identification counters are shown in Fig. 7. The time-of-flight discrimination is set at the 4σ level, where σ = 75 ps is the rms timing resolution. The highest momenta are covered by the RICH counter: π/K up to p=25 GeV/c and K/p up to p=35 GeV/c. Data from successful in-beam tests of a prototype RICH counter with a multianode photomultiplier readout[22] are presented in Fig. 8.

5. COUNTING RATES IN THE FORWARD SPECTROMETER

Event-generating models have been used to estimate the counting rates in the Forward Spectrometer for central Au+Au collisions. Table 2 lists the running time necessary to get high quality soft particle spectra, allowing for accurate determinations of the slope parameter, etc. Fritiof is used since this gives the lowest rates, and 50 events/sec is assumed. The full soft physics program will require about half a year at the RHIC design

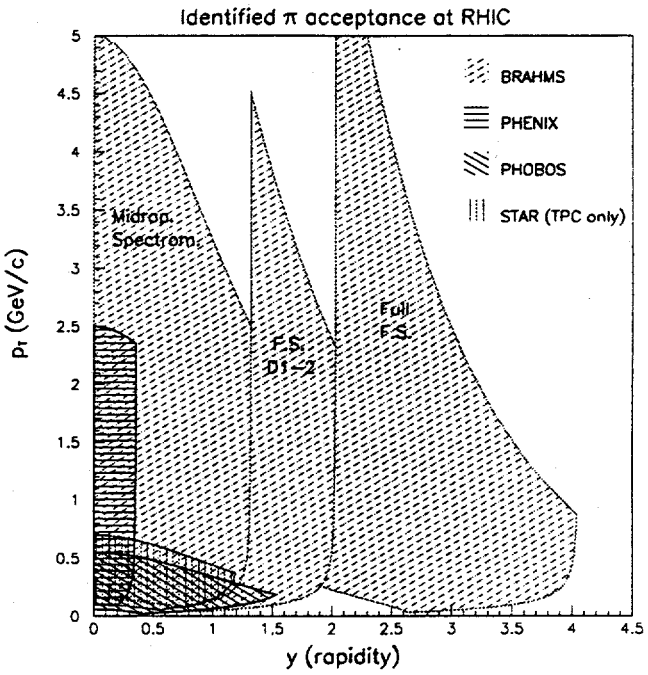

Figure 6. The identified pion acceptance for the four baseline RHIC experiments.

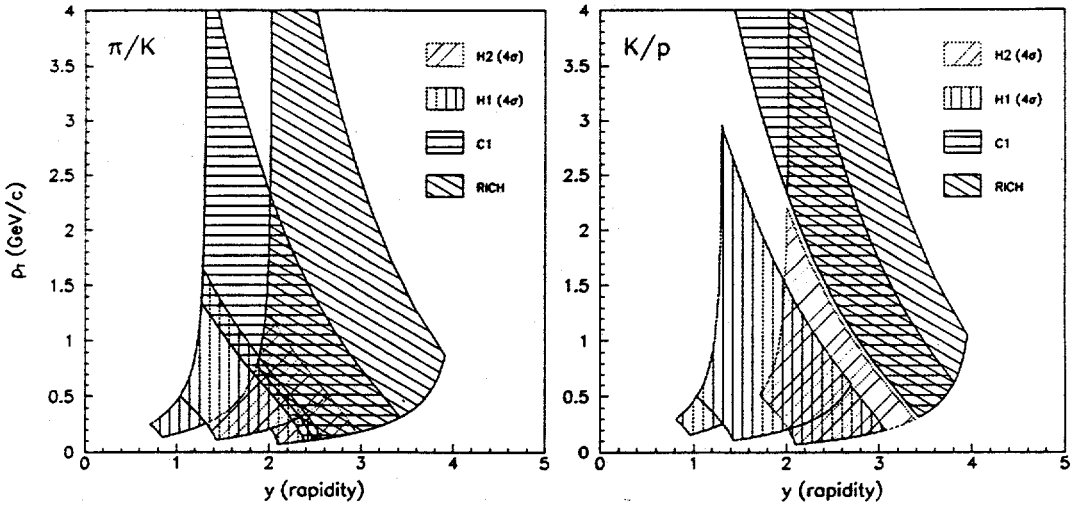

Figure 7. Coverage of the various particle identification counters in the BRAHMS Forward Spectrometer. The left panel shows the π/K separation and the right panel shows K/p.

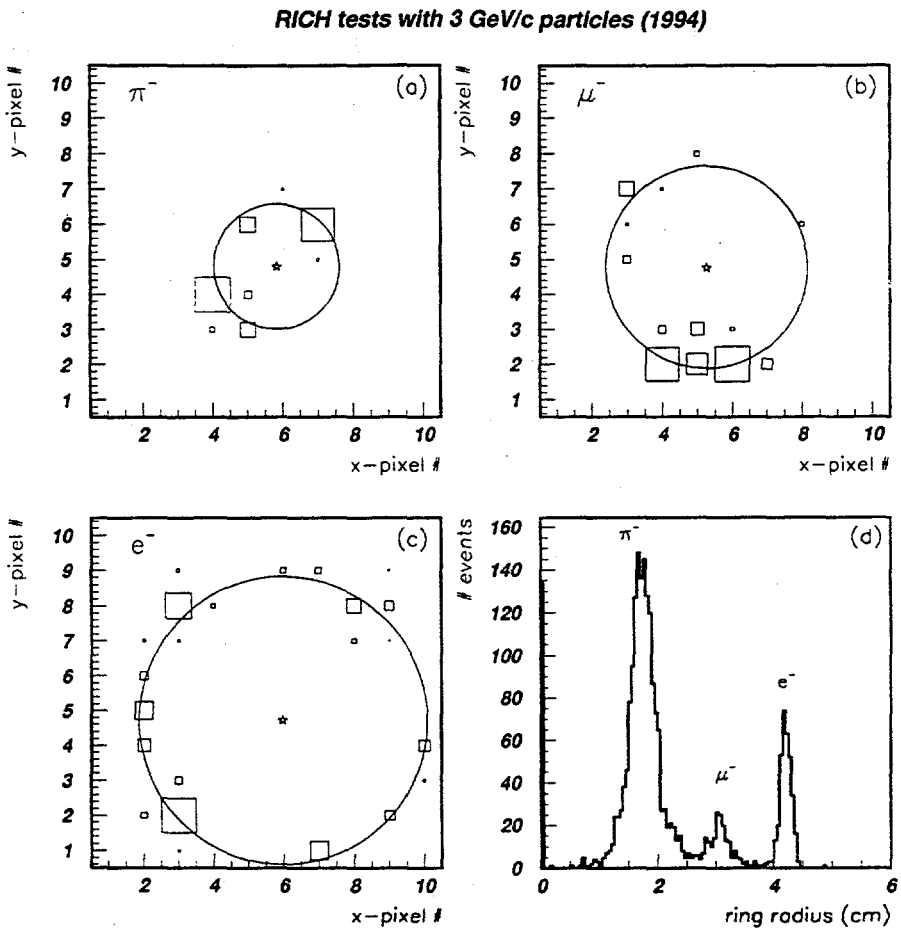

Figure 8. Results from Ref. [22] for a prototype RICH counter with a test beam of 3 GeV/c negative particles. Panels a, b and c show individual events with fitted rings; the ring centers are shown as stars and come from independent drift chamber tracking. Panel d is a histogram of the fitted ring radius from the entire run, showing peaks identified as π^-, μ^- and e^-.

luminosity.

A similar listing of running times for the minijet inclusive spectrum is found in Table 3. In this case, the demands on the statistics are not as strict as they were for the soft spectra, and we are willing to set a large p_T bin size (0.5 GeV/c). The table uses the predictions of Hijing, but Fritiof gives similar results. A minimum measurement to p_T=6 GeV/c at y=2 will require about one week of running time. BRAHMS will also be able to identify the minijet particle specie, allowing for "flavor tagging".

6. SUMMARY AND OUTLOOK

In conclusion, it should be emphasized that BRAHMS will be ready to take data on the day that RHIC turns on, and will handle all beams and energies. The broad range of data measured by the BRAHMS Experiment will provide extensive constraints on the conflicting models and will lead to a better understanding of the conditions produced in RHIC collisions.

7. ACKNOWLEDGEMENTS

I am grateful to my colleagues J.H. Lee, D. Beavis and F. Videbæk for their help in preparing the figures for this paper. W. Christie kindly provided the Hijing events used in the minijet rate calculation. Finally I thank the organizers, T. Hallman and J. Thomas, for all their efforts in making this workshop a reality.

REFERENCES

1. B. Andersson, G. Gustafson and B. Nielsson-Almqvist, Nucl. Phys. B281 (1987) 289.
2. K. Werner, Z. Physics **C42** (1989) 85.
3. Th. Schönfeld, H. Stöcker, W. Greiner and H. Sorge, Mod. Phys. Lett. **A8** (1993) 2631.
4. Th. Schönfeld *et al.*, Nucl. Phys. **A544** (1992) 439c.
5. H. Sorge, private communication (1995).
6. W. Busza and A.S. Goldhaber, Phys. Lett. **B139** (1984) 235; W. Busza and R. Ledoux, Ann. Rev. Nucl. Part. Sci. **38** (1988) 119. Unfortunately, this type of analysis has not yet been extended to collider energies.
7. F. Videbæk, private communication (1995).
8. W. Thomé *et al.*, Nucl. Phys. **B129** (1977) 365.
9. UA5 Collaboration, G.J. Alner *et al.*, Z. Phys. **C33** (1986) 1.
10. X.N. Wang and M. Gyulassy, Phys. Rev. **D44** (1991) 3501.
11. X.N. Wang and M. Gyulassy, Phys. Rev. Lett. **68** (1992) 1480.
12. T. Sjöstrand and M. van Zijl, Phys. Rev. **D36** (1987) 2019.
13. A. Capella, U. Sukhatme and J. Tran Tranh Van, Z. Phys. **C3** (1980) 329.
14. K. Geiger and B. Müller, Nucl. Phys. **B369** (1992) 600.
15. K. Geiger, Phys. Rev. **D47** (1993) 133.
16. X.N. Wang and M. Gyulassy, Phys. Rev. **D45** (1992) 844.
17. W. Christie, contribution to this volume.
18. F. Videbæk, Nucl. Phys. **A566** (1994) 299c.
19. K. Ashktorab *et al.*, BRAHMS Conceptual Design Report, Brookhaven National Laboratory (1994). This document is also available through the World Wide Web at address http://rsgi01.rhic.bnl.gov/export1/brahms/WWW/cdr/cdr.html.
20. D. Beavis, contribution to this volume.
21. D. Barton *et al.*, PHOBOS Conceptual Design Report, Brookhaven National Laboratory (1994).
22. R. Debbe *et al.*, BNL-61218, to be published in Nucl. Instrum. and Methods A (1995).

Table 1
Expected average charged particle multiplicities per event in the tracking chambers of the Forward Spectrometer, from GEANT simulations with 400 central Au+Au Venus events. The θ=2.1° angular setting for the spectrometer is assumed.

Momentum setting	Detector	# primaries	# secondaries	Total #	Density (particles/cm^2)
2–5 GeV/c	T1	6.6	10.0	16.5	0.04
"	T2	2.4	1.4	3.8	0.01
7.5–15 GeV/c	T2	4.1	3.5	7.6	0.02
"	T3	2.7	4.4	7.1	0.007
"	T4	1.5	0.8	2.4	0.002
"	T5	1.0	0.5	1.6	0.001
15–30 GeV/c	T2	2.2	2.5	4.7	0.01
"	T3	1.2	4.6	5.9	0.006
"	T4	0.6	1.0	1.6	0.001
"	T5	0.3	0.5	0.8	0.0004

Table 2
Counting rates for the soft physics spectra in the BRAHMS Forward Spectrometer for Au+Au central collisions, assuming 50 events/sec are written to tape. The model used is Fritiof 1.7 and 1000 π^+ are required to be in the highest p_T bin, with a bin size of 40 MeV/c.

Angle θ	Highest p_T bin (GeV/c)	p_{max} (GeV/c)	counts/collision in bin	time at p_{max} (hrs.)	total time at angle (hrs.)
3°	1.26-1.30	25	3×10^{-3}	2	3
5°	1.96-2.00	23	5×10^{-4}	12	20
10°	1.96-2.00	12	3×10^{-4}	18	28
15°	1.96-2.00	8	1×10^{-4}	56	80

Table 3
Counting rates for minijets in the BRAHMS Forward Spectrometer for Au+Au central collisions, assuming 50 events/sec are written to tape. The model used is Hijing 1.0 and 100 protons are required to be in the highest p_T bin, with a bin size of 0.5 GeV/c.

Angle θ	Highest p_T bin (GeV/c)	p_{max} (GeV/c)	counts/collision in bin	time at p_{max} (hrs.)
15° (y=2)	4.5-5.0	19	8×10^{-6}	70
15° (y=2)	5.5-6.0	23	3×10^{-6}	160

PHOBOS Physics Capabilities

Mark D. Baker[a] for the *PHOBOS* Collaboration *

[a]Laboratory for Nuclear Science, Massachusetts Institute of Technology,
MIT 26-407, 77 Mass. Ave, Cambridge, MA 02139

PHOBOS is the name of a detector and of a research program to study systematically the physics of relativistic heavy-ion collisions over a large range of impact parameters and nuclear species. Collisions with a center of mass energy of 200 $A\ GeV$ at RHIC are expected to produce the highest energy densities ever accessible in the laboratory.

In this writeup, we outline the physics capabilities of the *PHOBOS* detector and describe the detector design in terms of the general philosophy behind the *PHOBOS* research program. In order to make the discussion concrete, we then focus on two specific examples of physics measurements that we plan to make at RHIC: $dN/d\eta$ for charged particles and the mass spectrum from $\phi \rightarrow K^+K^-$ decays.

1. Overview

The aim of the *PHOBOS* research program is to study the collective behavior of hadronic matter under conditions of extreme energy density. This is interesting in its own right, but the primary goal is to see if, under these conditions, there are manifestations of new physics, such as a deconfinement phase transition leading to a Quark-Gluon Plasma (QGP). In particular, we know that there are partons in the nucleus, but we would like to see some evidence of long-range collective partonic phenomena. If new physics is discovered, the aim will shift to a thorough study of the new phenomena. This should lead to a better understanding of confinement and of the structure of the vacuum in strong interactions.

The central philosophy underlying the design of the *PHOBOS* detector is that we are entering a new physics regime and that theory can only provide us with rough guidance. For this reason we must examine our collisions in as unbiased a way as possible. We plan

*The *PHOBOS* collaboration includes members from the following institutions: Argonne National Laboratory, Brookhaven National Laboratory, Institute of Nuclear Physics Krakow, Jagiellonian University Krakow, Massachusetts Institute of Technology, Oak Ridge National Laboratory, University of Illinois at Chicago, University of Maryland, and Yale University. Special thanks to **Vince Cianciolo** and **Robin Verdier** for many of the figures.

to achieve this by studying the production of all hadronic particles in a detector which has essentially 4π coverage event-by-event and a high data taking rate - allowing the use of a minimum bias trigger. We can measure $d^2N/d\eta d\phi$ as well as the total charged multiplicity for every *Au-Au* collision within ± 10 cm of our nominal vertex. This should provide a rich unbiased database for the study of these collisions.

If a Quark Gluon Plasma is formed in such a collision, the color deconfinement will lead to a larger number of thermodynamic degrees of freedom — more entropy content — than would be present in the initial stages of the collision. This will be true even though the system will be thermodynamically small and even if the system doesn't fully equilibrate. In order to hadronize again without losing entropy, the system will have to undergo a large expansion, live a long time, and generate many more particles than a purely hadronic system would. If the transition is first order, we may be able to see a rapid change in some variable as a function of centrality or beam energy. If, instead, the transition is higher order, the entropy argument still holds — the system should still show expansion, long lifetime, and large particle production. Such a higher order phase transition would be more difficult to see because most variables wouldn't undergo a sharp change, but the large effects should still occur.

Therefore, we designed our detector assuming that long times, large volumes, and increased particle production will be associated with the phenomena of interest. Since large-volume collective phenomena are generally associated with lower values of p_T, we emphasized our ability to measure particles and also pairs of particles at low p_T. Another advantage of the $\mathcal{PHOBOS}$ configuration is that we will be able to make fairly subtle measurements in the mid-rapidity, low p_T region, such as the mass and width of the ϕ.

To summarize the above discussion, we want our detector to be able to handle large multiplicities, and we want it to be sensitive to low p_T particles, to large source sizes (through Bose-Einstein correlations), and to subtler effects, such as a change in the ϕ mass or width. In order to accomplish these goals, our detector consists of two parts: a multiplicity detector covering almost the entire psuedorapidity range of the produced particles and a two-arm spectrometer at mid-rapidity. Figure 1 shows the entire PHOBOS detector, including the spectrometer arms, the multiplicity and vertex array, and the lower half of the magnet. Figure 2 shows the multiplicity and vertex array alone.

The multiplicity detector covers the range $-5.4 < \eta < +5.4$, measuring total charged multiplicity, $dN/d\eta$, and even $d^2N/d\eta d\phi$ over almost the entire phase space. The focus of the spectrometer is on detailed measurements for central rapidity and low p_T. It covers about 0.4 radians in azimuth and one unit of pseudorapidity in the range $0 < \eta < 2$, depending on the interaction vertex, allowing us to measure the momenta and species of particles with p_T down to 40 MeV/c. Both detectors are read out together and are easily capable of handling the 600 Hz minimum bias rate expected for all collisions (within 10 cm of the nominal interaction point) at the nominal luminosity. More details can be found in the $\mathcal{PHOBOS}$ Conceptual Design Report [1].

The following sections discuss the $\mathcal{PHOBOS}$ detector capabilities in the context of two

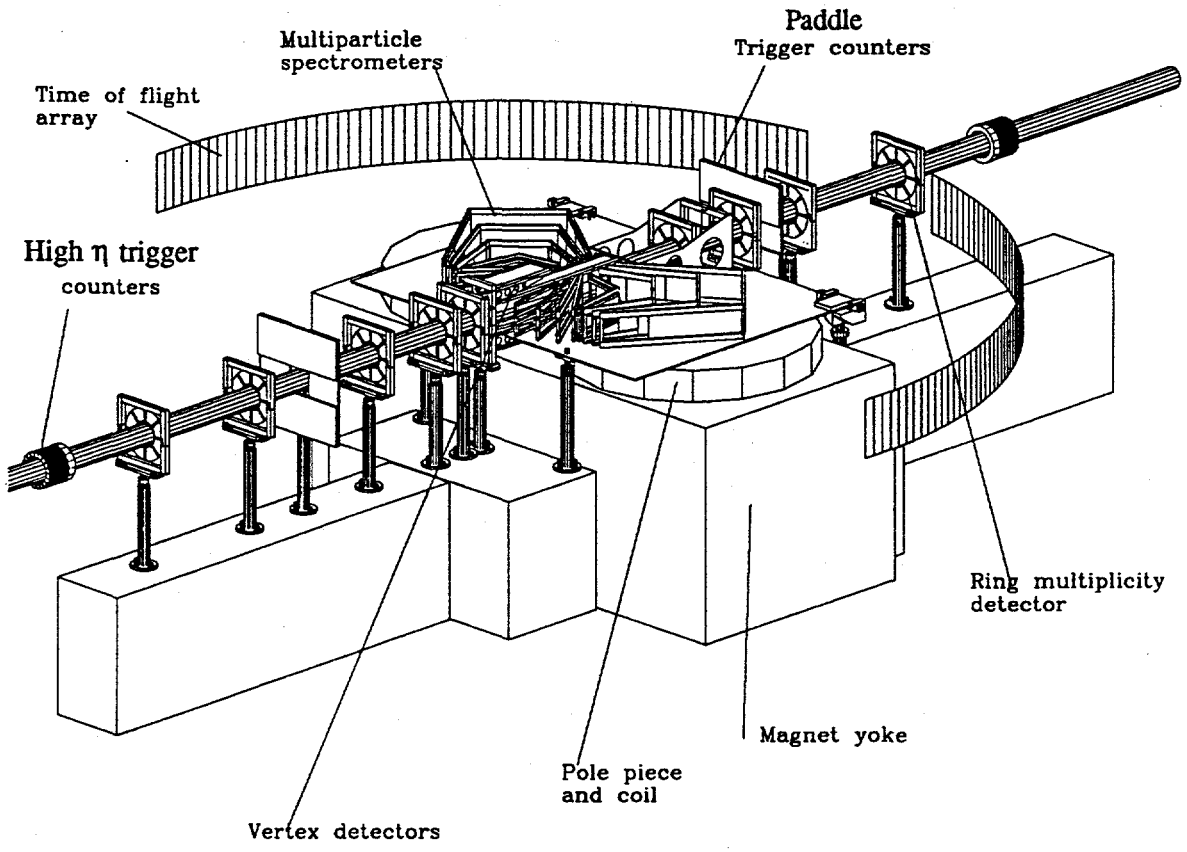

Figure 1. The PHOBOS detector.
The PHOBOS beam pipe, multiplicity and vertex detectors, spectrometer arms, lower half of the magnet, and a schematic TOF detector.

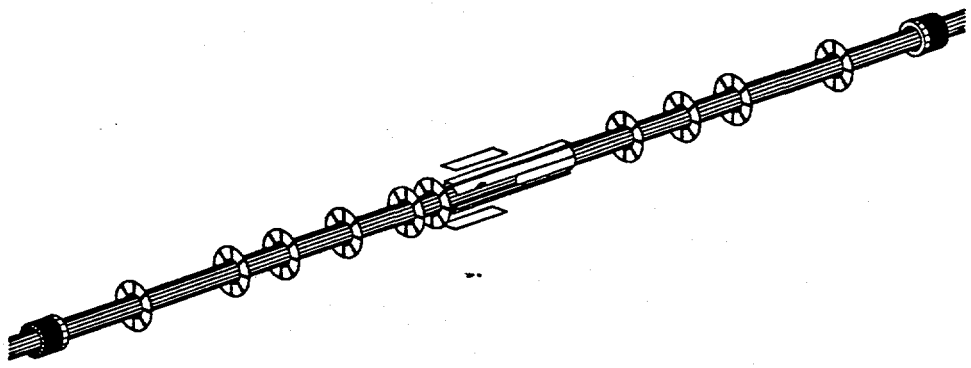

Figure 2. The PHOBOS multiplicity detector.
The PHOBOS beam pipe, multiplicity ring and barrel detectors, and vertex detector.

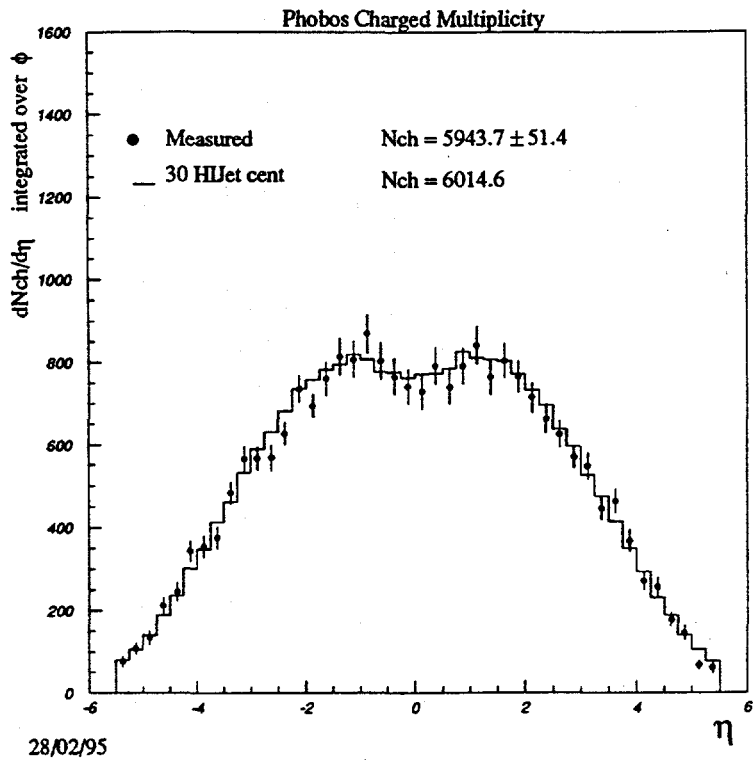

Figure 3. PHOBOS Single Event Multiplicity Measurement.
This plot illustrates our ability to measure $dN/d\eta$ on an event-by-event basis. The points show the results for a single central event using a full HIJET + GEANT simulation and multiplicity detector analysis. The histogram shows the average of 30 central HIJET events as generated.

specific examples of measurement topics: event-by-event $dN/d\eta$ and the mass and width of the ϕ meson. For a related discussion of the Bose-Einstein correlation measurement capabilities of $\mathcal{PHOBOS}$, see Günther Roland's contribution to these proceedings [2].

2. Multiplicity and $dN/d\eta$

Figure 3 illustrates our ability to measure $dN/d\eta$ as well as total N on an event-by-event basis. The curve represents the average of 30 central HIJET events as generated while the data points represent the measured value for $dN/d\eta$ for a single event resulting from a full GEANT simulation of the detector followed by a complete analysis, including corrections. The measurement is high precision (1% in total N) and covers almost the full acceptance. Because of our high rate capability, we can take 600 Hz of minimum bias data, or 60 Hz of central (10%). Figure 3 therefore represents 16 ms of beam time. We also have segmentation in ϕ, allowing a measurement of $dN/d\eta d\phi$ in bins of size $\Delta\phi = \pi/8, \Delta\eta = 0.25$ with errors bars 4 times larger than the corresponding ones in figure 3.

If there is a QGP, it is likely that the most striking signature will be a large tail of high multiplicity events in the total multiplicity distribution. This signature can then be correlated with other measurements to enhance other signals. Another, more subtle, signature of a phase transition would be fluctuations in the multiplicity distribution. In order to examine our sensitivity to such fluctuations, we added an anomaly to the single event and then compared it to 30 "normal" events from the Monte Carlo. In practice, such a comparison would be made with the average of hundreds or thousands of events with a similar multiplicity.

We chose to examine anomalies that contain more than 170 charged particles produced isotropically in some frame. For definiteness, we used Sean Gavin's model for the pion emission from disordered chiral condensates (*DCCs*) [3]. In this model, pions are emitted isotropically from a source in the central rapidity region. We chose the case where the *DCC* emits only charged pions. Since the largest *DCC* considered by Gavin (4 fm) yields very few particles ($\sim$ 85) compared to the several thousands that are created in the conventional hadronic fireball, we considered instead artificially enhanced signals. The first artifically enhanced signal consisted of simply doubling the number of particles to 170. In the model this corresponds to doubling the energy density in the *DCC* from 60 MeV/fm^3 to 120 MeV/fm^3. The second artificially enhanced signal was generated by assuming an even larger radius of 6 fm, yielding $\sim$ 280 particles.

Figures 4 and 5 show the measured distribution resulting from anomalous signals containing more than 170 particles with an isotropic distribution. Clearly if the particles were more focussed in either η or ϕ, we could pick out an even smaller signal on an event-by-event basis. Also, by measuring rapidity and phi correlations, we may be able to pick out smaller signals on a statistical basis.

3. ϕ Mass and Width

An interesting effect that has been predicted, but not yet seen, is the changing of resonance masses and widths in hot hadronic matter. Observing such a change would teach us something about high temperature QCD. These effects can be quite large. For instance, Lissauer and Shuryak [4] predict an increase in the ϕ width of a factor of 2–3 in the mid-rapidity region for central collisions at RHIC. The effect is dominated by low p_T ϕs in the midrapidity region, where *PHOBOS* excels.

Broadly speaking, there are two complementary ways to pursue these effects: if the ϕ mass or width changes, it should be visible in either the leptonic or hadronic decays. The leptonic channel has the advantage that the produced leptons interact very little with the hadronic medium, providing the most direct measure of what happens to ϕs that decay early in the collision process. The hadronic channel, $\phi \rightarrow K^+K^-$, has three main advantages: high branching ratio, low q value of the decay (making the kaon momenta very sensitive to changes in the ϕ mass), and the fact that kaons are easy to detect and identify. The main disadvantage of the kaon channel lies in the fact that the outgoing kaons will also be affected by the hadronic medium: they may undergo collisions and they

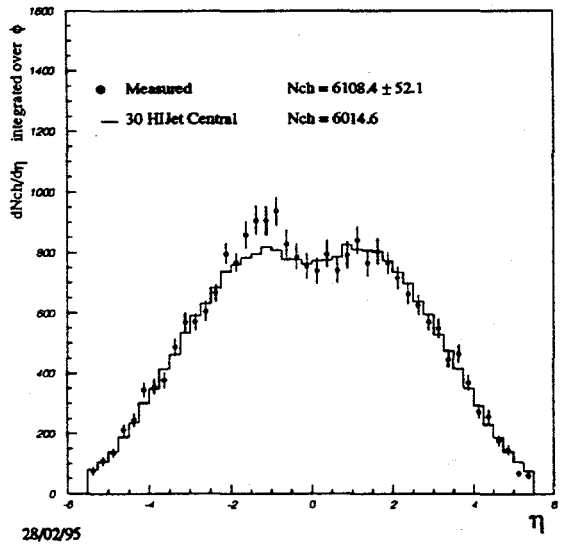

Figure 4. Single PHOBOS central event with 170 particle anomaly.
The points show the results for a single HIJET event with a 170-particle anomaly (4 fm DCC with $\varepsilon = 120 MeV/fm^3$) centered at a rapidity of -1. The histogram shows the average of 30 central HIJET events as generated, without an anomaly.

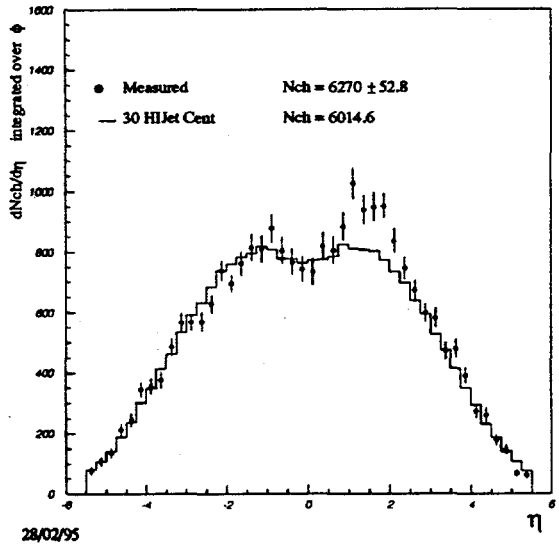

Figure 5. Single PHOBOS central event with 280 particle anomaly.
The points show the results for a single HIJET event with a 280-particle anomaly (6 fm DCC with "normal" $\varepsilon = 60 MeV/fm^3$) centered at a rapidity of +1. The histogram shows the average of 30 central HIJET events as generated, without an anomaly.

may interact with the medium in order to go on mass-shell as they leave it.

The *PHOBOS* collaboration will study the $\phi \rightarrow K^+K^-$ channel for midrapidity, low p_T ϕs. Our strategy will be to examine the width, mass, and number of ϕ particles found in this channel as a function of centrality and p_T. The medium effects should show up as a change in the width, mass, or number of ϕs for the most central collisions. This effect should be a decreasing function of p_T.

Figure 6 shows the total distribution of identified K^+K^- pairs accepted into the spectrometer from 19 hours of good running at the nominal beam luminosity, including those from ϕ decays as well as the continuum background. Figure 7 shows the distribution of ϕ particles accepted into the spectrometer (requiring 2 fully identified kaons) as a function of the ϕ invariant mass for 19 hours of running. The acceptance is not uniform as a function of M, leading to an increase in the tail on the low mass side. This effect is purely geometrical and can be corrected for. In the analysis that follows, we will ignore the effect and just exclude the low-energy tail from the fit. In a more complete analysis, we would, of course, just correct for the effect. Figure 8 shows the background-subtracted distribution of ϕs.

Figure 9a shows the event-by-event invariant mass resolution of the detector. A Breit-Wigner fit to this δM distribution yields a centroid of zero ($-8 \pm 5keV$) and a width Γ_{res} of 2.03 MeV, corresponding roughly to a σ of about 1 MeV (given equivalent FWHM). Figure 9b shows the background-subtracted ϕ distribution fit to a Breit-Wigner. This yields $M = 1019 \pm 0.2MeV$ and $\Gamma_{raw} = 6.57 \pm 0.48MeV$. Deconvoluting the resolution function yields $\Gamma_{meas.} = \Gamma_{raw} - \Gamma_{res.} = 4.5 \pm 0.5MeV$.

In summary, our resolution on the M and Γ of a sample, given 19 hours of running, is 0.2 MeV and 0.5 MeV respectively. For a full year's run, we should be able to plot the measured M and Γ of the ϕ in the hadronic decay channel as a function of other observables such as centrality and p_T. The key feature of PHOBOS that allows us to achieve such good statistical precision on the ϕ measurement, even with small acceptance, is our high data-taking rate.

4. Conclusions

The *PHOBOS* detector is a high-rate detector with good acceptance for charged particle detection, and with good particle identification and momentum measurement at low p_T in the mid-rapidity region. These features make it well-designed for studying collective phenomena at RHIC and complementary to other detectors planned for RHIC.

Two specific measurements were considered as examples: $dN/d\eta$ for charged particles and the mass spectrum from $\phi \rightarrow K^+K^-$ decays. It was shown that we have a resolution of about 1% on the total multiplicity event-by-event and can easily see anomalies of ~ 170 or more charged particles superimposed on a central event. It was also shown that 19 hours of beam time provides us with a measurement of the ϕ mass with an error of 0.2 MeV and

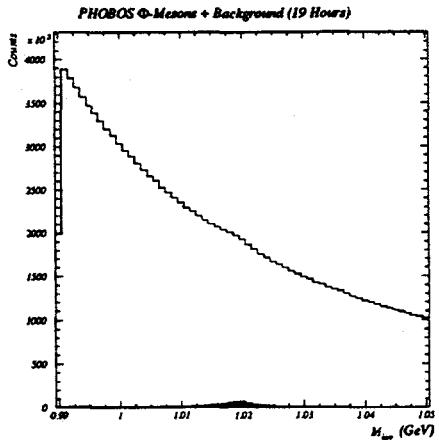

Figure 6. PHOBOS ϕ mesons + background in 19 hours.
The open histogram shows the invariant mass distribution of all fully identified K^+K^- pairs in the spectrometer, including both the ϕs and the background (19 hours - 10% central). The filled histogram shows only the accepted ϕs.

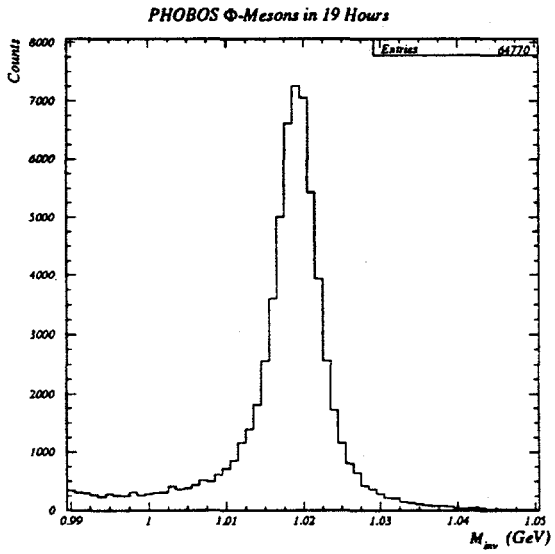

Figure 7. PHOBOS ϕ mesons in 19 hours.
This plot shows the invariant mass distribution of ϕ particles reconstructed from fully-identified K^+K^- pairs in 19 hours of good running (considering only the 10% central sample).

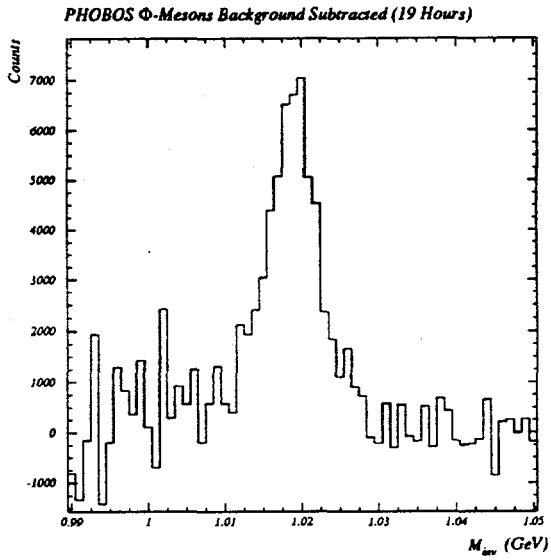

Figure 8. PHOBOS Background-subtracted ϕ mesons in 19 hours.
This histogram shows the invariant mass distribution of K^+K^- pairs after background-subtraction. This would be our ϕ signal for 19 hours of data assuming that only the most central 10% of the data contained ϕs.

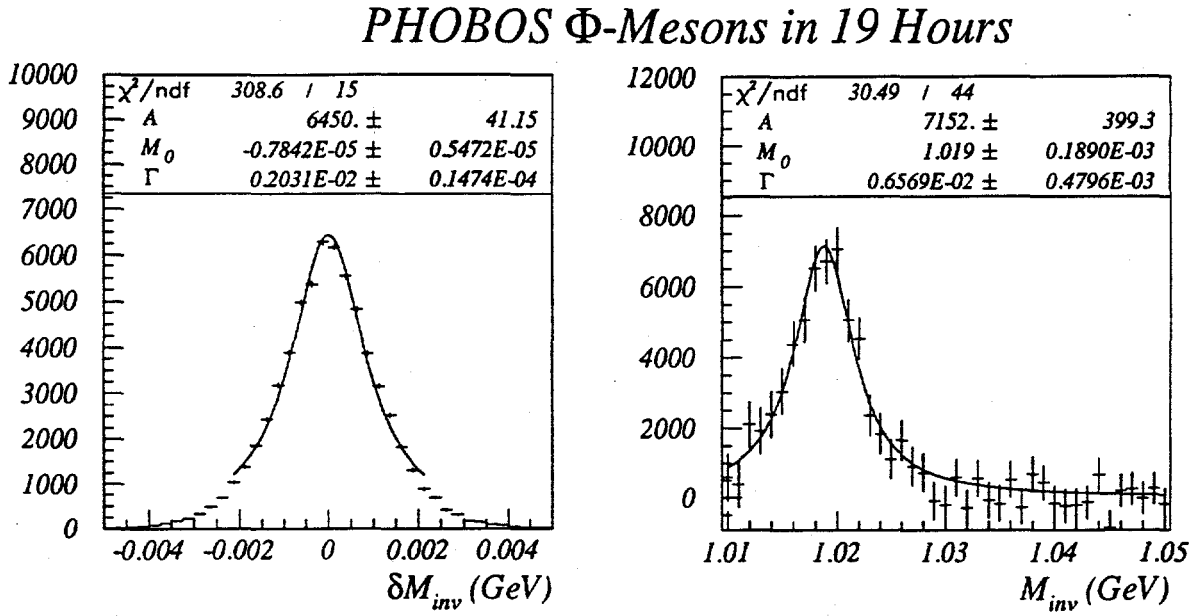

Figure 9. PHOBOS ϕ Mass and Width fits.
This shows a) the event-by-event mass resolution and b) the Breit-Wigner fit to the background-subtracted result after 19 hours (10% central). The final measured result corresponds to $M = 1019 \pm 0.2 MeV$ and $\Gamma_{meas.} = 4.54 \pm 0.5 MeV$ (see text).

of the width with an error of about 0.5 MeV. The multiplicity measurement covered the complete phase space and the phi measurements covered the mid-rapidity, low p_T region that should be the most important part of the phase space.

REFERENCES

1. *PHOBOS* Conceptual Design Report (April, 1994).
2. G. Roland et al., RHIC Detector Workshop at Quark Matter (1995).
3. S. Gavin, Proc. Quark Matter (1995).
4. D. Lissauer and E.V. Shuryak, Phys. Lett. B **253** (1991) 15.

The Measurement of Hadronic Observables with the Solenoidal Tracker at RHIC (STAR)

Rene Bellwied[a] for the STAR Collaboration

[a]Physics Department, Wayne State University,
Detroit, MI 48201, USA

We describe the capabilities of the STAR detector at RHIC regarding the measurement of hadronic observables. Special emphasis will be given to the determination of event-by-event observables deduced from particle spectra for protons (p), kaons (K) and pions (π). We will show that based on the present status of the simulations STAR will be able to measure quantities such as $<p_T>$, slope parameter, and particle ratios on an event-by-event basis. These parameters, in connection with charged particle multiplicities as a function of momentum and rapidity, may shed light on the occurance of a phase transition in ultrarelativistic heavy ion collisions.

1. Theoretical background

It is likely that the very first measurements reported from RHIC will be based on hadronic observables. Hadronic observables in relativistic heavy ion collisions have been used widely to determine the collision centrality (charged particle multiplicity) and to characterize the freeze-out properties of the final state (slope parameter, particle abundances etc.). At RHIC we will study these systematics, but in addition , we will ask whether hadrons may be used to determine possible signatures of a phase transition to the Quark Gluon Plasma.

Of particular interest is the fraction of projectile kinetic energy which is available for the excitation to a QGP. In any dynamic model, the 'stopping power' of the projectiles can be determined by measuring the baryon density at mid-rapidity. The amount of stopping determines the energy released to form a fireball and its composition. However, predictions of the baryon density are model dependent. Originally RHIC energies were conceived to provide a baryon-free region at mid-rapidity in central heavy ion collisions. Recent calculations based on models that include resonance formation and rescattering (RQMD, VENUS) now predict sizeable stopping, which will lead to finite baryon density at mid rapidity. An increase in baryon density should also lead to larger strange baryon densities [1]. According to these models, baryon-free regions will only be reached at LHC energies. On the other hand standard string models still predict less stopping and a baryon-free region at mid-rapidity at RHIC energies. As the current set of model parameters is not sufficiently constrained, a measurement of the proton rapidity spectrum will answer this question during early RHIC operation.

A decade ago, Gyulassy [2] suggested that a simple hadron gas description of hot, dense

matter would not be sufficient to describe the features of relativistic heavy ion collisions at RHIC energies. He proposed treating the initial collisions as hard parton-parton interactions with subsequent parton cascading resulting in increased hadron production during the mixed phase. Present parton cascade models [3], including effects of shadowing and screening, predict charged particle multiplicities, which are several times larger than the predictions of common string or hadron gas models [4,5]. A simple determination of the charged particle multiplicity in RHIC Au+Au collisions will therefore provide important information towards a better understanding of the initial conditions at RHIC energies. Based on present theoretical uncertainties, detectors should be designed, to perform at multiplicities several times the standard FRITIOF densities (see table 1).

Table 1
Average multiplicities of individual charged hadrons per event in $\eta \pm 1$

particle	FRITIOF	HIJING	PCM
π^+,π^-	600	920	1500
K^+,K^-	60	100	160
$p,\bar{p}$	30	75	60
Λ	6	24	40
Ξ^-	0.6	?	5

We have thus far only discussed measurements which will characterize the reaction, but will contribute little to the determination of a phase transition. Although the number of unambiguous signatures has been seriously constrained by theory in the last decade, there still are hadronic measurements which will study the question of plasma formation. Some of those measurements were suggested some time ago and are still valid, others are new and originate from the steady progress towards a better understanding of the dualism between single particle and collective effects in relativistic heavy ion collisions.

The simplest measurement was originally suggested by Shuryak [6]. Based on cosmic ray measurements [7] he proposed to measure the average momentum of the produced pions as a function of charged particle multiplicity at the same centrality and with varying incident energy. A phase transition would be indicated by a rapid rise in the effective number of degrees of freedom over a small temperature range. A density vs. temperature diagram can be translated into observables by plotting the mean transverse momentum $<p_T>$ (instead of T) as a function of dN/dy or dE_T/dy (representing the increase in the degrees of freedom). Hydrodynamic calculations corroborate this effect, although quantitatively less pronounced [8].

Other effects on the pion momentum spectrum were suggested. To first order the slope of the spectrum will describe the temperature of the emitting source assuming thermal equilibration. However, due to the strong probability of final state interaction of the produced mesons, any hadronic slope will always reflect the freeze-out condition rather than the original source temperature.

Effects of deflagration might be observed in the low momentum part of the spectrum, as suggested by Siemens and Rasmussen [9]. A sudden explosion of the hot phase will result in a suppression of the yield at low momentum, which is easily distinguishable from

the low momentum enhancement expected by models which emphasize resonance matter formation [10].

In addition to the pion momentum spectrum the pion rapidity distribution might also contain considerable information about the state of the matter. Strong rapidity fluctuations in the charged particle multiplicity, so called bubble formation, were suggested by van Hove [11]. The bubbles are due to formation and subsequent hadronization of large plasma droplets in the mixed phase.

Bjorken [12] and Wilczek [13] expanded this idea and postulated that, due to preferred orientation of the vacuum in a certain part of phase space (domain), part of the plasma might actually condense out in a chirally disoriented state. This DCC (disoriented chiral condensate) effect will lead to several effects in the pion emission, the most obvious of which is strong isospin fluctuations and a very large pion multiplicity enhancement at low momentum [14]. These effects will be measurable on an event-by-event basis if a detector with sufficient azimuthal and pseudo-rapidity coverage is built. The total charged particle multiplicity in the STAR coverage seems to be sufficient to investigate such effects.

A combination of the momentum and rapidity spectrum might reveal the collective nature of the source by exhibiting flow effects. Amelin and co-workers [15] calculated that according to the RQMD model collective flow might still exist at CERN energies in heavy systems. Whether this effect prevails at RHIC is still to be seen. Certainly, the recent measurement of collective flow at AGS energies [16] showed that elementary superposition models are insufficient for describing the collectivity of the reaction at very high energies.

The proton momentum spectrum, especially the high energy end, also carries important information. Geist [17] postulated that the high momentum proton formation in parton-parton collisions is mainly due to di-quark formation and subsequent fusion with the co-moving seaquarks. Single quark fusion is not expected to account for the cross section at high transverse momentum, simply because the high momentum carried by each quark makes a waveform overlap very improbable. In a deconfined phase the diquark formation is highly suppressed because of the high energy density. Di-quarks will simply 'melt away' since the binding energy is much lower than the excitation energy in the plasma. Plasma formation should therefore lead to high transverse momentum proton suppression. The shape of the spectrum will deviate considerably from a simple exponential tail at high transverse momentum.

In addition to the single particle observables, particle abundance ratios and two particle interferometry will provide further information on plasma formation. Interferometry is discussed in Zajc's contribution [18]. The measurement of particle ratios will help to determine important parameters of the equation of state. In a recent theoretical description of the phase transition by Heinz [19], the standard two dimensional phase boundary in the baryon density vs. temperature plot was extended to a 3-dimensional plot by including the strangeness chemical potential as the third dimension. The $p/\bar{p}$ ratio will determine the baryochemical potential, the K/π or Λ/p ratio will determine the strange chemical potential, and the d/p ratio will provide a measure of the entropy of the system [20]. This means that, by measuring the hadronic momentum spectra and the hadronic abundance ratios, the three dimensional phase space can be completely determined. Finally, there is no reason to expect a phase transition to occur in every single central heavy ion collision

at RHIC. In fact, the occurances could be rare, in which case the events should be classified based on their specific hadronic features. That requires one to measure all or most of the above signals on an event-by-event basis. Table 1 shows the average multiplicity of charged hadrons in a standard central Au+Au collision at RHIC for FRITIOF, HIJING and the parton cascade model (PCM) at mid-rapidity.

A detector that covers 2π in azimuth and measures most of the momentum range at mid-rapidity will certainly provide event-by-event capabilities. STAR at RHIC was designed specifically for this purpose of measuring event-by-event hadronic physics observables.

2. STAR detector

STAR is a large solid angle detector which consists in its baseline version of a time projection chamber (inner radius = 50 cm, outer radius = 200 cm, pseudo-rapidity coverage ± 2) plus the necessary trigger devices. In addition to the TPC, a Silicon Vertex Tracker (SVT), an electromagnetic calorimeter (EMC), an external time projection chamber (XTPC), and a time of flight array (TOF) have been proposed and are being considered for funding. In the simulations described below we utilize the capabilities of the complete STAR detector. In the summary we will distinguish between baseline and full detector capabilities.

The SVT, TPC and TOF reside inside a solenoidal magnetic field of 0.5 T. These three devices constitute the integrated, mid-rapidity charged particle tracker of STAR. By combining information from all three devices, STAR has a pseudo-rapidity coverage from +2 to -2 and momentum coverage from 60 MeV/c upward. The SVT consists of 3 barrels of Silicon Drift Detectors between 5 and 15 cm radius from the interaction region. The TPC adds 45 planes of tracking between 50 and 200 cm. The TOF is presently envisioned as a patch covering 2 units of pseudo-rapidity and about 90 degrees in azimuth.

The EMC aims to measure jets, fluctuations and high p_T phenomena in the nucleus-nucleus program and will provide hard probe capabilities for the RHIC pp- and pA-program [21]. The XTPC will cover the pseudo-rapidity range from η=2-4 to measure charged particle distributions and, to some extent, momentum spectra.

The capabilities of the inner tracking devices in STAR, to measure the single and many body observables discussed in the previous section, have been studied. In the following we summarize the charged particle capabilities of STAR in the pseudo-rapidity range between +2 and -2, plus some preliminary simulations for more forward rapidities, employing the XTPC.

3. Estimate of required measurement accuracies

Based on past experiences in relativistic heavy ion experiments, the relative accuracy of the parameters can be estimated. Several key quantities can be established by measuring hadrons: the charged particle multiplicity, the charged particle rapidity distribution, hadronic particle ratios, the slope parameters of the particle spectra, the mean transverse momentum for each particle species, and the shapes of the momentum spectra. The error depends on the analysis mode; inclusive errors will be much smaller than the uncertainty on an event-by-event basis.

If one relates the slope parameter of the momentum spectrum to the freeze-out temper-

ature (T), then CERN and AGS experience tells us that an absolute error of $\leq$ 10 MeV is required to determine T for single particle species and measure relative differences in T between various particle species. Fig.2 shows the difference between a 150 MeV and a 250 MeV slope parameter for a pion spectrum. 10 MeV corresponds roughly to a 5-10% error. The uncertainty of the mean transverse momentum will be comparable.

The accuracy of the shape of the spectrum, especially in the very low and high p_T range, depends strongly on the statistics and possible enhancement or suppression effects. Based on a FRITIOF input distribution, interesting deviations will be measurable if the spectral shape can be measured to a 15% accuracy. Effects like disoriented chiral condensate, deflagration or di-quark suppression are expected to be on a larger scale.

Particle ratios should be measured to an accuracy of $\leq$ 5%. Recent measurements at CERN and the AGS established d/p, K/π, and p/$\bar{p}$ ratios for various heavy ion collisions. The interpretation of these data regarding entropy, strange- and baryo-chemical potential required small errors. Whether this can be accomplished in STAR depends strongly on the actual particle abundance.

The charged particle multiplicity and rapidity distribution are of interest mostly in the event-by-event mode. The uncertainty in the rapidity distribution is strongly multiplicity dependent. Again, we use the FRITIOF distribution as a bench mark. The event-by-event charged particle fluctuations are on the order of 10% per rapidity unit at mid-rapidity. The fluctuations increase toward beam rapidity. The measurement error should not exceed the fluctuation level. The requirement on the tolerable uncertainty depends on the effect one wants to study. Observables of current interest include fluctuations caused by either plasma bubble formation or local disoriented chiral condensates. They will be visible if the increase or decrease in particle multiplicities exceeds the sum of error and particle fluctuations from event to event (estimated to be about 15%).

4. Simulation results

Before presenting some of the current simulations of the STAR detector system, we want to emphasize that the STAR simulation and analysis software will be further developed and will become more sophisticated in the next few years. The emphasis until recently was on developing code and interfaces for all detector subsystems. Now that the complete integrated software chain is in place, more emphasis will be given to optimizing each module. For example, alternate tracking and helix fitting algorithms will be developed to enhance the tracking capabilities of the baseline detector. The present status of simulations is presented here, but it should not be considered as the ultimate performance of the STAR detector.

Fig.3 shows the particle identification via dE/dx for the SVT/TPC system. By including the TOF in this measurement, good K/π separation can be accomplished up to 1.5 GeV/c, the π/p separation extends to 3 GeV/c.

Secondary vertex detection requires the addition of the SVT. Fig.4 shows the tracking efficiency for primary and secondary particles in the SVT and TPC. The tracking efficiencies are sufficiently high. In addition, a matching efficiency of 85 % between SVT and TPC tracks was found. After combining the two tracking detectors, the momentum resolution for low and high momentum particles is shown in Fig. 5a,b.

After establishing the particle identification capability and momentum resolution we studied the capabilities for the measurement of inclusive spectra of produced charged particles. Fig. 6 shows the reconstructed transverse mass spectra for pions, kaons, and protons using the combined information of SVT,TPC, and TOF. The mean transverse momentum can be deduced from these spectra.

Fig. 7 shows the charged particle rapidity spectrum measured by the three tracking devices (SVT, TPC, XTPC). The uncertainty in the XTPC sections is slightly larger, but the overall uncertainty is still less than 5%. A FRITIOF charged particle distribution was used as input.

The large coverage of the STAR detector allows the measurement of particle ratios with great accuracy. Besides the strange baryon ratios, which are discussed in Ken Wilson's contribution [22], the d/p (measure of entropy), $p/\bar{p}$ (measure of baryochemical potential), and K/π ratios (measure of strange chemical potential) are of particular interest, as pointed out in the previous section.

The abundances of antimatter ($\bar{p}$) and coalescence dependent particles (d) are strongly model dependent. Using a FRITIOF input we expect baryon ratio uncertainties between 10 and 25% event-by-event. The inclusive error is estimated to be below 5% for all relevant hadronic particle ratios.

Fig. 8 shows the present uncertainty of the K/π ratio in a single event as a function of momentum for matched SVT/TPC tracks.

The final test of the STAR capabilities was to determine the shape of the particle spectrum with great accuracy on an ensemble basis, specifically in the low and high p_T region, where we expect physics effects such as condensation or di-quark suppression. The low momentum region in the π-spectrum is covered by the SVT alone. The high tracking efficiency and low ghost track contamination allow us to measure the low momentum shape of the spectrum. Fig. 9 shows a simulation, taking into account a Bose-Einstein condensation effect. The condensation of low momentum particles shifts the mean momentum towards lower p_T. On an event by event basis the SVT is sensitive to shifts in excess of 30 MeV. The two curves in Fig.9 represent boundary conditions by comparing no condensation to a rather large effect. A more realistic estimate of the expected spectral shift as measured by the SVT is shown by Gavin in his contributions to QM95 [14] and this workshop.

The high momentum part of the proton spectrum (above 1 GeV/c) is only accessible with the additional time of flight. Including the TOF allows us to measure suppression effects, such as that predicted by Geist [17], with good accuracy. The uncertainty in the shape of the proton spectrum above 1 GeV/c is $\leq 10\%$ in an inclusive measurement. The statistics are too small, even with a TOF wall, for this measurement to be accessible on an event-by-event basis.

5. Conclusions

The STAR baseline detector will provide information for many hadronic observables (ratios, slopes, $<p_T>$, spectral shapes, rapidity distributions) in inclusive measurements. The TPC has good reconstruction capabilities and momentum resolution. It will identify π, K, p, d and their antiparticles in a momentum range given by its dE/dx particle

identification capabilities. It will also provide event-by-event information on π and p spectra.

The inclusion of the XTPC will allow us to measure the charged particle multiplicity and the charge ratios to very forward rapidities (up to η=4).

The inclusion of the TOF allows us to extend the momentum range for particle identification of all hadrons. In particular, the measurement of event by event variables for Kaons will be possible. The study of high momentum effects in the proton and pion spectra are also accessible by including the TOF.

The SVT will provide additional coverage in the low momentum region (below 100 MeV/c) and improved particle identification via dE/dx. It will allow us to measure low p_T enhancements on an event-by-event basis. Novel physics, e.g. disoriented chiral condensates or general Bose Einstein condensation effects, might impact on the behavior of the low momentum pions.

The complete STAR detector, with all its additional equipment will be the primary device at RHIC to measure hadronic observables. Its large solid angle coverage will allow high precision measurements on an event-by-event as well as an inclusive basis.

Although it is generally agreed that no single hadronic parameter will serve as a 'smoking gun' for the QGP, the wealth of data deduced from the hadrons (multiplicity, spectra, shapes, ratios) will provide the basis for a many-parameter approach to the determination of the equation of state. Hadronic measurements lead to complete information of the three dimensional phase space of the state of nuclear matter (as a function of T, μ_B, and μ_S). Correlations between hadronic observables might yield conclusive evidence for a phase transition to a quark gluon plasma.

6. Acknowledgement

Some of the simulations presented here were performed by Pablo Yepes (Rice), Jeff Mitchell (LBL), and Lanny Ray (UT Austin). I am indebted to the STAR software group for their help in putting the outline of the talk together. I would like to thank Ken Wilson, Claude Pruneau, Jay Marx, Matt Bloomer, Lanny Ray, and John Harris for useful, lively discussions and their help with the manuscript.

REFERENCES

1. H. Stoecker, invited talk at STAR Heavy Ion Physics Workshop, Monterey 1995
2. M. Gyulassy, Nucl. Phys. A 400 (1983) 31c
3. K. Kinder-Geiger and B. Mueller, Nucl. Phys. B 369 (1992) 600
4. B. Anderson et al., Nucl. Phys. B 281 (1987) 289
5. H. Sorge et al., Nucl. Phys. A 498 (1989) 567 c
6. E.V. Shuryak and O.V. Zhirov, Phys. Lett. B 171 (1986) 99
7. T.H. Burnett et al. (JACEE), Proc. Intern. Conf. on Cosmic Ray Physics (San Diego, 1985), Vol HE1.4-4, p.164
8. B. Mueller, Talk at the NATO conference, Il Ciocco (1992), Plenum Series B 303
9. P.J. Siemens and J.0. Rasmussen, Phys. Rev. Lett. 42 (1979) 880
10. G.E. Brown et al., Phys. Lett. B 253 (1991) 19
11. L. van Hove, Z. Phys. C 27 (1985) 135

12. J.D. Bjorken, Int. J. Mod. Phys. A 7 (1992) 4189
13. K. Rajagopal and F. Wilczek, Nucl. Phys. B 404 (1993) 577
14. S. Gavin, Invited talk at QM95, proceedings to be published, 1995
15. N.S. Amelin et al., Phys. Rev. Lett. 67 (1991) 1523
16. J. Barrette et al. (E877), Phys. Rev. Lett. (1995), to be published
17. W.M. Geist, Phys. Lett. B 211 (1988) 233
18. B. Zajc, contribution to this workshop (1995)
19. K.S. Lee and U. Heinz, Phys.. Rev. D 47 (1993) 2068
20. W. Siemens and J. Kapusta, Phys. Rev. Lett. 43 (1979) 1486
21. B. Christie, contribution to this workshop (1995)
22. K. Wilson, contribution to this workshop (1995)

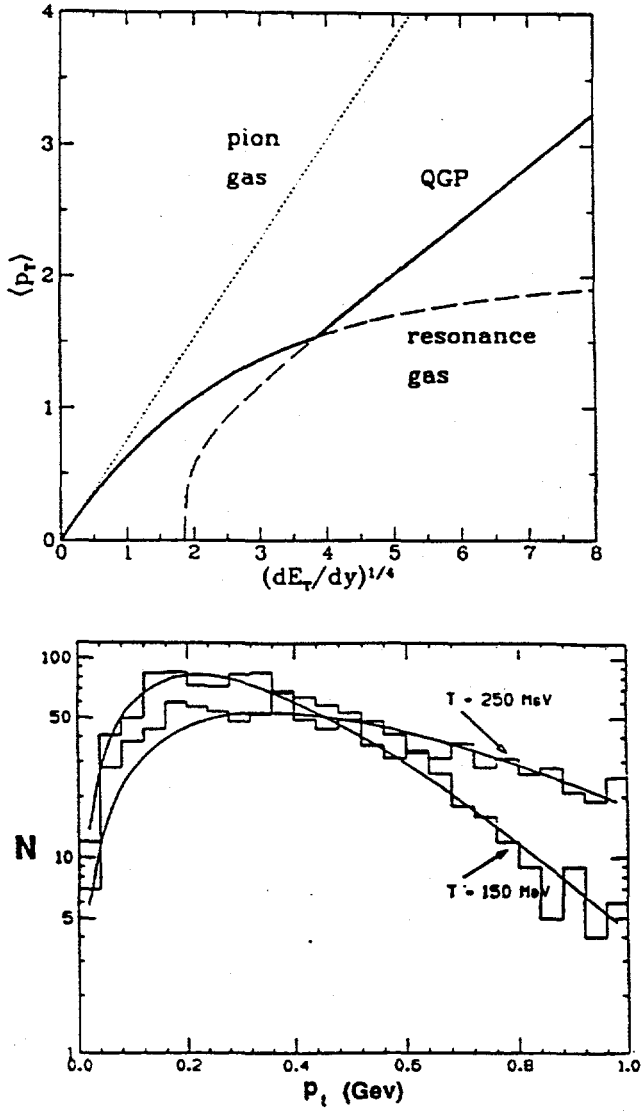

Figure 1. Average transverse momentum of emitted hadrons as a function of transverse energy or charged particle multiplicity, representing the energy density reached in a collision. The different curves correspond to: (a) pion gas, (b) Hagedorn resonance gas, (c) QGP. From ref. [8]

Figure 2. Simulation of the p_T spectrum for one event generated using a Boltzmann distribution of 1000 pions. The histograms correspond to single events generated with T = 150 MeV and 250 MeV. The curves are fits to the histograms using a Maxwell-Boltzmann distribution.

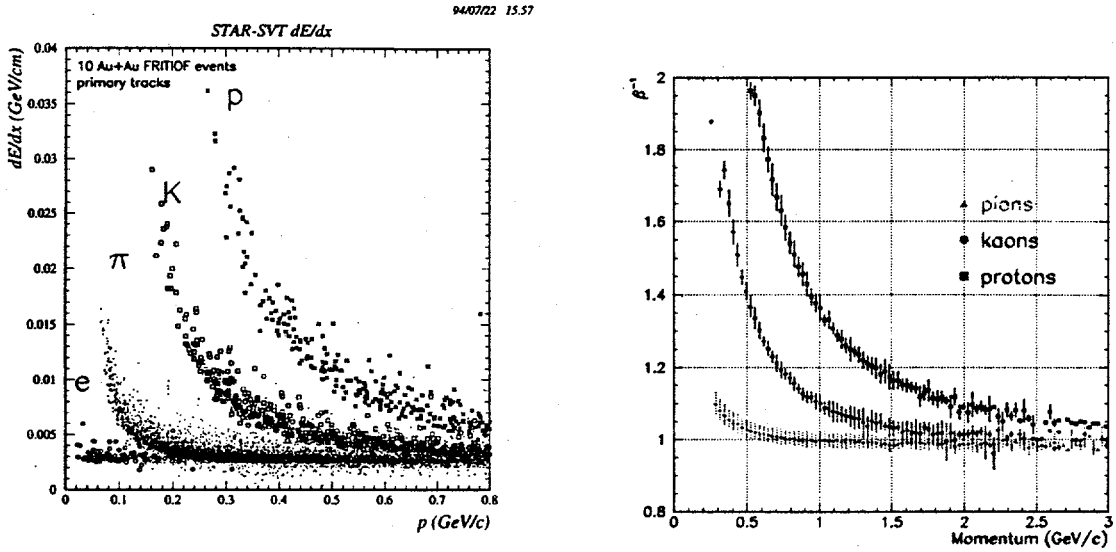

Figure 3. a.) particle identification capabilities (via de/dx) in the combined SVT/TPC tracking system, b.) extension of a.) by including a TOF patch

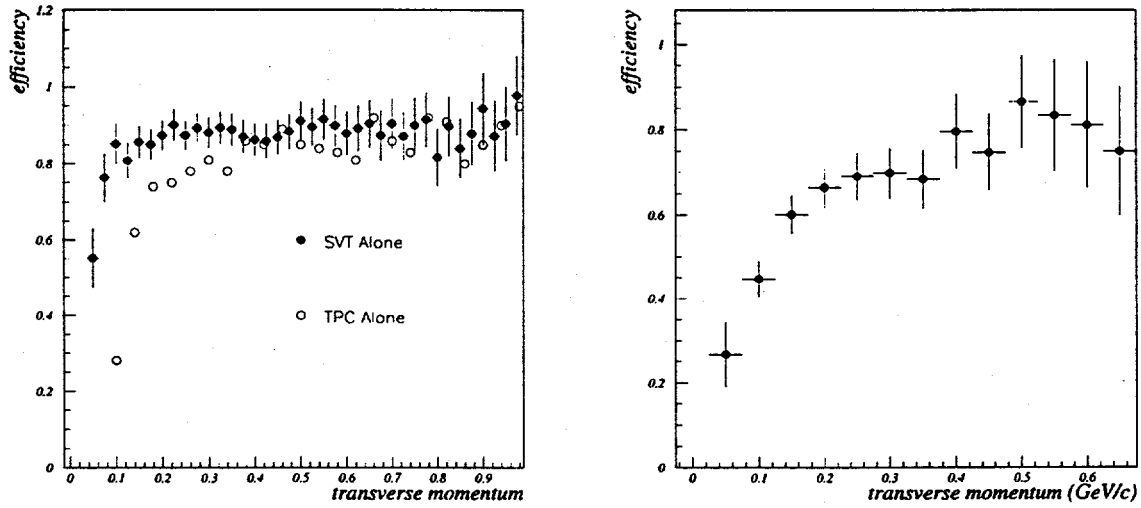

Figure 4. Tracking efficiency in SVT and TPC for primary (a.) and secondary (b.) vertices

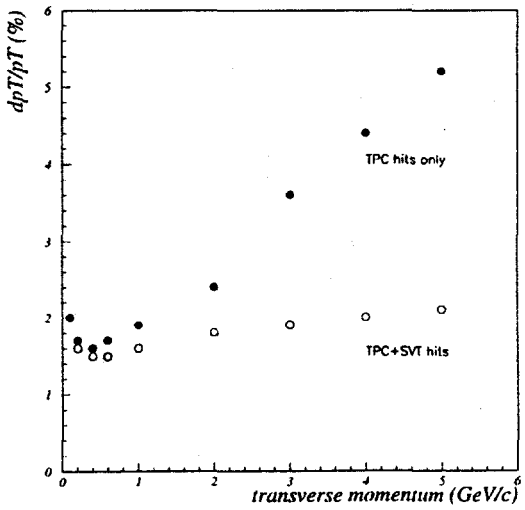

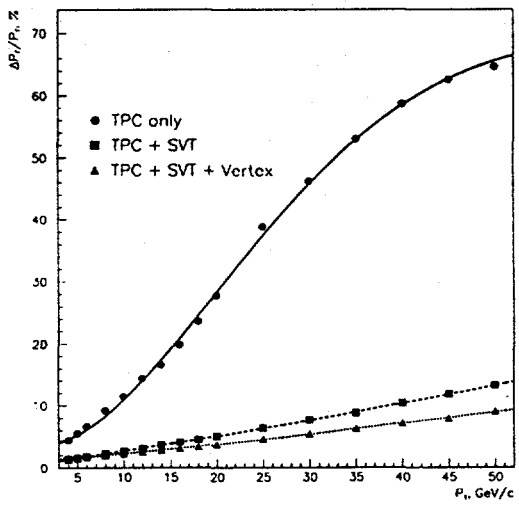

Figure 5. Momentum resolution of the integrated tracking system in STAR for low momentum (a.) and high momentum (b.) particles

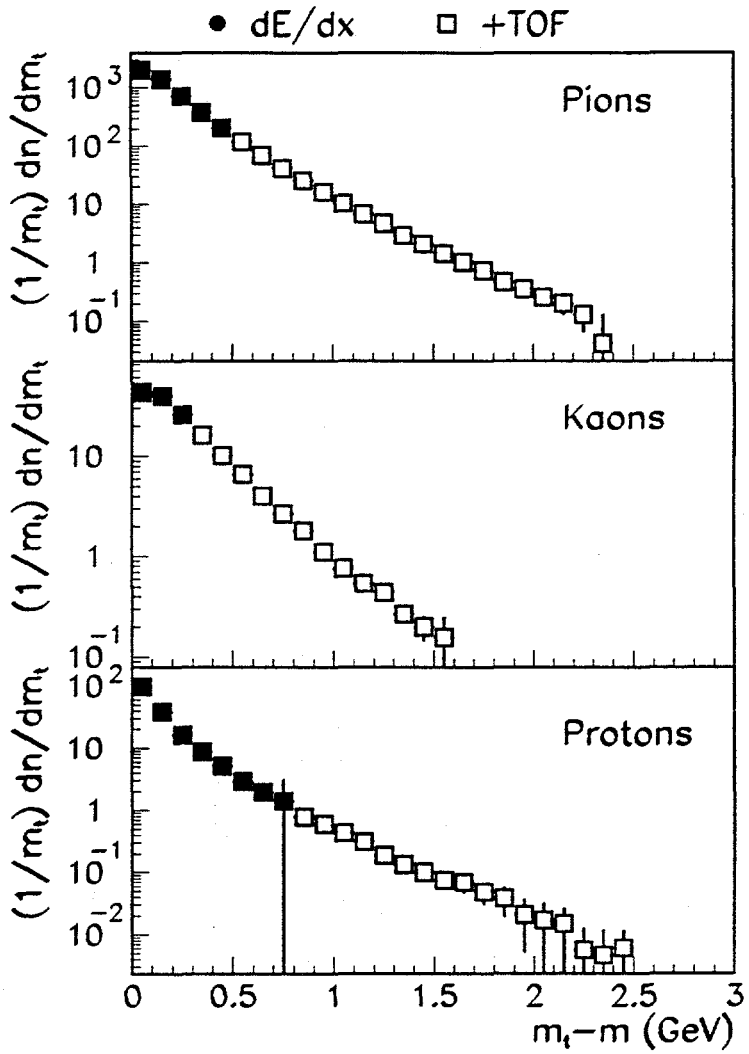

Figure 6. Invariant cross section versus transverse mass for π, K and p using SVT, TPC, and TOF

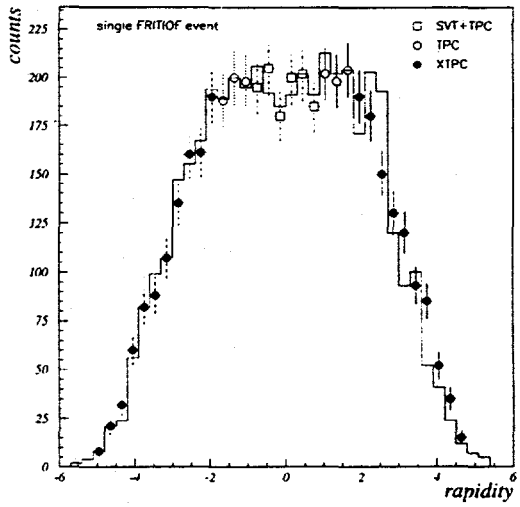

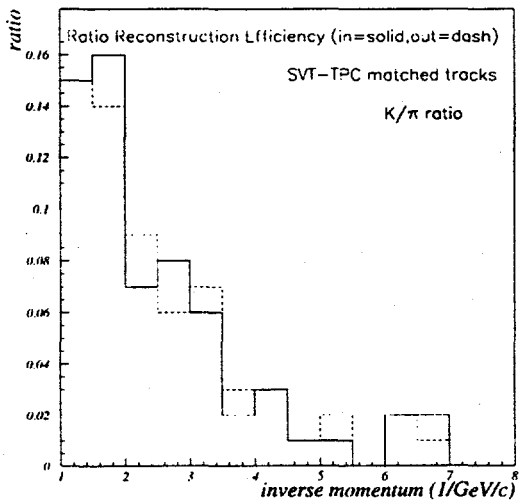

Figure 7. Event-by-event charged particle rapidity spectrum using SVT,TPC, and XTPC

Figure 8. Present uncertainty in K/π ratio measurement with the integrated STAR tracking system

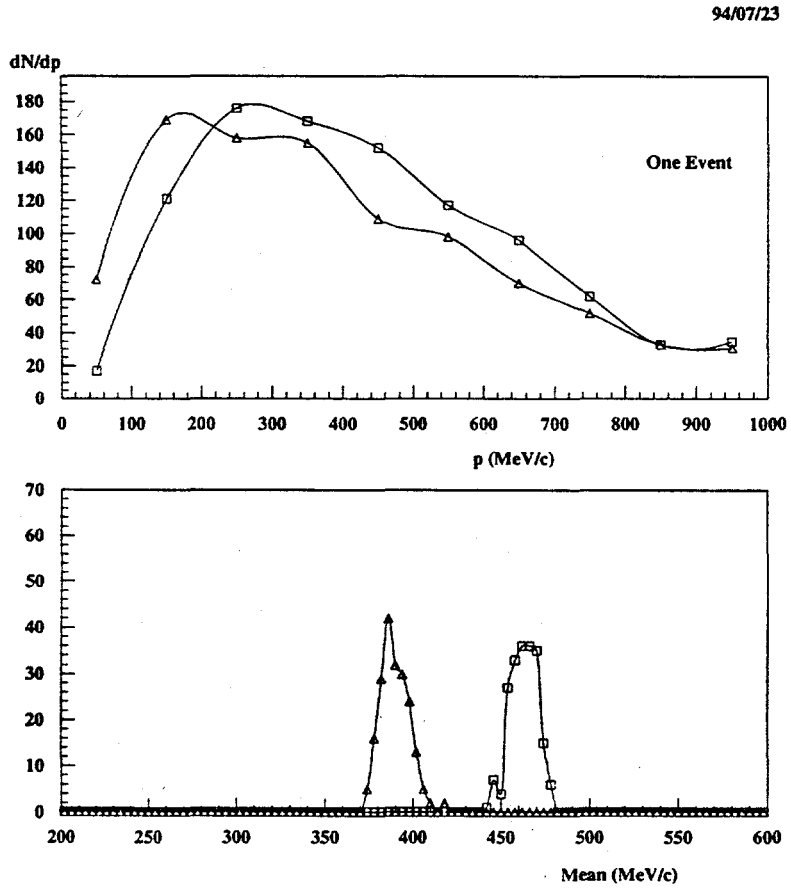

Figure 9. a.) Simulation of the spectral shape of the low momentum part of the π spectrum and b.) the resulting shift of mean transverse momentum for a single Au-Au event. The two curves represent different levels of a possible condensation effect. The resolution results by taking into account SVT and TPC information.

Measurements of Strangeness Production in the STAR Experiment at RHIC

W.K. Wilson[a] for the STAR Collaboration

[a]Physics Department, Wayne State University,
Detroit, MI USA 48201

Simulations of the ability of the STAR (Solenoidal Tracker at RHIC) detector to measure strangeness production in central Au+Au collisions at RHIC are presented. Emphasis is placed on the reconstruction of short lived particles using a high resolution inner tracker. The prospects for performing neutral kaon interferometry are discussed. Simulation results for measurements of strange and multi-strange baryons are presented.

1. Strangeness at RHIC

Strangeness production may help to distinguish between quark-gluon plasma (QGP) scenarios and simple hot hadron gas (HG) scenarios at RHIC.[1] Since the temperatures reached will be higher than the strange quark mass, strangeness will be copiously produced in both scenarios. However, the high cross section for strangeness production due to gluon fusion in a QGP causes the strangeness sector to reach its maximum value very rapidly, perhaps a few fm/c. This is an order of magnitude faster than in a HG phase, so the strangeness production is more likely to reach its chemical equilibrium limiting value in the QGP than in the HG scenario. Production of particles with two or more strange quarks should be particularly sensitive to the high strangeness density expected in a QGP. Strange particle yield ratios have already proven to be a use tools for measuring the degree of strangeness saturation and other thermodynamic properties of systems formed in heavy-ion collisions.[2]

One caveat should be mentioned, however. Even if a QGP is formed, the system must finally evolve through a hadron gas phase. A clear picture of the impact of hadronization on proposed strangeness QGP signals has not yet emerged in the modeling of these collisions. However, it is expected that the background from multi-strange baryons formed in the final HG phase should be small since their formation requires a chain of several collisions. In any case, it is certain that whatever impact hadronization has upon the strangeness content of the system, it will be necessary to measure strangeness production in order to obtain a clear picture of the hadronic sector in these collisions. Our simulations establish that the addition of the SVT (Silicon Vertex Tracker) inner tracker will provide STAR with measurements of particles with single and multi-strange quark content.

2. Simulations of STAR Performance

The baseline STAR detector[3] system will consist of a cylindrical TPC (Time Projection Chamber) within a 0.5 T magnetic field parallel to the beam axis. The TPC will have acceptance for charged particles with pseudo-rapidity $|\eta| \leq 2$. The strange mesons which are of interest to the STAR experiment include the charged kaons, the neutral kaon, and the ϕ meson. The strange baryons of interest are the Λ, the Ξ, and the Ω. The charged kaons are directly identifiable by their dE/dx in the SVT and the TPC up to transverse momenta of 600-700 MeV/c. The proposed addition of time-of-flight (TOF) elements to the STAR detector[4] would extend the kinematical region in which charged kaons can be identified up to transverse momenta of more than 1 GeV/c. The ϕ meson can be reconstructed from its decay charged kaons. Since this decay occurs essentially in the interaction region, all possible kaon pairs must be considered. Fortunately, the mass and width of the ϕ are such that it easily stands above the combinatoric background[5], even with the TPC momentum resolution taken into account. The proposed TOF system also extends the transverse momentum acceptance of STAR for the ϕ. The remainder of this report will be concerned with the reconstruction of strange particles whose lifetimes give them path lengths on the order of centimeters.

The high multiplicity of particles produced in these collisions places severe demands on the performance of the tracking system if secondary decays are to be distinguished from combinatoric background. Using TPC information alone, the position resolution near the main vertex is insufficient for eliminating the combinatoric background. Secondary reconstruction requires an inner tracker which provides the tracks with a few high precision points near the secondary vertices. The SVT upgrade to the STAR detector, shown in fig. 1, fulfills this requirement with three layers of silicon drift detectors arranged in cylindrical barrels at radii of 6, 10, and 15 cm. The detector covers $|\eta| \leq 1.0$ with 95% active area per layer. Combining the precision vectoring capability of the SVT with the good momentum resolution of the TPC (a few percent) allows one to place tight geometrical cuts on the decay which removes most of the combinatoric background.

Simulations of the SVT capacity for reconstructing strange particles which decay centimeters away from the main vertex have been performed previously.[5]. These preliminary studies employed assumptions such as perfect tracking in the SVT and perfect matching to TPC tracks. In the past year we have developed an integrated SVT-TPC tracking package which makes no such assumptions. This development has allowed us to update the strange particle reconstruction simulations and make a much more realistic appraisal of the SVT's performance. We have found that we are able to reconstruct the unstable particles which we studied previously. As expected, the efficiencies are lower than in our previous studies, but not to such a degree that it impacts our ability to perform the physics program.

The simulations presented in the following sections consist of $\sqrt{s} = 200$ GeV central Au+Au FRITIOF events passed through a full GEANT representation of the STAR detector followed by tracking and secondary vertex reconstruction software. Tracking is performed independently in the SVT and TPC, then the SVT and TPC tracks are extrapolated to a cylinder midway between the two detectors and matched. At present, a simple prescription for combining the SVT and TPC tracking information is in use. Only

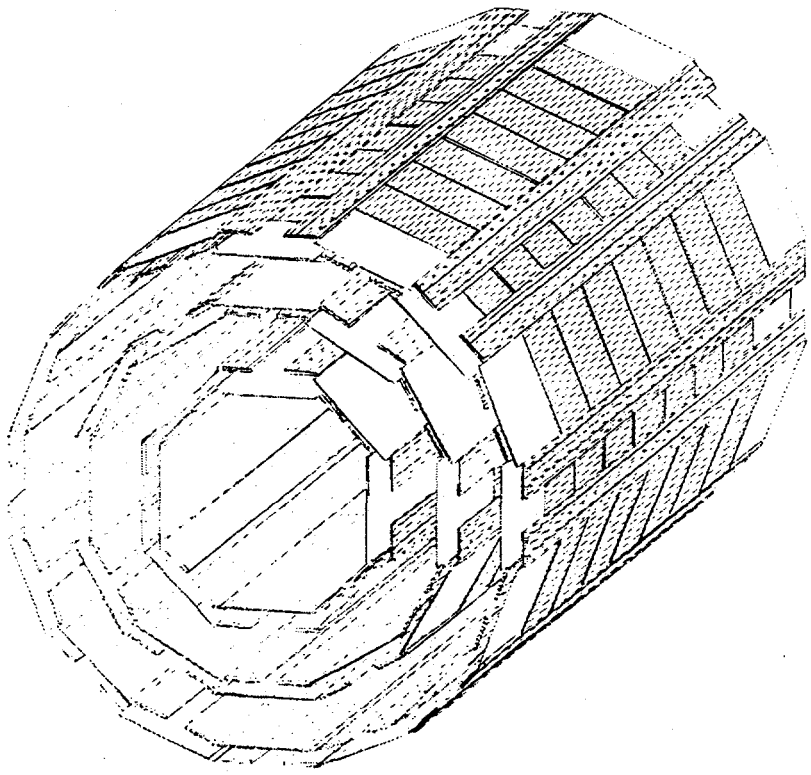

Figure 1. The three barrel structure of the SVT

the magnitude of the track's transverse momentum is taken from the TPC; all other helix parameters are better constrained by the SVT tracking. A full refit of the SVT and TPC space points taking into account the material between them will be implemented in the future.

After the tracking for an event is completed, the software searches for tracks which intersect away from the main vertex. In the case of reconstruction of the Λ, which decays into a proton and a negative pion, the code searches for tracks which come within 2 mm of each other at least 8 mm from the main vertex. The trajectory of the parent particle is then checked to see whether or not it came from the main vertex. Additional kinematical cuts were also used to reduce the combinatoric background. There is a trade off between efficiency on the one hand (open cuts) vs. purity on the other (tight cuts). Some effort has been made in the following results to maximize the efficiency even at the expense of allowing some combinatoric background to pass through the cuts.

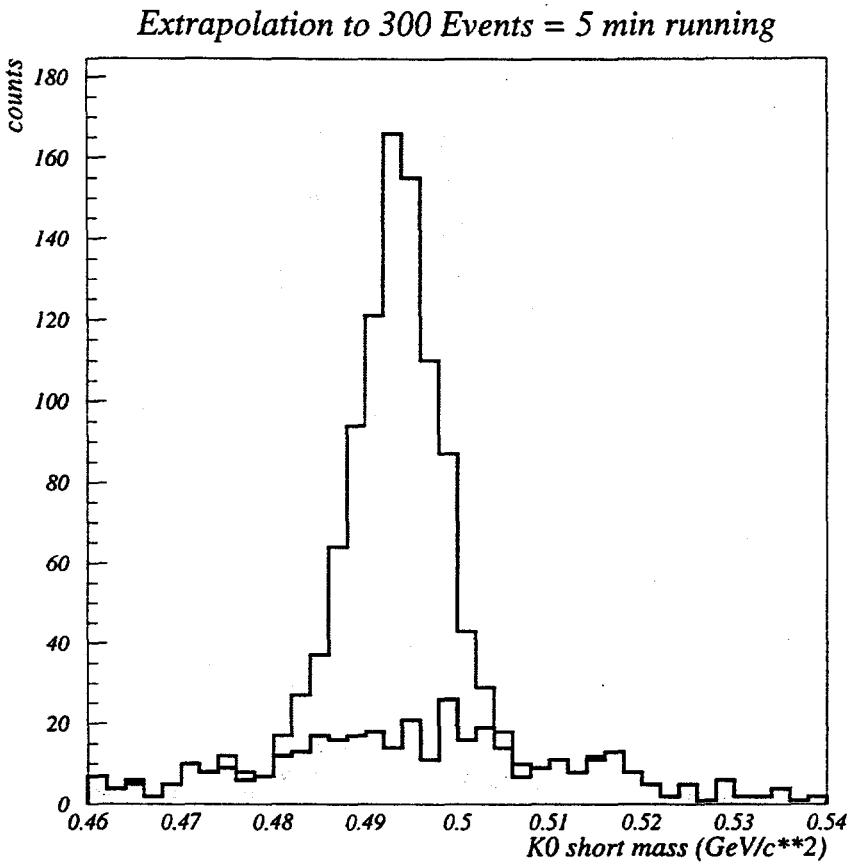

Figure 2. Reconstructed K_s° mass spectrum

3. Results

The FRITIOF event generator produces about 60 K_s° mesons per event within $|\eta| \leq 1.0$ under the collisions described above. We performed a full analysis of 20 events and found that about 2.55 are reconstructed per event. In fig. 2 we show the invariant mass spectrum we expect for 300 events. This and the following spectra were produced by analyzing K_s° events and background events separately, and combining the results according to the signal and background yields from the 20 event full analysis. The 2.55 K_s° per event yields ≈ 3 K_s° pairs per event on average, opening the possibility of K_s° interferometry. Interferometry using K_s° has two distinct advantages over charged pion and charged kaon interferometry. First, the correlation function for neutral kaons is not affected by the coulomb repulsion term which complicates the interpretation of charged particle correlation functions. Second, there is no degradation of two track resolution at low relative momentum since, even if two K_s° have identical momentum vectors,, the tracks of their daughters are usually well separated. Preliminary estimates of the number of events needed to begin to place limits on the size of a 10 fm source with K_s° interferometry are on the order of 100 thousand

events which corresponds to 28 hrs. running time at an event rate of 1.0 Hz. See Ref. [6] for more details.

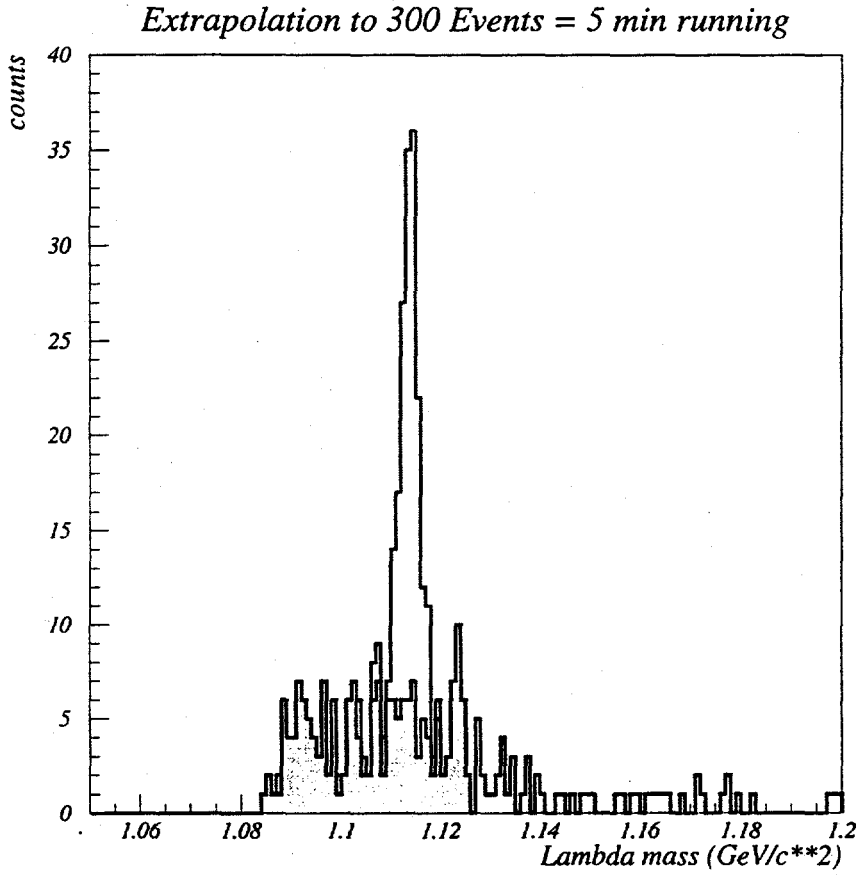

Figure 3. Reconstructed Λ mass spectrum

About 6.5 Λ particles are produced by FRITIOF in the SVT acceptance. These S=1 baryons decay into a proton and a pion. The proton may be easily identified by dE/dx measurements in either the SVT or the TPC since they are found at relatively low transverse momenta. Under the assumption of perfect PID information, we reconstruct 0.5 of the Λ particles per event. The signal/background relationship for these cuts can be seen in fig. 3 which shows the mass spectrum extrapolated to 300 events.

As mentioned in the introduction, multi-strange particles are predicted to be a sensitive probe of the strangeness density produced in the collisions.[1] The Ξ has strangeness S=2 and decays into a pion and a Λ which proceeds on to decay as described earlier. Both of these decays must occur before the first layer of the SVT to be reconstructed in the current version of our software. The top panel of fig. 4 shows our reconstructed mass spectrum extrapolated to 100 thousand events, or about 28 hours of running time. In the

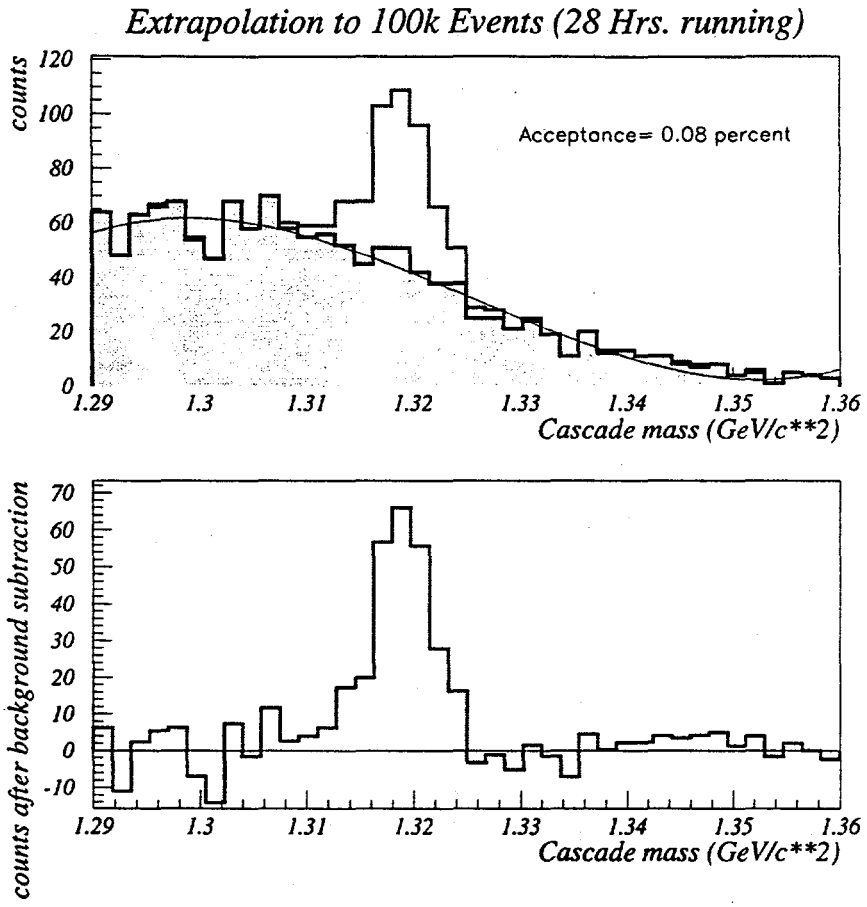

Figure 4. Reconstructed Xi mass spectrum

bottom panel the background has been parameterized by a polynomial and subtracted.

4. Conclusions

Simulations of the ability of the STAR experiment plus the SVT upgrade to reconstruct secondary vertices near the main vertex have been presented. These simulation show that the current SVT design should be able to fulfill its physics mission with regard to strange particle physics. In the future, we plan further studies of the ability to perform K°_{s} interferometry and to study the ability of the SVT to reconstruct the S=3 Ω meson.

REFERENCES

1. P. Koch, B. Muller, and J. Rafelski, Phys. Rep. **142** (1986) 167; J. Rafelski, NATO ASI Series **B303** (1993) 529.
2. S. Abatzis et al. (WA85 collaboration) Nucl. Phys. **A566** (1994) 225c; E. Anderson et al. (NA36 collaboration) Nucl. Phys. **A566** (1994) 217c.

3. J.W. Harris et al. (STAR collaboration) Nucl. Phys. **A566** (1994) 277c.
4. P. Yepes et al., Star Note in preparation (1995)
5. Star Conceptual Design Report, The STAR Collaboration, LBL PUB-5347 (1992); S. Margetis et al., STAR Note **72** (1992).
6. D. Keane, Private communication, (1995); D. Keane, Star Note **47** (1992). S. Margetis et al., STAR Note **72** (1992).

Hard Scattering of Partons as a Probe of Collisions at RHIC using the STAR Detector System

W.B. Christie[a]

[a]Physics Department, Brookhaven National Laboratory

Introduction

Presented here is the current state of our investigations into the use of hard probes to study pp, pA, and AA collisions at the Relativistic Heavy Ion Collider (RHIC) being built at Brookhaven National Laboratory. The overall goal of the RHIC program is the discovery and study of the Quark-Gluon Plasma (QGP), which is predicted to be formed at the high energy densities reached at RHIC in high energy AA collisions. The term "Hard probes" as used in this document includes those particles whose origin is the result of a direct hard parton scatter (i.e qq, qg, or gg). The final states of these hard parton scatters which we propose to study include dijets, gamma-jet coincidences, and inclusive high P_t particle spectra.

A brief discussion of the physics objectives is given in section 1. This is followed by an introduction to the STAR detector system in section 2, with particular details given for the proposed STAR Electromagnetic Calorimeter (EMC). Our present simulation studies and results are given in section 3. We conclude with a summary and a discussion of our future plans in section 4.

1. Physics Objectives

Relativistic Heavy Ion collisions have been studied in *fixed target* experiments in the laboratory setting since the late 1970's. These studies started at the Lawrence Berkeley Laboratory BEVALAC accelerator at energies up to ~ 2 GeV/u. The studies have since been carried on at the Brookhaven National Laboratory Alternating Gradient Synchrotron (AGS) at energies up to ~ 10 GeV/u, and at the CERN Super Proton Synchrotron (SPS) at energies up to 200 GeV/u. One of the difficulties in interpreting the results of these studies has been the lack of a well established and generally accepted theoretical framework for calculating the observables obtained in the experiments.

A major difference between these earlier studies and the experiments to be carried out at RHIC is that at the RHIC energy scale present theoretical estimates are that approximately half of the energy transfer from the projectile frame to the midrapidity region may be calculable using Perturbative Quantum Chromodynamics (PQCD). This makes available a well established model for comparison with the data to be obtained at RHIC.

With the lower energy beams used in the BEVALAC, AGS, and CERN heavy ion studies the most basic input to the calculational models has been the flux and energy of the projectile nuclei. In calculating the various observables measured in these experiments corrections are made to account for the Fermi momenta of the bound nucleons. At RHIC energies ($\sqrt{s}$ = 200 GeV) the basic inputs to the model (PQCD) are the flux and momentum *distributions* of the quarks and gluons in the colliding nuclei. An example of these quark and gluon momentum distributions, for partons in an unbound proton, are shown[1] in Fig.1

The horizontal axis in the histograms of Fig.1 are the variable Bjorken x. This variable is the portion of a nucleon's momentum which is carried by a particular parton. The vertical axes are the parton distribution function (i.e. the number of a particular type of parton) multiplied by Bjorken x. The Q^2 values for the two plots (10 and 100 GeV^2) are the four momentum transfer for the interactions at which these parton distributions are valid. The feature to notice in these plots is that the gluon distribution has been scaled down by a factor of ten so that it could be plotted on the same graph in the x regions lower than ~0.1. It is the scattering of these soft gluons, down to x values of ~0.01 - 0.02, which account for about half of the energy transferred from the projectile to the midrapidity frame at RHIC energies.

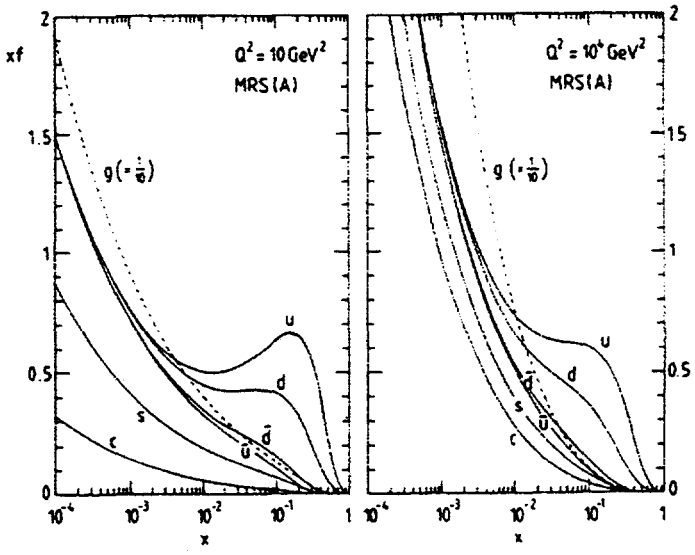

Fig. 1. MRS(A) partons shown as a function of x at Q^2 = 10 and 10^4 GeV^2.

While the quark distributions/structure functions shown are being determined in deep-inelastic scattering experiments, the same is not true for the gluon structure functions which will play such a vital role at RHIC. To quote from the conclusion in ref.1 "We believe that our analysis has considerably improved the detailed knowledge of the quark densities. However, the same is not true for the gluon distribution. At present there are, with the possible exception of the WA70 prompt photon measurements, no reliable direct constraints on the gluon".

An effect that further complicates the analysis for the RHIC data is the fact that there is a modification of the parton distributions for partons in nucleons which are bound together into a nucleus. This effect is known as shadowing. An example of shadowing for the quark distributions is shown[2] in Fig.2. What is shown is the ratio of the quark structure functions in bound nucleons divided by A times the quark structure function in unbound nucleons. What is observed is that there is a depletion in

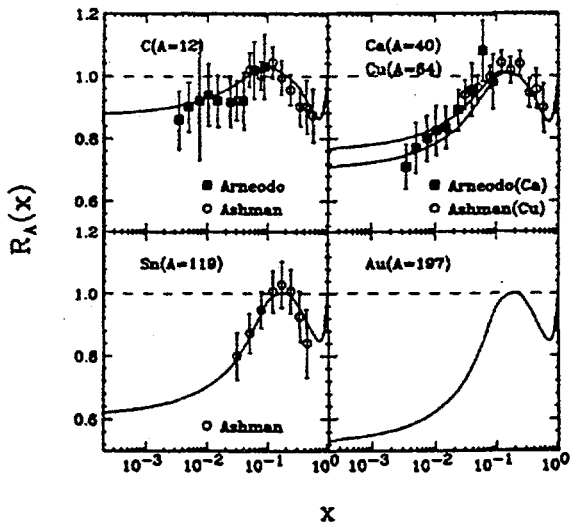

Fig. 2. The ratio of quark structure functions $R_A(x) \equiv F_2^A(x)/AF_2^N(x)$ as a function of x in small and medium x region for different nuclear mass number A.

the number of low x quarks and antiquarks. The magnitude of this depletion increases with increasing A. While no direct information is available that illustrates this shadowing effect for the gluon distributions, it is plausible to expect that the gluon distributions are modified in a similar fashion.

A Monte Carlo event generator model has been written by X.N.Wang and M.Gyulassy[2], which incorporates perturbative QCD models for multiple jet production and low P_t multistring phenomenology, to study jet and multiparticle production in high energy pp, pA, and AA collisions. Using this model (HIJING) the authors have investigated[3] the importance of minijets, nuclear shadowing, and jet quenching in high energy collisions. Fig. 3 shows some of their results.

The left hand panel of this figure shows the pseudorapidity density of charged particles expected at RHIC ($\sqrt{s}$ = 200 GeV) for central Au on Au collisions. The large increase in particle densities exhibited in the jump from the lowest (dotted) curve to the highest (dot-dashed) illustrates the importance of hard processes (jets) at the RHIC energy scale. The drop (~30%) from the top (dot-dashed) curve to the dashed curve demonstrates how large the effect of gluon shadowing may be on the observed particle multiplicities. The ~15% increase in the particle density at midrapidity from the dashed to the solid line shows how large the effect of jet quenching may be on the final particle multiplicities. The term jet quenching refers to the energy loss, dE/dl, of a high-p_T parton as it traverses the dense matter. There are PQCD estimates[4] that this energy loss may be dominated by induced gluon bremsstrahlung which depends on the infrared (Debye) screening scale for the medium. This infrared screening scale may vary significantly in the vicinity of the quark-gluon plasma transition.

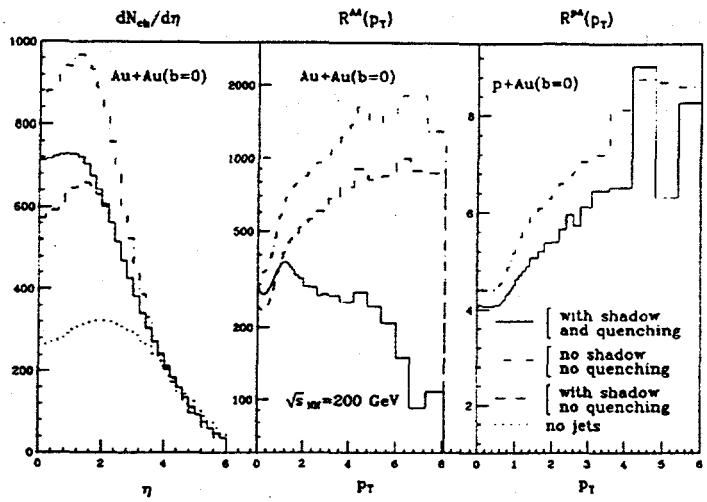

Fig. 3. Results of HIJING on the dependence of the inclusive charged-hadron spectra in central Au+Au and p+Au collisions on minijet production (dash-dotted), gluon shadowing (dashed), and jet quenching (solid line) assuming that gluon shadowing is identical to that of quarks and dE/dl = 2 GeV/fm. $R^{AB}(p_T)$ is the ratio of the inclusive p_T spectrum of charged hadrons in A+B collisions to that in p+p.

The middle panel of Fig.3 illustrates how these effects (gluon shadowing and jet quenching) change another of the final state observables, the inclusive transverse momentum spectra. From the figure it is seen that the gluon shadowing may decrease the yield of moderate P_t particles ($P_t \geq 5$ GeV/c) by a factor of two relative to the scaled pp yield. Also shown is the dramatic reduction (~ factor of 5) in the yield of these moderate P_t particles that may result from jet quenching.

The possible magnitude of the effects of gluon shadowing and jet quenching illustrated in Fig. 3 on such macroscopic final state observables as the pseudorapidity and P_t distributions points out the need to measure these effects directly to facilitate the

understanding of RHIC physics. While the magnitude of these effects may be large, it is not possible to deconvolute them by merely measuring something like the inclusive P_t spectrum. We plan to measure these effects directly using the STAR detector system with the Electromagnetic calorimeter.

There are a series of steps involved in such a study. The first step is to measure the gluon structure function in the proton using pp collisions at $\sqrt{s}$ = 200 GeV. One measures this structure function via two body kinematics[5] in hard qg scattering. The identifying tag for these events is a final state that consists of a γ and a jet. The γ and jet will be approximately back to back in the azimuthal angle φ, with roughly equal energies. The kinematic information is used to extract the x_{BJ} of the scattered gluon and quark. This preliminary measurement of the gluon structure function of the proton is significant in its own right as it has never been directly measured.

The next step is to measure the gluon structure function for nucleons bound in a gold nucleus. It is the modification of the structure function in the bound nucleon that is referred to as shadowing. One does this using p-Au running at RHIC. The final state kinematics allows one to select events in which the scattered gluon is from the Au nucleus.

Given the gluon structure function for nucleons bound in a gold nucleus, one now takes advantage of the available calculation tool, PQCD, to calculate what the inclusive moderate to high P_t spectrum should look like for AuAu collisions and compares this with the data. This allows for the possibility of studying modifications of the jet fragmentation function due to the media traversed by the hard scattered partons. It is this modification that is referred to as jet quenching.

This modification of the fragmentation function may yield a quantitative signal that the matter produced in the collisions has passed through a quark-gluon plasma.

An important consideration when evaluating the ability of the STAR detector to make the measurement of the gluon structure function is the acceptance of the detector and the range of Bjorken x over which one can make the measurement. These quantities are shown in Fig. 4. The vertical axis is the pseudorapidity of the γ and the horizontal axis is that of the jet for a qg $\rightarrow$ γ-jet event. The rectangular box in the lower left hand corner shows the acceptance for the barrel EMC alone. One sees that if $|\eta_\gamma|$ is $\leq$ 1.0 and $|\eta_{jet}|$ $\leq$ ~0.35 then the event is within the acceptance of the barrel. The η range for the jet in the barrel is due to the finite (~0.7) radius typically used in jet finding codes and the requirement that all of the jet energy is intercepted by the barrel. The large increase in acceptance that one achieves with the addition of a single endcap EMC is shown by the area of Fig. 4 which is outside of the rectangular (EMC barrel) box. The range of Bjorken x is shown in Fig. 4 with the dashed

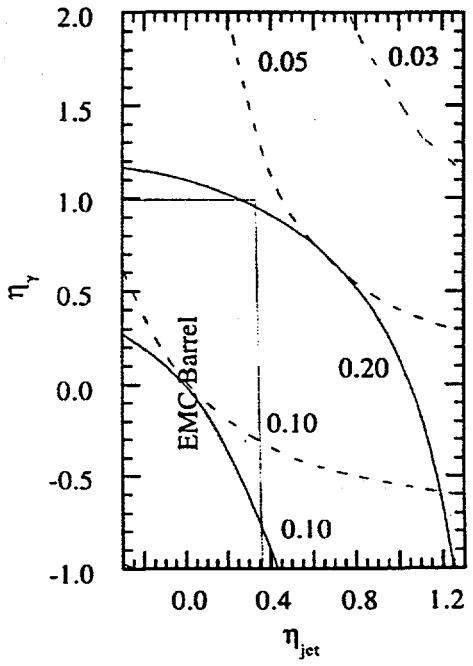

Fig. 4. Acceptance of STAR EMC (barrel + 1 endcap). Please see text for interpretation.

(gluon x value) and solid (quark x value) curved lines. The curve is not shown in this plot, but the lowest x value accessible for the gluon, ~0.02, has some acceptance in the upper right hand corner.

2. The STAR Detector

The STAR detector is a large acceptance device capable of tracking the large multiplicity of charged particles expected to be observed at RHIC. The baseline detector is a cylindrical Time Projection Chamber (TPC) located inside of a solenoidal magnet with a 0.5 T field to provide tracking, momentum analysis and particle identification of most of the charged particles at midrapidity. Momentum measurements will be made over a large pseudo-rapidity range ($|\eta| < 2$) with full azimuthal coverage ($\Delta\phi = 2\pi$). The Central Trigger Barrel (CTB), consisting of 240 scintillator slats, lies just outside of the TPC outer field cage and gives charged particle multiplicity information for $|\eta| \leq 1$ and 2π in azimuth. Vertex Position Detectors (VPD), consisting of lead converter directly in front of phototubes, are placed around the beam pipe on each side of the interaction region. The CTB ($|\eta|\leq 1$), VPD ($4.8\leq|\eta|\leq 5.0$), and direct readout of the wire planes incorporated in the TPC readout sectors ($1\leq|\eta|\leq 2$) will be utilized to supply trigger information to STAR and luminosity information to both the STAR detector and the RHIC accelerator.

Improvements planned for STAR should significantly increase its physics capabilities. These additional detectors are the Silicon Vertex Tracker (SVT), an Electro-Magnetic Calorimeter (EMC), a highly segmented Time-of-Flight array (TOF), external time projection chambers (XTPC), and a photon multiplicity detector (PMD). The addition of the EMC is imperative for the physics study presented here. A cutaway view of the STAR detector is shown in Fig. 5 below.

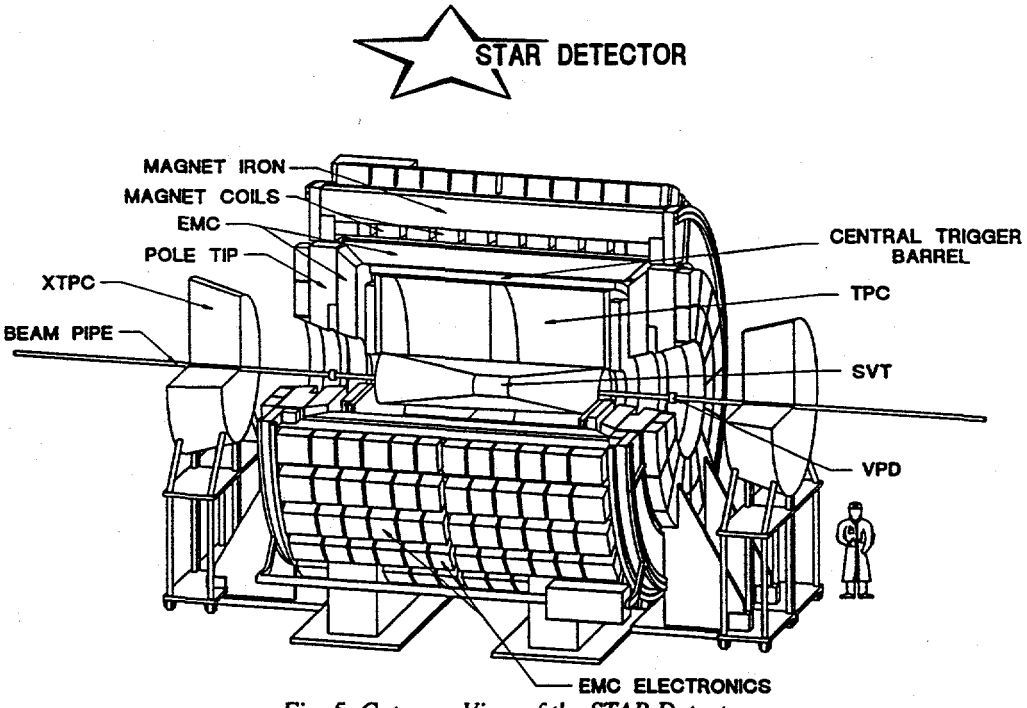

Fig. 5 Cutaway View of the STAR Detector

The proposed STAR Electromagnetic calorimeter consists of a barrel ($|\eta|\leq 1$, $\Delta\varphi = 2\pi$) and one endcap ($1\leq|\eta|\leq 2$, $\Delta\varphi = 2\pi$), both of which contain shower maximum

detectors. More information about the proposed calorimeter can be found in Ref. 5. Some of the basic parameters for the calorimeter are listed below:

Barrel

- ★ 20 layers of 5 mm thick Pb
- ★ 21 layers of 4 mm thick scintillator
- ★ ~18 radiation lengths thick
- ★ 1200 towers
- ★ 120 modules, 1 unit in η, 6° in φ
  - 10 towers/module
  - 2 tiles/layer/tower, 0.05 in η
  - Read-out with WLS fibers spliced to clear fibers
  - Fibers are coupled to edge of tiles with aluminized mylar
  - Allows depth, η segmentation

Endcap

- ★ 25 layers of 5 mm thick Pb
- ★ 26 layers of 4 mm thick scintillator
- ★ ~23 radiation lengths thick
- ★ 60 azimuthal sectors in two 180° halves, each composed of 9 towers
- ★ 540 towers

SMAX

- ★ wire/pad type

3. Simulation study and results

The investigation of STAR's ability to identify dijets via simulation studies has been an ongoing effort for a number of years. The results presented here are the outcome of recent efforts of Konstantin Shestermanov IHEP (Protvino Russia) and myself. As shall be elucidated in more detail in what follows, we utilize the STAR implementation of GEANT for detector simulation, the STAR analysis shell (TAS), and the full STAR Time Projection Chamber (TPC) tracking package.

STAR plans to carry out jet studies using the TPC and the EMC (i.e. no hadronic calorimetry). The general idea is that one uses the tracking information from the TPC for the charged final state particles and the EMC for the neutral energy.

Jet finding routines generally work by looking for directed energy flow coming from an event. The first part of our analysis entails how we get from the data that comes out of the STAR detectors to the energy flow out of the interaction vertex. The analysis starts with the momentum analyzed charged particle tracks found in the TPC. The pad row crossings (hits) in the TPC are passed to the present TPC tracking code. The tracks which are returned, and used in this analysis, contain the inefficiencies and finite momentum resolutions from the present tracking code. At no point is kinematic information from GEANT used to assist in this analysis. Each of the found TPC tracks is projected outward to see if it intersects with the barrel EMC. If the track intersects the barrel, a parameterized amount of energy is subtracted out of the struck tower. In the analysis presented here the parameterization is only a function of the momentum magnitude for the track. Whether or not a track intersects the barrel EMC, all the found TPC tracks are projected back to the primary interaction vertex. The total energy for the

track is calculated, assuming that the track is due to a pion, and this energy for the track is entered into the appropriate η-φ histogram bin. No particle ID is used at present so it is assumed that all tracks are charged pions.

Once the energy in the EMC has been corrected for all of the found TPC tracks which strike the barrel, the resulting energy in the EMC is multiplied by 1/sampling factor for neutral energy, to arrive at the deduced incident neutral energy. This quantity 1/sampling factor was extracted via the GEANT response to electromagnetic energy, and has a value of approximately 16.

At this point the charged energy histogram (evaluated at the primary vertex) is added bin by bin to the neutral energy histogram, to end up with the histogram (in η-φ) of the total energy flow out of the primary vertex. It is this last histogram that is used as the input to the jet finding code.

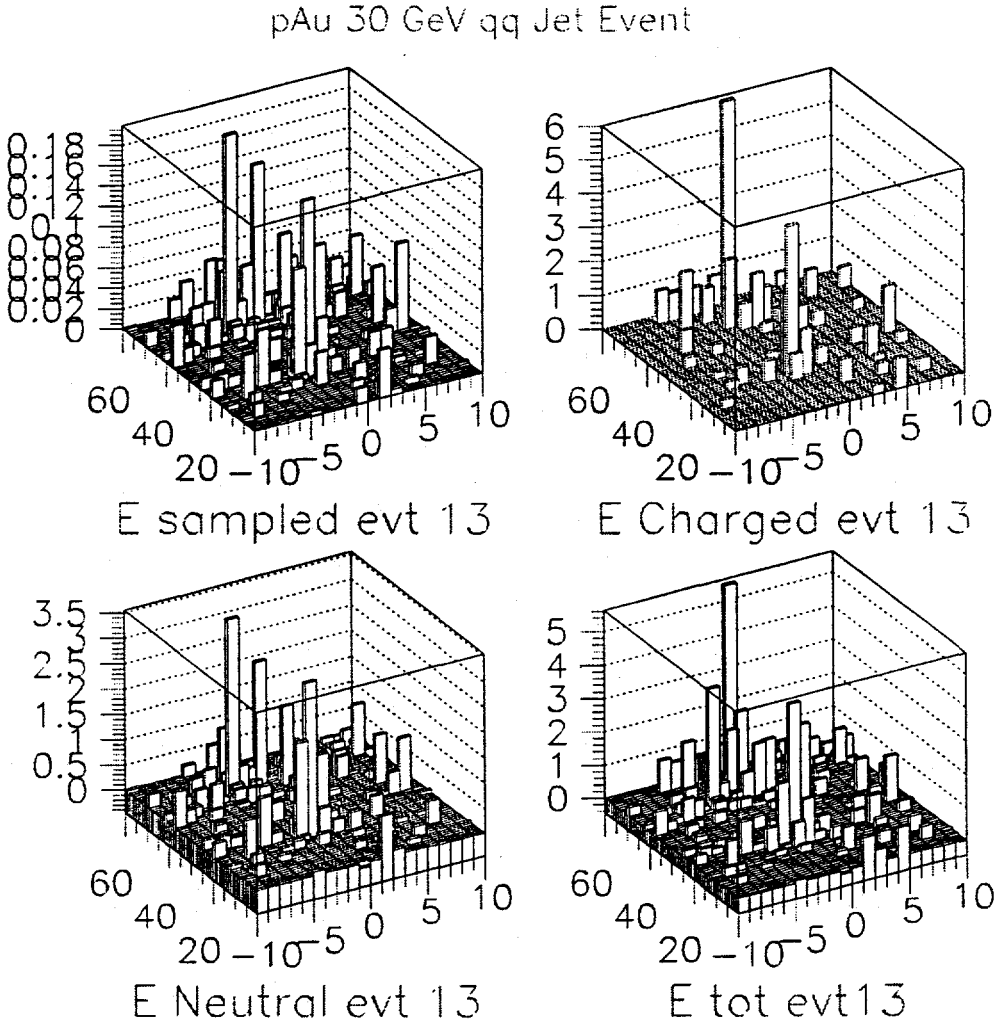

Figure 6. Pictorial representation of the Energy flow analysis. The axis that runs from -10 to 10 is the pseudorapidity bin number. This corresponds to a range of -1 to 1 in η. The axis that runs from 0 to 60 is the ϕ bin number. This corresponds to 360° in azimuth. The vertical scale in all the plots is energy in units of GeV.

This process is illustrated in Fig. 6. The event shown contained a 30 GeV/c P_t qq scatter in a pAu collision at $\sqrt{s}$ = 200 GeV. The upper left lego plot shows the sampled

energy in the EMC due to both the incident neutral and charged energy. The vertical scale in all of the lego plots of Fig. 6 is energy in units of GeV. The upper right lego plot shows the charged energy evaluated at the interaction vertex, as determined through the procedure described earlier using the TPC tracks and assuming that all tracks are pions. The lower left plot shows the deduced incident neutral energy for the event. Finally, the lower right plot shows the total energy flow out of the vertex for the event.

The jet finding code that we are using is a modified version of the UA1 jet finding code. The basic logic is that of a generic cluster finding algorithm. It looks through the η-φ bins in the energy flow histogram for bins that are greater than some threshold value, E_T^{Seed}. It orders these towers then, going from highest to lowest, sums all of the energy within some cone radius, R_0, around the seed tower. Finally these energy sums or clusters are compared to a final threshold, E_j. If they are greater than this final threshold then the energy cluster is identified as a jet. The modifications that have been made deal mainly with determining, on an event by event basis, what the soft background energy is in an event. This is done via an iterative process that sums all of the energy that is not included in a jet, divides this summed energy by the number of towers that are not included in jets, and then subtracts this background energy from all calorimeter towers. In the first pass of this iterative process this background energy is the sum of all the energy divided by the number of towers in the calorimeter. The user definable parameters in this jet finding code are the seed tower energy, E_T^{Seed}, the cone radius, R_0, and the minimum jet energy, Ej.

All of the results presented in this document were done using only the barrel component of the STAR EMC. For the purposes of this study it was desirable to separate the effect of STAR's acceptance from the efficiency of the jet finding algorithm when applied to the STAR data. This was accomplished by looking at the directions of the hard scattered partons generated with the HIJING code. If the partons scatter within the psuedorapidity range from -.3 to +.3 then the event is stored for input to the STAR GEANT package. The results for pp, CC, SiSi, and FeFe events at $\sqrt{s}$=200 GeV, where each event contains a hard qq scatter with a P_t of 30 GeV/c, are shown in Fig. 7. The efficiency is defined as the number of dijet events found by the code divided by the number of input events. A dijet was defined to be found if the angle between the found jet and the parton in the X-Y plane was less than one radian, the two jets were back to back in φ to within 30°, and the jets energy was greater than or equal to 5 GeV (9 GeV for the FeFe data). The error bars shown for

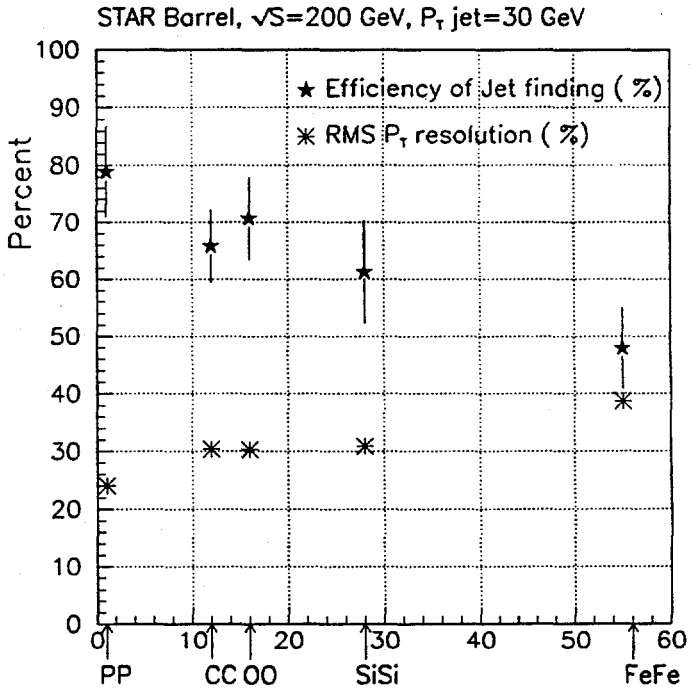

Figure 7. Jet finding Efficiencies

the efficiency just reflect the statistical errors.

Also plotted in Fig. 7 are the Pt resolutions of the found jets for the various systems. These resolutions are the rms widths of the distributions of Pt of the partons - Pt of the jets.

As discussed previously, the gluon structure function measurement for Au will be measured via qg scattering in pAu running. As a start towards understanding STAR's capabilities for this important measurement, we've done a study of the efficiency of our present code to find dijets in pAu events as a function of the Pt of the parton scatter. The results of this study are shown in Fig. 8 for parton Pt values of 30, 20, 15, and 10 GeV/c. Also shown are the P_t resolutions for the jets. The efficiencies and resolutions are defined in the same manner as in the AA case.

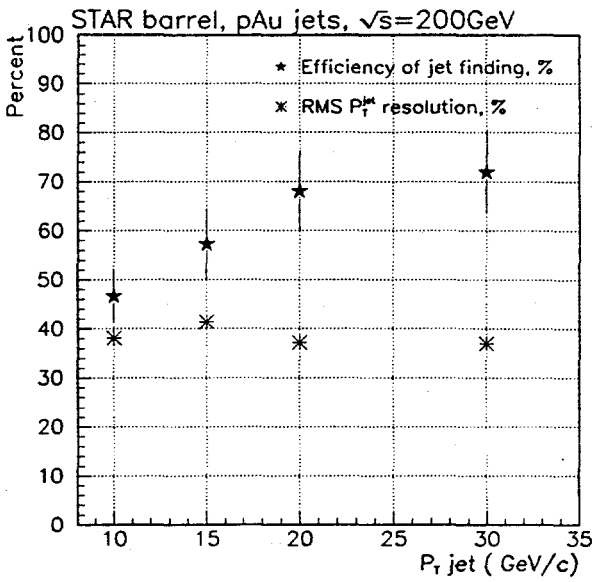

Fig. 8 Jet efficiencies and resolutions versus P_T.

3. Summary

Determining the initial conditions for the AA collisions that will take place at RHIC is important for understanding the data which will be taken at RHIC. A direct measurement of the gluon distributions for nucleons bound in a nucleus will enable the application of PQCD for understanding the RHIC data. This will allow us to deconvolute the effects of gluon shadowing and jet quenching on global final state observables such as the multiplicity density and the moderate to high portions of the P_t spectrum.

Our simulations to date give us confidence that STAR, with the addition of the proposed ElectroMagnetic Calorimeter, will be capable of pursuing this measurement. Among the current RHIC detectors STAR is unique in this capability.

---

[1]A.D Martin, W.J. Sterling, and R.G. Roberts, Phys. Rev. D **50** (1994) 6734.
[2]X.N.Wang and M.Gyulassy, Phys.Rev. D **44** (1991) 3501, and Refs. there in.
[3]X.N.Wang and M.Gyulassy, Phys.Rev.Lett. **68** (1992) 1480.
[4]M.Gyulassy, M.Thoma, and X.N.Wang, LBL Report No.LBL-31003, 1991 (to be published).
[5] Conceptual Design Report for the STAR Electromagnetic Calorimeter. LBL Pub-5380.

Strangeness detection in ALICE experiment at LHC

K. Šafařík[a] representing the ALICE collaboration

[a]CERN, European Laboratory for Particle Physics,
CH-1211 Geneva 23, Switzerland

We present some parameters of the ALICE detector which concern the detection of strange particles. The results of a simulation for neutral strange particles and cascades, together with estimated rates are presented. We also briefly discuss the detection of charged K-mesons. Finally, we mention the possibility of open charm particle detection.

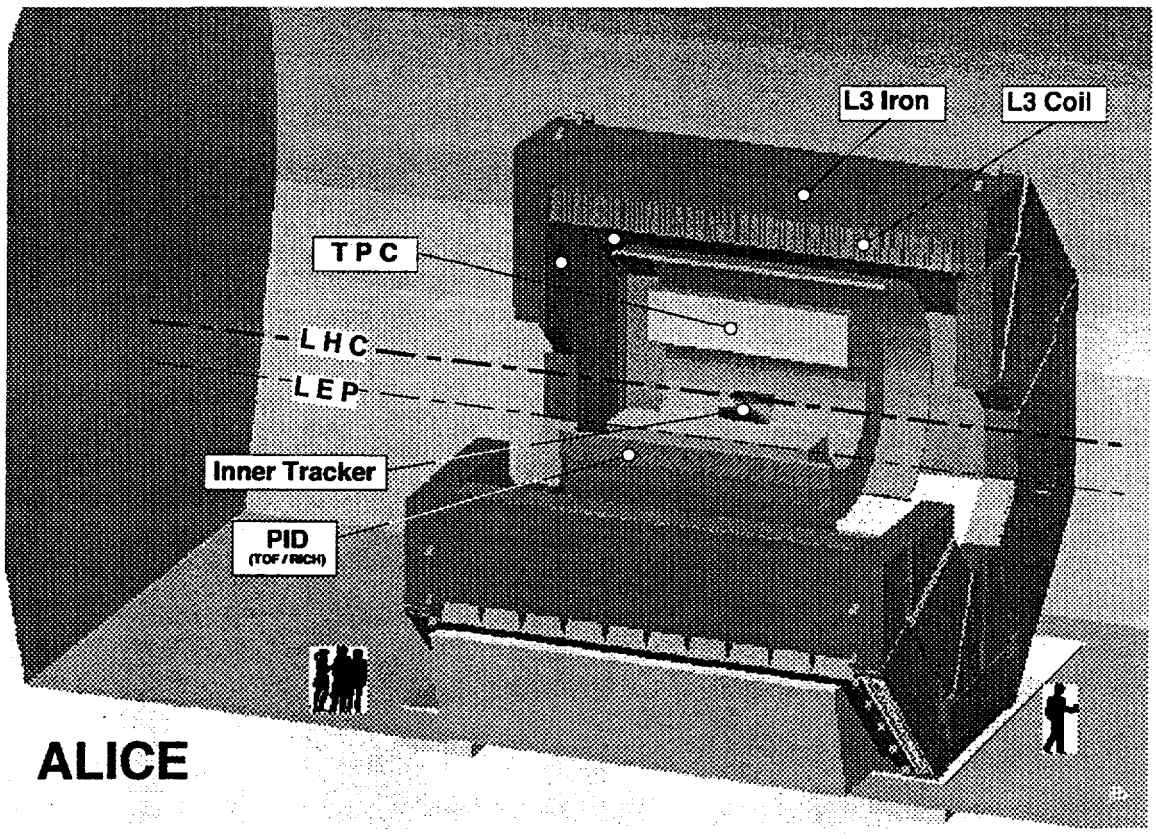

Figure 1. A three-dimensional view of the dedicated LHC heavy-ion detector ALICE.

1. INTRODUCTION

Heavy-ion physics has been from the beginning a part of the physics programme of the LHC (Large Hadron Collider) project. Among the three experimental proposals which have received "the green light" (i.e. permission to proceed with the technical project) one is the dedicated heavy-ion experiment ALICE (A Large Ion Collider Experiment). The two others (ATLAS and CMS) being designed mainly to detect the hard pp interactions, have only a limited capability to register heavy-ion collisions, with the possible exception of high-mass dimuon detection (Υ family). Therefore the ALICE detector has to cover a broad range of observables proposed to investigate dense hadronic matter and its possible phase transition as produced in ultrarelativistic heavy-ion collisions. One of the proposed observables is strangeness production, which is sensitive to the enhanced density of s

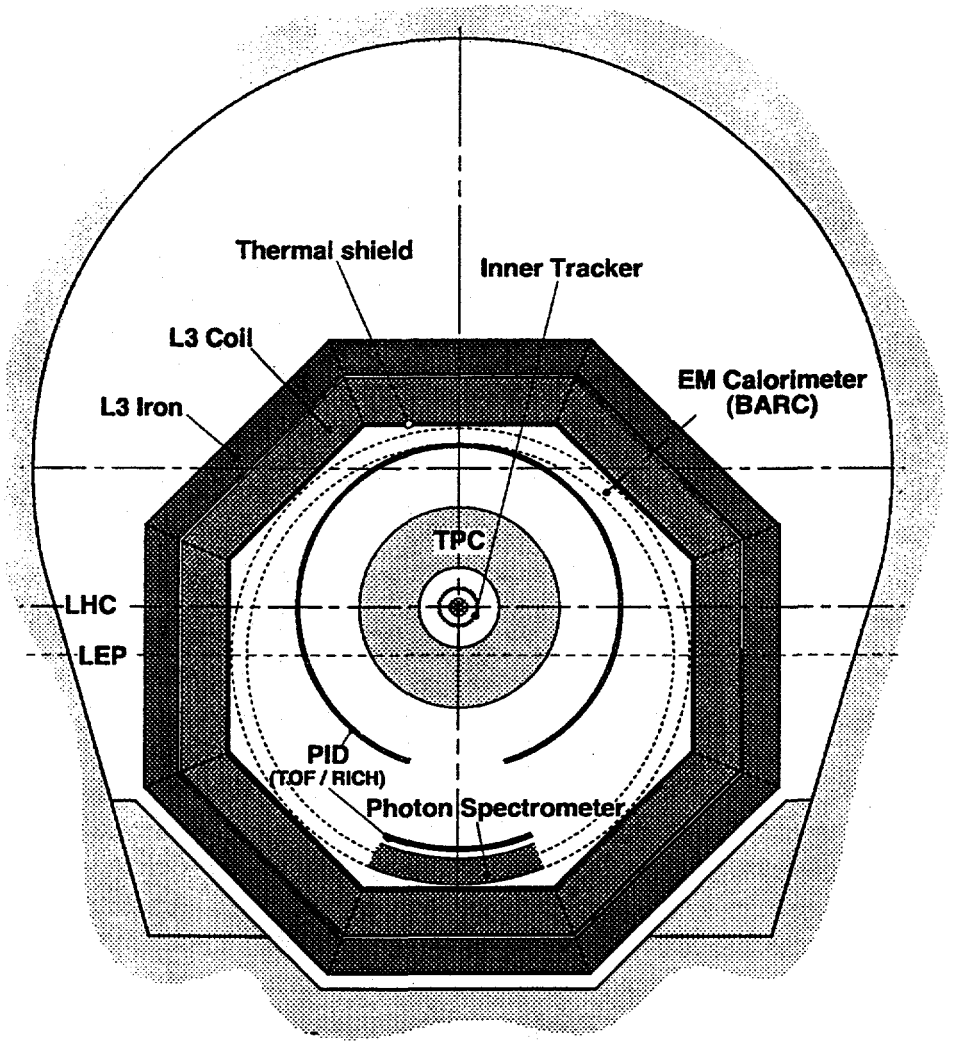

Figure 2. Transverse view of the ALICE detector.

quarks expected from (at least partial) chiral symmetry restoration in the plasma phase. The strange particle yields would also measure the approach to chemical equilibrium of the system at freeze-out. The composition of particles changes during the dynamical evolution. The large production cross-section particles, such as K-mesons, will quickly reach their equilibrium densities. On the other hand, heavier and multi-strange particles (Ξ, Ω) are of particular interest because they are difficult to produce in thermal collisions, and hence their abundances might not change significantly during the lifetime of a hadron gas. Therefore the yields of multi-strange hyperons are potentially a signature for the enhanced strangeness density expected in a QGP[1].

The efficient detection of V^0 type particles (K^0_s and Λ) and cascades requires a vertex detector close to the interaction point and a suitable tracking device for large track densities. For charged kaons in addition to the tracker a detector with particle identification capabilities is necessary. The main parts of ALICE detector[2] involved in strange particle detection are (see figures 1 and 2:

- inner tracking system (ITS);
- time projection chamber (TPC);
- particle identification detector (PID).

All these detectors are placed inside a large solenoidal magnet (the reuse of the L3 magnet[3] is considered as the baseline option) with low magnetic field (about 0.2 T), thus being able to reconstruct low p_T tracks down to 100 MeV/c. In the next section we shall discuss the estimates of track finding efficiency, resolution, efficiencies of V^0 and cascades finding, their acceptances and expected rates. The third section describes briefly the charged K-meson identification.

Although a little out of the scope of this presentation, the detection of open charm particles would be of great interest. A significant enhancement has been predicted for a dense system expected at LHC energies[4]. The finding of secondary vertices from charm particle decays will require a modification to ITS. Such a possibility is mentioned in the fourth section. Finally, we conclude on the strangeness detection capabilities of ALICE in the last section.

2. V^0 AND CASCADES DETECTION

We plan to detect strange particles with $c\tau$ of the order of a few cm by measuring the decay products and reconstructing secondary vertices. The main tracking device is a cylindrical TPC which has inner radius 1 m and outer radius 2.5 m. Its length along the beam direction ($z-$ axis) is 5 m thus it covers $(90 \pm 45)^o$ (pseudorapidity $|\eta| < 0.9$). Pad readout with a pad size of 3.2 mm $\times$20 mm (azimuthal $\times$ radial directions) arranged in 75 rows will be used. The expected space resolution for an average track is about 500 μm and about 900 μm in azimuthal and drift (along z) directions respectively. To improve momentum resolution especially for high momentum tracks and to be able to find secondary vertices we plan to use the ITS which consists of five concentric cylindrical layers around the beam pipe with radii from 7.5 cm up to 50 cm. The three innermost layers (the radius up to 22 cm) have to be truly two dimensional detectors due to the

large particle densities. The first layer is made from silicon pixel detectors[5] and for the next two layers we plan to use silicon drift detectors[6]. The two outermost layers will consist of either double-sided silicon strip detectors or micro-strip gas chambers[7] with small stereo angle. We assume the spatial resolution of the three innermost layers to be 30 μm $\times$ 60 μm (azimuthal $\times$ z directions) while for the outermost layers the resolution will be 60 μm $\times$ 1000 μm.

The track finding is based on TPC data. We have tried essentially two methods: backward track following and the Hough-Radon transform. Both methods work satisfactorily; we have reached an efficiency of about 96% for charged particle density $dy/N_{ch} = 2000$ and about 93% for the largest predicted density $dy/N_{ch} = 8000$ at negligible ghost contamination (below 1%). We try to connect tracks found in the TPC to the ITS. Depending on detailed assumptions on particular ITS designs and the possibility of hit matching in the two outermost layers using amplitude information, we find the track matching efficiency somewhat momentum-dependent but always higher than 90%. The global (TPC + ITS) momentum resolution can be approximated as $\Delta p/p = (1.2 \oplus 0.3 \times p)\%$ except for very

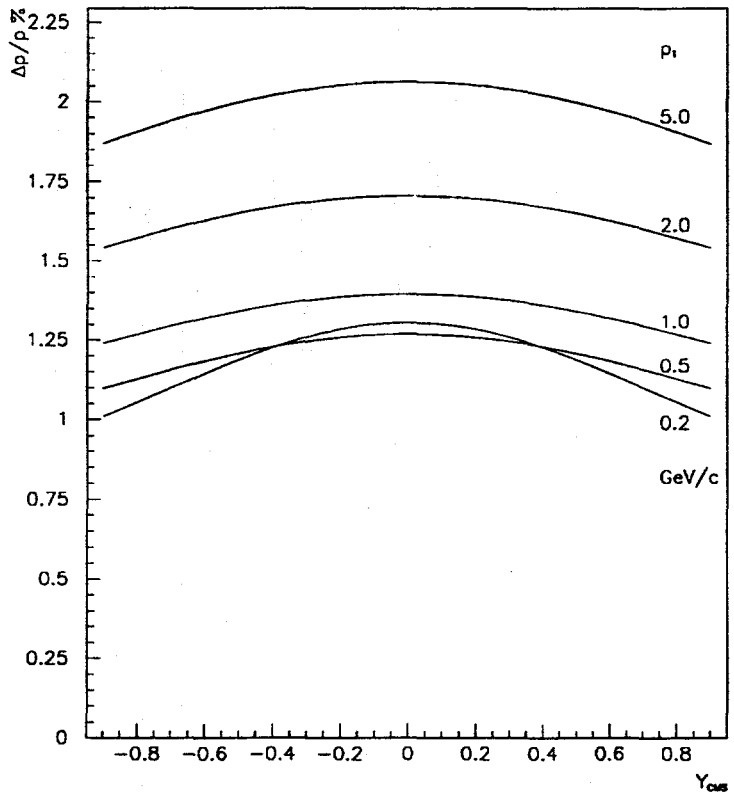

Figure 3. The momentum resolution as a function of rapidity for different p_T.

low momenta, where a $1/\beta$ term in multiple scattering dominates. The dependence of the momentum resolution on rapidity for different p_T is shown in figure 3. The angular resolution is significantly better than 1 mrad for most of the accessible momentum range. The impact parameter resolution, which is the most critical parameter for finding the secondary vertices near to the interaction point, for particles with momenta between 0.5 $\div$ 1.0 GeV/c is in the range 200 $\div$ 100 μm using the ITS, whereas using the TPC only, the resolution will be insufficient (of the order of 1 cm).

Following the tracks from the TPC towards the ITS we use the primary vertex constraint. In order to find the tracks not originating from this point we have to relax this condition. In fact we aim to find the tracks from secondary vertices which are only a few cm from the interaction point. We can treat these as if they come from the primary vertex but with enlarged margins (up to $\sim$ cm, depending on the momentum estimate from the TPC). From the quoted impact parameter resolution we can deduce that we shall be able to resolve secondary vertices starting from a few mm from the interaction point. We conservatively define the decay zone to be between 1 cm and 6 cm in radial distance from the interaction point (the maximum being determined by the beam vacuum chamber). We present here the estimates done for the following decay chains

- $K^0_s \rightarrow \pi^+\pi^-$

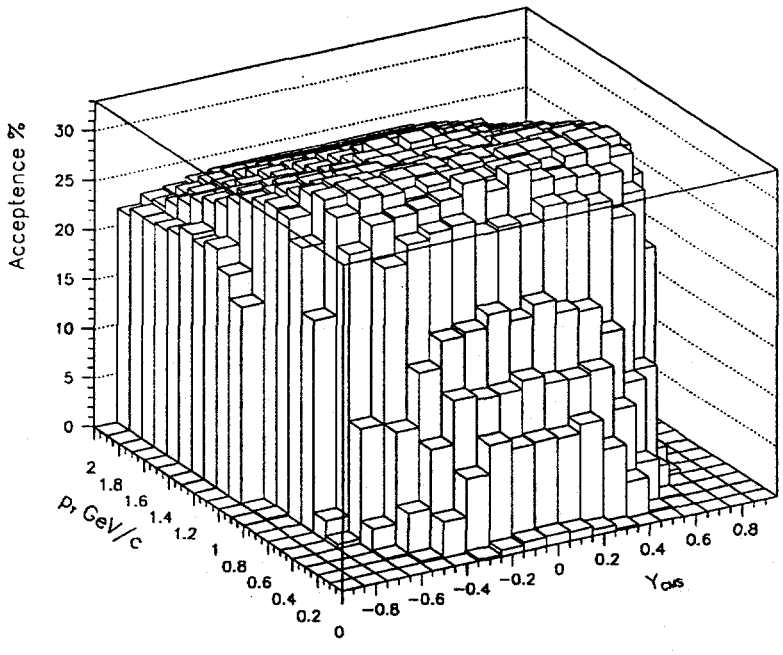

Figure 4. The K^0_s acceptance in rapidity and p_T.

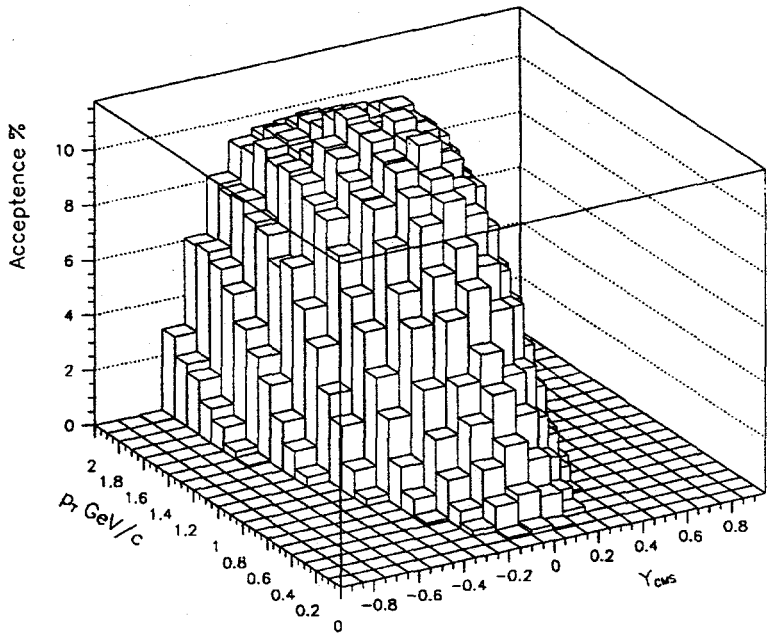

Figure 5. The Ω^- acceptance in rapidity and p_T.

- $\Lambda \rightarrow \pi^- \mathrm{p}$
- $\Xi^- \rightarrow \pi^- \Lambda \rightarrow \pi^- \pi^- \mathrm{p}$
- $\Omega^- \rightarrow \mathrm{K}^- \Lambda \rightarrow \mathrm{K}^- \pi^- \mathrm{p}$.

First, we calculate the geometrical acceptances as a function of rapidity and p_T (at this step the branching ratios are also included). As examples the results for K^0_s and Ω^- (which were not previously published) are shown in figures 4 and 5 respectively. Then we convolute the geometrical acceptance with the assumed particle distribution (flat in rapidity and m_T scaling for p_T dependence) in order to obtain the integrated acceptances. To estimate the reconstruction efficiency after track finding we collect all the tracks which do not point to the main vertex and try to combine them with all tracks with the opposite charge. Whenever the combination gives an acceptable secondary vertex within the decay zone, we reconstruct the total momentum vector and check the pointing to the primary vertex. For cascades we use a larger window at this step and then try to combine the Λ candidate with another unmatched negative track from the collection of tracks which have missed the interaction point. We intend to use particle identification in order to decrease the number of combinations. However, we find that the V^0 and cascade reconstruction efficiencies depend only weakly on whether we use the particle identification or not. Also the increase in fake combinations is not large after suppression of the particle identification. The simulated mass spectra for Λ together with background in 10 central

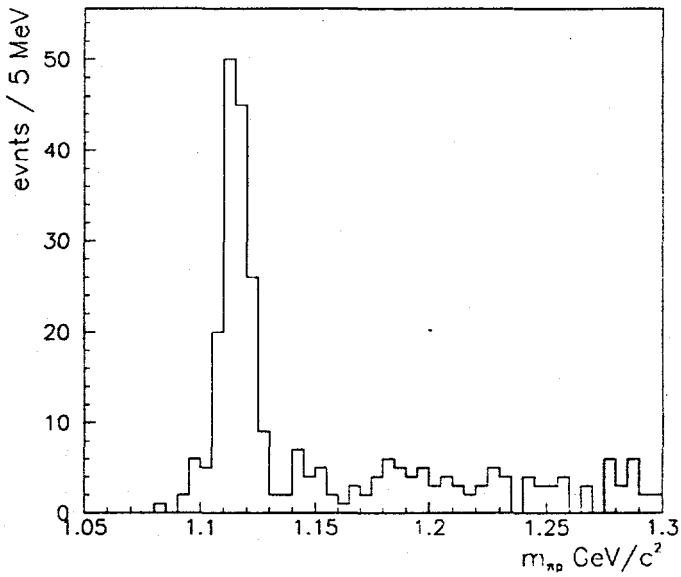

Figure 6. The Λ effective mass distribution from 10 central Pb - Pb events.

Pb - Pb events, using particle identification, is shown in figure 6. In order to estimate the detected particle rates, we use the production ratios relative to the charged π-mesons shown in the table 1. In this table we have summarized the results on the integrated ac-

Table 1
Summary of the integrated acceptances, the reconstruction efficiencies, the assumed production ratios and the expected detection rates for V^0 particles and cascades.

Particle → decay	Acceptance	Efficiency	Produced/π	Detected/event
$K^0_s \to \pi^+\pi^-$	21%	$(50 \pm 10)\%$	5%	56 ± 14
$\Lambda \to \pi^-p$	10%	$(50 \pm 10)\%$	2%	13 ± 4
$\Xi^- \to \pi^-\Lambda \to \pi^-\pi^-p$	2.7%	$(30 \pm 6)\%$	0.3%	0.15 ± 0.04
$\Omega^- \to K^-\Lambda \to K^-\pi^-p$	2.8%	$(30 \pm 6)\%$	0.05%	0.02 ± 0.01

ceptances, the reconstruction efficiencies, the assumed production ratios and the expected detection rates (for the largest predicted particle density mentioned above) in one central Pb - Pb event for all investigated decay chains. The expected multiplicities for K^0_s and Λ will allow the classification of events on event-by-event basis. The accumulated statistics for cascades during a typical LHC heavy-ion run (1 month) will be sufficient for any kind

of inclusive study.

3. CHARGED K-MESON IDENTIFICATION

We shall also use the two tracking detectors described above for particle identification by measuring $\mathrm{d}E/\mathrm{d}x$. For the ITS, we plan to readout analog pulse-height information at least from the silicon drift detectors and the silicon strip detectors. This measurement is foreseen mainly for e/π separation of very low momenta tracks (< 140 MeV/c) which due to the magnetic field cannot reach the PID. We intend to use the ITS also as a standalone tracker at even lower momenta down to 30 MeV/c in order to identify electrons from Dalitz decays. Using the ITS only, we shall measure $\mathrm{d}E/\mathrm{d}x$ with $(12 \div 14)\%$ precision which allows us to separate π/K below 0.5 GeV/c and K/p below 1 GeV/c (in $1/\beta^2$ region).

We estimate the TPC $\mathrm{d}E/\mathrm{d}x$ resolution in the high track density environment to be 7%. With such resolution we shall mainly extend the electron identification up to 3 GeV/c. The resolution is insufficient by itself for hadron identification in the region of relativistic rise, but will be helpful in combination with an additional particle identification method.

We have two options for the PID: either a time-of-flight (TOF) detector or a ring imaging Cherenkov (RICH) detector. The preferred solution for TOF measurement is high-pressure, parallel-plate, Pestov spark counters[8]. They have an excellent intrinsic time resolution (down to 25 ps). The backup options are atmospheric-pressure parallel-plate chambers working in the avalanche mode[9] or a grid of scintillator counters with multi-anode photomultipliers. The alternative solution is based on proximity-focusing

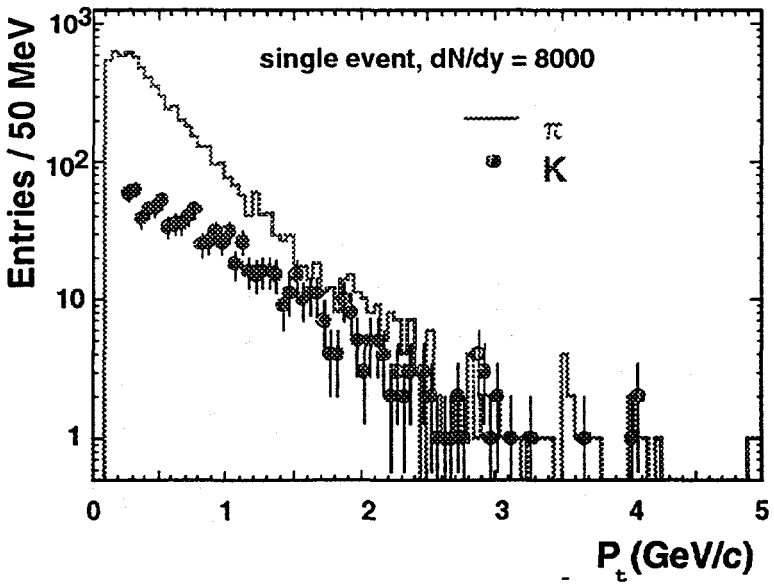

Figure 7. The p_T spectra for pions (full line) and kaons (circles) from a single event.

RICH detector with a liquid-Freon radiator and solid photocathode UV detector followed by a proportional chamber with pad readout[10].

In order to estimate the combined separation power of the TPC and the PID we have assumed the large-acceptance TOF to be at radius 3 m with time resolution 100 ps. For charged K-mesons we have more than 3 σ separation below 2 GeV/c, which we can use for event-by event analysis. The 2 σ separation, sufficient for inclusive ratios, will be possible for kaons up to 4 GeV/c. As an example of event-by-event analysis, we show in figure 7 the transverse momentum spectra for pions and kaons detected in one central Pb - Pb event (under the assumption of the largest predicted density, see above). The simulation includes tracking efficiency and particle decays.

4. OPEN CHARM DETECTION ?

In order to detect open charm particles by identifying charm decay vertices we need the impact parameter resolution to be significantly better than the typical impact of decay products from charm, $\sim$ 100 μm. The performance of the proposed detector with resolution between $(100 \div 200)\mu$m is clearly insufficient for this purpose. The main contribution to impact parameter resolution is the multiple scattering in the beam vacuum chamber and the innermost ITS detector layer. One of the ways to improve resolution is to place an

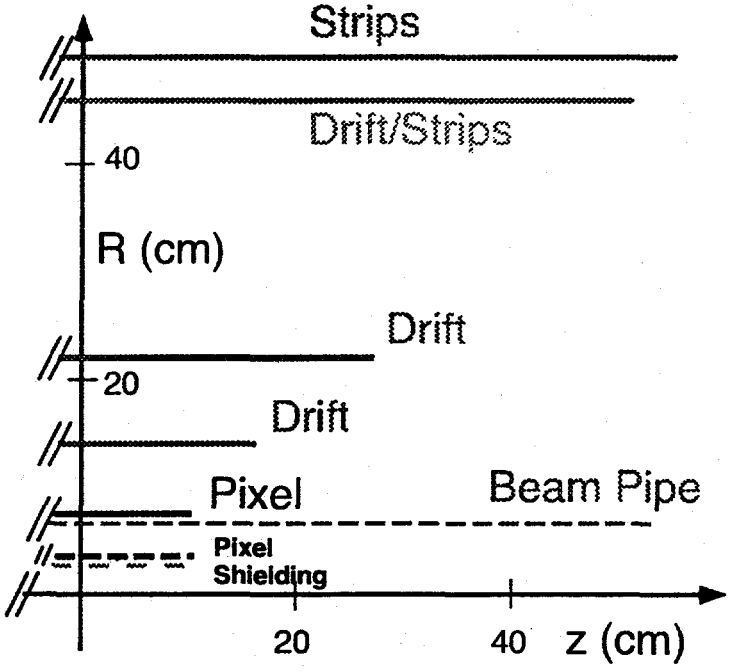

Figure 8. Schematic view of the inner tracking system with additional pixel plane for charm detection.

additional silicon pixel plane inside the vacuum chamber as shown schematically in figure 8. If it will be possible to keep the thickness of this detector below about $(300 \div 400)\mu$m and to obtain sufficient rf-shielding with only $\sim$ 50 μm of aluminium, we shall achieve the impact parameter resolution $\sim$ 30 μm for 1 GeV/c particles. In this case charm detection starts to be thinkable. It is clear, that such a solution is very complicated and has drawbacks (i.e. how to protect the detector from beam instabilities during filling ?). Another possibility would be to decrease the radius of the vacuum chamber which would allow us to make it thinner. On the other hand, the latter solution could degrade the angular resolution, which is needed for correlation studies.

5. CONCLUSIONS

We have discussed the performance of the ALICE detector for strange particle detection. The detected multiplicities of single-strange particles, K^0_s and Λ, in one central Pb - Pb collision will be sufficient for event classification on an event-by-event basis. The statistics for multi-strange hyperons (Ξ^- and Ω^-) registered during a typical heavy-ion run at the LHC will allow a high precision inclusive study of strangeness production. Using the combination of the TPC and the PID we can select in a single central Pb - Pb event enough K-mesons to investigate event-by-event particle spectra (i.e. to measure the m_T slope). Finally, we have mentioned the possibility of open charm detection with the ALICE detector. However this point needs further more detailed study.

6. ACKNOWLEDGEMENTS

I am very grateful to many of my colleagues who have helped me with this publication, submitting calculations and useful discussions, especially to F. Antinori, D. Evans, E. Quercigh, J. Schukraft and O. Villalobos Baillie.

REFERENCES

1. P. Koch, B. Müller and J. Rafelski Phys. Rep. 142 (1986) 167.
2. N. Antoniou et al., Letter of Intent for A Large Ion Collider Experiment CERN/LHCC/93-16, LHCC/I4 (1993); J. Schukraft, Nucl. Phys. A566 (1994) 311c.
3. B. Adeva et al., Nucl. Instr. and Meth. A289 (1990) 35.
4. E. Shuryak, Phys. Rep. 61C (1980) 71; Nucl. Phys. A566 (1994) 559c.
5. E. H. M. Heijne et al., Nucl. Instr. and Meth. A349 (1994) 138.
6. P. Rehak et al., Nucl. Instr. and Meth. A248 (1986) 367.
7. A. Oed, Nucl. Instr. and Meth. A263 (1988) 351; A. Oed et al., Nucl. Instr. and Meth. A284 (1989) 223.
8. Yu. N. Pestov, Nucl. Instr. and Meth. 196 (1982) 45; Nucl. Instr. and Meth. A265 (1988) 150.
9. Y. Galaktionov et al., Nucl. Instr. and Meth. A317 (1991) 497.
10. F. Puiz et al., preprint CERN/PPE 92-200.

Analysis of Single Events in Ultrarelativistic Nuclear Collisions: A New Method to search for Critical Fluctuations

R. Stock[a]

[a]Fachbereich Physik
Univ. of Frankfurt, Germany

1. Introduction

The upcoming generation of experiments with ultrarelativistic heavy nuclear projectiles, at the CERN SPS and at RHIC and LHC, will confront us with several thousand identified hadrons per event, suitable detectors provided. An analysis of individual events becomes meaningful concerning a multitude of hadronic signals thought to reveal a transient deconfinement phase transition, or the related critical precursor fluctuations. Transverse momentum spectra, the kaon to pion ratio, and pionic Bose-Einstein correlation are examined, showing now to separate the extreme, probably rare candidate events from the bulk of average events. This type of observables can already be investigated with the Pb beam of the SPS. I will then discuss single event signals that add to the above at RHIC and LHC energies, kaon interferometry, rapidity fluctuation, jet and Υ production.

Event by event analysis of the final state hadrons is, by no means, a novel concept of particle physics: it has been successfully employed in the analysis of two - or three - jet events created in electron-positron collider experiments. We recall the corresponding plots, now shown on textbook covers, exhibiting highly ordered hadron emission patterns, with low background. Owing to the development of suitable collective observables [1,2] such as planarity, thrust, jettiness, triaxiality etc., concerning the relevant multi-hadron momentum space correlations, it was possible to separate the candidate events from millions of irrelevant ones. Here we first encounter the characteristics of all event by event analysis: the average hadronic final state possesses a sufficient number of microscopic degrees of freedom (hadron multiplicity, first of all), in order to support the definition of collective observables characterizing the event as a whole. The signal to noise ratio, governing the collective jettiness observables, is determined by finite particle number statistics, and it was impossible until the advent of high energy colliders to clearly separate the jet correlations from trivial finite number fluctuations. It was possible to isolate a small cross

section phenomenon from a predominant soft collision background, the interesting events constituting a minute fraction of the overall collision event sample. This phenomenological pattern, resolving non-trivial, rare candidate events from a predominant background of lesser informational value, will be the subject of the present study.

Event by event analysis in application to relativistic heavy ion collisions, at the lower Bevalac/SIS energies has also demonstrated the existence of collective nuclear matter flow [3,4]. This effect is not seen in a few rare events but in every semi-central collision of heavy nuclei, but its manifestation is in a weak signal only - a small directed momentum component superimposed on an otherwise statistical distribution typical of a Hagedorn fireball emission. A significant analysis requires above hundred charged hadrons per event to be recorded, in order for the collective effect to stand out beyond trivial finite number fluctuations.

The subject of this paper, identification of deconfinement signals in central collisions of Au on Au or Pb on Pb at the CERN SPS and at future colliders, presents a situation in which the interesting events may be rare, *and* the relevant signal not large. However, an ideal multihadron detector system would now record about 1000 charged particles in an interval of c.m. system rapidity $|y| < 1$, at the SPS Pb beam of 160 GeV per nucleon, this number expected to be even larger, by factors of about four at RHIC and of about 15 at the LHC. Frightening to the detector builder, such high rapidity densities make event by event analysis an extremely powerful, novel possibility of analysis.

At the SPS we may expect the 'ideal' quark gluon continuum state to be formed only very seldom, as the limit of a broad fluctuation in the reaction dynamics trajectory. Event by event analysis may thus be the only viable approach to pin down the relevant hadronic observables.

We are now considering, not some kind of collective ordering in space of the microscopic particle vectors, but properties typical of a thermodynamic description: transverse momentum spectra and 'temperatures', hadron density vs. reaction time, production rates as well as yield ratios of various hadronic species. This is the terminology of the Hagedorn model [5], however with a different, new aim. That is why our topic lends itself to contribute to the celebration of his 70^{th} birthday.

What is new here: we are one step beyond the traditional fireball model. There, the individual event does not reveal the features that become *visible* in an ensemble of events - temperatures, K/π ratios etc.. Here, each event is a rudimentary ensemble, the whole acting as a heat bath for its parts. A phase transition does, or does not occur in a single, given event. The event itself must be inspected, an ensemble average over many events rendering the signals *invisible* if the relevant events are rare, and if the observable effects represent changes, not by orders of magnitude but by factors of order two or three.

This is obviously the case in hadronic signals. For example, an event exhibiting a pion mean transverse momentum of 700 MeV/c, i.e. twice the standard at SPS energy, would obviously be worth further inspection: and a K/π ratio rising, from the standard value of about 0.15, to a value of about 0.5 suggests the sensational assumption of equal flavor population among up, down and strange, i.e. formation of a perfect n_f=3 system.

Thus, the margin by which the interesting events differ from the average events is not really dramatic. But if a transient partonic state near equilibrium does, in fact, cause these fluctuations, they must occur *simultaneously* in the candidate events. We need to look for a class of events exhibiting a simultaneous fluctuation in the relevant observables. The more such signals we get proposed from theory, and the more of them can be defined in single events with sufficient significance, the more conclusive is the evidence for an unusual dynamics inferred from the correlation between anomalous features.

Obviously, if all central collision events went through a plasma phase there would be no fundamental need for event by event analysis, with the exception perhaps of jet quenching [6], deflagration volcanos [7] and other observables consisting in local enhancements in real space. However one intuitively doubts as to whether every event produces the plasma state, at least at the SPS energy: the critical levels of energy density, life-time and reaction volume may be just about reached here [8], making the equilibrium plasma phase occur only as the limit of precursor situations with local bubbles, i.e. less homogeneity, more pre-equilibrium chaos. That such intuitive arguments are applicable in the specific case of a QCD phase transition has recently been shown by Kapusta et al. [9]. Furthermore the various parton cascade models now under investigation [10] seem to indicate a partial approach toward chemical equilibrium only [11], in the average event. The interesting events thus should represent a fluctuation, and relevant observables should be correlated in their fluctuation.

2. Schematic Examples of Event Observables

Which of the hadronic observables, regarded to be sensitive to a plasma phase, lend themselves to event by event determination? The answer follows from consideration both of the average multiplicities of hadronic species per event, and of the detection/identification efficiency plus acceptance attained by the detector systems. We will, for the sake of a first survey, leave the second aspect unattended (see next chapter) assuming an 'ideal' detector covering a sufficiently wide interval in longitudinal phase space, $|y| < 1$, or even < 1.5. This is the aim of the experiments NA49, STAR and ALICE at the SPS, RHIC and LHC respectively [12–14]. Clearly, all hadrons with $\langle m \rangle \gg 1$ can be studied event by event in principle but we will not consider Φ, η, K^0 and strange hyperons here because they are recorded by measuring their decay products which is seldom accom-

plished with high overall efficiency (with exception perhaps of K^0 at RHIC and LHC). This leaves $\pi^{+,-,0}$, $K^{+,-}$, p and $\bar{p}$: in central Pb+Pb collisions at 160 GeV/nucleon, the corresponding mid-rapidity densities dN/dy are expected to be about 500 for $\pi^+ + \pi^-$, 65 for $K^+ + K^-$, 80 for p and 10 for $\bar{p}$. We can also define the quantities of total negative and positive hadrons, and h^+ - h^- giving the charge excess distribution, (h^+ - h^-) $\approx$ 60 at mid-rapidity. This latter quantity approximates the net baryon density distribution, giving the position of the initial valence quarks in final phase space. An upward fluctuation of dN/dy (h^+ - h^-) at $y=y_{cm}$ indicates events with high stopping of incoming longitudinal quark energy ('hot events').

2.1. Transverse Momentum Spectra

As a first example, Fig. 1 shows the transverse momentum distribution of the negative plus positive pions in the domain $2 < y < 4$ in a single central Pb+Pb collision at the SPS energy. It was simulated with the Fritiof event generator [15]. We see a well expressed, typical 'thermal' spectrum up to $p_T \approx 1$ GeV/c, all points being well fitted by an exponential with inverse slope or 'temperature' parameter T=176 MeV. At RHIC and LHC such event spectra will extend up to 1.5 to 2 GeV/c where the influence of hard QCD processes (minijet activity) sets in. At the SPS inspection of the shape differences from an exponential will be of marginal significance but clearly we obtain firmly established values for $\langle p_T \rangle$ and T. In Fig. 2 I illustrate what is meant by 'firmly' for the temperature T distribution obtained from individual fits of 1000 Fritiof events. The mean value $\langle T \rangle$=183 MeV agrees well with the slope parameter obtained for the p_T distribution of the whole ensemble, which is not surprising in view of the symmetric distribution of single event temperatures. The width of this distribution is small, $\sigma \approx 10$ MeV only! It results, both from the microscopic collision mechanism built into Fritiof which lead to a genuine fluctuation from event to event, and from the degree of accuracy with which the ca. 800 charged pions seen in each event in $2 < y < 4$ fix the inverse slope parameter of each event fit. Thus, any high $\langle p_T \rangle$ and high T event occurring in the real data due to a 'critical opalescence' mechanism, related to the plasma phase transition, would be identified by the event by event fit, even if it occurred once only in every hundred events and has a typical T only 20 % higher than the average event. More realistically, such mechanism would produce a shoulder of the distribution and would be selected with reasonably low background by applying a cut at $T > \langle T \rangle + 3\sigma$.

2.2. The-Kaon to Pion Ratio

Our second example refers to the K/π ratio which we define here as $(K^+ + K^-)/(\pi^+ + \pi^-)$. From this observable, an estimate can be made [16] of the overall freeze-out ratio of strange to non-strange quarks in the final state. Defining a strangeness suppression factor

$\lambda = 2(s+\bar{s})/(u+\bar{u}+d+\bar{d})$ we find a value of λ=0.34± 0.05 in light ion collision at SPS energy, corresponding to a K/π ratio of 0.14 at mid-rapidity. Strangeness enhancement, expected to be a characteristic feature of events with a plasma [17] is, in reality, a reversal of strangeness suppression. Ideally, λ should then approach unity but several factors (presence of u, d valence quarks, finite s-quark mass etc.) let us expect $\lambda \leq 0.65$ in Pb+Pb at the SPS. Thus, the 'plasma candidate' events might exhibit a twofold enhancement of the K/π ratio.

Fig. 3 shows the distribution of the K/π ratios found in the above sample of 1000 Fritiof Pb+Pb events. Again we observe a symmetric, rather narrow distribution. Its relative width, $\sigma/\langle K/\pi \rangle \approx 0.12$ is higher than that of the T distribution due to the modest kaon statistics. Nevertheless, there is zero background at twice the mean, i.e. $K/\pi \approx 0.25$. Thus we encounter the same high selectivity toward fluctuations in this ratio due to the reaction dynamics. We shall see in the next chapter that consideration of the realistic detector dampens our evaluation, the relative width increasing from the ideal 0.12 to about 0.30 in NA49. But even then a twofold increase in the K/π ratio is worth 3σ.

2.3. Two Pion Momentum Correlations

Our last example is negative pion Bose-Einstein correlation. I shall only give a very brief sketch of the relevant physics here; the detail may be found in recent state of the art publications [18], and the idea of event by event pion correlation study has already been explored by Ferenc [19] in a simulation of conditions expected with the LHC detector ALICE.

In a multi-pion final state the symmetry of the total wave function leads to a clumping in momentum space of identical pions as their 4-momentum difference goes to zero. Over a certain distance Δ^4p the probability to find pion pairs, triplets etc. is enhanced with respect to the probability expected from the single pion momentum space distribution. Thus, for a pair, $P(p_1,p_1) > P(p_1)\cdot P(p_2)$ over a characteristic distance $|p_1 - p_2| = \Delta p_{1,2}$ which turns out to be related to the average size R in configuration space of the pion emitting source by the relation $\Delta p \cdot R = \hbar$ characteristic of a Fourier transform. More accurately, one defines a correlation function in momentum space, $C(\Delta p_{1,2})$ as the ratio (with proper normalization) of $P(p_1,p_2)/P(p_1)\cdot P(p_2)$. For a pion pair, $C \rightarrow 2$ as $\Delta p \rightarrow 0$, and $C \rightarrow 1$ for large Δp. For a source of average space-time dimensions 10 fm the enhancement domain, where $C > 1$, extends up to about 40 MeV/c in pair momentum difference. We see that the momentum difference of multi-GeV pions must be measured with high accuracy in order to determine the correlation function.

Two important observations are in order here, to understand the physics significance of the correlation effect. *Firstly*, the total Bose-symmetric wave function of the final multipion state gets established during the time interval Δt in which, on the average,

each pion encounters its last strong interaction. This occurs after an expansion of the dense hadronic fireball which takes the average time t_0 in order to arrive at sufficient dilution. The correlation function thus refers to the space-time dimension of the pion source at freeze-out from strong interaction. This is a very late stage of the overall reaction dynamics but the average expansion time t_0 depends critically the dynamics of the collision. *Secondly*, closer inspection of the space related components of the correlation function shows [20] that they depend, not only on the spatial dimensions of the freeze-out state but also on the dynamics through which the system arrived at freeze-out. The dynamics depends on the equation of state of superdense matter, and on the existence and nature of a phase transition from an early plasma to an expanding hadron fireball. This explains why we want to analyze two pion correlation functions at the event by event level.

In practice one analyzes the correlation function in terms of Fourier transforms of plausible Gaussian space-time pion sources. This determines the expansion duration parameter t_0 and an effective transverse dimension of the freeze-out volume, R_{side}. For a definition of this quantity and an evaluation of its significance the reader is referred to ref. [20]. The informational value of an event by event study of this quantity will be illustrated below. I refer to the SPS experiment NA49 which will cover the rapidity domain $1.5 < y < 5.5$ for negative pions. Restricting the analysis, of to the region $1.5 < y_{lab} < 3.5$ (mid-rapidity is at $y_{lab} = 2.8$ in Pb+Pb collisions), NA49 will record about 350 negative pions per event, resulting in a pair statistics of about 60.000 per event. Of these pairs, only a small fraction falls into the relevant domain, of $\Delta p \leq 40$ MeV/c, which contains the relevant information. The significance of fitting that fraction of the two pion correlation function by means of a Gaussian ansatz for $C(\Delta p_{side})$, as a Fourier transform of a spatial Gaussian source distribution $\Phi(R_{side})$, will thus be marginal due to small pair statistics. The expected results are illustrated in Fig. 4. They are taken from a Fritiof-based simulation of Pb+Pb collisions by Ferenc [21]. The Fritiof model ignores the effects of Bose-symmetrization, which are subsequently implemented in a manner analogous to the procedure described by Sullivan et al. [22]. This implementation of correlations was carried out for two values of the transverse source dimension, $R_{side} = 7$ and 11 fm. Fig. 4 sketches the resulting distributions of output R_{side} values. A relatively narrow distribution results for the input source size $R_{side} = 7$ fm with $\sigma \approx 4$ fm, but the output distribution for the $R_{side} = 11$ fm source is very broad, with a σ of about 10 fm. This is due to the fact that the region of the correlation function which contains the signal (i.e. $C > 1$) is narrower in relative pair momentum for the source with 11 fm radius, the fit thus based on a smaller fraction of the total pair statistics. Nevertheless, a cut at $R_{side} > 20$ fm would select predominantly $R = 11$ fm events.

We conclude that event by event analysis for the transverse pion source dimension becomes just about meaningfull under SPS Pb+Pb collision conditions. The same holds for an analogous analysis of the total expansion time parameter t_0. The selectivity for non-average events improves at collider energies [19] but not dramatically. We have deliberately chosen the correlation observable to illustrate the most ambitious and complicated end of the range of possible event by event signals.

3. Event by Event Analysis with realistic Detector Systems

No realistic detector system, of finite cost and dimension, can be constructed with present experiment technique that could uniformly cover a wide rapidity interval providing 'perfect' efficiency for momentum measurement and hadron identification - even if we restrict the task to charged hadrons. The tracking efficiency, determining particle momenta, may well suffice but the track by track hadron identification capabilities remain restricted even if detector layouts combine several signals aiding in the task of identification, such as specific ionization and time of flight. The fixed target experiments with Pb beams of 160 GeV/A at the SPS are, apparently, confronted with the most complicated task. Mid-rapidity pions have Lab. momenta of about 2-4 GeV/c, the Kaons found at 6-8 GeV/c, and protons/antiprotons at 12-15 GeV/c. Moreover, as a satisfactory rapidity domain needs to be covered, the essential range of hadronic Lab. momenta is of formidable extent, of about 1 to 50 GeV/c, facing experimental technique with an unprecedented task in order to secure a uniform acceptance. Collider experiments are, at first sight, easier because at $|y| < 1.5$ in the c.m. frame, which coincides with the Lab. frame, the momentum spread of the hadrons is more compact, and independent of the accelerator energy, with only the multiplicity density increasing which concerns chiefly the tracking capabilities, the minor difficulty in comparison to hadron identification.

Before discussing the implementation of event by event analysis in realistic detectors, a brief consideration is in order of the non-hadronic observables relevant toward plasma production diagnostics. Among those, direct photon and lepton pair spectroscopy requires an experimental effort commensurable to the task of exclusive hadron spectroscopy. In principle, the ideal solution would be a detector that covers all together. However it turns out that, at least under CERN SPS fixed target conditions, the optimal layouts for exclusive hadron and for lepton/dilepton measurement are contradictory. Moreover, as almost all the lepton/dilepton observables result from subtraction of ensembles the fact that, e.g., a J/Ψ particle was created can not be traced to the event that produced it: this physics is not genuinely an event by event physics, and both approaches must seek separate optimization also at RHIC and LHC.

Proceeding to a consideration of realistic conditions in realizable experiments, Fig. 5

shows [23] the distributions of negative hadron (essentially negative pion) multiplicity and event mean transverse momentum in 14.000 central S+Ag collisions at 200 GeV/A, as observed in the NA35 streamer chamber. This detector type gets over-exposed by the multiplicity density in this reaction and thus was artificially blindfolded in 2/3 of the total azimuthal acceptance; thus the relatively small observed mean h^- multiplicity of 50 in $1.0 < y < 3.5$. The extrapolated, true $\langle h^- \rangle$ is about 170 but that is irrelevant as far as the quality of event by event analysis is concerned - somehow only the honest, primary data yielded by the detectors are relevant. It is therefore not surprising that the event $\langle p_T \rangle$ distribution is fairly broad, $\sigma / \langle p_T \rangle$ of the entire ensemble being of order 0.15. As $T \approx 0.5 \langle p_T \rangle$ in a thermal system, we would get a $\sigma(T) \approx 25$ MeV in this case. Compare to the plot of Fig. 2: the $\sigma(T) \approx 10$ MeV observed there refer to 800 pions per event. Actually, the width of the $\langle p_T \rangle$ distribution in Fig. 5 shows that we are entirely counting statistics limited in the S+Ag streamer chamber case, $\langle m \rangle \approx 50$ letting us expect about 15 % accuracy. Doing the sampling 14.000 times over, in different events, merely exhibits the full (nearly) Gaussian distribution corresponding to the elementary statistics. The detector momentum tracking accuracy, of order $\Delta p/p = 0.01$, does not surface in this low multiplicity case. If the streamer chamber experiment were designed only for $\langle p_T \rangle$ study its tracking resolution would thus represent an unnecessary level of accuracy. This is not the case in the Pb+Pb simulation of the NA49 design, illustrated in Figs. 1 and 2. Counting statistics alone, with 800 negative plus positive pions per event, would suggest a 3.5 % accuracy of the $\langle p_T \rangle$ and T parameters of each event. The relative width of the T distribution in Fig. 2, however, is larger: $\sigma / \langle T \rangle = 0.055$. At this level of counting statistics the fluctuation at the microscopic level of the single event reaction dynamics becomes visible, and this is precisely the design goal of the experiment. Momentum tracking inaccuracy (not incorporated in the simulations leading to Figs. 1 and 2), at a mean level of $\Delta p/p = 0.01p$, will not significantly change the picture presented by Figs. 1 and 2. However, the outcome of the streamer chamber experiment, Fig. 5, implies a warning; we recognize a non-Gaussian high p_T tail in the data of a real detector. Experience with 4π tracking detectors shows a common trend in developing such tails, perhaps resulting from the asymmetry of the momentum observable which is bounded at $p_T = 0$ MeV/c but unbounded toward high p_T. Poisson statistics analysis may take care of this, to extract the truly non-average events in the high $\langle p_T \rangle$ or T tails.

In concluding this section a brief consideration follows of the real detector implementation of two much more ambitious event signals: the K/π ratio and the pion source dimensions.

As we have seen from Fig. 3, elementary counting statistics alone limits the quality of the event K/π ratio signal in central Pb+Pb collisions at the SPS. Furthermore, the

simulation resulting in the Fig. 3 data leaves the finite particle identification resolution restrictions unconsidered. This factor, however, dominates the uncertainty of the signal, and it will stay with us in all future collider experiments in spite of the better counting statistics. The difficulty arises from the task of identifying a 15 % fraction of kaons next to the 85 % fraction of pions. A state of the art detector system will achieve a 3 σ separation between kaons and pions. The traditional method of K cross section measurement is based on gathering a huge ensemble of events, then unfolding with high precision the composite particle identification variable (specific ionization, time of flight etc.) with a multi-Gaussian superposition fit for the π, K, p relative composition fractions. Thus, the 3 σ elementary separation may be recovered in a 3 σ quality of relative cross section assessment for the entire ensemble. This method is very unaccurate as applied to the meager statistics of a single event, the ill-determined tail of the high pion count invading the kaon signal. A new method, based on a track by track maximum likelyhood fit has been developed by Gazdzicki [24]. In its application to a 3 σ average kaon to pion separation detector such as NA49 this model still predicts a considerable broadening of the 'ideal' event K/π distribution (Fig. 3), which thus acquires a relative width of 25-30 %.At RHIC and LHC this width should come down to about 20 %, or below.

Bose-Einstein pion pair correlation analysis of single events, finally, suffers from the principal difficulty to determine the denominator in the correlation function, i.e. the single pion space distribution P(p_i) with sufficient accuracy. In the standard analysis of extended ensembles one uses a sample of pion momenta mixed up from all different events to determine $P(p_i)$ free of pair correlation distortions. One way out may be to employ a primitive event generator, adapted in each event to reproduce the observed pion multiplicity, rapidity distribution, $\langle p_T \rangle$ and T parameters, then generating a high statistics single particle distribution. Alternative methods are now being developed that employ a maximum likelyhood method to extract maximum information from the single event input [25]. From among the properties of a realistic tracking detector, the momentum measurement accuracy and the resolution capability for close tracks play the crucial role here: the most important information stems from pion pairs that are as close as Δp=10 MeV/c if source dimensions in excess of 10 fm are to be analyzed. Thin targets, minimum material in the particles path, high magnetic bending power, low diffusion broading over the drift-length in TPC-type gas tracking detectors, and high granularity readout systems are the chief characteristics of suitable detector systems. The corresponding experimental technique for collider experiments is still under development. In the end, the 'ideal' detector will try to reduce the momentum tracking accuracy to just a bit below the multiple scattering uncertainty, the latter presenting a considerable limitation particularly at colliders where mid-rapidity particles are relatively slow.

4. Event by Event Analysis Strategy

In this article I have stressed the new methods of event by event analysis, perhaps at the risk of creating an 'ideology' as H. Satz has critically remarked. Let us put it back into perspective:

It is restricted to high cross section hadronic signals, with the exception of jet formation analysis and exotica searches (Centauro-type events, Chiral disordering etc.).

It is based on the intuitive idea that - at least at the low CERN SPS energy - the interesting/relevant events should be rare and need to be recognized one by one. This should be different at the ten times higher c.m. energies at RHIC, and most certainly at the 250 times higher LHC energy.

It is not the end (but only the initial step) of data analysis with detector systems optimized to its specific demands.

In order to illustrate the last remark let us sketch the analysis strategy of such an experiment. Assume that it recorded, say, $5 \cdot 10^6$ central Pb+Pb collision events in one running period. A first round of analysis (actually the most CPU-time consuming step) would determine the event characteristics. From among those we have mentioned only a few here, just enough to develop the ideas. Further event observables are the total particle density and the proton density at mid-rapidity that are related to the total energy density achieved in the event. One may also want to examine the $\overline{p}/p$ and K^-/K^+ ratios at mid-rapidity. This fixes the baryo-chemical and strangeness-chemical potentials, and a complete, approximate, thermo-chemical analysis may ideally be achieved at the event level by determining the temperature, energy density and reaction volume along with these potentials.

One will then define sub-ensembles, say at the 1 % level of $5 \cdot 10^4$ events each, that contain the extreme tail events corresponding to each of the considered event variables. I.e. extremely strange or dense or hot or large (small) or net-baryon rich (or pure) fluctuations with in the overall central event class. If all such signatures are necessary ingredients of a reaction dynamics in the presence of a phase transition the fluctuations have to be correlated. One would then proceed to a final sub-ensemble, say of 10^4 events which are multiply extreme. *It is of prime importance*, at this stage, to be aware of the fact that this ensemble of 'candidate events', stemming from a 4π detector, is still wide enough, containing a total of $10^7 - 10^8$ analyzed hadrons, allowing *not only* the observables mentioned above now to be studied with the traditional ensemble precision, *but also* the detailed shapes of all hadronic p_T distributions, the yield ratios of the neutral strange particles $K^0, \Lambda, \overline{\Lambda}$ and Φ (which do not lend themselves to single event analysis), as well as intermittency, kaon interferometry etc.. If hadronic signals bear any memory at all of the transient deconfinement stage it will be identified here, with little chance of 'trivial

scenarios' coming up with a simultaneous explanation of the physics information thus unfolded.

5. Event Analysis specific to RHIC and LHC Physics

The previous evaluation of event by event analysis tools was guided by the conditions of SPS Pb collisions, now under study. Obviously, the increased multiplicities at RHIC and LHC will improve the observational conditions. This might perhaps be crucial to establish Bose-Einstein correlation observables as event by event signals. Moreover, new specific probes into the structure of individual events are offered by production cross sections increasing with beam energy. This section will be rather sketchy, and carry me beyond the level of presently assured detector performance.

5.1. Kaon Bose interferometry

Firstly, the number of K^{+-} created per unit rapidity will increase to a level that - proper identification efficiency provided - a rudimentary Bose-Einstein correlation signal could be obtained for individual events. The physics advantage of the kaon interferometry signal results from the smaller influence of late expansion stage resonance decays, that dominate pion interferometry. Thus the decoupling stage from strong interaction-driven expansion may be layed out more clearly by K^+ in particular, rendering interpretation of the 'source dimensions' more straight forward. Any satisfactory K^+ identification efficiency rests on the development of a cheap time of flight detector type which can be deployed in 100 m^2 dimension.

K^0 interferometry offers the additional advantage to be free of final state Coulomb rescattering which might wash out the relative pair momenta established at the strong interaction decoupling point in a high hadron density environment. This correlation function also does not require the problem-laden Gamov correction procedure, which becomes inaccurate (wrong) as a consequence of Coulomb screening in a dense medium of charged hadrons. K^0 interferometry thus appears to be the eventual goal of Bose-HBT study but a sufficient detection efficiency puts high demands on the Si-vertex tracking detector systems, under development both for STAR and ALICE.

5.2. Flavor composition ratios

Talking about SVT micro-vertex detectors for RHC and LHC let me mention the possibility to detect $D, \overline{D}$ open charm mesons with sufficient efficiency - clearly not in hand as -of yet. The idea first, then the caveats. In all previous discussions concerning strangeness enhancement, due to approximate up-down-strange flavor symmetry being established with ease in a partonic state, it was an obstacle towards the determination of a 'primordial' strange to non-strange quark abundance ratio that the up-down component rises

during hadronic expansion by resonance decay to pions. A cumbersome procedure, developed by Wroblewski [16] for single hadron interactions and never re-established for nuclear collisions serves to obtain an estimate of primordial $u, \overline{u}, d, \overline{d}$ concentrations and, thus, the strange to non-strange quark flavor ratio. At SPS energy the vanishingly small concentration of charmed quarks prevents us from extending this consideration to the primordial $[s + \overline{s}]$ to $[c + \overline{c}]$ abundance ratio the latter being a pre-equilibrium signal anyhow. However at RHIC and LHC energies the open charm abundance level becomes measurable. Furthermore, note that this ratio is free of final state effects to first order, production ceasing and annihilation being minimal. The ratio of strange to charm abundance should acquire a level characteristic of the partonic state at high density, as suggested by parton cascade models [11].

The caveat: no stretch of experimental technique will render the total $[c + \overline{c}]$ content measurable at the single event level, in a manner analogous to the total $[s + \overline{s}]$ content estimated by the K yield. Nevertheless, recalling the line of argument presented in section 4, identification of interesting events by means of other event observables should result in the selection of 'interesting' sub-ensembles, of ca. $5 \cdot 10^4$ events. Could the efficiency of SVT techniques be increased to a degree that ensembles of this magnitude permit a reasonably accurate $D + \overline{D}$ study? The same question, actually, holds true for estimates of the J/Ψ and Υ content of such sub-ensembles.

5.3. Long range fluctuations in rapidity density

At RHIC and LHC we may expect an interval of several rapidity units, symmetric about mid rapidity, in which basic average quantities like energy density, net baryon density etc. exhibit nearly constant values. If the collision created something interesting rather than a boring boost invariant longitudinal tube of hadrons in equilibrium - what types of y dependence could we see at the single event level?

Before trying an answer let us ask a general question. How extended in rapidity (and azimuth) are certain phenomena? The fragmentation domains of a 60 GeV jet, for example, are two back to back regions extending over about 1-1.5 units of rapidity. Likewise, an isotropically expanding Hagedorn 'fireball' of T=200 MeV spreads pions over about $\Delta y = 2$. Note, by the way, that heavier fireball products like kaons, antiprotons exhibit a narrower spread, Δy decreasing with the rest mass (the different widths will make particle ratios depend on y although the entire fireball state can be characterized by one single overall value for, say, K/π). Thus, both jets and thermal sources require $\Delta y \approx 2$ for exclusive observation, and this sets the scale for the STAR and ALICE central detector acceptances.

A local plasma region (or bubble) located somewhere in the expanding tube would thus exert its influence on decay products over a similar, characteristic interval $\Delta y \approx 2$, (the

same holds true for a decaying region of chiral disorder). At RHIC and LHC such plasma bubble states might occur frequently, perhaps even in the *average* central collision. This might give our ideas concerning event by event analysis a further, final turn:

Slices of magnitude $\Delta y \approx 2$ contain sufficiently many particles already to permit analysis along the lines described in sect. 2 to 4. *Subevents* thus might substantiate observables, referring to a specific window in rapidity. The full event could now be analyzed by sliding this window over the full rapidity space, and characteristic fluctuations might be observed reflecting the size distribution of such bubbles of a new phase. Other relevant fluctuating parameters, beyond just size, could also be outlined (life-time, critical temperature).

Thus, in the end, I have stretched the concept of exclusive analysis to its absolute limit, looking for the fluctuations from one local state to another *within single events.* Of course this would require a wide acceptance detector, of covering $|y| \leq 4$, and a good fraction of the azimuth - a detector of the future?

REFERENCES

1. S. L. Wu and G. Zobernig, Z. Phys. C2 (1979) 107;
   S. Brandt and H. Dahmen, Z. Phys. C1 (1979) 61.
2. P. Söding and G. Wolf, Ann. Rev. Nuc. Part. Sci. 31 (1981) 231.
3. H. A. Gustafsson et al., Phys. Rev. Lett. 52 (1984) 1590.
4. P. Danielewicz and G. Odyniec, Phys. Lett. 157B (1985) 146;
   J. J. Molitoris, D. Hahn and H. Stöcker, Nucl. Phys. A447 (1985) 13.
5. R. Hagedorn and J. Ranft, Nuovo Cimento 6 (1968) 300;
   R. Hagedorn, in Cargese Lectures in Physics VI, p. 643,
   Gordon and Breach New York 1973.
6. X. N. Wang and M. Gyulassy, Nucl. Phys. A544 (1992) 559.
7. M. Gyulassy, K. Kajantie and L. McLerran, Nucl. Phys. B237 (1984) 477;
   D. Seibert, Phys. Rev. C47 (1993) 2320.
8. T. Celik, J. Engels, and H. Satz, Nucl. Phys. B205 (1983) 545.
9. J. Kapusta et al., Univ. of Minnesota Report 1994.
10. H. Sorge, H. Stöcker, and W. Greiner, Nucl. Phys. A498 (1989) 567;
    K. Geiger and B. Müller, Nucl. Phys. B369 (1992) 600.
11. K. Geiger, Nucl. Phys. A566 (1994) 257.
12. NA49 proposal CERN/SPS LC 91-31, 1991.
13. J. W. Harris, Nucl. Phys. A566 (1994) 277.
14. ALICE Letter of Intent, CERN/LHC C93-16, 1993.
15. FRITIOF version 1.6 adapted to NA35 data.
16. H. Bialkowska et al., Z. Phys. C55 (1992) 491;
    M. Gazdzicki et al., Nucl. Phys. A566 (1994) 503.
17. J. Rafelski and B. Müller, Phys. Rev. Lett. 48 (1982) 1066.
18. D. Boal, C. K. Gelbke, and B. Jennings, Rev. Mod. Phys. 62 (1990) 553.
19. D. Ferenc, CERN ALICE Note 93-14, 1993.
20. S. Pratt, Phys. Rev. D33 (1986) 33;
    G. Bertsch, M. Gong, and M. Tohyama, Phys. Rev. C37 (1988) 1896.
21. D. Ferenc, private communication.
22. J. P. Sullivan et al., Phys. Rev. Lett. 70 (1993) 3000.
23. D. Brinkmann, to be published, Frankfurt PhD Thesis (1994).
24. M. Gazdzicki, Nucl. Instr. Meth. A345 (1994) 148.
25. J. G. Cramer, D. Ferenc, and M. Gazdzicki, Univ. Frankfurt Report
    IKF-HENPG/92-3, 1992.

Figure 1. Transverse momentum spectrum of negative and positive pions in a single central Pb+Pb collision at SPS energy; the rapidity domain is $2 < y < 4$; Fritiof event simulation

Figure 2. Distribution of the single event inverse slope parameter T from 1000 Fritiof simulated central Pb+Pb events. The width is $\sigma = 10$ MeV, $\langle T \rangle$=183 MeV.

Figure 3. The distribution of the Kaon to Pion ratio from an ensemble of 1000 central Pb+Pb collisions at SPS energy generated with the Fritiof model. The width is σ=0.015, and $\langle K/\pi \rangle$=0.14.

Figure 4. Sketch of the expected outcome of R_{side} determination by two-π^--correlation analysis of single Pb+Pb central collision events. The two distributions correspond to input values R_{side}=7 and 11 fm, the corresponding width are σ=4 and 10 MeV, respectively

Figure 5. Distributions of multiplicity and mean transverse momentum for negative hadrons in the acceptance of NA35, for single central S+Ag collision events, also showing a Gaussian fit. The $\langle p_T \rangle$ width is σ=50 MeV/c.

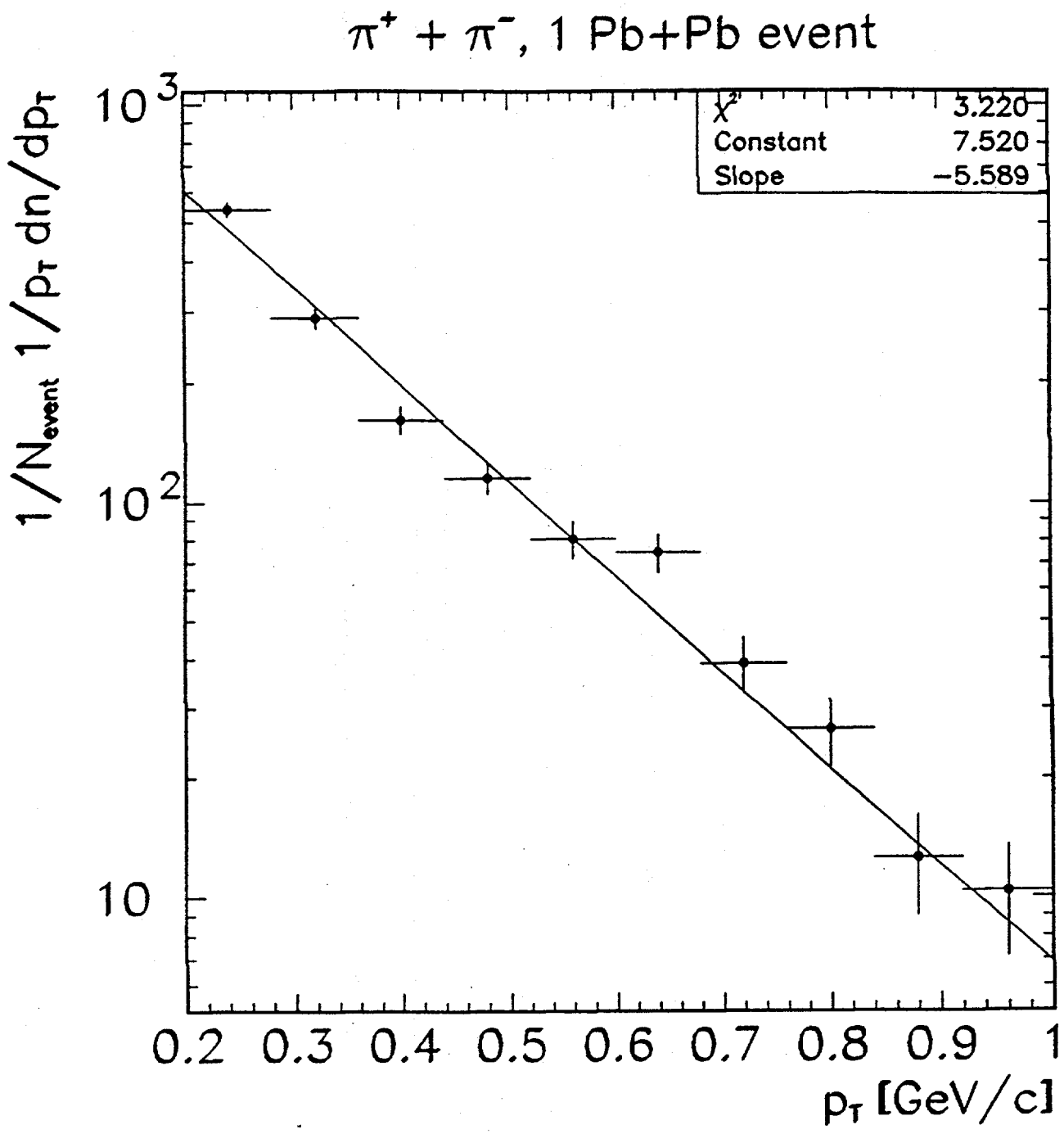
$\pi^+ + \pi^-$, 1 Pb+Pb event
χ^2 3.220
Constant 7.520
Slope −5.589
$1/N_{event}\ 1/p_T\ dn/dp_T$
10^3
10^2
10
0.2 0.3 0.4 0.5 0.6 0.7 0.8 0.9 1
p_T [GeV/c]

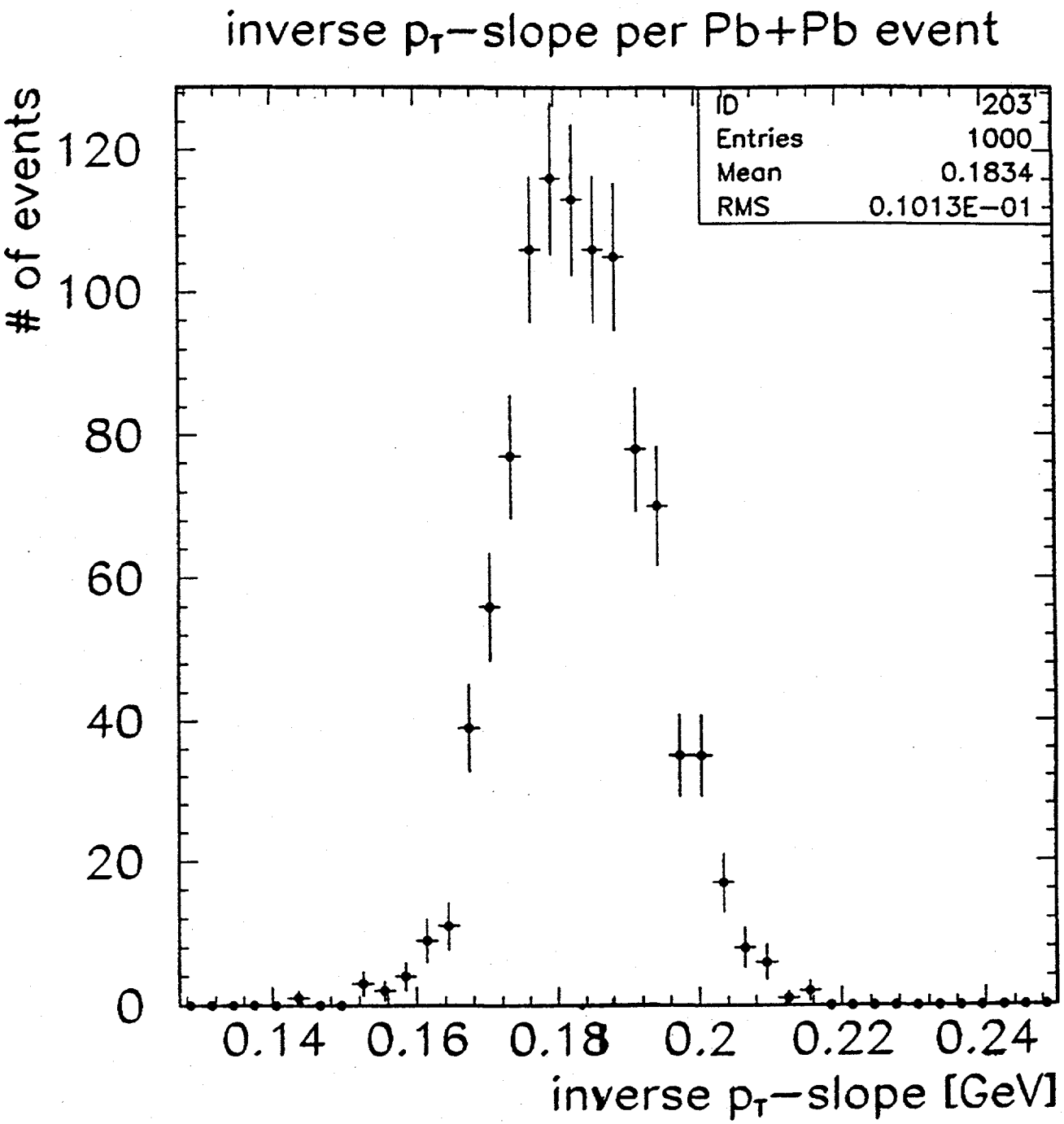
inverse p_T–slope per Pb+Pb event
ID 203
Entries 1000
Mean 0.1834
RMS 0.1013E–01
# of events
0
20
40
60
80
100
120
0.14
0.16
0.18
0.2
0.22
0.24
inverse p_T–slope [GeV]

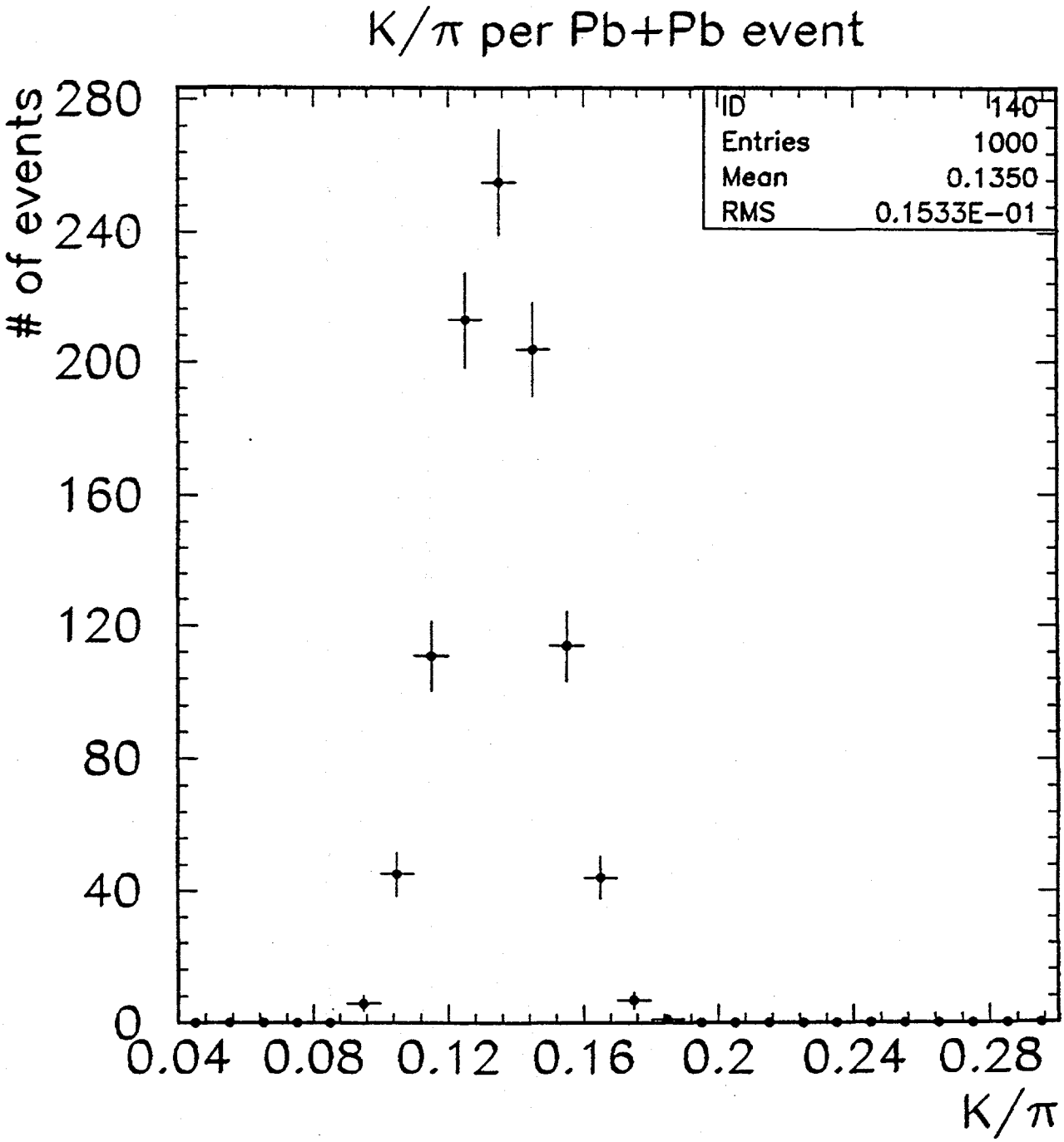
K/π per Pb+Pb event
ID 140
Entries 1000
Mean 0.1350
RMS 0.1533E-01
# of events
280
240
200
160
120
80
40
0
0.04
0.08
0.12
0.16
0.2
0.24
0.28
K/π

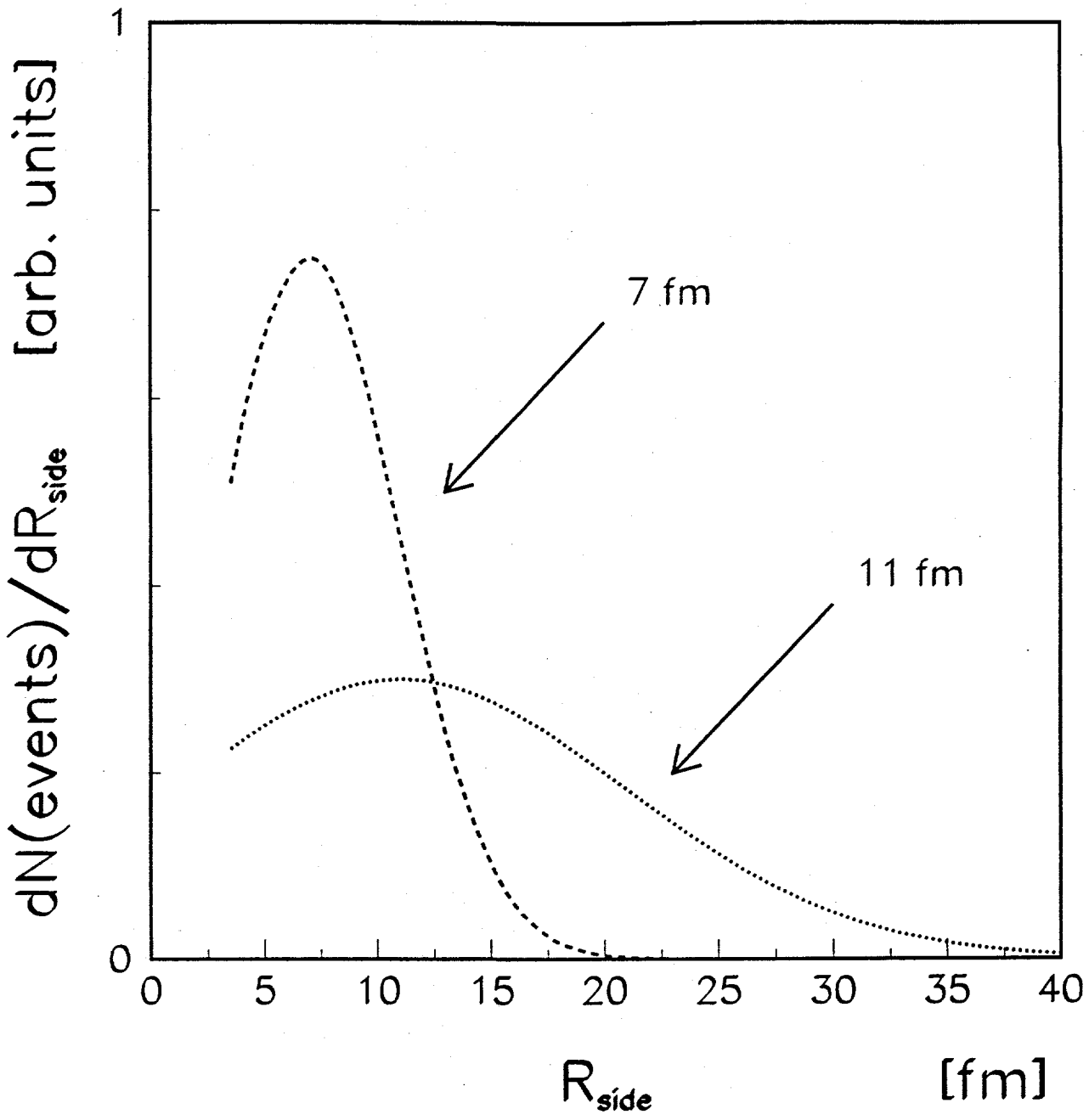
1
0
dN(events)/dR_side [arb. units]
7 fm
11 fm
0
5
10
15
20
25
30
35
40
R_side [fm]

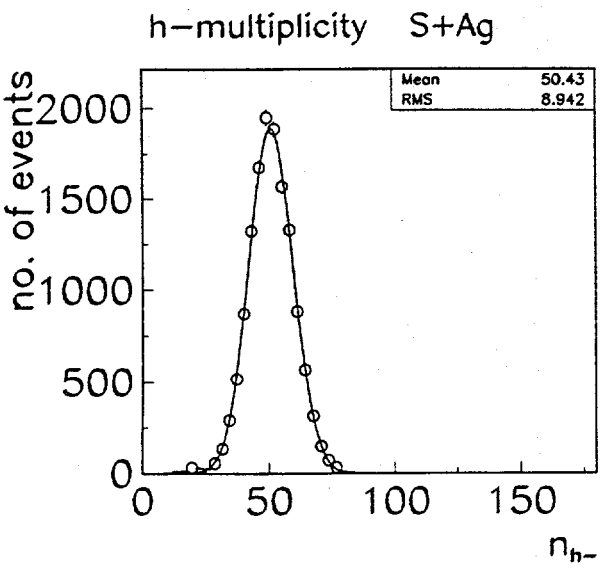
h−multiplicity S+Ag
Mean 50.43
RMS 8.942
no. of events
2000
1500
1000
500
0
0
50
100
150
n_{h-}

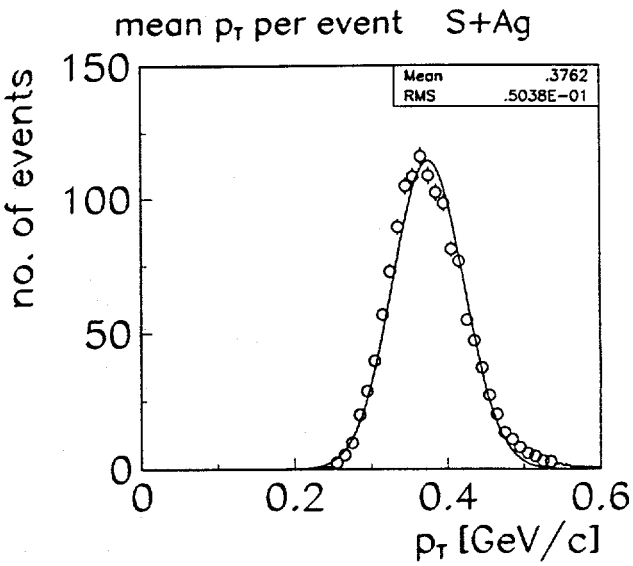
mean p_T per event S+Ag
Mean .3762
RMS .5038E−01
no. of events
150
100
50
0
0
0.2
0.4
0.6
p_T [GeV/c]

Concepts of Event-by-Event Analysis

Herbert Ströbele, Universität Frankfurt

1. Introduction

The particles observed in the final state of nuclear collisions can be divided into two classes: those which are susceptible to strong interactions and those which are not, like leptons and the photon. The bulk properties of the "matter" in the reaction zone may be read-off the kinematical characteristics of the particles observable in the final state. These characteristics are strongly depending on the last interaction these particles have undergone. In a densly populated reaction zone strongly interacting particles will experience many collisions after they have been formed and before they emerge into the asymptotic final state. For the particles which are not sensitive to strong interactions their formation is also their last interaction. Thus photons and leptons probe the period during which they are produced whereas hadrons reflect the so called freeze-out processes, which occur during the late stage in the evolution of the reaction when the population density becomes small and the mean free paths long. The disadvantage of the leptons and photons is their small production cross section; they cannot be used in an analysis of the characteristics of individual collision events, because the number of particles produced per event is too small. The hadrons, on the other hand, stem from the freeze-out period. Information from earlier periods requires multiparticle observables in the most general sense. It is one of the challenges of present day high energy nuclear physics to establish and understand global observables which differentiate between mere hadronic scenarios, i.e. superposition of hadronic interactions, and the formation of a partonic (short duration) steady state which can be considered a new state of matter, the Quark-Gluon Plasma.

2. From Hadron-Hadron to Nucleus-Nucleus Collisions

Today the physics of high energy nuclear collisions is in a situation similar to the one prevailing in hadron physics 20 years ago. Then, the reaction mechanisms of hadronic interactions were studied in exclusive experiments using 4π detectors. The term exclusive means that for some selected collision events all final state particles were identified and their momenta determined. For example the reaction $p+p \rightarrow p+p+\pi^+ +\pi^- +\pi^+ +\pi^- +\pi^0$ had been measured in a bubble chamber and the final state analysed in a multidimensional analysis for $\pi-\pi$ and $p-\pi$ resonances. The resulting information on the reaction mechanism answered the question which resonances contribute with which strength to different sphase space region. For such an analysis the measurement of the complete final state event-by-event was appropriate, because it allowed to use four-momentum conservation

to reconstruct a missing neutral particle and verify at the same time the identity of all particles. Obviously, this was possible only for certain classes of events. It nevertheless allowed to study resonance production together with the associated reaction dynamics. One may translate this scheme to high energy nuclear collisions not by attempting to measure all particles in the final state, but rather by characterizing collision events by global observables. At least one global observable had been already used in hadron-hadron interactions: events were classified acording to their multiplicity leading to the concept of topological cross sections[1]. It allowed to study the differences between violent and soft collisions in terms of, e.g., rapidity distributions[2]. Fig.1 demonstrates the change of the pionic rapidity distributions for various topologies in $p+p$ interactions at 205 GeV/c beam momentum. Another global observable is the mean transverse momentum (e.g. of all charged particles or only negatively charged particles) of each event. More recently events have been characterized by the presence or absence of jets[3].

In general, event-by-event observables suffer from large statistical fluctuations which can be overcome at very high energies or in nuclear collisions. In the most simple picture the latter are a superposition of many hadronic interactions which justifies the use of average quantities. One of the main questions asked in the study of nuclear collisions is the degree of correlation between the final state particles, or, in other words, the existence of collective effects. The study of the average transverse momenta has lead to the discovery of collective effects like the directed[4,5] and radial flow [6] of nuclear matter out of the reaction zone and strong deviations from azimuthal symmetry in pion production[7]. Similarily the study of average quantities event-by-event will provide the tools to detect deviations from trivial statistical behavior which are expected to occur, if the final state hadrons are emitted from a system of deconfined quarks and gluons (the Quark-Gluon Plasma) rather than from a superposition of independent hadron-hadron collisions. The study of the reaction dynamics in p+p interactions by means of (e.g.) resonance production is replaced by the search for equilibration, critical fluctuation, and long range correlation effects induced by strong interactions.

A concrete example of an observable, which is determined "semi-inclusively" in p+p interactions, but could be obtained event-by-event in ultrarelativistic nuclear collisions, is the dispersion of the charge transfer distribution. This quantity was studied in 205 GeV/c p+p interactions as function of rapidity and for different multiplicity classes[8]. It probes the local charge conservation or rather its fluctuations along the rapidity axis. It turns out that violent p+p interactions, i.e. high multiplicity events, exhibit a larger dispersion of the charge transfer than the standard collisions in contrast to a mere statistical scenario in which higher particles numbers go along with smaller dispersions. Such a behavior of the dispersion is to be expected in hadron-hadron collisions, because different final state particle multiplicities mean different reaction dynamics. In the study of nucleus-nucleus collisions we can use the same line of argument to identify changes in the reaction dynamics event-by-event: the dispersion of the charge transfer should decrease with increasing multiplicity (N) as $\sqrt{N}$, if the reaction dynamics remains unchanged; on the other hand any increase of the dispersion with multiplicity would point towards the increasing influence of new dynamical processes.

In the next section we will discuss another specific observable which is meant to define and quantify the degree of (local) energy deposition or stopping.

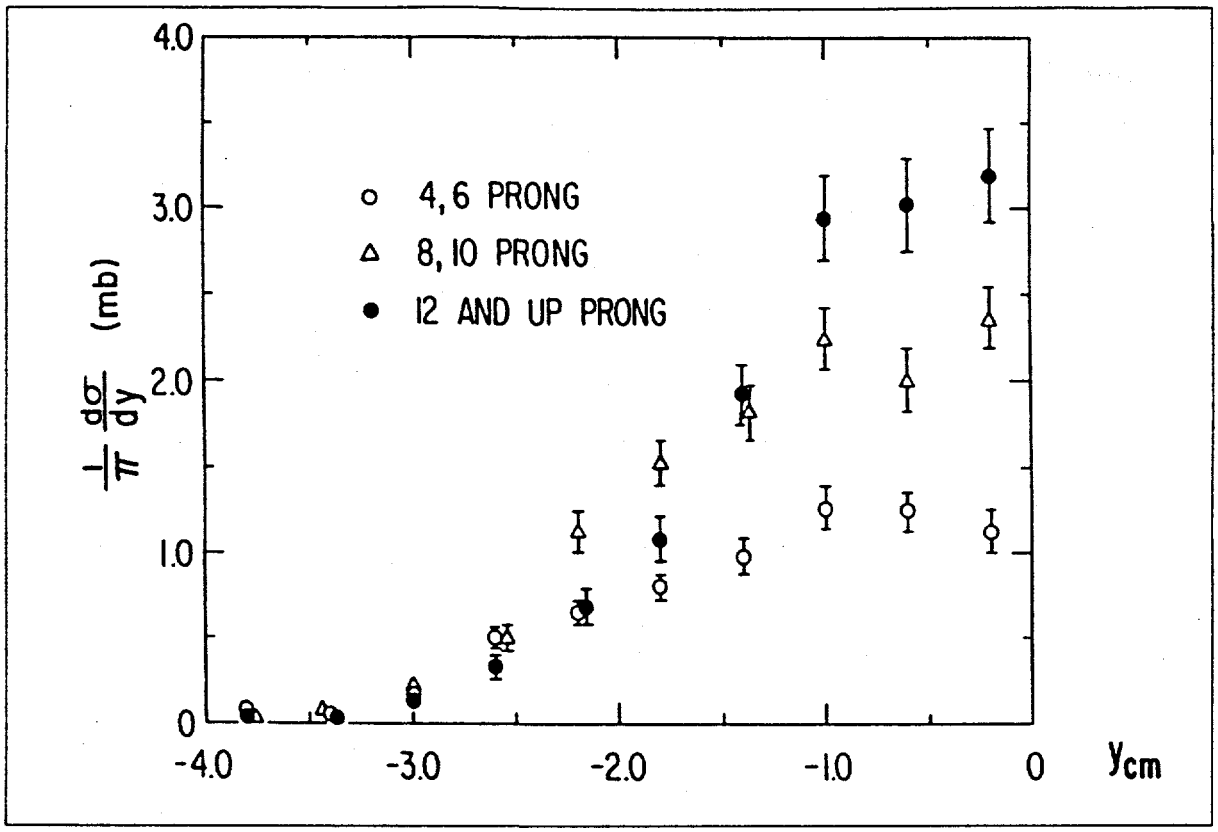

Figure 1. The rapidity distributions for negatively charged hadrons treated as π^-–mesons produced in $p+p$ interactions at 205 GeV/c for various multiplicities

3. The Effective Mass as a Measure of Local Stopping

The standard method of determining the energy density reached in energetic heavy ion collisons uses the rapidity density, the average transverse mass. the overlap cross section of the two nuclei and the 'proper time' τ_0[9]

$$\varepsilon = dn/dy < m_T > /(A \cdot \tau_0)$$

Up to now ε has been computed for event ensembles. because large fluctuations are present, if dn/dy is determined event-by-event. With the advent of real high multiplicity events in in central Pb+Pb collisions at CERN (and even more so later at RHIC and LHC) the energy density may become an event-by-event observable. Then it is even possible to consider the local energy density in small intervals of rapidity and study its fluctuations and short/long range correlations. In the following we will propose to study the energy density and stopping by means of a slightly modified observable which combines the characteristic features of boost invariance with the concept of invariant mass.

The term $dn/dy \cdot < m_T >$ represents the local total energy of the particles considered per rapidity interval. Normally the experimental information is more detailed; e.g. the distribution of the transverse energy or even all (charged) particle momenta may have

been measured event-by event. Under these conditions one can distinguish between kinetic energy and mass. Here mass denotes (in addition to the masses of the final state particles) the total invariant mass of all considered particles. This concept can be illustrated in the following picture:

- Part of the incoming longitudinal energy can be deposited in a fireball at rest in a given rapidity interval. The fireball is equivalent to a fixed mass object which explodes into the final state particles. It might happen that this fireball has a nonzero transverse momentum (which must be balanced in another rapidity interval to conserve overall transverse momentum). In this case the fireball's total energy is given by its mass and kinetic energy. The mass of the fireball is nothing else than the invariant mass computed from all the particles it is made up of, and the kinetic energy is given by the collective momentum of this invariant mass.

It is clear that the concept of invariant mass and kinetic energy of a single fireball cannot describe the situation at high energies (it is obviously not compatible with boost invariance). For example, diffractively produced pions near projectile rapidity are not created in a fireball at midrapidity: their center-of-mass system is a smaller and probably cooler fireball having a large rapidity in the overall c.m. system. Also, Hagedorn has suggested already 30 years ago[10] to interpret the results of high energy hadronic collisions as a string of fireballs extended over all rapidities which are characterized mainly by the transverse momentum spectra of the different particle types. The invariant masses of these fireballs can be considered a measure of local energy deposition or local stopping whereas their kinetic energy could be interpreted as local elasticity which has deflected the bulk matter away from the longitudinal direction. At this point we have to be more specific in the interpretation of 'invariant mass': the standard calculus takes three dimensions into account; it is measure of the energy present in a certain interval of longitudinal kinematical phase space. To connect this with energy density the volume has to be know, especially its longitudinal dimension. Bjorken's approach does not need this third dimension. The transverse energy gives directly the energy density (in space!). With this in mind we propose to modify the concept of invariant mass. Instead of considering all three momentum components in the calculation of the energy and momentum sums ($M^2 = ([\sum(E_i)]^2 - [\sum(px_i)]^2 - [\sum(py_i)]^2 - [\sum(pz_i)]^2)$ we take only the transverse components and define a new quantity 'Effective Mass' (EM) as

$$EM^2 = [\sum(m_T^i)]^2 - [\sum(px_T^i)]^2 - [\sum(py_T^i)]^2$$

where m_T is the transverse mass $m_T^2 = m_0^2 + p_T^2$. The difference between m_T and EM is a measure of the (tranverse) kinetic energy or, in other words, the directed flow.

In an ideal experiment one measures all particles and calculates EM and m_T in rapidity intervals event-by-event. The result would reveal possible fluctuations in energy deposition and directed flow and their correlation in rapidity. It is easy to predict the outcome of such an analysis for the scenario of a simple superposition of independent hadronic collisions: The result from real events will be different from properly mixed events only if bulk phenomena like mean fields, compression, multiparticle correlations come into play. (It is clear that quantum effects due to Bose-Einstein and Fermi-Dirac statistics will always be present, but we are here interested only in the influence of strong interactions.) At this

point we dare to speculate in very general terms about the differences seen in collective effects caused by the partonic properties of hadrons as compared to the outcome of pure hadronic interactions:

- The generic properties of free partons will come into play only if the partons can move freely in extended regions of configuration space. This implies that the color forces which normally confine the partons to the interior of the hadrons are largely absent and regions populated predominantly with only one color may develop. The hadronization of such regions should lead to an enhancement of of $q\overline{q}$-pairs (mesons) as compared to qqq ($\overline{qqq}$) triplets, because in a single color environment it is easier to make color neutral objects by combining q and $\overline{q}$ than qqq with each q having another color.

- Liberating the partonic degrees of freedom of hadrons will facilitate the approach to chemical equilibrium of the different parton abundances. Particle ratios which are far from chemical equilibrium values will be strongly affected. The corresponding experimental observables is the strange to nonstrange particle ratio. It is off chemical equilibrium in hadron-hadron collisions (at CERN SPS energies) but expected to be boosted towards equilibrium values in partonic systems.

In real experiments not all particles are measured or identified. This causes unwanted statistical fluctuations. Another problem is the the limited validity of boost invariance. At least at SPS energies and below its failure becomes evident in the variation of the particle ratios as function of rapidity. With these two caveats we conclude this contribution by showing experimental results from Sulphur induced nuclear collisions and from microscopic model calculations in terms of the Effective Mass observable. These figures are meant only as an illustration of the problems and questions connected with this observable. Significant physics results can only be expected from the forthcoming Pb+Pb data taken at the CERN SPS or even later from experiments at RHIC.

We have chosen the rapidity interval $4.5 < y < 4.9$ to calculate EM for each event. The experimental data are taken from 3100 central S+Au events recorded in a special configuration of the NA35 experiment[11]. This acceptance and experimental configuration was chosen, because it combines high rapidity densities with good azimuthal symmetry in detection efficiency. The distribution of EM is compared in Fig. 2 with the multiplicity distribution determined in the same rapidity interval[12]. All charged particles (assuming the pion mass) enter into the analysis. The Effective Mass (per event and rapidity interval) is divided by the number of particles contributing to remove the influence of multiplicity fluctuations. This procedure removes to a large extend the effects we want to study but, on the other hand, stresses the kinematical aspects of the the EM observable. It should be noted that in this representation the EM observable has a trivial offset of 140 MeV due to the pion mass contained in the definition of EM. In Fig. 3 we show the result from FRITIOF calculations[13] in the same rapidity range from central S+S collisions. As expected no interesting features emerge from the comparison.

In summary, systematic studies of distributions of the Effective Mass as presented in Fig. 2a as function of rapidity are proposed. This observable should be more sensitive to nonstatistical fluctuations than the rapidity density distributions of particles. Unusual

low (high) values of EM would indicate small (large) local energy deposition into charged particles. Furthermore systematic differences between EM and m_T can be used to measure sidewards flow. As for all multiparticle observables, a comparison of distributions obtained from real events and from 'mixed' events will reveal the presence of correlations. The proposed analysis requires high particle densities as expected in nuclear collisions at RHIC and LHC.

This work was supported by the German BMFB. H. Rothard kindly provided Figures 2 and 3.

REFERENCES

1. J. Allday et al., NA5 Collaboration, Z. Phys. C40(1988)29
2. Y. Cho et al., Phys. Rev. Lett. 31(1973)413
3. F. Ceradini, UA1 Collaboration, CERN-EP/85-196
4. H.A. Gustafsson et al., Phys. Rev. Lett. 52(1984)1590
5. J. Barrette et al., Phys. Rev Lett. 73(1994)2532
6. S.C. Jeong et al., FOPI Collaboration, Phys. Rev. Lett.72 (1994)3468
7. D. Brill et al., Phys. Rev. Lett. 71(1993)835
8. T. Kafka et al., Phys. Rev D16(1977)1261
9. J.D. Bjorken Phys. Rev. D27(1983)140; replace $< E >$ by $< m_T >$cos(y) and t by $\tau_0$cosh(y) in (4) to obtain the quoted formula
10. R. Hagedorn, Suppl. Nuovo Cim. 3(1965)147
11. T. Alber et al., NA35 Collaboration, Z. Phys. C64(1994)195
12. H. Rothard, Thesis Universität, Frankfurt 1995, unpublished
13. B. Andersson et al., Nucl. Phys. B281(1987)289(version1.6)

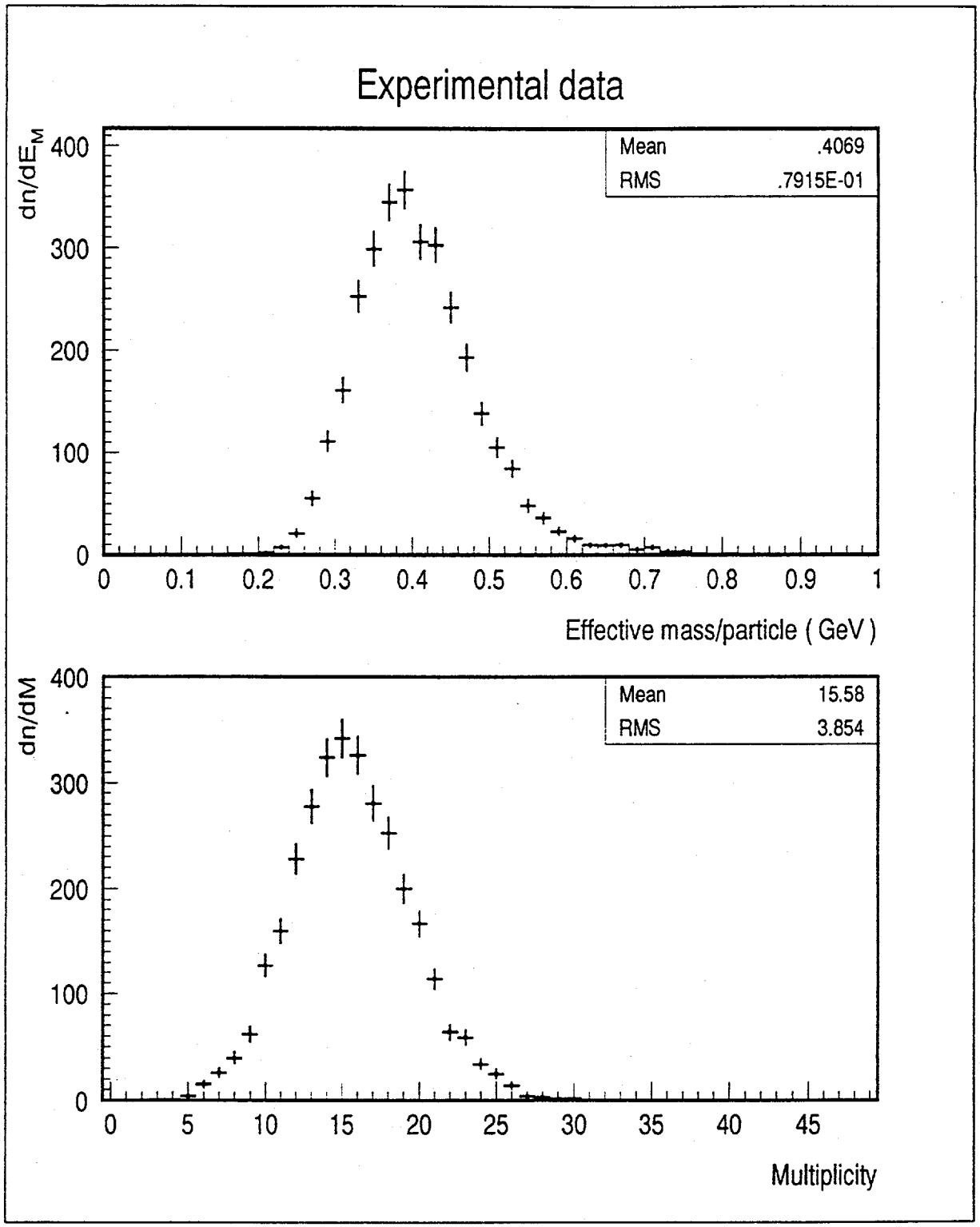

Figure 2. Distribution of the Effective Mass (EM) per particle (a) and of the multiplicity density(b) in the rapidity interval $4.5 < y < 4.9$ from 3100 central ^{32}S+Au collisions as measured by the NA35 collaboration.

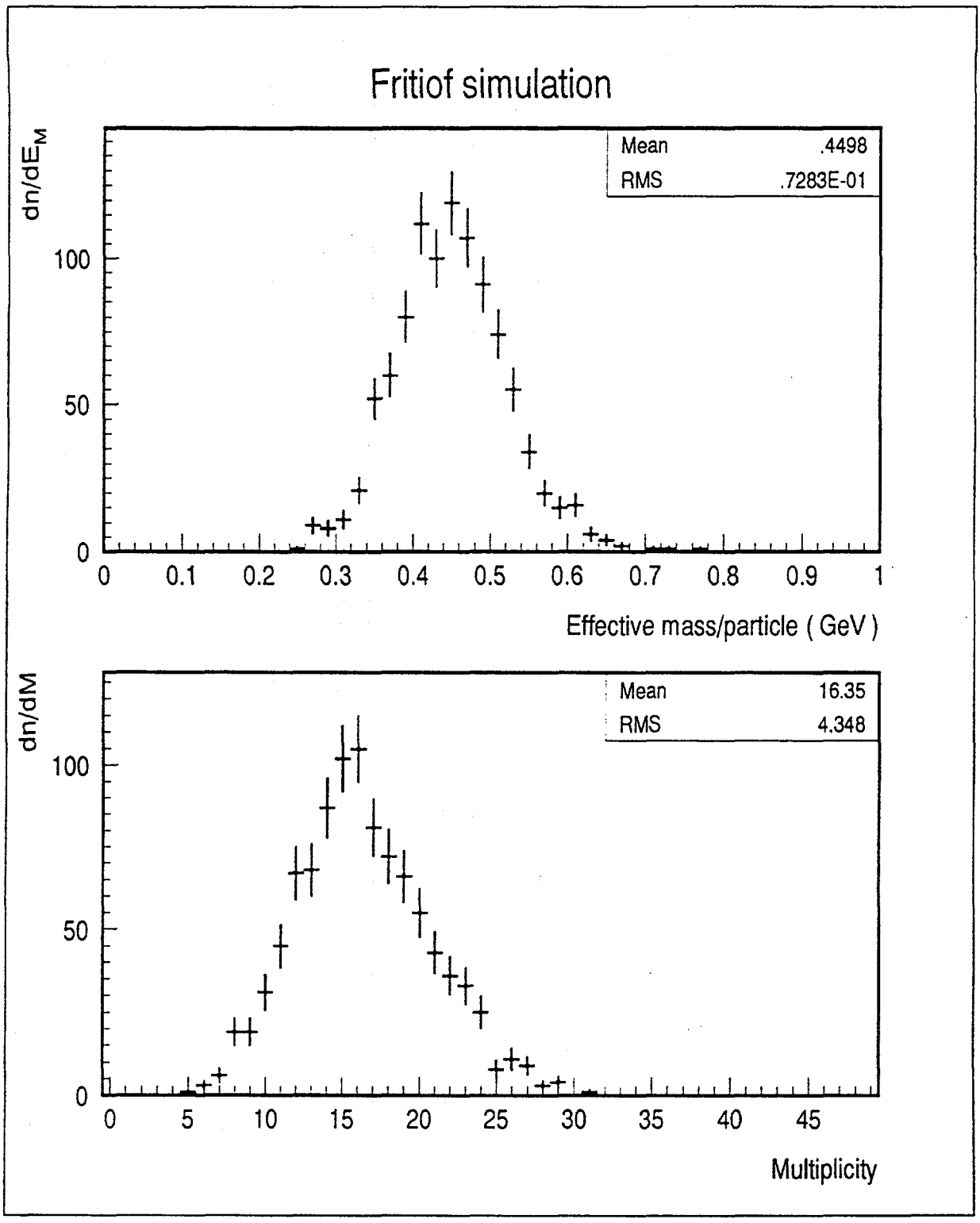

Figure 3. Same as Figure 2 but from 1000 central $^{32}S+^{32}S$ collisions obtained from the FRITIOF model.

Measuring two-particle Bose-Einstein correlations with PHOBOS@RHIC

Gunther Roland for the PHOBOS collaboration

Argonne National Laboratory
R. Betts

Brookhaven National Laboratory
D. Barton, A. Carroll, Y.Y. Chu, S. Gushue, H.W. Kraner, L.P. Remsberg

Institute of Nuclear Physics, Krakow
A. Budzanowski, T. Coghen, R. Holynski, J. Kotula, H. Palarczyk, P. Malecki, A. Olszewski, K. Pakoński, M. Stodulski, A. Trzupek, H. Wilczyński, B. Wosiek, K. Woźniak, K. Zalewski

Jagiellonian University, Krakow
A. Bialas, W. Czyż

Massachusetts Institute of Technology
M.D. Baker, W. Busza, P. Kulinich, M. Pleško, G. Roland, L. Rosenberg, J.J. Ryan, S.G. Steadman, P. Steinberg, G.S.F. Stephans, R. Verdier, B. Wadsworth, D. Woodruff, B. Wysłouch

Oak Ridge National Laboratory
C. Britton

University of Illinois at Chicago
C. Conner, C. Halliwell, D. McLeod

University of Maryland
A. Mignerey, J. Shea

Yale University
S. Manly

We present results of a simulation of the measurement of two-particle Bose-Einstein correlations in central Au-Au collisions with the PHOBOS detector at RHIC. This measurement is expected to yield information on the relevant time and distance scales in these collisions. As the space-time scale is directly connected with the equation of state governing the evolution of the particle source, this information will be essential in understanding the physics of nucleus-nucleus collisions at RHIC energies. We demonstrate that the PHOBOS detector has sufficient resolution and acceptance to distinguish a variety of physics scenarios.

1. Introduction

The measurement of two-particle Bose-Einstein correlations (called HBT-measurement in the following) is the most important tool for obtaining information on the space-time evolution of the extended hadron source created in ultrarelativistic heavy ion collisions [1–4]. The experimental observable in this study is the two-particle correlation function for pairs of identical bosons. It is defined as the ratio of the two-particle inclusive distribution for particles with momenta k_1 and k_2, divided by the product of the single particle inclusive distributions:

$$C_2(k_1, k_2) = \frac{P_2(k_1, k_2)}{P_1(k_1) \cdot P_1(k_2)}. \tag{1}$$

For identical bosons the correlation function is enhanced at low relative momenta and the width of the enhancement region in momentum space is inversely proportional to a typical length scale (called the 'HBT radius') of the particle source. For a static thermal source this length scale (or radius) is given by the geometrical size of the source. In general however the length scale will be influenced by so-called dynamical correlations, which lead to a correlation between position and momentum of the particles at freeze-out. The most important type of dynamical correlations are those caused by a rapid expansion of the particle source. In this case a dependence of the effective radii (corresponding to different components of the momentum difference $\vec{Q}$) on the longitudinal and transverse momentum of the particles is introduced. The dynamical correlations therefore link the observables studied in the analysis of two-particle correlations to the dynamics of the expansion of the particle source. The expansion in turn is governed by the equation of state of the strongly interacting matter produced in the collision. A definition of the different HBT parameters and a detailed description of the connection between the space-time parameters of the particle emission and the HBT parameters can be found in [5]. One of the main aims of the PHOBOS experiment is to study the correlation function as a function of all relevant degrees of freedom in momentum space for pions and kaons.

2. The PHOBOS detector

The PHOBOS detector consists of two main components [6]: One is a 4-π multiplicity array that measures the angular distribution of charged particles and (to some extent) photons. The other part is a two arm magnetic spectrometer near mid-rapidity. The spectrometer provides momentum analysis and particle identification in the $1/\beta^2$ region for about 1 % of all charged particles. Though not part of the PHOBOS baseline design, we expect to use a Time-of-flight wall to extend the particle identification capabilities to higher momenta.

The most important aspect of the PHOBOS design is that all detector elements are produced in a common technology, namely as Silicon Pad detectors and are read out by one type of electronics. We will use a total of around 80.000 detector channels. The simplicity of the PHOBOS design should enable us to quickly debug and understand our detector at RHIC startup.

One consequence of the technology choice made for PHOBOS is that the size and relative position of the basic detector pixel are determined solely by the production of

the Si wafers and are not subject to any further calibration. This a substantial difference compared to other charged particle detectors where the charge deposited by an ionizing particle is drifting to a readout anode over some distance. In the context of this paper the fact that the PHOBOS position resolution is essentially calibration-free ensures that the estimates we obtain from the detector simulation will actually apply to the real detector. Another important factor for the PHOBOS HBT studies is the very high rate capability of our Silicon Pad detectors and the readout chain, which will allow us to record all central events occuring within ± 10 cm of the nominal interaction point, without any bias.

3. Pattern Recognition

A meaningful assessment of the HBT capabilities of a detector in the high particle density environment of high energy nucleus-nucleus collisions can only be obtained by studying the performance of a *full pattern recognition chain* on simulated detector data. Only in this way one can obtain the necessary information about complex questions like the two track resolution or the distribution of ghost tracks in relative momentum space. We have developed a complete pattern recognition chain that starts from the raw pixeled detector hits in high multiplicity events and performs the necessary pattern recognition and momentum determination steps and also does particle identification by energy loss measurements in the $1/\beta^2$ region.

The particular pattern recognition algorithm that we have employed for this study consists of the following steps:
First track candidates are independently formed in two regions of the spectrometer. For hits in the first 6 planes, which lie outside the magnetic field, a Hough transformation of the hit coordinates into a two-dimensional space given by the polar and azimuthal angles Θ and ϕ is performed. For the planes inside the magnetic field a similar transformation is done for *pairs* of hits in adjacent planes, this time into Θ and $1/p$, where p is the total momentum of the particles. In this way hits on tracks originating at the vertex are transformed into clusters of hits in (Θ, ϕ) and $(\Theta, 1/p)$ space, respectively. Based on these hit–clusters straight line and curved track candidates are formed. One should note that this method does not imply any approximation regarding the shape or uniformity of the magnetic field and can be based on look-up tables, thus making it very cpu time-efficient.

In the next step full candidate tracks are formed by matching straight line and curved track candidates based on the polar angle Θ and on the limited ϕ information that is available from the coarse vertical segmentation of the planes inside the magnetic field. For the low-momentum tracks (e.g. pions with $p < 250$ MeV/c) it has turned out to be necessary to also include the dE/dx particle ID information at this step.

The track candidates are then subjected to a χ^2-fit and those with a χ^2-probability of less than 3 % are rejected. To achieve the PHOBOS goal of measuring tracks with very low momenta it was essential to use the full covariance matrix in this fit, to account for the correlation in the fit residuals due to multiple scattering. As mentioned before, the fact that the PHOBOS position resolution is calibration-free assures that we will also have a sufficient understanding of the fit residuals for the real detector to apply this method.

In the final step successful track candidates are checked for shared hits and in case of conflicting candidates the one with the better χ^2 is retained. In this step another check

is done for potential close ghost-pairs, i.e. pairs that are close in momentum space and were created out of the same input track plus a number of alien hits.

In the following a 'Ghost track' is defined as an output track that shares less than 8 out of a possible 11 hits with an input track or has a momentum that is more than 5% different from that of the corresponding input track. Only one output track is allowed to be matched to any given input track. This criterion ensures that all the 'true' found tracks have both momentum and PID-characteristics close to the corresponding input track.

4. Performance

In this section we will discuss the performance of the PHOBOS pattern recognition for high multiplicity events with respect to the variables that are relevant for two-particle correlation measurements. In figs. 1 and 2 the p_t-y distributions for negatively charged pions and kaons originating from collsions at the the nominal vertex position at $z = 0$ cm are shown. For the magnetic field configuration used here negative particles are bent towards the beampipe.

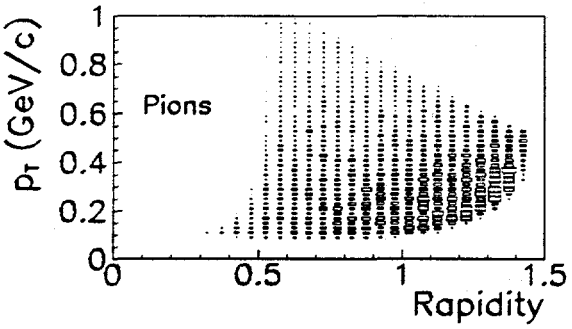

Figure 1. p_T-y distributions for reconstructed negative pions produced in collisions at $z = 0$ cm.

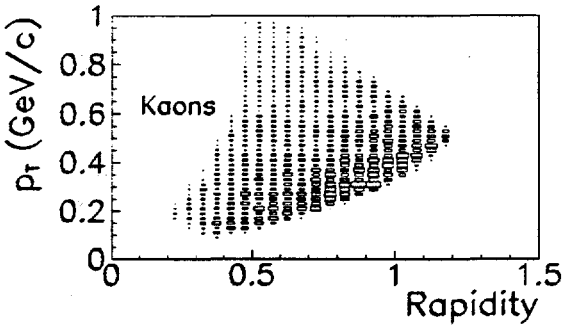

Figure 2. p_T-y distributions for reconstructed negative kaons produced in collisions at $z = 0$ cm.

The low momentum cutoff is given by the geometrical acceptance of the detector for these tracks (the particles were required to traverse all 11 planes of one detector arm) and the high momentum cutoff is determined by the limit of the TOF particle ID of approximately 1150 MeV/c. The width of the rapidity distribution for a *single* event is around one unit of rapidity. This fulfills one important requirement for HBT measurements, as a minimal acceptance in rapidity is needed to perform a reliable fit of the Q_{long} component of the correlation function, especially in a low p_T bin. Also, the expected correlation length for a locally thermalized particle source along the longitudinal axis is on the order of 0.5 rapidity units.

To investigate the correlation function in different rapidity regions and to extend the low-p_T coverage, PHOBOS will accept collisions over an intervall of vertex positions ranging from -10 cm to 10 cm around the nominal interaction point. The corresponding p_T-y

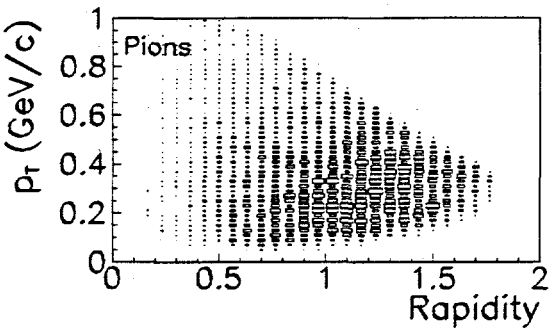

Figure 3. p_T-y distributions for reconstructed pions produced in collisions at $-10 < z < 10$ cm.

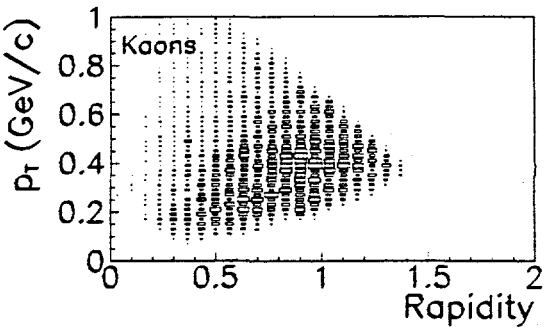

Figure 4. p_T-y distributions for reconstructed kaons produced in collisions at $-10 < z < 10$ cm.

distributions for pions and kaons of both charges are shown in figs. 3 and 4. Fig. 3 also demonstrates that the PHOBOS acceptance for pions indeed reaches down to very low transverse momenta of about 40 MeV/c.

The reconstruction efficiency of the PHOBOS detector was determined for tracks in central events, with an average primary charged particle multiplicity of 6000. To get a meaningful estimate of the overall efficiciency and the production of false ('Ghost') tracks, the effects of multiple coulomb scattering and the hits of non-vertex tracks from weak decays of primary particles and secondary interactions were taken into account.

The resulting momentum and Θ distributions of found tracks and ghost tracks. together with the distributions of input tracks are shown in fig. 5. The lower plot in fig. 5 shows the ratios of the momentum distributions for found tracks over input tracks and ghost tracks over input tracks. For the present algorithm an average reconstruction efficiency of 76% was obtained, with a very low rate of ghost tracks of only 3–4%. We expect that with some fine tuning of the reconstruction algorithm an efficiency of 85-90% can be achieved with the same rate of ghost tracks. For the present study however the efficiency shown here was deemed sufficient, as the emphasis for two-particle correlation studies has to be on the two-particle acceptance as a function of relative momentum and especially on the suppression of artificial close pairs, which would distort the correlation function.

One of the most important questions for studying two-particle correlations is the distribution of ghost tracks in momentum space relative to other tracks. One has to keep in mind that for the large particle sources expected at RHIC HBT essentially becomes a very small effect. While a correction for two-particle efficiency is relatively straightforward it is in general not possible to reliably correct for artificial close pairs, once they have been created by the pattern recognition. Therefore fig. 6 provides a very important piece of information, showing that there is no pile-up of ghost pairs at low values of the invariant momentum difference Q_{inv}.

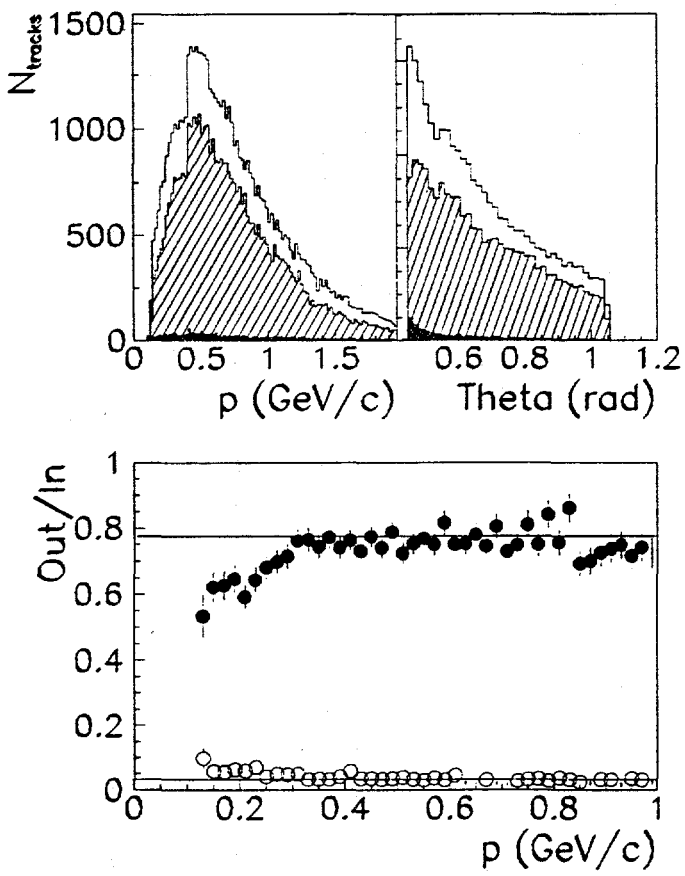

Figure 5. The upper plots show the momentum distribution (left) and Θ-distribution (right) for input tracks (solid line), correctly found tracks (dashed histogram) and ghost tracks (dark histogram). The lower plot shows the ratio of correctly found tracks to input tracks (full symbols) and ghost tracks to input tracks (open symbols).

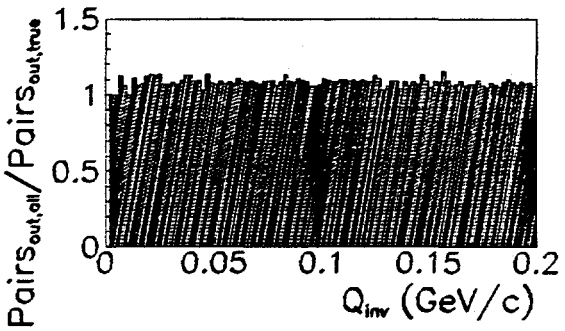

Figure 6. This plot shows the ratio of two Q_{inv} distributions. The numerator was formed using all output tracks of the pattern recognition, including ghost tracks. The denominator only includes 'true' output tracks. There is no excess of ghost pairs at low Q_{inv}.

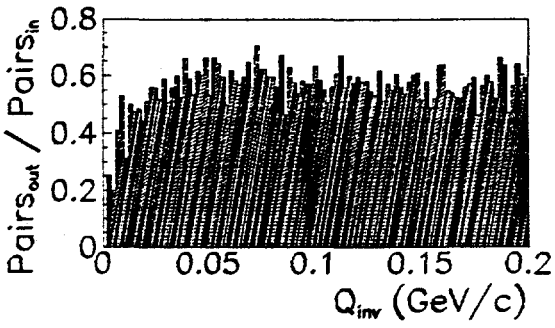

Figure 7. This plot shows the ratio of two Q_{inv} distributions. The numerator was formed using the output tracks of the pattern recognition, the denominator was formed using the input tracks.

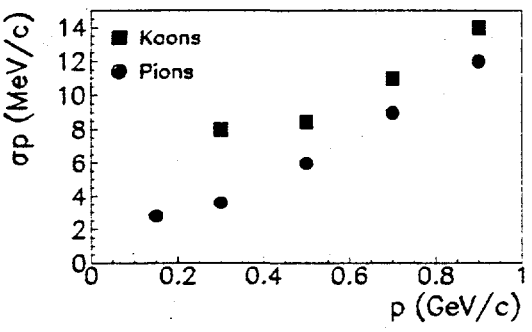

Figure 8. Average momentum error as a function of total momentum for pions (circles) and kaons (squares).

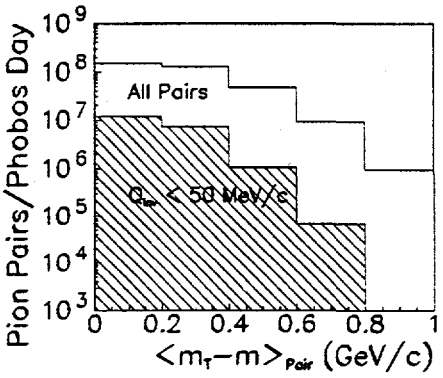

Figure 9. Number of pion pairs per day of PHOBOS running. The solid line shows the number of all pairs per m_T-bin, the dashed histogram shows the number of pairs with $Q_{inv} < 50$ MeV/c per m_T-bin.

In fig. 7 we show the two-track resolution obtained for the present pattern recognition chain. The two-track efficiency is constant (and equal to the square of the single particle efficiency) up to about 25 MeV/c and then gradually drops to about 50% of the plateau-value. For very large sources we will therefore need to apply a two-particle acceptance correction, which is a standard procedure in the study of two-particle correlations. Again the relative simplicity of the PHOBOS detector elements will ensure that we will be able to perform this correction with little uncertainty.

The momentum resolution that was achieved for tracks in high-multiplicity events is shown in fig. 8 as a function of momentum. For low momentum tracks the resolution is dominated by the effects of multiple scattering, which also guided our choice of the detector granularity.

In the final performance plot (fig. 9) we show the number of pion pairs measured in one day of PHOBOS running at the RHIC design luminosity for different bins of transverse momentum. Clearly the errors on the HBT parameters as measured by PHOBOS will be dominated by systematic errors arising from e.g. the uncertainties of the Coulomb correction or the fitting procedure, rather than the statistical errors.

5. Physics simulations

Here we will demonstrate the PHOBOS physics capabilities based on the performance figures that were shown in the previous section. We have studied the response of the PHOBOS detector to three very different physics scenarios that cover some part of the predictions of what is going to happen at RHIC. We did not try to include effects of resonance decays in the present study.

In performing the physics simulation we had to use a somewhat simplified approach.

The ideal solution would consist of using an event generator to generate a number of events that is comparable to that expected for one day of PHOBOS running at RHIC and symmetrize the momenta of all identical particles according to the distribution of emission points. This approach however is unfeasible as we don't yet have access to the computing power that will be needed for the simulation and analysis of such a number of events. Also symmetrising all the particle momenta in a high multiplicity event is a non-trivial problem.

We have therefore developed a HBT-simulation chain that is based on a parametrization of the PHOBOS two-particle acceptance and momentum resolution as obtained for high multiplicity events. Particles according to different space-time evolution scenarios were generated and combined to particle pairs. Using the code developed by S. Pratt (based on the Wigner-function formalism) [10], a weight for each pair was calculated according to the symmetrization requirements and the Coulomb repulsion between the two particles. The particle pairs are then passed through a simulation of the PHOBOS pair response. The correlation function is formed using weighted and non-weigthed particle pairs and applying the standard Gamov penetration factor to account for the Coulomb repulsion. To extract values for the HBT radii, fits to the correlation functions were performed with the following functional form:

$$C_2 = 1 + \lambda \exp(-Q_{side}^2 R_{side}^2 - Q_{out}^2 R_{out}^2 - Q_{long}^2 R_{long}^2), \quad (2)$$

without a factor $\frac{1}{2}$ in the exponent. The statistics used in all three scenarios correspond to one day of running for the pions and one week of running for the kaons.

The first physics scenario is based on a straightforward extrapolation of HBT results that were obtained for collisions of heavy ions at SPS-energies. The HBT results at the SPS can be summarized as follows [5,7–9]:

- The transverse radii R_{side} scale as $dN/dy^{\frac{1}{3}}$. This leads to radii of the order of 10 fm for the expected multiplicity densities at RHIC.
- The longitudinal radius R_{long} shows the rapidity and p_T dependence expected for a scaling longitudinal expansion. The duration of the expansion is on the order of 4-5 fm/c. It follows a similar dN/dy-dependence as the transverse radius.
- There is a dependence of the transverse radius on p_T that seems to be somewhat weaker than for the longitudinal radius and can be explained by a combination of a weak transverse expansion and the p_T dependence of resonance contributions.
- For kaons significantly smaller radii have been observed than for pions.

The result of taking this 'standard' scenario and extrapolating to RHIC energies is shown in fig. 10. The points, showing the result from fitting the correlation function that was obtained for the simulated PHOBOS response, follow closely the results for an ideal detector, which are shown as solid lines. An example of a pion correlation function is shown in fig. 11. For this scenario PHOBOS allows a detailed quantitative analysis of the correlation function in all relevant degrees of freedom for both pions and kaons.

A second scenario that has been predicted for RHIC is that of a particle source rapidly expanding in longitudinal *and* transverse direction. This case has been investigated in a

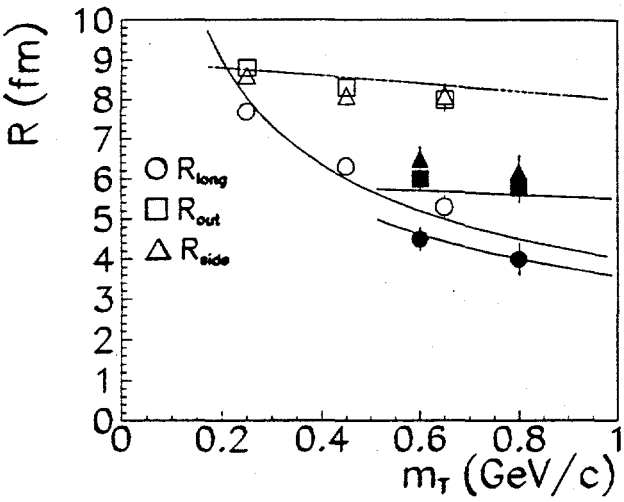

Figure 10. HBT radii for the 'standard' scenario. Points give the fitted radii including PHOBOS detector response; solid lines are radii for an 'ideal' detector. Open symbols are pions, full symbols are kaons.

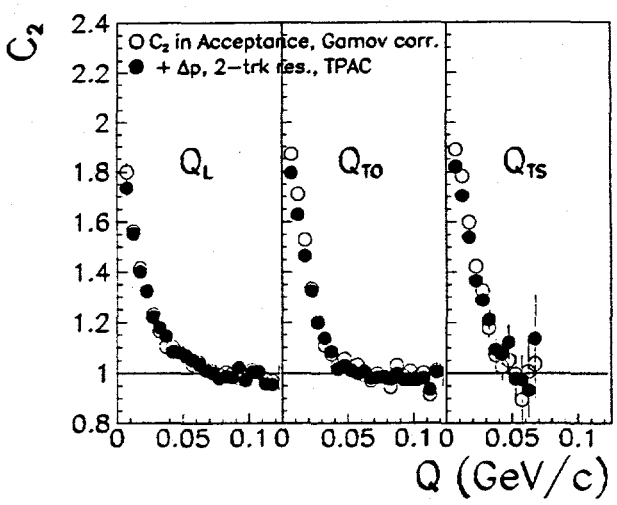

Figure 11. Projected pion correlation function for an ideal detector (open symbols) and the simulated PHOBOS response (full symbols).

recent paper by Csörgö and Lörstad [11]. They conclude that in this situation all three radii will show a common $1/\sqrt{m_T}$ dependence. The observed radii will not reflect the size of the particle source at freezeout (which may be very large) but will measure a common thermal correlation length. A possible signature of such a scenario is shown in fig. 12, where we assumed that kaon freezeout will occur earlier than pion freezeout.

This has to be compared to a third scenario, in which we assume a strong first phase transition with a large latent heat. In this case one expects a long lifetime of the particle source and a weak transverse expansion due to the 'softness' of the equation of state near the phase transition point. Only in the case of a very long source lifetime could one expect to obtain very large measured radii on the order of 20 fm. The PHOBOS response for this scenario is shown in fig. 13. Here we see that for the low transverse momentum bin, PHOBOS can accurately measure even very large radii. as we look at tracks of very low total momentum with a very small absolute momentum error of only a few MeV/c.

For the kaons the observed radii somewhat overshoot those for an ideal detector. One reason for this is that the Coulomb correction was performed using the standard Gamov factor, which leads to an overcorrection due to the finite size of the particle source. To reduce systematical errors caused by the Coulomb correction when real data will become available more theoretical work is required.

6. Conclusions

The measurement of two-particle Bose-Einstein correlations presents one of the few direct ways of probing the space-time evolution in ultra-relativistic heavy ion collisions. Using a detailed simulation of our detector and a full pattern recognition chain we have

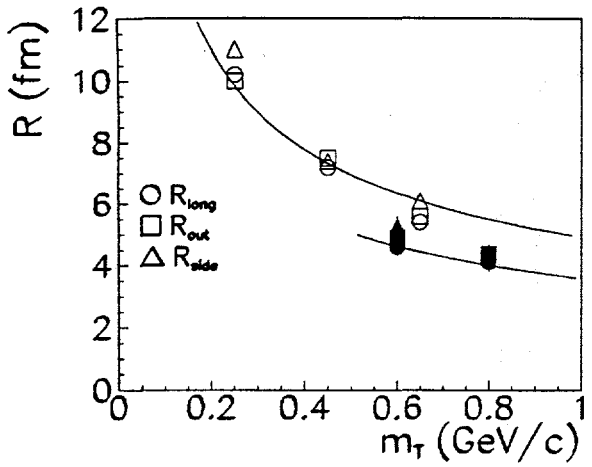

Figure 12. HBT radii for the 'rapid expansion' scenario. Points give the fitted radii including PHOBOS detector response; solid lines are radii for an 'ideal' detector. Open symbols are pions, full symbols are kaons.

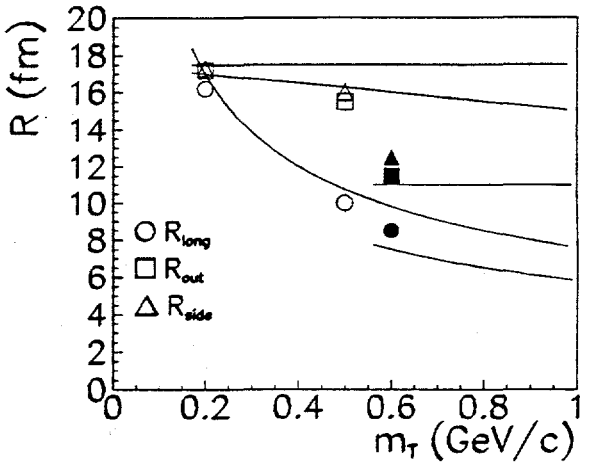

Figure 13. HBT radii for the 'long lifetime' scenario. Points give the fitted radii including PHOBOS detector response; solid lines are radii for an 'ideal' detector. Open symbols are pions, full symbols are kaons.

demonstrated that PHOBOS has the necessary resolution and acceptance to distinguish a variety of physics scenarios. The high rate capability ensures that we can perform a detailed investigation even for two-kaon correlations. The fact that PHOBOS is able to measure particles with small total momentum, allows for the observation of very large sources sizes. Finally the simplicity of the PHOBOS design will help us in minimizing the systematical uncertainties of the HBT measurement.

REFERENCES

1. S. Pratt, Phys. Rev. **D33** (1986) 1314
2. G. Bertsch, M. Gong, M. Tohyama, Phys. Rev. **D37** (1988) 1896
3. K. Kolehmainen, M. Gyulassy, Phys. Lett. **180** (1986) 203
4. A. N. Mahklin, Yu. M. Sinyukhov, Z. Phys. Lett. **C39** (1988) 69
   Yu. M. Sinyukhov, Nucl. Phys. **A498** (1989) 151
5. D. Ferenc et al. in 'Quark Matter '91', Nucl. Phys. **A544** (1992) 531
6. See also the contribution of M. Baker to these proceedings
7. G. Roland et al. Nucl. Phys. **A566** (1994) 527c
8. T. J. Humanic et al. Nucl. Phys. **A566** (1994) 115c
9. For a recent review see the contributions by Th. Alber et al. (NA35) and B. Jacak et al. (NA44) to the Quark Matter '95 conference, Monterey
10. S. Pratt, Th. Csörgö, J. Zymanyi, Phys. Rev. **C42** (1990) 2646
11. See Th. Csörgös contribution to Quark Matter '95 conference, Monterey.

HBT Measurements in PHENIX, STAR and ALICE

W.A. Zajc[a*]

[a]Columbia University, Nevis Labs,
P.O. Box 137, Irvington, NY 10533

The experimental prospects for performing Hanbury-Brown–Twiss (HBT) measurements in the large detectors planned for heavy ion physics at RHIC and LHC are reviewed.

1. INTRODUCTION

The primary motivation for colliding heavy ions at ultra-relativistic energies is the search for the QCD phase transition. The fundamental parameter for characterizing that phase transition is energy density[1]. Experimentally, the energy density will be determined by separately measuring some "total" energy, and dividing by some "volume". The measurement of "total" energy in some region is achievable by a straightforward extension of the methods familiar from particle physics, e.g., momentum measurement on a track-by-track basis, or calorimetric measurement of the transverse energy. The determination of the corresponding space-time volume is considerably more difficult. There is of course a long tradition in particle physics, dating back to Rutherford, of using *external* probes to measure nuclear and sub-nuclear sizes. However, in these cases the object being measured has an exceedingly long lifetime relative to nuclear phenomena. However, in the case of a nuclear collision, the region of interest exists for only $\sim 10^{-23}$s, so that only *internal* probes are available. Fortunately, *correlations* between two (usually but not necessarily) identical particles can be used to measure the size of the space-time region of emission. This technique, often loosely called Hanbury-Brown–Twiss (HBT) interferometry after the astronomers who pioneered its application to stellar measurements[2], has been extensively reviewed elsewhere[3–5].

In this article I will briefly explore the experimental prospects for HBT in the large detectors envisaged for RHIC and LHC[6]. No attempt will be made to perform a technical evaluation of these large detectors. Instead, I will take as a given their stated acceptances, resolution and particle identification capabilities, and apply them to the various HBT topics of interest: single-event interferometry, multi-pion HBT, $2K^o_s$ and 2 $\bar{n}$ correlations, and non-identical particle measurements.

*Work supported by the Department of Energy grant FG02-86ER40281.

TABLE 1	PHENIX	STAR	ALICE
Acceptance	$\|\eta\| < 0.35$ $\Delta\Phi = 2 \times 90^0$	$\|\eta\| < 2.0$ $\Delta\Phi = 2\pi$	$\|\eta\| < 0.9$ $\Delta\Phi = 2\pi$
Tracking technology	Drift chambers Pad chambers TEC	TPC	TPC
Magnetic Field	Axial	Solenoid	Solenoid
Momentum resolution ($\frac{\Delta p_T}{p_T}$, p_T in GeV)	$0.5\% \oplus 0.4\% \cdot p_T$	$1.3\% \oplus 1.0\% \cdot p_T$	$1.2\% \oplus 0.3\% \cdot p_T$
Two-track resolution	1.5mm	2.0cm at R=2m	0.8-1.5cm
Particle ID			
π/K	< 2.5 GeV/c	< 0.7 GeV/c	< 2.0 GeV/c
K/p	< 4.0 GeV/c	< 1.0 GeV/c	< 3.0 GeV/c
	($\Delta\Phi < 30^0$)		
DAQ rate (central Au-Au)	65 Hz	1 Hz	50 Hz (1.5 GB/s (!))

2. IMPORTANT DETECTOR PARAMETERS

The assumed parameters for the three detectors are given in Table 1.

If I take these parameters as a given, then there is no doubt that each detector should easily accomplish its primary HBT goals, which might be characterized as "measurement of two-particle correlations with identified pions and kaons for radii ranging from 1 to 10 fermis". Additionally, confining for the moment our view to this very limited set of objectives, each detector will achieve statistical precision in these measurements one to two orders-of-magnitude beyond current experiments.

The preceding paragraph was prefaced by a very important caveat. To what extent are the design parameters provided in Table 1 technically feasible? A full answer to this question would require volumes. This is not idle speculation– in the case of STAR and PHENIX the volumes exist, in the form of extensive technical reviews that address issues of performance, feasibility, cost, and schedule. ALICE has not (yet) been so rigorously examined (as appropriate for a detector still in the design process and whose data-taking is a decade away). As its design matures, it is likely that it will be forced to make the same trade-offs and optimizations imposed on STAR and PHENIX by fiscal reality (e.g., perhaps in the ambitious goal of high-precision time-of-flight covering a large aperture).

3. SINGLE-EVENT INTERFEROMETRY

There are (at least) two motivations for attempting to extend the solid-angle coverage to as large a region as is possible. The first follows from the desire to measure *small* sources, or small-scale structure in large sources. Either requires measuring relative momenta $q \sim \hbar/R_{small}$. Taking $R_{small} \sim 1$ fm leads to the requirement that the range in relative momentum must extend to at least several hundred MeV/c. The dominance of soft single-particle spectra at RHIC with $\langle p_T \rangle \sim 400$ MeV/c in turn translates this requirement on q into one on solid-angle, i.e., one must have an angular aperture of $\gtrsim 30°$ in each dimension. This is what sets the size for the PHENIX "high-resolution" aperture.

The much larger solid-angles covered by STAR and ALICE provide the ability to attempt *single-event interferometry*; i.e., using the pions measured in one event to determine the "radius" of that event. Here I will develop a crude criterion to estimate the feasibility of such a measurement: Assume that the statistical precision with which a radius can be measured is given by $\frac{\Delta R}{R} = \frac{1}{\sqrt{N_{counts}}}$, where N_{counts} is the number of counts in some region $Q < Q_{peak}$, with $Q_{peak} = \frac{\hbar c}{R}$. The fraction f relative-momentum phase space in the peak region will be given by $f = \left(\frac{Q_{peak}}{Q_{max}}\right)^3$, where Q_{max} is some appropriate cutoff, e.g., $Q_{max} = \langle p_T \rangle$. The number of "useful" counts is then

$$N_{counts} = \left(\frac{\hbar c}{\langle p_T \rangle R}\right)^3 \cdot \frac{N_\pi(N_\pi - 1)}{2} \cdot N_{events} \quad ,$$

where N_π is the number of like pions per event. Taking $\langle p_T \rangle = 400$ MeV/c , and $N_\pi = 400$ (appropriate for identified pions in STAR) gives

$$\frac{\Delta R}{R} = \frac{R^{\frac{3}{2}}}{\sqrt{N_{events}}} \% \quad ,$$

for R in fermis, implying that a 10 fermi source can be measured to an a relative precision of about 30% in STAR. This result, and the dependence on R and N_{events} is in good agreement with a much more detailed study performed by R. Morse[7], at least for $R >$ a few fermis. (For $R \sim 1$ fermi, Morse finds little improvement over $R = 10$ fm, presumably because the "peak" now fills most of phase space, and one therefore loses lever arm for seeing its variation with Q.)

A roughly similar result should apply to ALICE: The solid-angle is a factor of two smaller, but the pion multiplicity is 2-3 times larger[8], leading to values somewhat better than those for STAR (note that since one is looking at the number of *pairs*, one wins linearly with increasing multiplicity). Perhaps more importantly, the precisions of order 10-30% are for an *average* radius. There is little or no chance of resolving this into directional components on an event-by-event basis. For this reason, I am inclined to regard single-event interferometry as an important classification tool, but certainly not as a precision technique.

4. MULTI-PION CORRELATIONS

To what extent do multi-pion correlations contain information not present in the two-particle correlation function? To my knowledge, this remains an open question. There

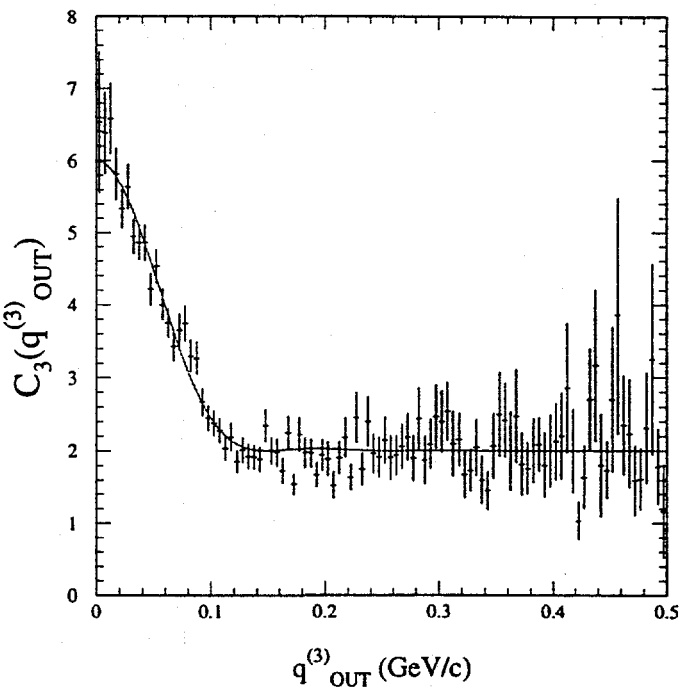

Figure 1. The three-pion correlation function for Au+Au collisions expected to be measured in the PHENIX high-resolution aperture in one hour of running at RHIC. It is assumed that $R_L = R_S = R_{OUT} = 6$ fm, and all longitudinal and sidewards components of relative momentum are required to satisfy $q_L < \hbar/R_L$, $q_S < \hbar/R_S$.

is some weak evidence that any analysis that looks at pair-wise densities (e.g., intensity correlations in a speckle analysis) has the same information content as the pair correlation function[9], but this argument has not been developed to a convincing conclusion. This is somewhat unfortunate, in that the one thing we can be sure of regarding multi-pion rates in the large-aperture detectors at RHIC and LHC is that they will be large. One can readily compare the rates for two-pion versus three-pion correlations using a simple scaling argument: Assume that the multiplicity of pions in some detector is given by $\langle n_\pi \rangle = mA^\alpha$, where m is determined by the geometric acceptance, A is the mass of the colliding species, and α is observed to be about 1.1. We then compare the rate for pairs and triplets to throw events into the "useful" region of the correlation function.

PAIRS	TRIPLETS
$n_2 = \frac{n(n-1)}{2} \sim \frac{1}{2}m^2A^{2\alpha}$	$n_3 = \frac{n(n-1)(n-2)}{6} \sim \frac{1}{6}m^3A^{3\alpha}$
$q_L, q_S < \frac{\hbar}{R} \sim \frac{1}{A^{2/3}}$	$q_L^{12}, q_S^{12} < \frac{\hbar}{R} \sim \frac{1}{A^{2/3}}$ $q_L^{23}, q_S^{23} < \frac{\hbar}{R} \sim \frac{1}{A^{2/3}}$
$q_{OUT} < \frac{\hbar}{R} \sim \frac{1}{A^{1/3}}$	one of 3 $q_{OUT}^{ij} < \frac{\hbar}{R} \sim \frac{3}{A^{1/3}}$
useful yield $\sim \frac{1}{2}m^2A^{1.2}$	useful yield $\sim \frac{1}{2}m^3A^{1.6}$

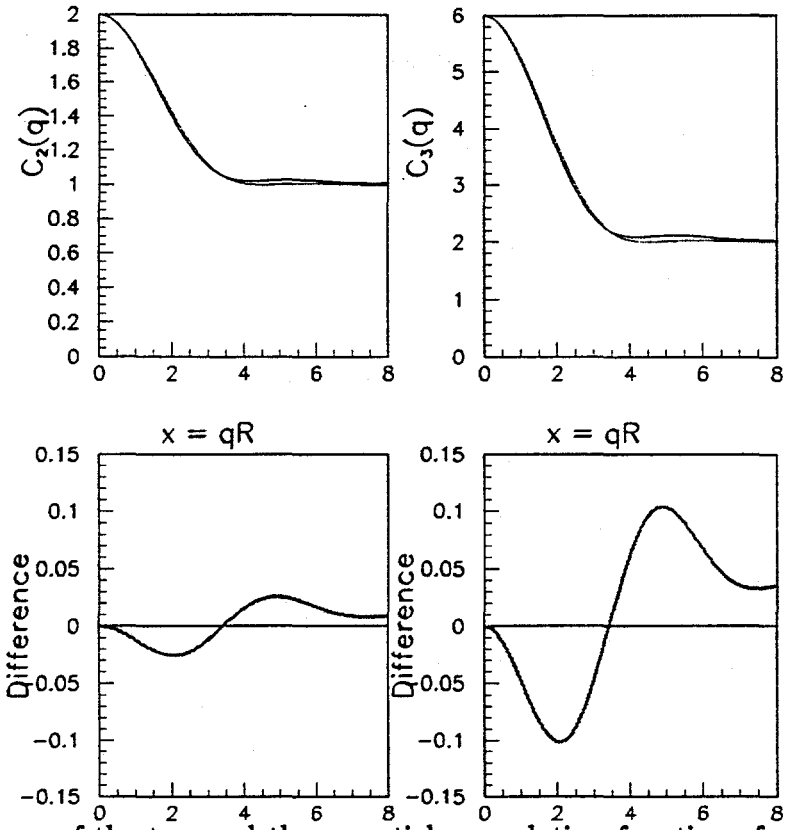

Figure 2. Comparison of the two and three particle correlation functions for a sphere of radius R compared to a hemisphere of radius $1.9R$, versus the reduced variable $x = qR$. The lower panels show the differences between the correlation functions.

For PHENIX, the detector with the smallest value of $m \sim \frac{1}{8}$, these arguments indicate a roughly equal rate for useful triplets as for useful pairs. How large that rate is may be seen in Figure 1, which shows that measurement of a three-pion correlation function in roughly an hour of running is possible. For STAR and ALICE, the triplet rates far exceed the pair rates, since $m \sim 1-2$. The implication is clear– we should find something useful to do with all those triplets! (Not to mention the higher-order correlations.)

In principle, three-pion correlations have a term sensitive to the *phase* of the Fourier transform of the source distribution:

$$C_3(\vec{p}_1,\vec{p}_2,\vec{p}_3) = 1 + |\tilde{\rho}(\vec{q}_{12})|^2 + |\tilde{\rho}(\vec{q}_{23})|^2 + |\tilde{\rho}(\vec{q}_{31})|^2 + 2\Re\left[\tilde{\rho}(\vec{q}_{12})\tilde{\rho}(\vec{q}_{23})\tilde{\rho}(\vec{q}_{31})\right] \quad ,$$

where

$$\tilde{\rho} \equiv \int \rho(\vec{r}) e^{i\vec{q}\cdot\vec{r}}\, d\vec{r} \quad .$$

This is in contrast to the standard expression for C_2, which, as a squared-Fourier transform, loses all phase information in $\tilde{\rho}$. The phase information is in turn related to the *shape*, and in particular the *asymmetry* of $\rho(\vec{r})$, since a non-trivial phase can arise only from a lack of inversion symmetry in $\rho(\vec{r})$. Precisely such asymmetries are predicted by ARC and RQMD to exist in the distributions imaged by a given detector, presumably due to shadowing[10]. Can we use three-pion correlations to directly establish this?

The answer is "Maybe". To demonstrate just how perverse the "information hiding" ability of squared-Fourier transforms is, compare the correlation functions expected for a sphere of radius R, compared to a hemisphere of radius $1.9R$, when viewed along the

symmetry axis of the hemisphere. As shown in Figure 2, there is very little difference in either C_2 or C_3. Here I have chosen $\vec{p}_1 = \vec{p}_2$, and plotted the correlation function versus $|\vec{p}_1 - \vec{p}_3|R$. A little experimentation shows that this choice maximizes any differences between the correlation functions for the sphere and hemisphere. Curiously, this choice of momenta is precisely the one that makes the value of the last term in Equation 4 equal to $|\tilde{\rho}(q)|^2$, so that there is no "direct" phase sensitivity[11]! While it is clear that it will be possible to obtain the statistical accuracy to disinguish between the curves in Figure 2, it is also obvious that some qualitatively new approach is required to extract additional information using three-pion correlations. For instance, the toy model chosen here is essentially a one-dimensional one. It may be that extending this approach to all three dimensions can help determine the phase information.

5. TWO-K^o_s INTERFEROMETRY

Two-kaon interferometry is a very promising probe of nuclear collisions. The small interaction cross sections[12] and the smaller contributions from the decay of higher resonances in principle make two-kaon interferometry somewhat cleaner than two-pion measurements[13]. Mitigating this is the much larger two-particle Coulomb interactions (see Section 6.1) for the two-kaon system. This leads one to consider correlations between neutral kaons. This system of course famously violates CP conservation, so that the pairs available for study are two-K^o_s pairs, with $|K^o_s\rangle = \frac{1}{\sqrt{2}}\left[|K^o\rangle + |\bar{K}^o\rangle\right]$, i.e., a particle of mixed-strangeness. The interference leading to the observed correlations is diagonal in the strangeness basis states, which leads to a two-K^o_s correlation function[14] that is a mixture of that for $2K^+$'s and $2K^-$'s:

$$C_2(q) = 1 + f_+^2|\tilde{\rho}^w_+(q)|^2 + (1-f_+)^2|\tilde{\rho}^w_-(q)|^2 + 2f_+(1-f_+)\Re\left[\tilde{\rho}^w_+(q)\tilde{\rho}^w_-(q)\right] \quad ,$$

where f_+ is the fractional yield of K^+'s and $\rho^w_\pm(q)$ is a Wigner-transform in q of the distributions for $K^\pm$'s. This presents many intriguing possibilities, since mechanisms such as distillation are expected to operate only on the S=-1 quarks.

In addition to avoiding the Coulomb effects that severely distort two charged-kaon measurements, $2K^o_s$ interferometry has another nice experimental feature: since each K^o_s is observed via $K^o_s \rightarrow \pi^+\pi^-$, K^o_s pairs at low relative momentum have daughters that are well-separated, so that the tracking ambiguities that plague HBT at low relative momentum are eliminated. The feature comes at some cost, namely the difficulties of identifying decay vertices and reconstructing invariant masses in a high multiplicity environment. The feasibility of making such measurements in the STAR detector has been investigated by Keane[15]. His results for 10^4 Au+Au events are shown in Figure 3 for a 10 fermi source. While the statistics in the figure are low, note that this corresponds to about three hours of running time, indicating that rate should not be an issue for this channel. Note also the huge Coulomb effect in the charged channels, indicated by the dashed lines.

It is worth noting that Equation 5 has some special features that may provide the solution to those discussed in the previous section. Suppose one can measure the $2K^+$ and $2K^-$ correlations separately, and therefore determine $|\tilde{\rho}^w_+|^2$ and $|\tilde{\rho}^w_-|^2$. One will of course also know the value of f_+, since this is just a matter of counting charged kaons. Then all quantities except the last term in Equation 5 are known, and one again has a

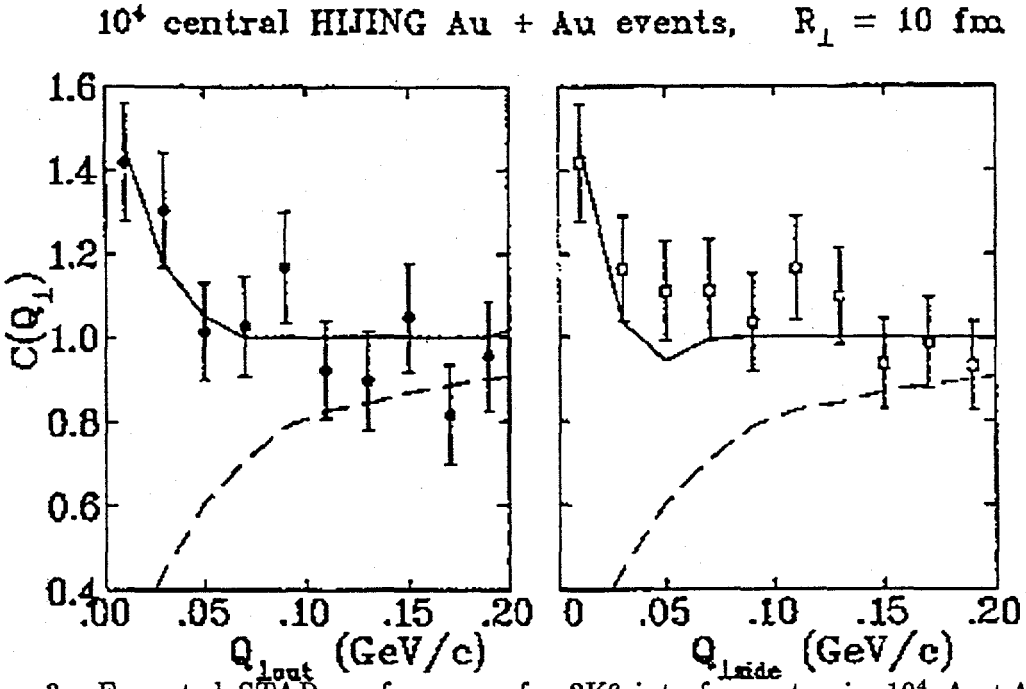

Figure 3. Expected STAR performance for $2K^o_s$ interferometry in 10^4 Au+Au events assuming a 10 fermi source. The dashed curves are the correlation functions for $2K^+$'s from the same source.

chance to get at the phase information present in $\tilde{\rho}^w_\pm$'s, especially if the different cross-section for strange and anti-strange kaons lead to different shadowing effects (and hence different asymmetries).

6. NEW INTERFEROMETRY CANDIDATES

The abundance of particles produced at RHIC and LHC will allow one to examine previously unavailable channels and methods for studying the space-time geometry. Here I will briefly consider two such possibilities.

6.1. Two-Coulomb "Interferometry"

As alluded to in Section 5, there are serious problems in using HBT to measure large source sizes which arise from the mutual Coulomb repulsion between the identical charged particles. This more massive the particle, the larger the problem. To see this, recall that the Coulomb repulsion is usually described in terms of the Gamow factor:

$$G(Q) \equiv \frac{|\Psi_q(\vec{r}=0)|^2}{|\Psi_q(\infty)|^2} = \frac{2\pi\eta}{e^{2\pi\eta}-1}$$

$$\eta \equiv \frac{e^2}{\hbar v_{rel}} = \alpha\frac{m}{Q} \quad .$$

Since the suppression depends on the relative *velocity*, it extends to larger Q as the mass of the particles increases. The scale is set by the Bohr radius $a_o = \hbar/m_{red}e^2$ of the two-particle system. The values for various systems are tabulated in Table 2; it should be kept in mind that the interferometry peak is essentially destroyed for sources of size $\gtrsim \frac{1}{10}a_o$.

However, once can turn this vice to a virtue by looking at *unlike* pairs such as π^+K^+ . Clearly one expects no Bose enhancement in such channels, but the Coulomb suppression

Table 2: Bohr radii for various systems	
System	a_o (fm)
$\pi\pi$	387
πK	249
πp	224
KK	108
Kp	83
pp	57

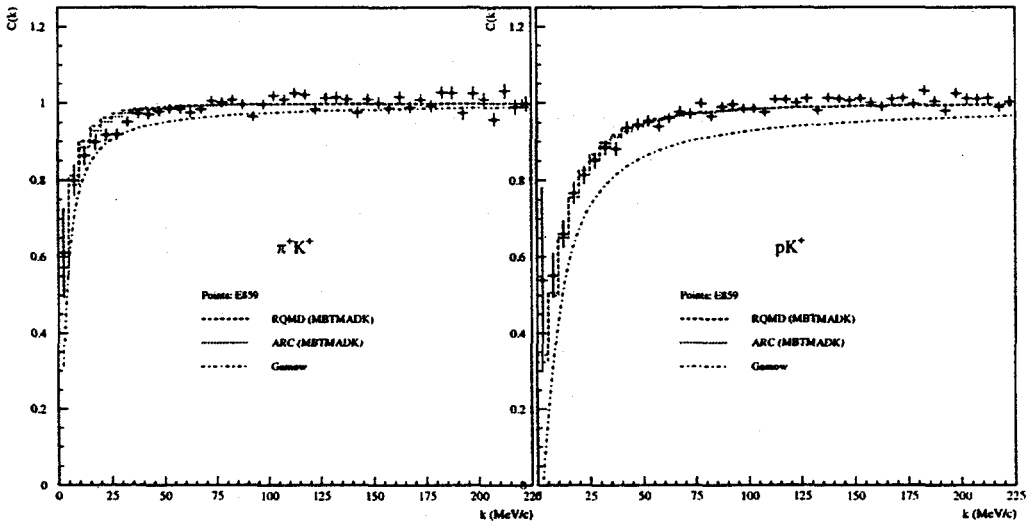

Figure 4. Preliminary data for two-particle correlations from Si+Au collisions measured by E859, compared to Gamow and full Coulomb wave treatments. The correlations are plotted versus the momentum of one of the particles in the pair rest-frame.

still operates on a scale determined by the appropriate Bohr radius. In the pure Gamow limit of Equation 1 this provides no additional information , since the definition of $G(Q)$ explicitly assumes the particles are emitted from the same space-time point. This of course is not the case, and modifies the Gamow function. To first order, the correction is given by

$$G(Q) \rightarrow G(Q)\left[1 + 2\frac{\langle r \rangle}{a_0} + \cdots\right] \quad ,$$

where $\langle r \rangle$ is the mean separation in the source between the particles[16]. (A full treatment requires integrating Coulomb waves over the source distribution.)

There is some evidence that existing data sets may already be sensitive to this effect. Figure 4 shows the π^+K$^+$ and pK$^+$ correlation data from E859[17] compared to Gamow and full Coulomb treatments. The Coulomb waves are integrated over source distributions taken from ARC and RQMD, and clearly describe the data much better than the Gamow factor. Such techniques should be straightforward to apply at RHIC and LHC, where the huge particle abundances will allow one to examine many such pair combinations. It is worth noting that this approach is quite insensitive to two-particle tracking ambiguities, since the suppression occurs at $Q_{PAIR-CM} \sim 0$, but for $m_1 \neq m_2$, this leads to $Q_{LAB} \neq 0$ by (typically) a few hundred MeV/c.

6.2. Anti-neutron interferometry

An excellent indicator that particle production rates are large at RHIC is the possibility of performing correlation measurements with anti-baryons. It is likely that it is more feasible to do this with anti-neutrons than anti-protons, since the anti-protons will undergo significant multiple scattering in passing through the detectors (to the extent that a significant number actually range out), and the 2 $\bar{p}$ correlation function will have the Coulomb repulsion problems discussed in the previous section. Anti-neutrons neatly get around these difficulties, provided one can detect them. The PHENIX electromagnetic calorimeter may provide such a tool. It has excellent spatial segmentation ($\sim$ 5 cm$\times$5 cm at 5 meters) and superior timing resolution $\sigma_T \sim$ 300 ps. Applied to the detection of 300 MeV/c $\bar{n}$'s this gives single-particle momentum resolution of a few MeV/c, and a guess-timated two-particle relative momentum resolution on the order of 10 MeV/c. Since the calorimeter covers a relatively large solid angle, and the PHENIX DAQ system is designed for high-rate capability, rate estimates for central Au+Au collisions lead to high values for pair-collection rates (10^{5-6} 2 $\bar{n}$ pairs per week, conservatively assuming a net detection efficiency of 0.01-0.001). This provides the exciting prospect of direct probes of the anti-matter production in RHIC collisions. Regardless of the utility of these pairs, it will be necessary for PHENIX to carefully measure the anti-neutrons, since they are expected to be a significant background to direct photon measurements[18].

7. CONCLUSIONS

Relativistic heavy ion collisions are the perfect environment to apply interferometry, since the large rates allow examination of both mundane and exotic systems, and these are *precisely* the sort of measurements required to to study the bulk hadronic matter formed in these systems. It is thus not too surprising that PHENIX, STAR and ALICE are the first large collider detectors designed "from the start" with HBT in mind. As a result of this process, there are no *obvious* flaws in the approaches chosen to meet these goals. But the high particle yields at these colliders which make HBT rates so large of course come at some price, since they of course result from the high per-event multiplicities. There are plenty of simulations as yet undone to determine the true operating characteristics of these detectors in this environment. A ridiculously incomplete list would nonetheless include

- Effects of π decay on momentum resolution
- Effects of kaon decay on track-finding
- Reconstruction efficiency versus ghost generation
- Real detector effects:
  - Inefficiencies
  - Noise
  - Cross-talk
  - Real pulse-pair resolution function

- Backgrounds from neutrals
- Particle ID efficiencies
- Albedo

While many of these effects are amenable to detailed simulation, the best simulator will always be Nature. Her(?) results are eagerly awaited.

8. ACKNOWLEDGMENTS

It is a pleasure to thanks J. Harris, P. Jacobs, M. Moulson, I. Sakreda, J. Schukraft, and S. White for their assistance in preparing this talk and manuscript. It is a duty to note that any mistakes are exclusively mine.

REFERENCES

1. In the thermodynamic limit, one might argue that temperature, as an extensive variable, is better choice than energy density for characterizing the phase transition, but this of course begs the question as to whether one is in that happy limit.
2. R. Hanbury Brown and R.Q. Twiss, Nature **178**, 1046 (1956).
3. W.A. Zajc. Bose-Einstein Correlations: From Statistics to Dynamics. In P. Carruthers, editor, *Hadronic Multiparticle Production.* World Scientific Press, 1988.
4. B. Lorstad, Int. J. Mod. Phys. **A4**, 2861 (1988).
5. D.H. Boal, C.K. Gelbke, and B.K. Jennings, Rev. Mod. Phys. **62**, 553 (1990).
6. For a discussion of the capabilities of the BRAHMS and PHOBOS detectors, see the contributions of D. Beavis and M. Baker, respectively, to these proceedings.
7. *A Rate/Sensitivity Study for Two-Particle Correlations in STAR*, R.J. Morse, STAR Note #67 (1992).
8. Substantially better single-event precisions are presented in the ALICE design report, which follow directly from the assumed $dN_{ch}/dy = 8000$ for LHC energies. A much more conservative estimate would be a rapdity density of ~ 2000, leading to results roughly consistent with those obtained for STAR. There are *large* undertainties here, since both the elementary p-p multiplicity dN_{ch}/dy is unknown, and the methods for calculating the expected scaling with projectile mass at these energies are in their infancy. This remark of course applies to all LHC heavy ion physics!
9. W.A. Zajc, Phys. Rev. **D35**, 3396 (1987).
10. O. Vossnack it et al., Nucl. Phys. **A566**, 535c (1994).
11. I would like to thank Mark Baker for this valuable observation.
12. The smaller cross sections argument only applies to $S = +1$ kaons interacting with *baryonic* matter.
13. S.S. Padula and M. Gyulassy, Phys. Lett. **217**, 181 (1989).
14. M. Gyulassy, Phys. Lett. **286**, 211 (1992).
15. *STAR Capabilities for* K^0_S *Interferometry*, D. Keane, STAR Note #47 (1992).
16. *Two Pion Correlations in Heavy Ion Collisions*, W.A. Zajc, PhD thesis, University of California, 1982. (Available as LBL-14864.).
17. O. Vossnack, Columbia Ph.D thesis (to be published).
18. P. Braun-Munzinger, private communication.

Electron Measurement in PHENIX

Y. Akiba[a]

[a]Institute for Nuclear Study, University of Tokyo,
Midori-cho 3-2-1, Tanashi, Tokyo 188, Japan

Electron Measurement in PHENIX detector at RHIC is discussed. The yield and S/N ratio at vector meson peaks (ϕ, ω, ρ^0, and J/ψ) are evaluated. The electrons from open charm decay, and its consequence to the di-electron measurement is discussed.

1. INTRODUCTION

PHENIX [1] is one of the two major experiments of Relativistic Heavy Ion Collider (RHIC), now being constructed at Brookhaven National Laboratory. The experiment aims to study Au+Au collisions at $\sqrt{s} = 200$ GeV per nucleon, and to search for the phase transition from normal nuclear matter to quark-gluon plasma (QGP). The detector measures electrons, photons, and hadrons in the central detector, and measures muons in the forward muon arm. In this talk, we discuss electron measurement in PHENIX central detector. Other aspects of the experiment are presented in this workshop [2–4].

2. PHENIX Central Detector

PHENIX central detector is made of an axial field magnet and two almost identical arms placed left and right of the magnet. Each arm covers $\pm$ 0.35 units of pseudo-rapidity and 90 degrees in azimuthal angle. They are separated by 67.5 degrees in ϕ. A beam view of the PHENIX central arm is shown in figure 1.

Each arm is made of several detector subsystems. From the beam line, there is an inner tracking system made of 2 sets of drift chambers and a pad chamber. The inner tracker is followed by a Ring Image Cherenkov Detector (RICH), which provides electron/hadron separation from a few hundred MeV/c to about 4 GeV/c. Outside of the RICH detector is an outer tracking system made of a Time Expansion Chamber (TEC) sandwiched by two pad chambers. The TEC have a electron/hadron separation capability by a fine sampling dE/dx measurement. The last layer of the detector is an electromagnetic calorimeter (EMCAL) for photon measurement and for electron/hadron separation. A quarter of EMCAL is lead-glass calorimeter, and three quarter is Pb-Scintillator sampling calorimeter. The Pb-scintillator calorimeter have a good time of flight (TOF) capability that is useful for e/π separation at low energies. A part of one arm is equipped with high resolution TOF counters for hadron identification, but we will not discuss it here.

Electron identification is provided by the following three subsystems: RICH, TEC, and EMCAL. The RICH detector is a gas Cherenkov counter with 5120 PMT read-

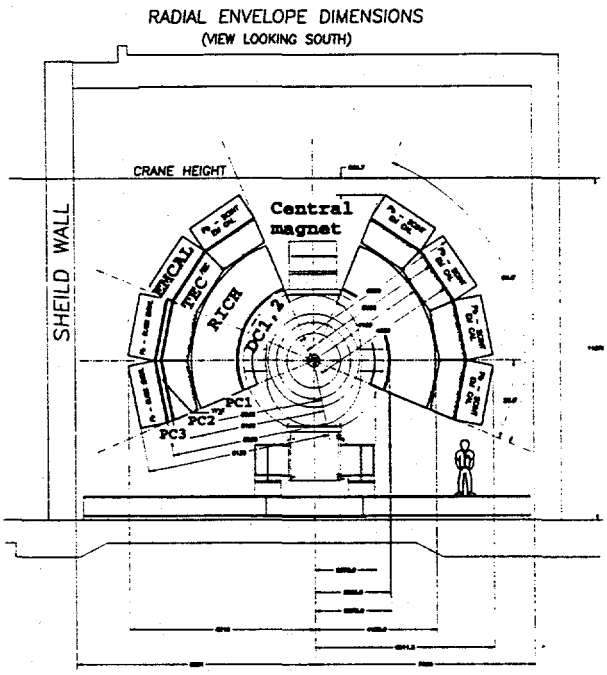

Figure 1. A beam view of PHENIX central detector.

out, and the main electron identification device in PHENIX central detector. The high segmentation of the read-out is required to uniquely associate Cherenkov light signals to tracks measured by the tracking system. A beam test of a small prototype of the device shows that it has a pion rejection better than 10^4 with electron acceptance $>$ 99 % for a single isolated track. However, this excellent e/π rejection is reduced in a high particle density environment expected in RHIC Au+Au central collision because of ambiguities in association of Cherenkov signals with particle tracks. From a detailed GEANT Monte Carlo simulation, it is estimated that its e/π separation in Au+Au central collision is about 10^3. The TEC provides e/π separation by its dE/dx measurement. A beam test shows that its pion rejection factor is about 10^2 for a single isolated track with momentum $<$ 2 GeV/c. The EMCAL provides about factor 10^2 pion rejection for tracks with momentum $>$ 1 GeV/c. Combining all three subsystems, the PHENIX central arm has e/π separation better than 10^4 from a few hundred MeV/c to 4 GeV/c.

The acceptance of the detector is $dYd\phi = 0.7\pi$ for single e^+ or e^-, and about 4 % of $\frac{d\sigma}{dy}$ for e^+e^- pairs. The acceptance for the pair depends on $\frac{m}{p_t}$ of the pair.

One of the important design goals of the PHENIX central detector is high mass resolution to detect changes in properties of vector mesons in high energy density created in Au+Au central collisions. The expected mass resolution for J/ψ and ϕ as a function of transverse momentum is shown in figure 2. Mass resolution for ϕ is expected better than 4 MeV in r.m.s, which is comparable to its natural width (Γ = 4.4 MeV)[5]. The resolution gives us a high sensitivity to detect the changes in mass and width of ϕ if such

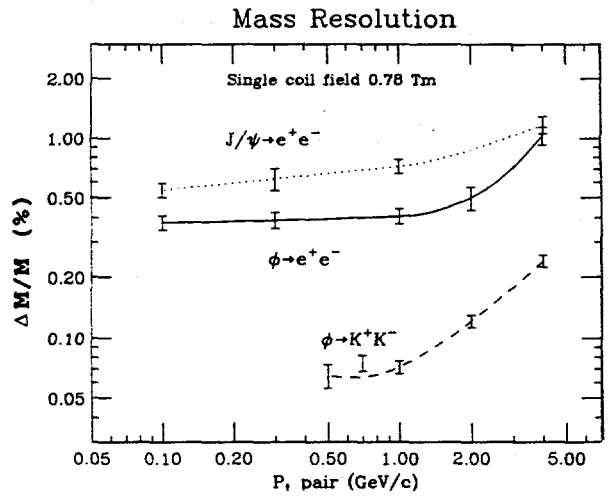

Figure 2. Mass resolution in PHENIX central detector.

changes occur in heavy ion collisions at RHIC.

3. Light Vector Mesons

There are many theoretical predictions on how the properties of light vector mesons (mass, width, and branching ratios of ρ, ω, and ϕ) can be changed in high density and/or high temperature state [6–21]. Measurement of light vector mesons through its leptonic decay mode is particularly useful to detect such changes, since we can probe the state of vector mesons deep inside the high density/temperature matter without the complication of final state interactions.

Figure 3 shows an expected di-electron mass spectrum measured in PHENIX central detector. The figure corresponds to 32 M central Au+Au collisions, roughly one week of data taking with nominal RHIC luminosity of $L = 2 \times 10^{26} cm^{-2} s^{-1}$. This is based on a full GEANT simulation of the detector that includes all backgrounds coming from shower particles in magnet yoke, gamma conversions in beam pipe, Dalitz decays of π^0. The particle tracks are reconstructed from hit positions in the tracking chambers, and electrons/positrons are identified from simulated responses of RICH and EMCAL detector. The figure is before background subtraction.

The broad continuum of dilepton spectrum are mostly combinatorial backgrounds from π^0 Dalitz decays and gamma conversions in beam pipe with small contributions from misidentified hadrons. The conversion in MVD (Multiplicity Vertex Detector), which surrounds the beam pipe, is not included in the simulation. If it is included, the background level increases by about 60 % [25]. Although backgrounds are large, we can clearly see signals of narrow vector mesons, ϕ and ω, above the background. We can also see J/ψ and $\psi(2S)$ in high mass region. However, ρ^0 resonance is buried in the background because of its broad width (Γ = 151 MeV[5]).

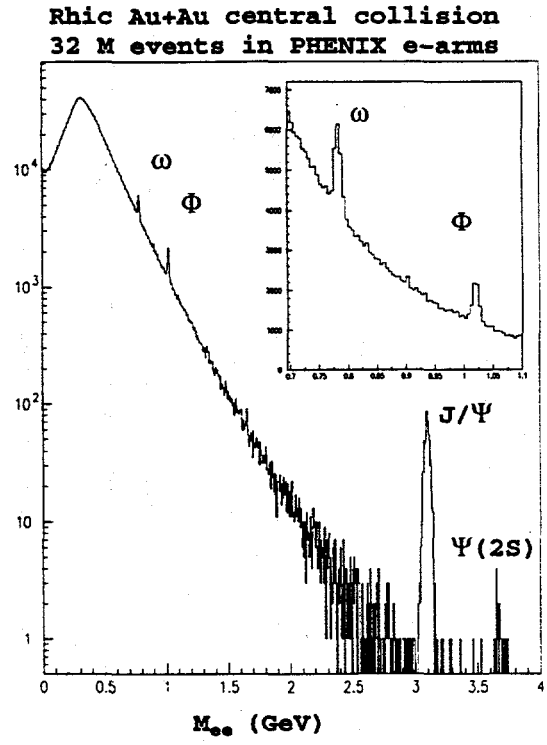

Figure 3. Mass spectrum of di-electrons in PHENIX central detector.

Expected yield of light vector mesons measured in PHENIX central arms in one year is summarized in table 1. Here we assume that the luminosity of RHIC is $L = 2 \times 10^{26} cm^{-2} s^{-1}$ for Au+Au, and one year is 3000 hours ($= 1.08 \times 10^8$ sec) of data taking. Assuming that we collect all central collision event (10 % of minimum bias event), we have about 1 G central events per year. In this calculation, we assume the following particle yield ratios: $\frac{N_{\rho 0}}{N_{\pi 0}} = 20$ %, $\frac{N_{\omega}}{N_{\rho 0}} = 1.0$, and $\frac{N_{\phi}}{N_{\pi 0}} = 2$ %. Those yield ratios are based on p+p data at the ISR [26].

Table 1
Yield of vector mesons and S/N ratios in one year of measurement in PHENIX central detector

	Yield (per year)	Background	S/N ratio	(Background)$^{1/2}$
ρ	110K	3.9M	1/35	2K
ω	170K	500K	1/3	0.7K
ϕ	75K	150K	1/2	0.4K

As one can see from the figure 3 as well as table 1, we have a reasonable S/N ratio and

large statistics for measurement of ω and ϕ. For ρ^0, the S/N ratio is rather poor (S/N $\sim$ 1/35). Although in principle we have enough statistic after the background subtraction, we need to understand the background shape very well to extract the signal.

We want to note that the reason we expect a poor S/N ratio for ρ^0 is that we use a conservative estimate for the ρ^0 production cross section, a simple scaling of particle ratio from p+p collisions. In nucleus-nucleus collisions at RHIC energies, it is expected that a mixed phase state or a hot hadronic gas is formed with a long life time ($\sim$ 10 fm/c). Since life time of ρ is short ($c\tau$ = 1.2 fm), they are formed for several generations by $\pi\pi \rightarrow \rho^0$reaction in this high energy density / high temperature state [24]. Therefore the yield of $\rho^0 \rightarrow e^+e^-$ can be larger than that of simple scaling from p+p collisions used in our yield estimation unless the life time of the "fireball" is short or ρ^0 is desolved in the hot dense matter. In other words, in table 1, we neglect the contribution of $\pi\pi \rightarrow \rho^0 \rightarrow e^+e^-$ reaction, and thus the yield and S/N ratio of ρ in the table should be considered as a conservative minimum value.

4. J/ψ Measurement

"Suppression" of J/ψ is one of the proposed signals of quark gluon plasma formation[27], and such "suppression" has been observed in di-muon experiment at the CERN SPS [28]. It is, therefore, very important to measure J/ψ at RHIC energy.

As show in figure 3, we have an excellent S/N ratio for J/ψ measurement because of high mass resolution of the detector. The measurement is limited by a rather small solid angle of the detector, whose acceptance is about 4 % of dN/dy for J/ψ. The expected yield of J/ψ and ψ(2S) detected in PHENIX central arms are summarized in table 2. Here we assume that the cross section $\frac{B_{ee}d\sigma}{dy}$ ($pp \rightarrow J/\psi$) is 50 nb [30,31] at $\sqrt{s}$ = 200 GeV, and that the cross section scales as $\sigma(AA) \propto A^{2\alpha}$ with α = 0.92[29,32]. In other words, we do not include additional "J/ψ suppression" other than observed in pA collisions in this estimate.

Table 2
Yield of J/ψ ψ(2S) in one year of measurement in PHENIX central detector

	Yield (minimum bias)	Yield (central)
J/ψ	70K/year	14K/year
ψ(2S)	1.4K/year	300/year

J/ψ cross section should be measured for a wide range of transverse momentum to clarify the "suppression mechanism", that is, to distinguish the "suppression" in normal nuclear matter and that in quark gluon plasma. Therefore, it is worthwhile to evaluate how high in p_t we can measure J/ψ in PHENIX central detector.

There are a few measurement of $pp(p\bar{p}) \rightarrow J/\psi$ at high transverse momentum.

$\sqrt{s}$ = 63 GeV (pp) $\quad \frac{B_{ee}d\sigma}{dy} \simeq$ 5 pb ($p_t \geq$ 5 GeV/c)[33]

$\sqrt{s}$ = 630 GeV ($p\bar{p}$) $\quad \frac{B_{\mu\mu}d\sigma}{dy} \simeq$ 1.7 nb ($p_t \geq$ 5 GeV/c) [34]

$\sqrt{s} = 1.8$ TeV $(p\bar{p})$ $\quad \frac{B_{\mu\mu}d\sigma}{dy} \simeq 6.9$ nb $(p_t \geq 6$ GeV/c) [35]

From those values, we estimate that $\frac{Bd\sigma}{dy}$ $(pp \rightarrow J/\psi) \simeq 200$ pb for $p_t \geq 5$ GeV/c at $\sqrt{s} = 200$ GeV. To scale this cross section to Au+Au collisions, we use nuclear dependence slope $\alpha = 1.0$, since there will be less nuclear effect in high p_t region. The acceptance of PHENIX central detector for high p_t J/ψ is about 2 % of dN/dy. We expect about 300 (60) events above $p_t \geq 5$ GeV/c for minimum bias (central) Au+Au collisions in one year. This means that we can measure J/ψ cross section up to ~ 6 GeV/c, where "J/ψ suppression" in the QGP model becomes small[36].

Strictly speaking, we are not measuring the "J/ψ suppression" in this high transverse momentum region, since most of the J/ψ's above 5 GeV/c in p_t are decay product of χ_c meson[37]. However, since p_t dependence of "suppression" of χ_c in the QGP model is similar to that of J/ψ[36], the measurement of high p_t is useful to clarify the suppression mechanism.

5. Charm and single electrons

Enhanced production of charm is proposed as a "signature" of QGP[38], and charm production is proposed as a sensitive "thermometer" and a "probe" [39,40] of the early stage of nucleus-nucleus collisions. If there is an enhanced production of charm in nucleus-nucleus collisions, such phenomena can be observed as an enhanced production of "single electron" in $p_t = 1$ to 5 GeV/c. Open charm is also a major source of background for dilepton continuum measurement [41]. Therefore, it is very important to evaluate the charm production at RHIC, and its consequence to electron measurement.

Here we briefly summarize the charm production at RHIC energy. There are several measurements of hadronic charm production at SPS and FNAL fixed target energies. They showed that $\sigma(pp \rightarrow c\bar{c})$ is about 15 μb at $\sqrt{s} = 28$ GeV [42], and 20 to 40 μb at $\sqrt{s} = 40$ GeV[43–46]. Perturbative QCD calculations predict that charm production cross section $\sigma(pp \rightarrow c\bar{c})$ increases by factor 5 to 10 from $\sqrt{s} = 40$ to 200 GeV [47–49]. Although there is uncertainty in pQCD calculations of charm production, which depends on the choice of gluon distribution function, the mass of c-quark, and the normalization scale, it is generally agreed that the charm cross section $\sigma(pp \rightarrow c\bar{c})$ is 150 to 250 μb at RHIC energy ($\sqrt{s} = 200$ GeV)[48–50].

To scale this elementary cross section to nucleus-nucleus collision, we need the nuclear dependence α, defined as $\sigma(pA) \propto A^{\alpha}$. Recent measurement of $p + A \rightarrow D\bar{D}$ at FNAL shows that $\alpha_{D\bar{D}} = 1.02 \pm 0.03 \pm 0.02$ near center-of-mass rapidity[44]. This behavior is consistent with charm production by gluon fusion model ($gg \rightarrow c\bar{c}$), if nuclear shadowing of gluons can be neglected. There is a theoretical estimates that charm production at RHIC Au+Au central collisions is reduced by 30 % [50]to 50 % [39,51] from the value of $\alpha_{c\bar{c}} = 1.0$ by nuclear shadowing. On the other hand, there are theoretical predictions that charm pairs produced in "pre-equilibrium stage" in Au+Au central collisions is comparable to that of initial pQCD production [39,40]. If there is a significant "pre-equilibrium" production, $\alpha_{c\bar{c}}$ becomes larger than 1.0.

Figure 4 shows p_t distribution of electron expected for central Au+Au collisions at RHIC. Momentum distribution of e^+ from various sources (π^0 Dalitz decay, decay of

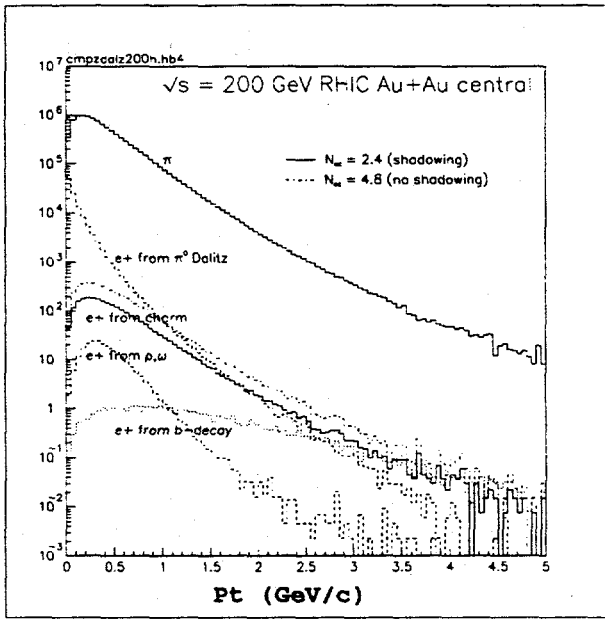

Figure 4. P_t distributions of e^+ from π^0 Dalitz decays, from decay of charm and bottom quarks, and from decay of vector mesons in central Au+Au collision at RHIC. P_t distribution of π^0 is also shown in the figure.

charm quark, ρ, ω, and bottom quark) are shown. In this calculation, we use the p_t distribution of π^0 based on the data from UA1 at $\sqrt{s} = 200$ GeV[52], and we use ISAJET 7.6 [53] to calculate p_t distribution of D and B mesons. The leptonic branching ratio of charm quark is assumed as 12 %, an average of Br($D^+ \to l^+X$) and Br($D^0 \to l^+X$). The figure shows two cases for charm e^+ spectrum, one for $N_{c\bar{c}} = 2.4$ and one for $N_{c\bar{c}} = 4.8$. The case $N_{c\bar{c}} = 4.8$ corresponds to $\sigma(pp \to c\bar{c}) = 160\mu b$ and $\alpha_{c\bar{c}} = 1.0$ with no nuclear shadowing, and the case $N_{c\bar{c}} = 2.4$ assumes a uniform 50 % suppression. Since there will be less nuclear shadowing at high p_t charm production[39,50], the latter underestimate the electron yield at high p_t. To evaluate bottom e^+ spectrum, we use the cross section $\sigma(pp \to b\bar{b}) = 2.5\ \mu b$ and $\alpha_{b\bar{b}} = 1.0$.

As one can see from the figure, the yield of charm decay e^+ is as large as that of π^0 Dalitz e^+ for p_t above 1.5 GeV/c. The e^+ from light vector meson decay is less than 10 % of charm e^+. For very high p_t (> 5 GeV/c), the contribution from the bottom decay can not be neglected.

The ratio $e^+(\text{charm})/\pi^0 \sim 5 \times 10^{-4}$ is several times higher than that observed at ISR energy, where the ratio "single e^+"$/\pi$ is about 10^{-4} [54]. This larger value of e/π ratio is explained by two reasons. First, the charm production cross section at $\sqrt{s} = 200$ GeV is several times larger than that of ISR energy. Second, the charm cross section have larger nuclear dependence ($\alpha_{c\bar{c}} = 1.0$) than that of pions ($\alpha_\pi \sim 0.75$[55]) at mid-rapidity. Both effects favor larger c/π ratio, and thus larger e/π ratio, for Au+Au collisions at

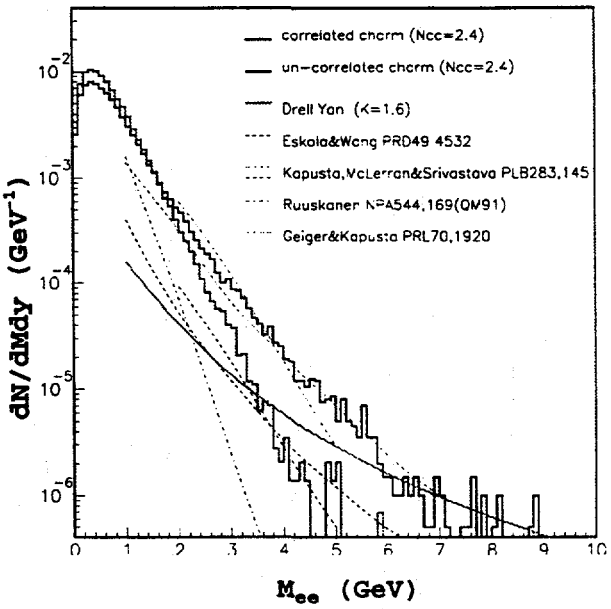

Figure 5. A dilepton mass distribution from charm decay and theoretical predictions of thermal dileptons.

RHIC compared with pp collisions at the ISR. If there is a significant $c\bar{c}$ production in "pre-equilibrium" stage of nucleus-nucleus collision, we expect an even larger e/π ratio.

We expect copious "single" electrons from charm decay in RHIC Au+Au collisions. The number of charm electrons with $p_t > 1$ GeV/c detected in PHENIX central arms is about 2×10^{-3} per central Au+Au collisions, or about 2 million per year. The measurement of "single" electron can be used as indirect measurement of charm production and its nuclear dependence.

6. Dilepton continuum and charm

The open charm is the major background for "thermal dilepton" continuum from the QGP. In figure 5, we compare the di-electron mass spectrum from charm decay and recent theoretical predictions of "thermal dilepton" mass distributions[56–59]. The mass spectrum from Drell-Yan process is also shown. The Drell-Yan cross section is evaluated with the K-factor 1.6, which reproduces the low energy data. We use $N_{c\bar{c}} = 2.4$ to calculate charm dilepton mass distribution.

There are two "charm dilepton" lines in the figure. One is that from "uncorrelated" charm leptonic decay, and the other is from "correlated" charm decay. The "correlated" charm di-electrons are produce by the process $gg(q\bar{q}) \rightarrow c\bar{c} \rightarrow e^+e^-X$, and it is proportional to the $c\bar{c}$ production. The "uncorrelated" charm dilepton is a pure combinatorial background of two e^+ and e^- from unrelated charm (anti-charm) decays. This background is proportional to $N^2_{c\bar{c}}$, and can not be neglected in high energy nucleus-nucleus collision.

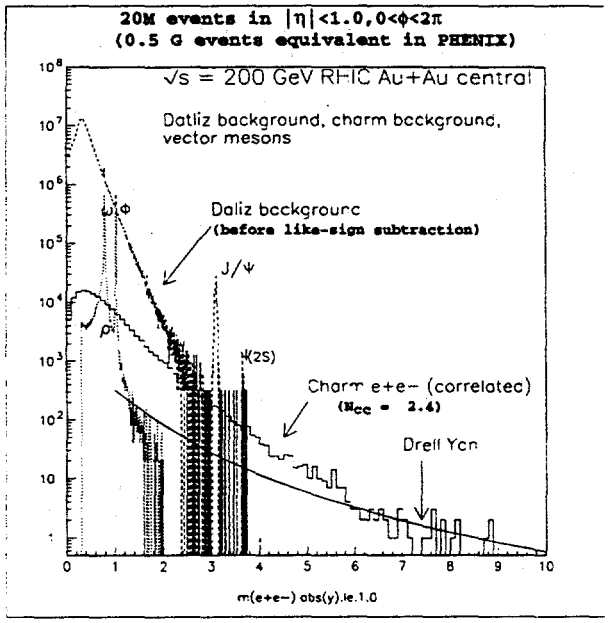

Figure 6. Dilepton mass distribution from Drell-Yan and charm decay compared with the vector meson signals and Dalitz/conversion backgrounds in PHENIX central detector.

However, the yield of the background can be estimated from link-sign pairs or from event mixing, and therefore it can be subtracted from the data.

The figure shows that the yield of "correlated" charm e^+e^- pairs are larger than that of Drell-Yan process below $M_{ee} = 6$ GeV, and larger than most of the theoretical predictions of dilepton continuum from QGP. In order to separate the thermal continuum, we need a direct measurement of charm dilepton spectrum. In PHENIX, this can be done by a measurement of $e^{\pm} - \mu^{\mp}$ pair using the central detector and the muon arm.

The "correlated" charm leptons have harder mass spectrum than that of "uncorrelated" charm lepton pairs. This is because the correlated pairs have strong back to back correlation, and tend to produce higher mass. It is possible that our calculation overestimates the momentum correlation of $c\bar{c}$ pair, and therefore the yield of charm dileptons in high mass region ($M_{ee} > 3$ GeV). The correlation can be reduced in collisions of heavy nucleus as c ($\bar{c}$) quark traverses through high density matter. We may be able to probe re-scattering/energy loss of c quarks from the angular correlations of charm dileptons.

Figure 6 shows the mass spectrum of Drell-Yan process, correlated charm dielectrons in $|y| < 1.0$. A mass spectrum of vector meson resonances and combinatorial background of π^0 Dalitz decays and γ conversions in PHENIX central arm is overlaid in the figure. The statistic of the figure is roughly equivalent to one year of data taking in PHENIX central arms. The figure shows that the charm dileptons is larger than Dalitz background above $M_{ee} \sim 3$ GeV.

7. Summary

We discussed on electron measurements in PHENIX detector at RHIC. Although we expect large Dalitz/conversion background in low mass region ($M_{ee} < 3$ GeV), we can clearly separate signals of narrow vector mesons (ω, ϕ) from the background. J/ψ is measured in $p_t < 6$ GeV/c. We discussed the consequence of large charm production expected in RHIC Au+Au collisions. The yield of charm decay electron is expected to be larger than Dalitz/conversion background for p_t above ~ 1.5 GeV/c. The lepton pairs from charm decay dominates over Drell-Yan process for mass as high as 6 GeV, and its yield is larger than most of theoretical predictions of thermal lepton pairs from QGP.

REFERENCES

1. PHENIX Conceptual Design Report, BNL 1993 (unpublished).
2. P. McGaughey, in these proceedings.
3. S. White, in these proceedings.
4. W. Zajc, in these proceedings.
5. Particle Data Group, Phys. Rev. D50 (1994) 1173.
6. R. D. Pisarski, Phys. Lett. 110B (1982) 155.
7. J. P. Blaizot and R. M. Galain, Phys. Lett. B271 (1991) 32.
8. G. E. Brown, Nucl. Phys. A522 (1991) 397c.
9. H. W. Barz, *et al.*, Phys. Lett. B265 (1991) 219.
10. P. Bi and J. Rafelski, Phys. Lett. B262 (1991) 485.
11. C. Gale and J. Kapusta, Nucl. Phys. B357 (1991) 65.
12. D. Lissauer and E. Shuryak, Phy. Lett. B253, (1991) 15.
13. C. M. Ko, P. Levai, X. J. Qju and C. T. Li, Phys. Rev. C45 (1992) 1400.
14. M. Asakawa, C. M. Ko, P. Levai, and X. J. Qiu, Phys. Rev. C46 (1992) R1159.
15. T. Hatsuda, Nucl. Phys. A544 (1992) 27c.
16. T. Hatsuda and S. H. Lee, Phys. Rev. C46 (1992) R34.
17. M. Asakawa and C. M. Ko, Rhys. Rev. C48 (1993) R526.
18. T. Hatsuda, Y. Koike, and S. H. Lee, Phys. Rev. D47 (1993) 1225.
19. C. A. Dominguez, M. Loewe and J. C. Rojas, Z. Phys. C59 (1993) 63.
20. C. M. Ko and D. Seibert, Phys. Rev. C49 (1994) 2198.
21. C. M. Ko and M. Asakawa, Nucl. Phys. A566 (1993) 447c.
22. S. Gupta, Nucl. Phys. A566 (1994) 69c.
23. M. Asakawa and C. M. Ko, Nucl. Phys. A572 (1994) 732.
24. U. Heinz and K. S. Lee, Nucl. Phys. A544 (1992) 503c.
25. PHENIX Conceptual Design Report Update, BNL 1994 (unpublished).
26. T. Åkesson *et al.*, Nucl. Phys. B203 (1982) 27.
27. T. Matsui and H. Satz, Phys. Lett. B178 (1986) 416.
28. M. C. Abreu *et al.*, Z. Phys. C38 (1988) 117.
    M. C. Abreu *et al.*, Nucl. Phys. A544 (1992) 209c.
29. M. C. Abreu *et al.*, Nucl. Phys. A566 (1994) 77c.
30. N. S. Craigie, Phys. Rep. 47 (1978) 1.
31. V. Barger and A. D. Martin, Phys. Rev. D31 (1985) 1051.
32. M. J. Leitch *et al.*, Nucl. Phys. A544 (1992) 197c.

33. C. Kourkoumelis *et al.*, Phys. Lett. 91B (1980) 481.
34. C. Ajbajar *et al.*, Phys. Lett. B200 (1988) 380.
C. Ajbajar *et al.*, Phys. Lett. B256 (1991) 112.
35. F. Abe *et al.*, Phys. Rev. Lett. 69 (1992) 3704.
36. F. Karsch, Proceedings of the International Workshop on Quark Gluon Plasma Signatures, Strasbourg, France (1990).
37. E. W. N. Glover, F. Halzen, and A. D. Martin, Phys. Lett. B185 (1987) 441.
38. A. Shor, Phys. Lett. B215 (1988) 375.
A. Shor, Phys. Lett. B233 (1989) 231.
39. B. Müller and X. N. Wang, Phys. Rev. Lett. 68 (1992) 2437.
40. Z. Lin and M. Gyulassy, NUCL-TH-9409007.
41. R. Vogt, B. V. Jacak, P. L. McGaughey, and P. V. Ruuskanen, Phys. Rev. D49 (1994) 3345.
42. M. Aguilar-Benitez *et al.*, Phys. Lett. B189 (1987) 476.
43. R. Ammar *et al.*, Phys. Rev. Lett. 61 (1988) 2185.
44. M. J. Leitch *et al.*, Phys. Rev. Lett. 72 (1994) 2542.
45. C. S. Mishra *et al.*, Phys. Rev. D50 (1994) R9.
46. K. Kodama *et al.*, Phys. Lett. B263 (1991) 573.
47. B. L. Combridge, Nucl. Phys. B151 (1979) 429.
48. M. L. Mangano, P. Nason, and G. Ridolfi, Nucl. Phys. B405 (1993) 507.
49. R. V. Gavai *et al.*, HEP-PH-9411438.
50. I. Sarcevic and P. Valerio, HEP-PH-9411317.
51. I. Sarcevic and P. Valerio, AZPH-TH/94-13.
52. C. Albajar *et al.*, Nucl. Phys. B335 (1990) 261.
53. H. Baer, F. E. Paige, S. D. Protopopescu, and X. Tata FSU-HEP-930329
54. F. W. Büsser *et al.*, Phys. Lett. 53B (1974) 212.
F. W. Büsser *et a.*, Nucl. Phys. B113 (1976) 189.
55. W. M. Geist, Nucl. Phys. A525 (1991) 149c.
56. K. J. Eskola and X. N. Wang, Phys. Rev. D49 (1994) 4533.
57. J. Kapusta, L. McLerran, and D. K. Srivastava, Phys. Lett. B283 (1992) 145.
58. P. V. Ruuskanen, Nucl. Phys. A544 (1992) 169c.
59. K. Geiger and J. Kapusta, Phys. Rev. Lett. 70 (1993) 1920.

Photon Physics with PHENIX

Sebastian White [a*]

[a]Brookhaven National Laboratory,
Upton, N.Y. 11973

In this Paper I discuss briefly the physics motivation for extending measurements of particle production with high granularity and particle id capabilities to neutrals in PHENIX. I then discuss the technique of direct photon measurement in the presence of copious background photons from π^o decays. We will measure relatively low p_t photons near y=0 in the lab frame. This new experimental environment of high multiplicity and low γ momenta will affect both the techniques used and the type of analysis which can be performed. The Phenix Electromagnetic calorimeter is described and its capabilities illustrated with results from simulation and beam tests of the first production array.

1. Introduction

Our primary motivation is that the photon spectrum from heavy ion collisions is a record of the temperature history of the collision. This record even extends back to the earliest instants when collision energy is transferred to the constituents of the nucleus. As the collision evolves and its temperature changes, photons are emitted according to the Stefan-Boltzman law. This implies a very strong temperature dependence of photon production:

$$dN_\gamma(\tau) \propto T^3, < E_\gamma > \propto T. \tag{1}$$

So thermal photons tend to originate early in the collision in contrast to observed hadrons whose mean free path is too short to escape from the early phase. The situation can be contrasted with photons from cosmic background radiation. In Heavy Ion collisions the photon mean free path is much greater than the source size so photons from all stages are visible. The cosmic photon background takes us only back to the era when atoms were formed and the mean free path suddenly increased.

1.1. The shape of the direct photon spectrum

The spectrum of photons from heavy ion collisions has been calculated by a number of authors as an integral over time,τ , of eqn. 1 taking into account the equations governing isoentropic expansion.

$$T_f^3 \times \tau_f = \frac{\kappa}{a_1} \times \frac{dN^\pi}{dy} = T_i^3 \times \tau_i \tag{2}$$

*This research supported in part by the U.S.Department of Energy under Contract No. DE-AC02-76CH00016.

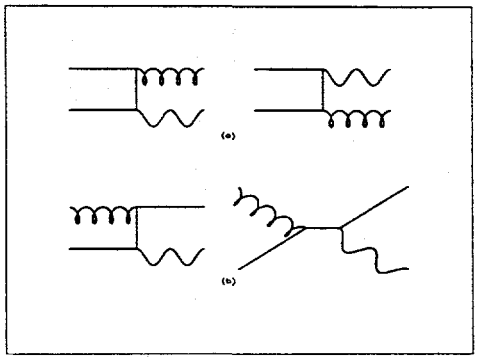

Figure 1. Annihilation and Compton which lead to direct γ production.

where κ is a constant, $\frac{dN^\pi}{dy}$-the observed pion multiplicity is related to the final entropy density and a_1 is larger([2]) by about a factor of eight for a quark gluon phase than in the hadron gas phase.

Contributions from both hadron gas phase and a quark gluon plasma phase have been calculated. In the latter case annihilation and Compton diagrams depicted in Figure 1 dominate. The final spectrum depends on

- the initial time,τ_i, at which thermal conditions are reached,
- whether a quark-gluon phase is formed and
- the existence of a long lived mixed phase.

Srivastava[2] argues that, if a large direct photon signal has been observed in the WA80 experiment at CERN, then the quark gluon phase must be absent in SPS collisions. This conclusion follows from eqn. 2 when we hold τ_i fixed at, say, 1 fm/c. The hadron phase, which has less degrees of freedom would reach T_i= 408MeV/c whereas if the system evolved from a quark gluon phase the same equations of isoentropic expansion yield T_i=203.4 MeV/c. On the other hand, it has been pointed out by Shuryak[1] that early thermalization in the so-called "hot glue scenario" would also raise the initial temperature.

At the highest photon transverse momenta (ie $p_t \geq 2$ GeV/c) the dominant source of photons will be from pre-equilibrium collisions. Hard photon production has been studied in $pp(\bar{p})$[5] and p-Nucleus collisions. In this case the diagrams are again those of Figure 1, however the initial state is determined by structure functions of the incident hadrons rather than temperature.

Finally the π^o and η^o mesons, because of their dominant electromagnetic decay modes (to $\gamma\gamma$) will result in copious photon production. While this provides an opportunity to measure the π^o production spectrum - it also becomes a serious background to the more interesting sources described above.

2. Extracting the direct photon signal

There are 2 basic techniques that can be used to extract the direct photon signal in the presence of meson decay photons, applicable under different conditions.

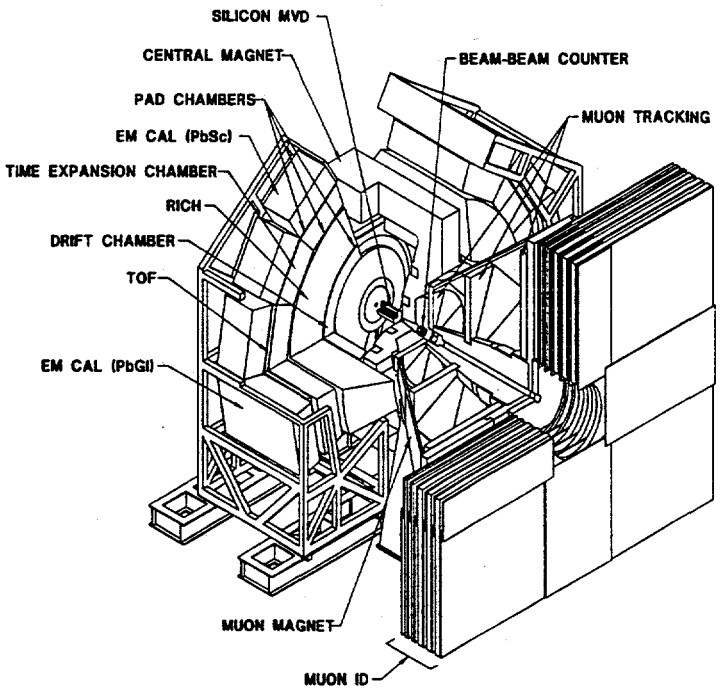

Figure 2. PHENIX detector showing a cutaway through the East Arm which contains both Pb/Glass and Pb/Scintillator Emcal octants.

2.1. high p_t, low multiplicity

To study high p_t photons in relatively low multiplicity collisions, the fraction of 'isolated' photons as a function of p_t is measured with the electromagnetic calorimeter. A nearby electromagnetic shower is assumed to be the associated π^o decay γ, even if it is partially merged with the photon candidate. The most probable decay configuration in isotropic π^o decay results in equal energy γ's and the minimum opening angle in the lab frame:

$$\theta_\gamma^{min} = 2 \times \frac{m_\pi}{p_\pi} \tag{3}$$

The angle should be small compared to the mean angle between particles in the event- a condition not satisfied in heavy ion collisions of interest at RHIC. (This technique would be used for the "RHIC Spin" program and low multiplicity ion collisions.)

The WA80 group[6] has studied the efficiency to recognize two nearby showers and finds $\epsilon \geq 50\%$ once θ_γ corresponds to at least one calorimeter cell spacing. This could give rise to a natural limit of $p_t \leq 20 - 30 GeV/c$ as we'll see below. On the other hand some groups (see eg. [7]) have also used a statistical technique to measure $\frac{\gamma}{\pi^o}$ recognizing that two nearby γ's have a larger conversion probability in material in front of the calorimeter. In this way, the direct γ measurement could be extended to arbitrarily high p_t.

2.2. low p_t, high multiplicity

To see that this is our case, consider the expected hit multiplicity for central Au-Au collisions in the Phenix central detector, which covers $|d\eta| \leq 0.35$ and 50% of 2π in

azimuth:

$$\frac{dN^{\pm,\gamma}}{d\eta} \times d\eta \times \frac{d\phi}{2\pi} \simeq 1,500. \times 0.7 \times 0.5 = 525 \quad (4)$$

The mean angular separation between hits can be derived from this and is greater than θ_γ^{min} only when $p_{\pi^o}^t \geq 2GeV/c$. Since thermal direct photons are likely only to be measurable for $p_t \leq 2GeV/c$, the meson can't be measured with isolation cuts but instead is extracted from the 2γ mass spectrum.

To achieve a reasonable occupancy, the calorimeter is segmented into 25,000 cells. Since the Moliere radius of the calorimeter is $R_M = 3.4$cms, the calorimeter is placed at a distance of 5m from the beam and covers $64m^2$.

Fits will be made to the level of the π^o mass peak out of all randomly chosen 2γ combinations. After subtracting the smooth combinatorial background under the π^o peak, correcting for photon reconstruction efficiency, acceptance,etc., the π^o decay γ spectrum will be calculated and subtracted from the total inclusive γ spectrum.

How well can this daughter γ spectrum be determined? This obviously bounds the thermal direct photon spectrum which can be measured in our experiment. The dominant systematic errors arise from:

1. photon reconstruction efficiency

2. extraction of the meson decay mass peaks

Previous attempts- notably WA80- have concluded that $\delta(\frac{\gamma}{\pi^o}) \sim 0.05$ is reachable [9].

Another p_t dependent limit to this uncertainty is the ratio of the fit to $\frac{peak}{total}$ in the 2γ mass plot. We consider that a meaningful measurement can't be made unless this ratio is larger than a few percent. Since both energy(and hence mass) resolution and photon multiplicity decrease with p_t, there will be a minimum measurable p_t bin -estimated to be 1.0 GeV/c with the PHENIX baseline detector.

2.3. Experimental consequences

We have seen that one of the main limitations resulting from the environment at $y_{lab} = 0$ in Heavy Ion Collisions is that spectroscopy with π^o decay photons is often overwhelmed by combinatorial background. Typically the $(\pi^o \rightarrow \gamma\gamma)$ peak signal-to-noise will be less than 1:1. This dilution of π^o's will make it difficult to do π^o spectroscopy. Similarly, searches for fluctuations in rapidity space of the fraction of π^o relative to $\pi^{\pm}$(ie for disoriented chiral condensates [10]) must take into account the smearing of the π^o momentum vector in the decay to photons which are actually measured.

Typically, a source (such as the DCC 'bubble') decaying isotropically will appear as a cluster of secondaries with $\sigma_\eta \sim 0.7$ recognizable as an enhancement in $\frac{dN^{\pi^o}}{dydp_t}$ above the underlying event. Because of π^o decay kinematics, this fluctuation would be smeared by an additional $10 - 20\%$ in rapidity, resulting in a small dilution of the signal.

3. The Phenix Detector

A cutaway view of the PHENIX detector is shown in Figure 2, with the 2 Pb/Glass calorimeter sectors in the foreground. Taken together with the remaining 6 sectors of

Pb/Scintillator sampling calorimeters, these EM calorimeter sectors have the same coverage as the PHENIX central magnetic spectrometer($\delta\eta = 0.7$ and $\delta\phi = 50\% \times 2\pi$). The inner detectors (silicon MVD) provide full charged particle tracking over $|\eta| \leq 2.5$, without magnetic analysis. The properties of the EM calorimeter relevant to the photon measurement are summarized in table 1.

The Pb/Glass calorimeter is currently being used in the WA98 experiement at CERN and will be installed in PHENIX during the first half of 1998. We expect that, because of the experience gained with this calorimeter in a fixed target environment, we will be ready to make measurements early on in PHENIX. The main difference between PHENIX and WA98 (fixed target) environments is that the lab momentum of low p_t photons is not boosted in the collider experiment. Thus measurements will be extended to lower energy for PHENIX.

Table 1
Characteristics of the baseline EMcal sectors and of the proposed BaF_2 array.

	PbSc	**PbGl**	**BaF_2**
η cov.	$\Delta\eta = 0.7$	$\Delta\eta = 0.7$	$\Delta\eta = 0.1$
ϕ cov.	$90° + 45°$	$45°$	$90°$
Mod. (cm^2)	5.5×5.5	4.0×4.0	3.5×3.5
$\delta\phi, \eta$/mod	0.011	.008	.007
$\sigma_E/\sqrt{E(GeV)}$	$.078/\sqrt{E} \oplus .015$	$.058/\sqrt{E} \oplus .01$	$.019/\sqrt{E} \oplus .008$
σ_x (mm)	$10./\sqrt{E}$	$5./\sqrt{E} \oplus 1.0$	$4.7/\sqrt{E} \oplus 0.5$
MIP peak(MeV)	227	480	220
σ_t (ps)	$70 \oplus 70/\sqrt{E}$	$75 \oplus 143/\sqrt{E}$	80 ps
γ/π w. Δt	700 MeV/c	580 MeV/c	750 MeV/c

The remaining area is covered by a Pb/Scintillator calorimeter with 'shish-kebab' type waveshifter fiber readout geometry. The PHENIX EM calorimeter group recently completed the R & D phase in the development of this calorimeter[11] and in January 1995, the first production array of 144 channels arrived at BNL.

Figure 3 some odf the first π^o data recorded with this new detector. This online mass distribution from the current test run confirms the cosmic ray calibration of the calorimeter. The fitted π^0 mass peak without offline corrections is within 2 MeV of the databook value.

From Table I it can be seen that development of the Pb/Scintillator calorimeter emphasized low energy capabilities appropriate to the RHIC environment. In particular:

- good energy resolution at low energies due to fine sampling and high light yield
- $\sim$ 100 psec time resolution which can be used to discriminate between γ and hadron hits to $p_t \sim 700 MeV/c$

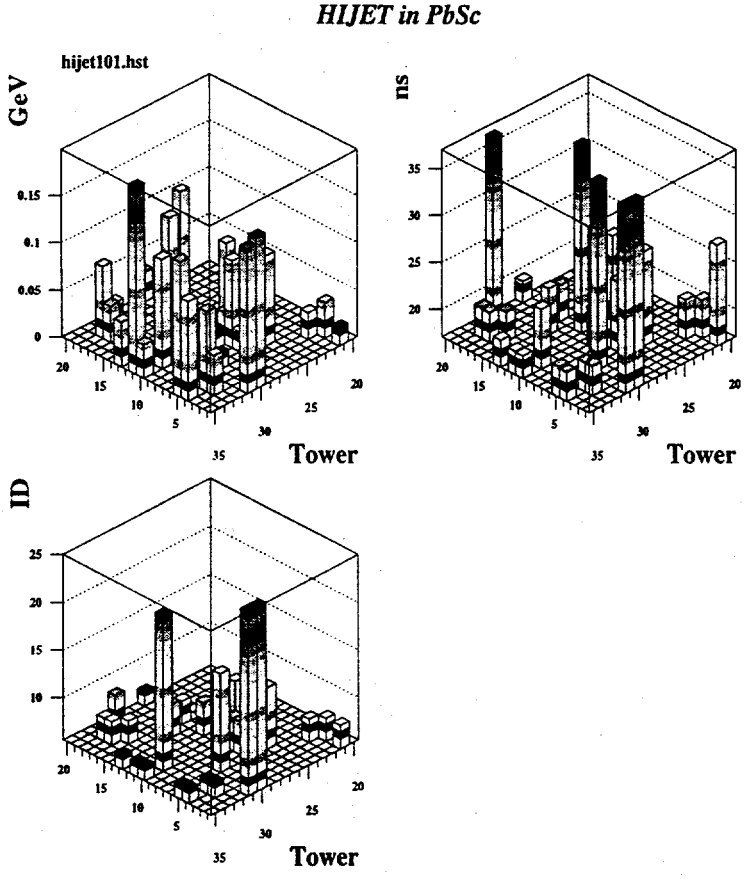

Figure 3. Three views of a typical HIJET event as seen by the calorimeter which illustrate the particle id capabilities of the Pb/scintillator calorimeter.

- a low response to minimum ionizing particles which suppresses the signal from misidentified charged hadrons.

In most respects, the same physics measurements can be carried out with both calorimeter subsystems. This will provide a useful cross-check on the direct γ signal since the two systems differ in granularity, energy resolution and particle i.d. capabilities. As part of its long term plan, PHENIX has proposed to replace subunits of each Pb/scintillator sector with high resolution BaF2 arrays [8]. This would provide the ultimate electromagnetic energy resolution and hence signal-to-noise ratio for extracting the π^o decay background contribution to the γ spectrum. Typically the same signal-to-noise as in the baseline detector will be achieved at 0.5 GeV/c lower in p_t. The scale of the array summarized in Table I will allow us to measure the η^o spectrum down to at least 1.4 GeV/c. Even with a small fraction of this coverage, we could measure the inclusive γ spectrum thereby elimination essentially all contributions of resolution smearing.

The actual installation of the BaF2 array is completely determined by funding. It is expected that at least a fraction of the full array will be installed on Day-1.

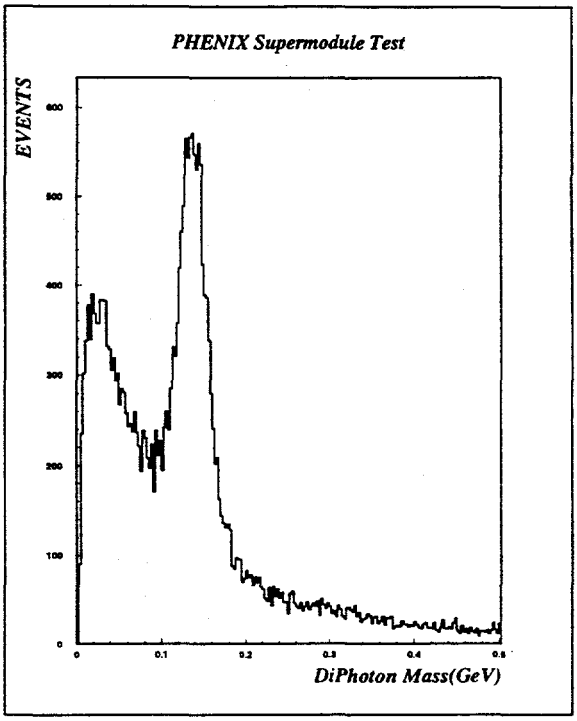

Figure 4. Mass distribution of two photon events measured with the first production Supermodule in the 1995 test beam run at the AGS. A 7 GeV π^- beam was incident on a lucite target and the event trigger was chosen to enhance charge exchange reactions.

4. Particle Identification

The particle i.d. capability of the Pb/Scintillator array and its usefulness for the direct photon anlysis are illustrated in Figure 3. This figure shows three views of calorimeter cell hits from the same HIJET event. The view labelled with the parent type (ID) shows the primary produced particle's i.d. from the Monte Carlo generator. This index is lowest for π^o's and is highest for the $\bar{n}$ in this event. The other 2 views are the ones observed in PHENIX- energy deposition and time of arrival. In this event the four γ clusters from π^o decay (foreground in display) are readily identified by their early time of arrival which is about 17 nsec at the calorimeter wall (r=5.1 m).

The case of the $\bar{n}$ is an interesting one. The expected level of production ($\frac{\bar{n}}{\pi^o} \simeq 0.05$) will lead to an apparent $\frac{\gamma}{\pi^o}$ signal above 0.5 at p_t=1 GeV/c, because of the larger energy deposit of stopping $\bar{n}$'s. This background is reduced to a negligible level [8] with a time cut of $(t - t_{predicted}) \leq 1.5nsec$. Incidentally, this easily identified background could be used to extend the measurement of antibaryon production to lower momenta than is possible with $\bar{p}$'s.

REFERENCES

1. E.Shuryak and L.Xiong, Phys.Rev.Lett.70(1993) 2241.
2. D.K.Srivastava and B.Sinha, Phys.Rev.Lett.73(1994) 2421.

3. J.D.Bjorken Phys. Rev.D 27 (1983) 140.
4. J.Kapusta, P.Lichard and D.Siebert Phys.Rev. D 44(1991) 2774.
5. F.Abe et al., Phys. Rev. D 48 (1993) 2998.
6. F.Berger et al., Nucl. Instr. and Meth. A321 (1992) 152.
7. A.L.S. Angelis et al., Phys. Lett. 94B (1980) 106.
8. "A High Resolution Photon Detector for PHENIX at RHIC", Phenix note no.79 (1993).
9. T. Awes, these proceedings.
10. see discussion by S. Gavin of Disoriented Chiral Condensates, these procedings.
11. G.David et al. IEEE Trans.Nucl.Sci. (1994), E. Kistenev et al., Proceedings of the Vth International Conference Calorimetry in High Energy Physics, Brookhaven National Lab. (1994) and S. White, 6th Pisa Mtg.on Advanced Detectors, Nucl.Instr.Meth. A 360 (1995).

A photon spectrometer PHOS for the ALICE experiment at the LHC.

V. Manko for the ALICE Collaboration

1 Physics motivation

Electromagnetic probes are a unique tool to study the early and hot phases of nuclear collisions, because the produced photons (as well as lepton pairs) escape from the finite system without re-enteraction. Prompt photons is one among very few signals which can provide direct information on these, partonic phases. [1, 2, 3, 4]

The thermal radiation from the quark-gluon plasma (QGP) and mixed phase could be observable in the medium p_t range (around 1—3 GeV/c). Direct photons from the pre-equilibrium phase (3—6 GeV/c) contain information on the parton dynamics at very early stages, about equilibration times, and about the transition from perturbative to non-perturbative phenomena. At still higher momenta, direct photons originate mainly from initial hard processes and can be used to extract structure functions in nuclei.

Therefore, the measurement of prompt photons is a prime physical goal of heavy ion experimentation. The measurement with the PHOS spectrometer will be concentrated on physics at mid-rapidity, i.e. on the regions of minimum barion and maximum energy density. Thus, the PHOS spectrometer will be situated at 90°.

Indeed, the prompt photons will be superimposed on the large background arising from hadronic decays. It in turn is dominated by π^0 and η mesons decays. Hence, a photon spectrometer has to ensure the measurement of the rates and p_t spectra of photons, π^0 and η mesons.

Prompt photons are only a small fraction of the hadron decay background. The predicted signal of thermal photons is of the order of a few to a few tens per cent of the total inclusive photon yield, depending on initial conditions and the shape of the meson p_t spectra. It is mandatory to measure photon and neutral meson yields and spectra with a high accuracy in order the sensitivity to the prompt photon component to be high. We aim at a sensitivity, limited by the systematic errors, of $\approx$5% for the measurement of prompt photons in tne energy range of 1—10 GeV.

2 Requirements and general design considerations

General concepts of the proposed ALICE experiment can be found in [5].

Transverse view of the ALICE detector is shown in Fig.1

The PHOS spectrometer is to measure all photons at mid-rapidity with the rapidity coverage of about one unit. Thus, the PHOS spectrometer will be centered at $y = 0$, covering the rapidity range of $-0.5 \leq y \leq 0.5$.

The measurement has to be done over a solid angle large enough so that both π^0's and η's can be reconstructed (from 2γ decays) and their cross-sections determined with high precision above some minimal p_t, which is different for π^0 and η.

The minimal value of p_t depends on the size as well as the geometrical configuration of the detector. For rectangular detector shape, at the same area, it will be different for different length to width ratios. For the PHOS spectrometer, with the total area of 25 m^2, this ratio is chosen to be two to one. The π^0 and η acceptances are shown for this configuration in Fig.2. The minimal p_t is $\sim 1GeV/c$ and $\sim 2GeV/c$ for π^0 and η respectively.

The π^0 and η yields will be extracted from a $\gamma\gamma$ invariant mass spectrum. The neutral meson signals will sit on a huge combinatorial background, since the measurement is to be done in a very high multiplicity environment, the predicted charged particle densities at mid-rapidity ranging between :

$dN_{ch}/dy \approx 2000$ to ≈ 6000 and in extreme cases up to 8000 [6, 7].

The signal to background ratio is directly proportional to the mass resolution σ_M, and, therefore, at the same signal statistics, the higher is the mass resolution, the lower are the systematic errors of the extracted meson yields and spectra.

The mass resolution is given by the following expression:

$$\frac{\sigma_M}{M} = \frac{1}{2}\left[\frac{\sigma_{E_1}}{E_1} \oplus \frac{\sigma_{E_2}}{E_2} \oplus \frac{\sigma_\theta}{\tan\theta/2}\right],$$

where $\oplus$ denotes a quadratic sum.

It has terms that depend on the resolution in energy (E_1, E_2) and the two photon angular separation (θ), the latter translates into the position resolution.

Thus, the energy and position resolution has to be as high as possible.

The energy resolution is usually parametrised as:

$$\frac{\sigma_E}{E} = \left[\frac{a}{\sqrt{E}} \oplus \frac{b}{E} \oplus c\right]$$

Here, a is the stochastic term, b is determined by the readout noise, and c is determined by the detector inhomogeneity and calibration error. In order to achieve a good energy resolution all three terms have to be kept small and should be of the same order at the relevant photon energy ($E \sim 3GeV$).

The position resolution is improving with increasing granularity of the detector, and the optimum cell size is of the order of one Molière radius R_M.

Little shower overlap is mandatory in order to ensure reliable reconstruction of photons and mesons. Based on the experience of the WA80 experiment at CERN, this requires a pixel occupancy not exceeding $\sim$ 3% (there should be no more than one photon or hadron every 33 cells). At this occupancy, the photon reconstruction efficiency should be measurable to an accuracy of $\approx$4%.

For the ALICE geometry this requires small Molière radius (and, therefore, high granularity), because of the following limitation, which can be readily derived:

$$R_M \leq D\sqrt{\frac{2\pi \times occupancy}{dN/d\eta}},$$

where D is a distance from the interaction point.

For the PHOS spectrometer $D \approx 6m$, and then, assuming $dN/d\eta = 16000$, one obtains:

$R_M \leq 2cm$

Chosen the cell size of this order, the PHOS spectrometer, at the total area of 25 m^3, will consist of $\sim$50000 modules.

The large size of the spectrometer, which will be made of such a large number of individual modules, requires the cost of the individual module being reasonable.

Having in mind all the above requirements on the detector material, a newcomer among the scintillating heavy crystals is chosen as the most promising candidate: lead tungstate ($PbWO_4$), having Molière radius of 2.0 cm.

The next requirement concerns the photoreadout system. All the detector systems of the ALICE experiment are to be operated inside a magnetic field $\approx 0.2T$. This requires a readout which is able to operate in such a field. The PIN-photodiode with amplifier is being considered as the best candidate readout photodetector.

The photon identification and hadron rejection are further crucial parameters of interest. Recently it was demonstrated [8], that by using longitudinally segmented detectors the performance for particle identification and two showers separation can be essentially improved.

Thus, two options of the individual module design are under consideration:

- A module of single lead tungstate crystal of the length of 20 cm.
- A longitudinally segmented module of two crystals: $\sim$7 cm and $\sim$13 cm of the same total length.

The light yield of lead tungstate scintillator is strongly dependent on the temperature, the temperature coefficient being $\sim$-2% per °C at 20°C. Thus, a temperature stabilisation and monitoring system is required for keeping the energy resolution good.

On the other hand, one even may try to make use of the light yield temperature dependence for improving the energy resolution by cooling down the spectrometer. The effect of cooling will be twofold: the light yield will increase, and, at the same

time, the signal to noise ratio will increase. Both should lead to improved energy resolution. This possibility is also under study now.

In summary:

- The PHOS spectrometer is centered at $y = 0$, covering the rapidity range of $-0.5 \leq y \leq 0.5$
- It measures photons in the p_t range of $1GeV/c \leq p_t \leq 10GeV/c$, π^0's and η's in the p_t ranges of $1GeV/c \leq p_t \leq 10GeV/c$ and $2GeV/c \leq p_t \leq 10GeV/c$ respectively.
- The spectrometer has rectangular shape with the length to width ratio of 2/1 and the total area of 25 m^2.
- It has to be of high granularity, consisting of ~50000 individual modules made of material of Molière radius of ~2cm.
- The energy energy and position resolution has to be good, as well as ability to separate photons and hadrons.
- Lead tungstate crystal is being considered as the most promising candidate for the detector.
- A longitudinally segmented module is under consideration for improving particle identification and two showers separation.
- The possibility of cooling the spectrometer is under study for improving the energy resolution.

3 Properties of the lead tungstate crystals

Lead tungstate has been known for a long time [9]. Possibility of using this crystal for electromagnetic calorimetry has been studied in the recent years [10, 11, 12, 13].

Its physical and chemical properties are given below:

• Density	8.28 g/cm^3
• Radiation length	0.89 cm
• Molière radius	2.0 cm
• Melting point	1123°C
• Hardness	4 Moh
• Refractive index along Z axis ($\lambda = 632nm$)	2.16

- Hygroscopicity — none
- Chemical activity — inert

Lead tungstate is a scintillating crystal. Considerable variation of its optical properties are induced by even small changes of the technology of crystal growing.

At room temperature, it has the light yield of ~5% of that of BGO crystal (at room temperature, the light yield is 50-80 photons/MeV for ~20 cm long crystal).

The decay time constant has a mean value of about 10 ns at room temperature.

The emission spectrum is rather complex with two broad bands at 440 nm and 530 nm.

The light yield is strongly dependent on the temperature. The temperature coefficient is ~-2% per °C at 20°C.

Lead tungstate ($PbWO_4$) is grown from a 50%-50% mixture of lead oxide (PbO) and tungsten oxide (WO_3). The crystals are grown by the Czochralski technique in a platinum crucible. The total time necessary to produce a ~20 cm long ingot is ~130 hours.

The growth technology and the equipment for large scale and cost effective production still have to be optimised.

4 Physics performance

Prompt photon production will be determined on a statistical basis for different centrality classes. The analysis reconstructs the p_t distributions for π^0 and η, then calculates the photon yield expected from the decay of these mesons alone. Additional minor contri' utions from other radiative decays, (e.g., ω and η') can be estimated assuming transverse mass scaling. The prompt photons is then found by subtracting the calculated photon yields from these sources from the measured spectrum. This method is free of cross-section normalization errors. However, there are sources of systematic errors, most importantly the precise knowledge of the photon and π^0 reconstruction efficiencies.

The π^0 and η signals must be extracted from the inclusive spectrum of the two photon invariant mass. In this spectrum the π^0 and η peaks sit on a combinatorial background due to the many possible photon pairs.

An example of simulated two photon invariant mass spectrum is shown in Fig.3. For the event simulation, SHAKER is used to generate particles with the desired multiplicity ($dN_{ch}/dy = 8000$). The η/π^0 ratio is taken to be 0.55 [14] for $p_t \geq 1GeV/c$ and m_t scaling is assumed. The energy resolution parameters $a = 0.03$, $b = 0.03$ and $c = 0.01$ are used in the simulation.

The signal-to-background ratio in such a plot decreases inversely with the phase-space density of photons. This problems worsens in heavy ion collisions relative to p+p or p+A collisions due to the much higher multiplicity of produced photons. The combinatorial background problem also becomes worse at low p_t both due to

the increased phase space-density of low energy photons, and to the fact that at low p_t the opening angle of the meson decay pairs is getting larger.

The simulated signal-to-total ratios for π^0 and η are plotted in Fig.4 vs p_t. For π^0, in the low p_t region around $p_t = 1GeV/c$ the simulations indicate that this ratio will only be about 1%. The η peak-to-total ratio will be below 0.1% in the p_t region around $p_t = 2GeV/c$. Fortunately, it is possible to obtain sufficient statistics such that the statistical uncertainty for the π^0 yield extraction will fall below 1% over the low p_t region of interest.

A greater concern is the estimation of the systematic error of the extracted yield when dealing with peak-to-total ratios of the order of a percent. Simulation results suggest that an event-mixing technique [15] can be applied to determined the form of the combinatorial background with little or no systematic error. An example of the simulation results is shown in Fig.5. This technique has been applied in an analysis of lead-glass detector photon data from CERN experiment WA80 [15] and appears to work well. An example of results of the WA80 experimental data analysis is shown in Fig.6. For this case the π^0 peak-to-total ratio is about 2%. This analysis method appears to work with values of the peak-to-total ratio as low as 0.2%, as indicateed by the observation of a weak η peak seen in Fig.6.

The extraction efficiency of the π^0 or η signal depends both on the signal statistics and the signal-to-total ratio. The simulation implies that it depends on the quantity:
$\sqrt{Signal \times Signal/Total}$,
as it is demonstrated in Fig.7.

One may conclude that this quantity should be greater than $\sim$10 in order the efficiency to be close to 100%.

The statistical error of the extracted π^0 or η signal depends on the same quantity and reads:

$$\frac{\sigma_S}{S} = \frac{1}{\sqrt{N_{ev}}} \times \frac{\sqrt{S+B}}{S},$$

where S and B stand for the signal and background multiplicities respectively, and N_{ev} stands for the total event number.

Based on this formula, one may estimate the event statistics, which is needed for achieving the required statistical accuracy of the signal. The needed event statistics for the 1% π^0- and 10% η- signal accuracy are plotted vs p_t in Fig.8.

For 10^7 events, one finds that the statistical error on the π^0 cross section will be less than 1% in the p_t range of $0.4GeV/c \leq p_t \leq 6GeV/c$, and the statistical error on the η cross-section will be less than 10% in the p_t range of $1.6GeV/c \leq p_t \leq 5GeV/c$.

References

[1] E.V.Shuryak, Phys. Lett. B78(1978)15.

[2] R.Hwa and K.Kajantie, Phys. Rev. D32(1985)1109.

[3] M.Kataja et al., Phys. Rev. D34(1986)2755.

[4] M. Neubert Zs. Phys.C 42(1989)231.

[5] ALICE Collaboration, Letter of Intent for A Large Ion Collider Experiment, CERN preprint CERN/LHCC/93-16(1993).

[6] Proc. of the Large Hadron Collider Workshop, Aachen, Germany, 1990, ECFA 90-133, CERN 90-10

[7] N.X. Wang et al., Phys. Rev. D44(1991)3521 and Phys. Rev. Lett.68(1992)1480.

[8] K.-H. Kampert et al., A High Resolution BGO Calorimeter with Longitudinal Segmentation, Münster University preprint IKP-MS-94/0301(1994)

[9] W.van Loo, Phys. Stat. Sol. 28(1975)227

[10] W.Moses and S.E.Derenzo, IEEE Trans. Nucl. Sci. NS-36(1989)173

[11] M.Kobayashi et al., Nucl. Instr. Methods A333(1993)429

[12] V.G.Baryshevsky et al., Nucl. Instr. Methods A322(1992)231

[13] P.Lecoq et al., Lead tungstate scintillators for LHC e.m. calorimetry, CMS TN/94-308(1994)

[14] M.Bourquin and J.M.Gaillard, Nucl. Phys., B114(1976)334.

[15] A. Lebedev et al., Nucl. Phys. A566(1994)355c

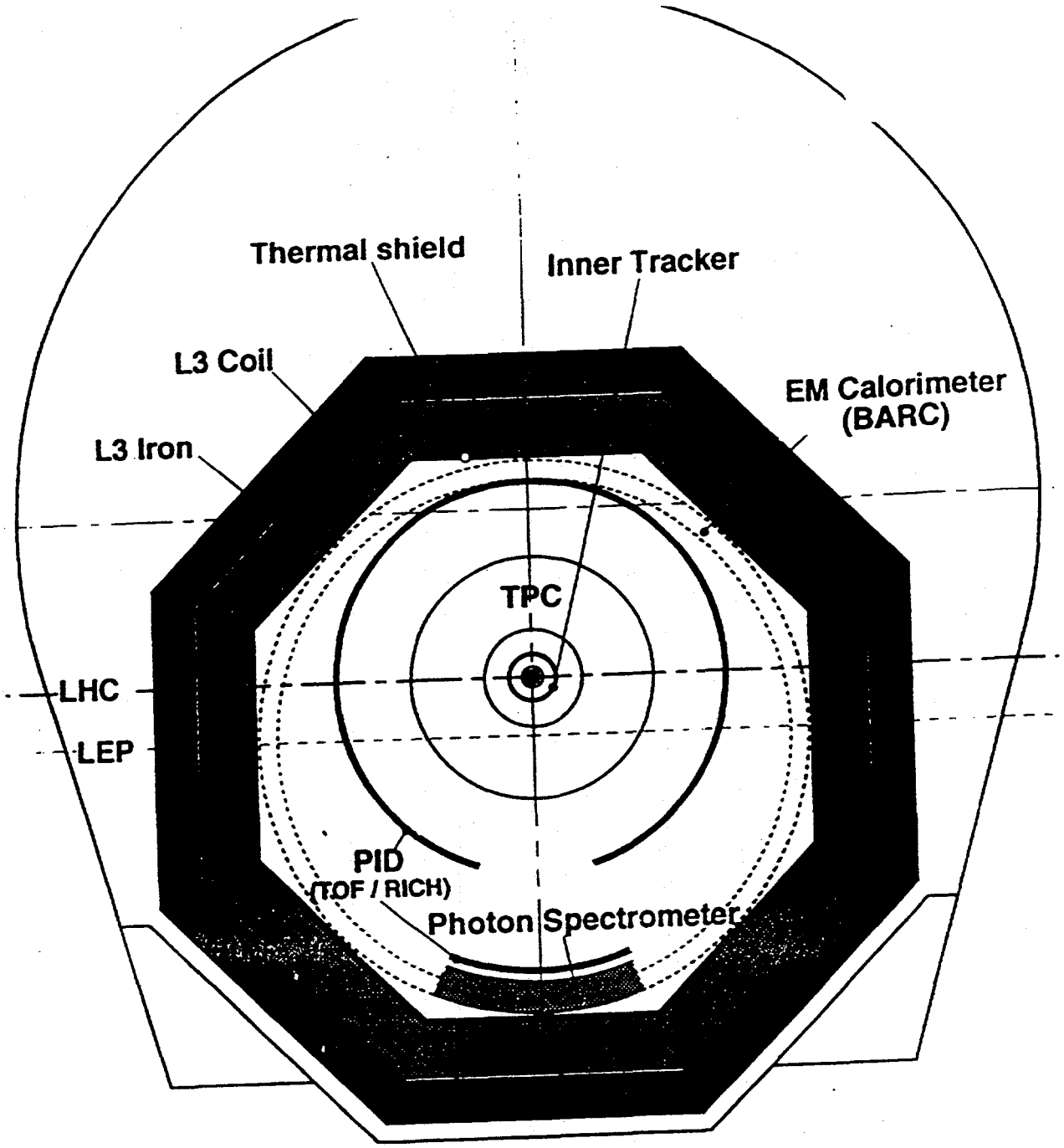

Fig.1 Transverse view of the ALICE detector.

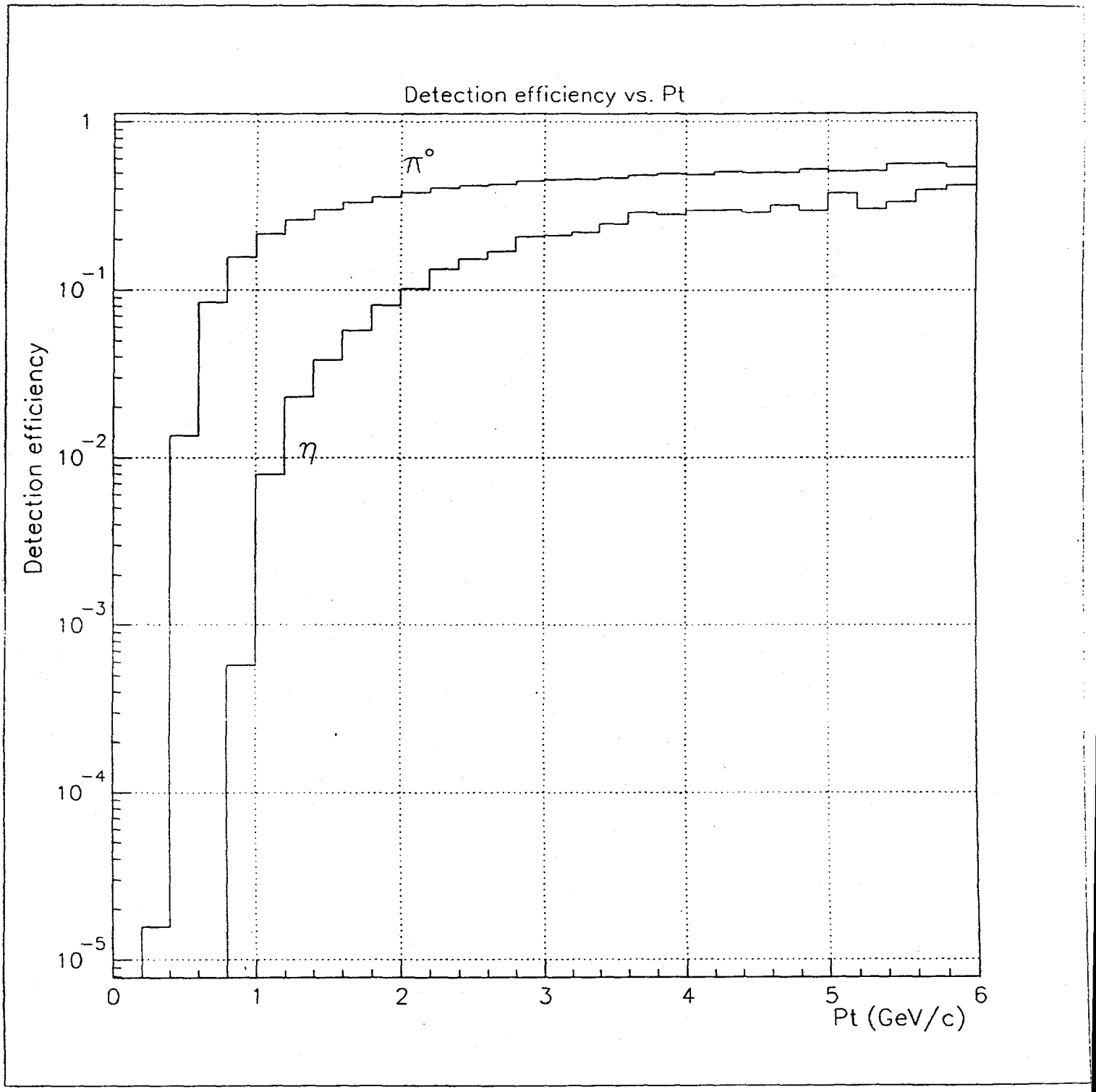

Fig.2 The π^0 and η geometrical acceptance vs p_t.
($L/W = 2$, the total area 25 m^2).

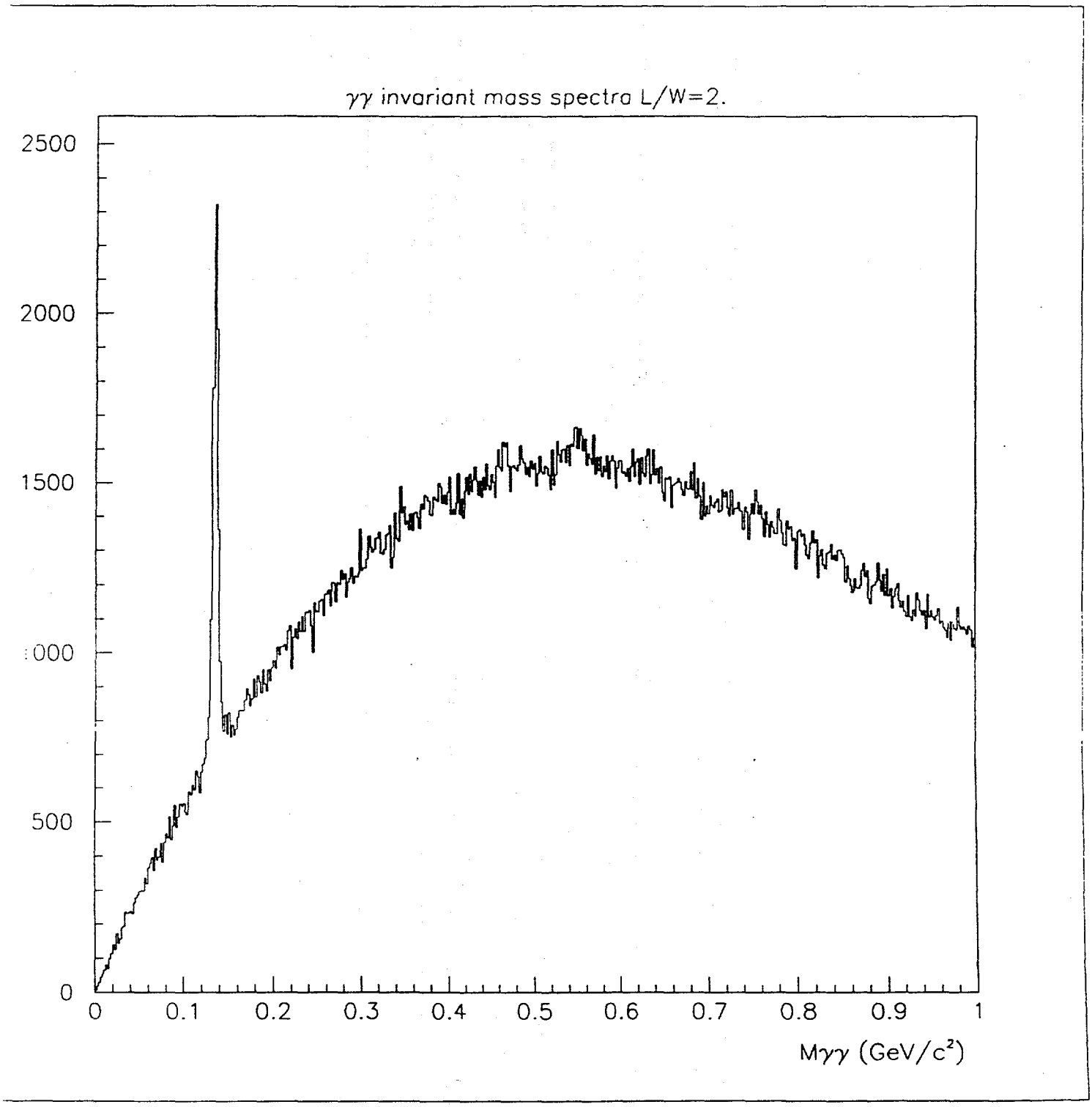

Fig.3 An example of simulated two photon invariant mass spectrum.

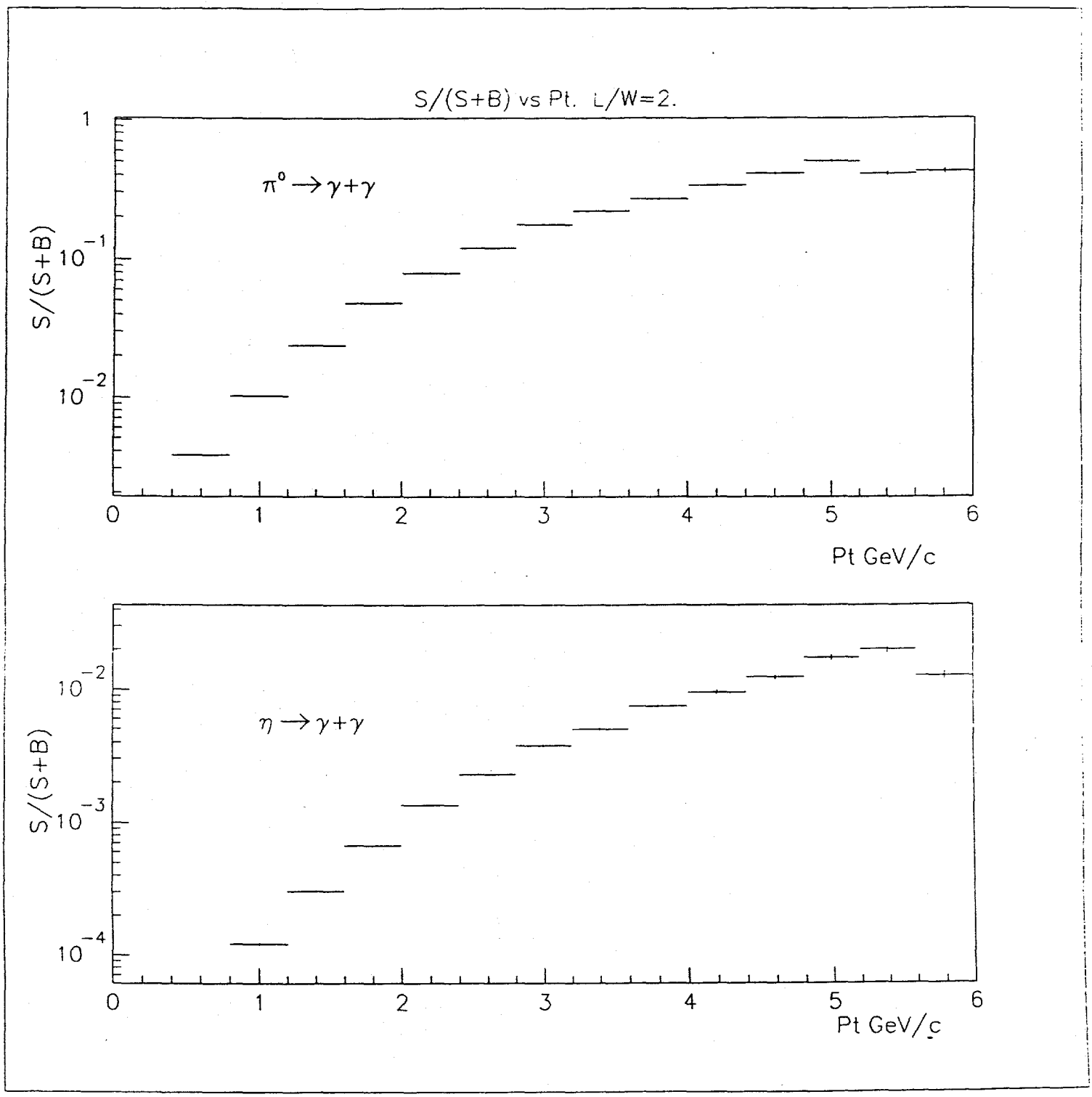

Fig.4 The signal-to-total ratios for π^0 and η vs p_t (simulation).

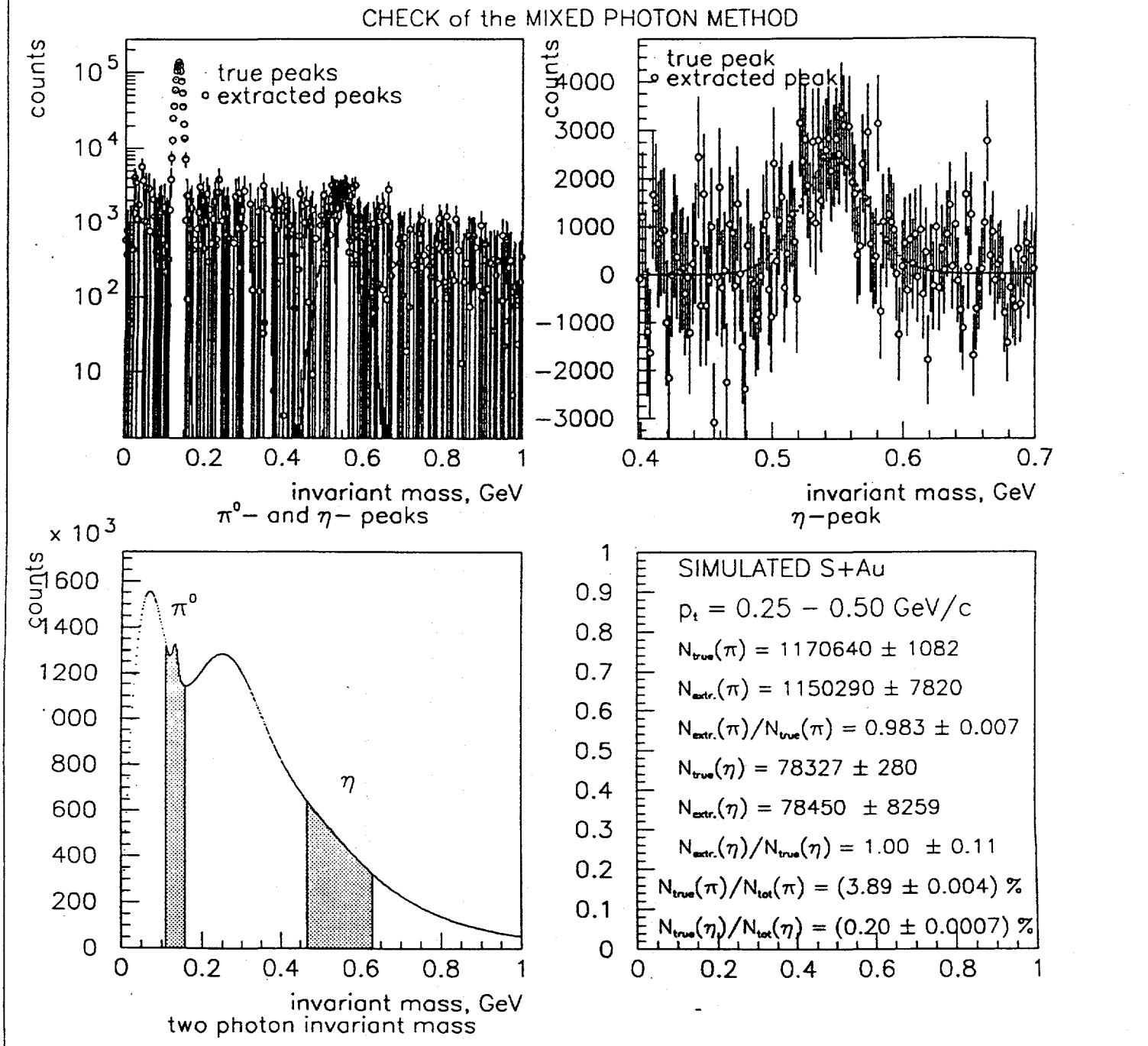

Fig.5 An example of extraction of the π^0 and η peaks from two photon invariant mass spectrum by the event-mixing technique (simulation).

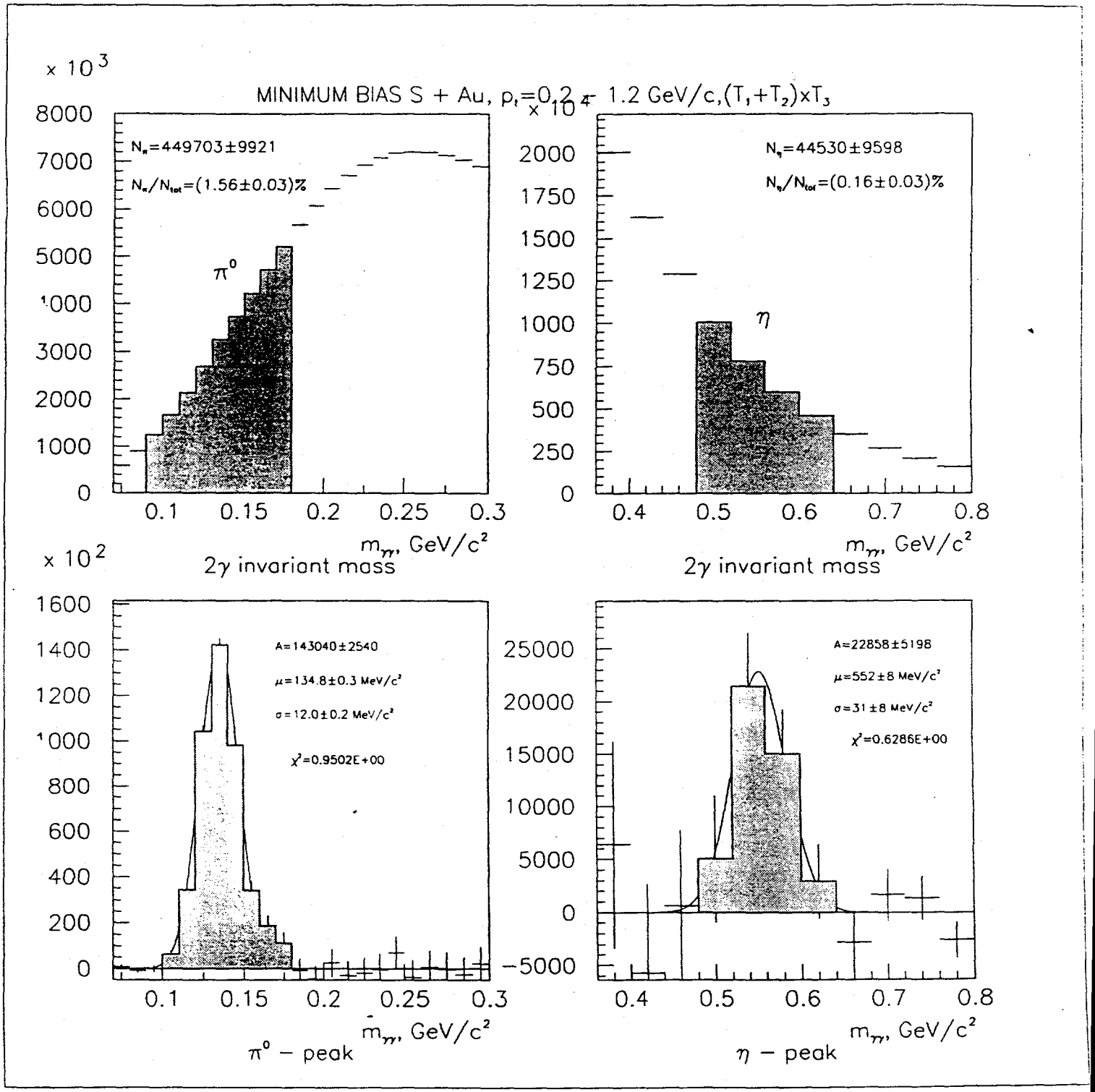

Fig.6 An example of extraction of the π^0 and η peaks from two photon invariant mass spectrum by the event-mixing technique (WA80 data).

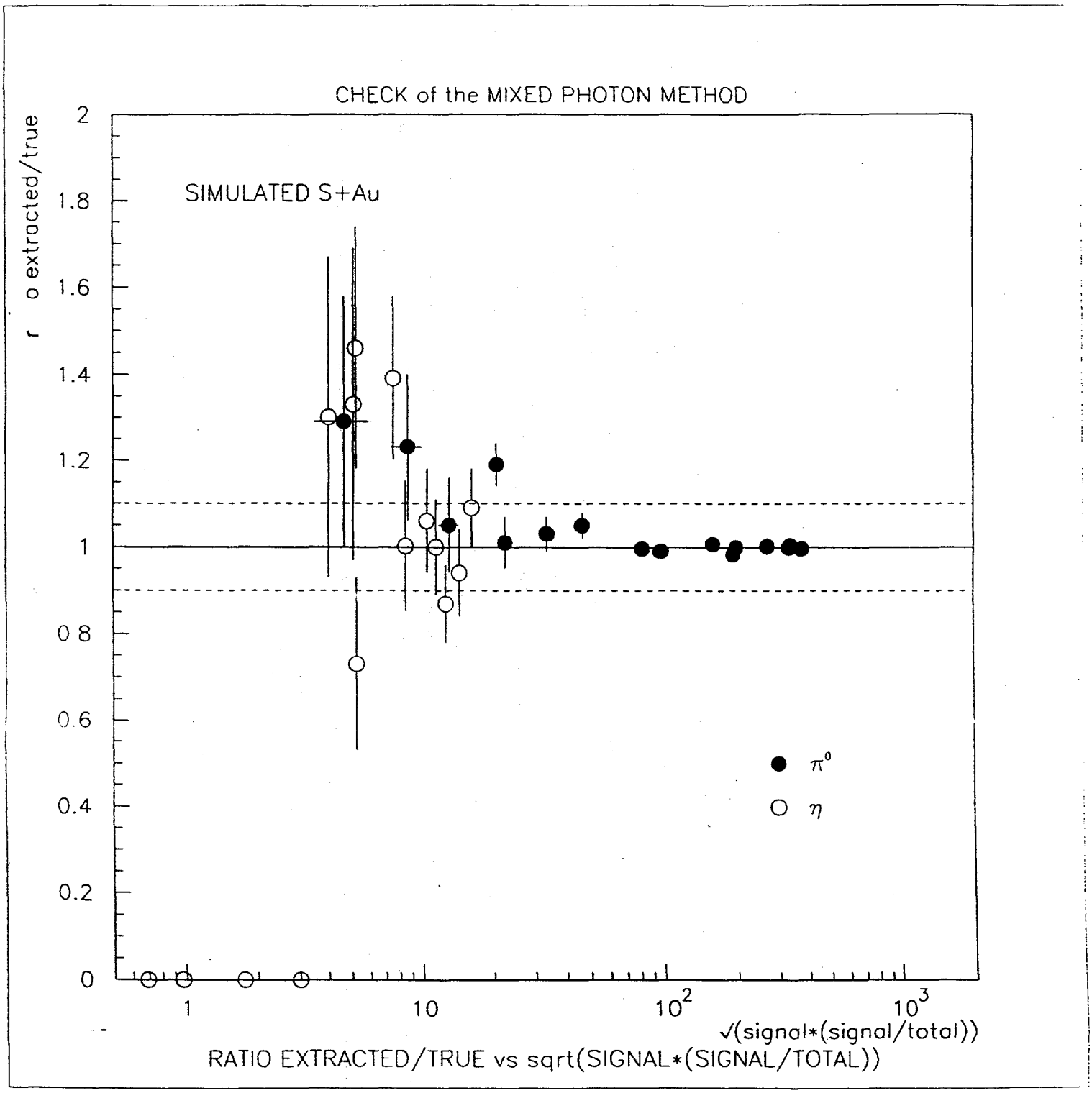

Fig.7 Dependence of the extraction efficiency on the quantity $\sqrt{Signal \times Signal/Total}$ (simulation).

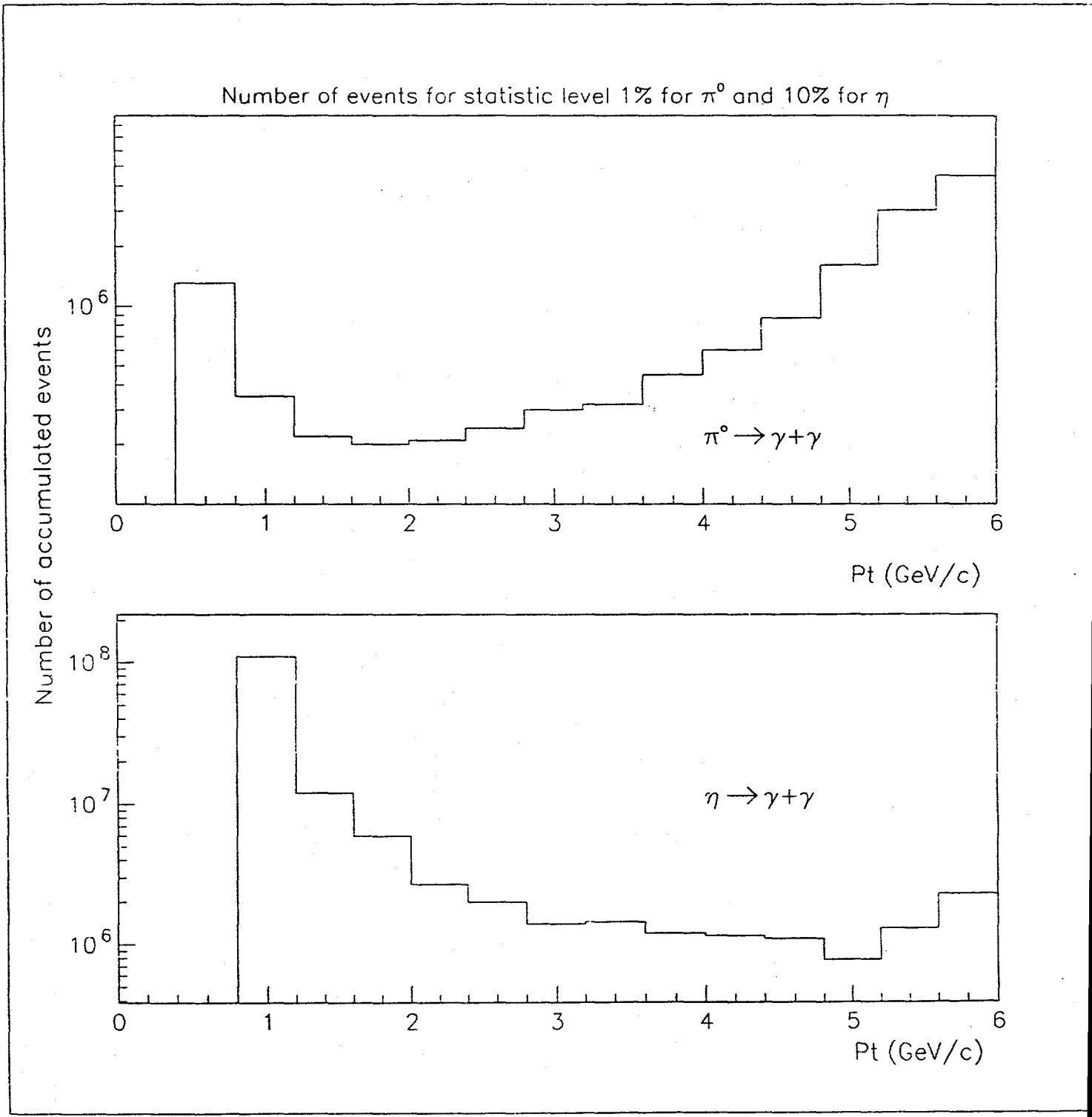

Fig.8 The event statistics needed for achieving the required statistical accuracy of the signal (1% for π^0 and 10% for η).

Studies for dimuon measurement with ALICE
ALICE collaboration

Presented by D.Jouan [a] *

[a]Institut de Physique Nucléaire, 91406 Orsay Cedex, France

The idea of measuring dimuon in the ALICE detector is not new, since it already appeared in the Aachen Conference [1]. In the meantime studies were aiming at the use of the two detectors of LHC p-p physics, CMS and ATLAS, already dedicated to dimuon measurement, for these same measurements in heavy ion collisions, whereas the detector dedicated to heavy ions physic at LHC, ALICE, was considering all the other observables.

Recently, the interest for dimuon measurements in ALICE was renewed by demands from LHC committee, stiring the activities of a working group in the ALICE collaboration, also associated to a more recent move from new groups.

In the following I will briefly describe the interest of measuring dimuons in heavy ion collisions, particularly in ALICE, then the experimental strategy and first estimates of the performances that could be reached with the proposed system.

1. Dimuons in heavy ions collisions

In central Pb-Pb collisions at LHC, the matter will reach energy densities well beyond the 1 to 3 GeV/fm^3 predicted as a threshold for the transition toward a new deconfined state of matter, the plasma of quarks and gluons (QGP).

One of the most interesting signatures proposed so far [2] for QGP is the color screening phenomenon that could yield to the suppression of high masses resonances rarely produced at the beginning of the collisions, acting thus as direct probes of the deconfining nature of the medium. In itself, the measurement of these resonances is not sufficient, but needs to be associated with a comparison to another one originating from the same production mechanism but nevertheless insensitive to the existence of plasma.

The measurement of dimuons is, already at SPS energies [3,4] a very rich one, yielding in particular to high masses vector mesons J/ψ and ψ' . At LHC energies, the Υ family will become available [5], together with open beauty and charm that could be the ideal reference at LHC[6]

Measuring dimuons is thus of paramount importance for QGP studies, and measuring them in ALICE in correlation with the other observable could be a decisive asset at LHC.

Indeed looking for QGP formation is fundamentally a challenging experimental task, since the QGP is a transient phase in the history of the system and that all measurements take place after hadronization and freeze out.

---

*IN2P3/CNRS

The evidence for QGP formation could thus not arize from a unique signature, but from the combination of several or all of them leading to a failure of the predictive power of the hadronic model.

The ultimate goal could be to select a class of events, on an event by event basis that will be a specific feature of these energies [7], whose combined characteristics would not be explainable by ordinary hadronic models, strongly constrained by the requirement to reproduce data from p-p to p-A collisions and from AGS to LHC energies [8]. The study of the Υ /$b\bar{b}$ ratio for these specific classes of events could be a very decisive point, only accessible in the ALICE detector.

2. Experimental strategy

The most basic question related to the experimental measurement of these resonances is probably the expected cross sections. At c.m. energies of the order of 10-100 GeV, the whole high mass dimuon production, i.e. continuum and resonances, displays an experimental scaling behaviour with respect to $\sqrt{\tau} = M/\sqrt{S}$ [9,10]. At LHC energies, such an exponential parametrisation leads to a saturation of the cross section, independantly of the cdm energy.

This trend ignores the effects of the structure functions of relevance for $Y < 4$ (10^{-3} to 10^{-5}), not yet measured, but which are expected to create an increase of the production cross section as a function of the energy [11,12].

The exact cross section will thus remain unknown until measured, but nevertheless the exponential fit and its saturation does not seem relevant, so in the following we will consider intermediate values, between the saturation and the higher increase ($\times 30$).

The differential cross sections $Br(d\sigma/dY)^{pp}_{Y=0}$ that we consider for dimuon production from J/ψ , Υ , $c\bar{c}$ and $b\bar{b}$ will be respectively : 0.1 μb, 1.5 nb, 4 μb and 0.2 μb, yielding respectively to 700.000, 15.000, 4.10^7 and 2.10^6 muon pairs for $5.5.10^8$ central collisions (1 month), per one unit central rapidity.

This level of production could be sufficient for a measurement in one or two units of rapidity.

The general requirements for this dimuon measurement are thus :

- to be in the central region free of baryon, [13]
- a good mass resolution (1 % to separate the Υ ")
- a low background from mesons decays

This last requirement implies the use of a thick absorber as close as possible to the interaction point, and it can also benefit from a measurement at high rapidities, where the decay lenght increases.

Previous studies have shown([14,15] that the L3 magnet could be most convenient for measuring dimuons with a minimal decay background, in the ± 1 rapidity domain.

Nevertheless, this involves major modifications of the ALICE setup, and cannot run simultaneously with it, forbidding the correlated measurements of dimuons with other particles.

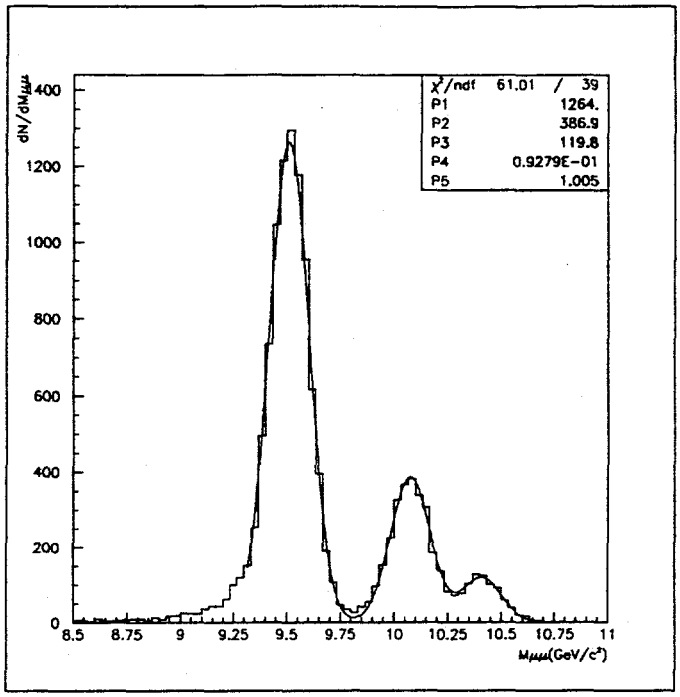

Figure 1. mass resolution for a 4 m carbon and one month running (see text)

It is then natural to look for possible dimuon measurements in rapidity domains complementary to the ALICE one.

With its maximal field B=0.6T, the L3 magnet could allow sufficient bending to obtain a momentum resolution better than 1 % in the pseudorapidity range $1 < \eta < 2$.

But the use of several meters of absorber will destroy this performance, and moreover the low threshold for particle detection in the central tracker require a low field. So the L3 field cannot easily be used for a muon detection satisfying our requirements.

We are thus led to consider the use of an additional dedicated magnet for this purpose, which could be located in the forward region of the L3 magnet, below 15 degrees.

In the following we will consider a dimuon spectrometer consisting of a thick ($10\lambda_I$) absorber starting 90 cm from the interaction point, a shielding around the beam, and a dimuon spectrometer consisting of a dipole magnet with B = 0.7 T and L = 3m and the measurement of trajectories before and after the magnet with 50 μm precision, allowing measurement of muons with pseudorapidities between 2 and 4.

3. Performances

3.1. Mass resolution

The energy straggling and the multiple scattering in the absorber contribute to the decrease of the mass resolution. For a given number of interaction length, a low Z material will minimize these effects and therefore be a natural choice. Nevertheless GEANT simu-

lations have shown that a high Z material is more efficient for minimizing the background in TPC originating from the absorber.

Studies are under way about an absorber made of a low Z material in the domain of relevance for muons, surrounded by a shielding of high Z material.

The mass resolution associated with such a setup will be close to the one induced by the 4m carbon absorber that we have considered in the following.

The tracking resolution is deduced from the magnet geometry and the chambers precision, and at the level of 0.7 % in average for the Υ family in this pseudorapidity range.

Taking into account this tracking precision, the effect of the energy straggling and of the multiple scattering in the absorber, and also a correction to multiple scattering using the interaction vertex and the exit point from the absorber, one obtains the spectrum of figure 1 , displaying the upsilon family production for 10^6 second (1 month) running.

A fit with 3 gaussians of identical width and mean values accorded to the Υ , Υ' and Υ " mass lead to a mass resolution less than 1 % (parameter P4). The parameters P1 to P3 are the amplitudes associated respectively with the Υ , Υ' and Υ ". They show that such a simple treatment already allows to extract the contributions from the 3 resonances, whose original yields are in the ratio 1:0.3:01 .

4. Signal and background

The shape and magnitude of the rapidity distribution of charged particle vary of 50 % according to the model used to extrapolate to LHC energies.

Following the cascade parton model predictions [16] we have considered a rapidity distribution which is probably in the lower range. The relative decrease of combinatorial background resulting from π and k decays is thus not only an effect of forward kinematics, but also a decrease of dN/dY when going to higher Y, associated to a general lowering of the distribution and an increase of the upsilon cross section considered, when comparing to central rapidity previous calculations yielding to signal/background of the order of 1 for the upsilon peak [14].

The result is a vanishing combinatorial background below the Υ , and a clear J/ψ peak above this background, which thus does not seem to be a major experimental difficulty for the extraction of resonances in this forward region (Figure 2).

Nevertheless the dimuon mass continuum also contains other contributions and at these energies the $c\bar{c}$ production will probably prevail.

To simulate $b\bar{b}$ and $c\bar{c}$ production in a simple way, we have considered the mass distributions inspired by the predictions made by Gavai et al[17], whereas the other variables are distributed as for Υ and J/ψ .

The different kinematical distributions considered can be summarized as follows:

1. Υ , J/ψ , $b\bar{b}$ and $c\bar{c}$

$$d\sigma/dP_t \propto P_t/(1+(P_t/P_t^0)^2)^{3.5})$$
$$d\sigma/dY \propto 1. \text{ if } Y < Y_0$$
$$d\sigma/dY \propto exp(-(Y-Y_0)^2/2) \text{ if } Y > Y_0$$
$$J/\psi \rightarrow P_t^0 = 2.3,\ Y_0{=}4$$

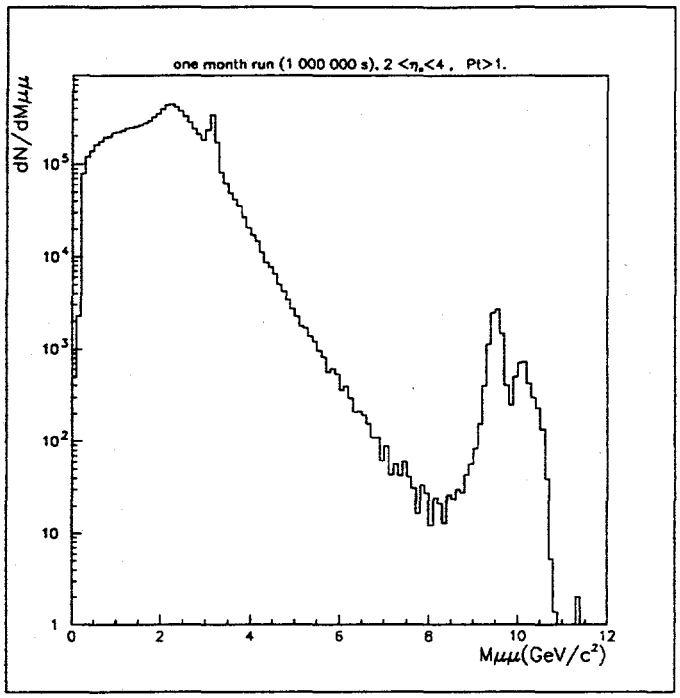

Figure 2. comparison between resonances and background from π and K decay (see text)

$\Upsilon \rightarrow P_t^0 = 4.7$, Y_0=3

2. PIONS and KAONS

pions:

$d\sigma/dP_t \propto P_t exp(-M_t/0.16)$ if $P_t < 0.5 GeV/c$

$d\sigma/dP_t \propto P_t/(1.3 + P_t)^{8.28}$ if $P_t > 0.5 GeV/c$

$dM/d\eta = 3000$ si $\eta < 2$

$dM/d\eta = 4000 exp(-\eta^2/12.5)$ if $\eta < 2$ (close to the distributions predicted by the Cascade Parton Model)

The Kaon distributions are deduced from the one of the pions thanks to the parametrisations from Bourquin and Gaillard [18]

The muon production is then deduced thanks to a 3 body semileptonic decay of c and b, with branching ratios 0.14 and 0.1 respectively, and the fragmentation of the quarks is taken into account through the parametrisation of reference[19]. It is clear that such a simulation is not aiming at a detailed description of the $b\bar{b}$ and $c\bar{c}$ production and decay, but only at a rough estimate of the components involved in the mass spectrum and of the effects of the main kinematical characteristics of the process.

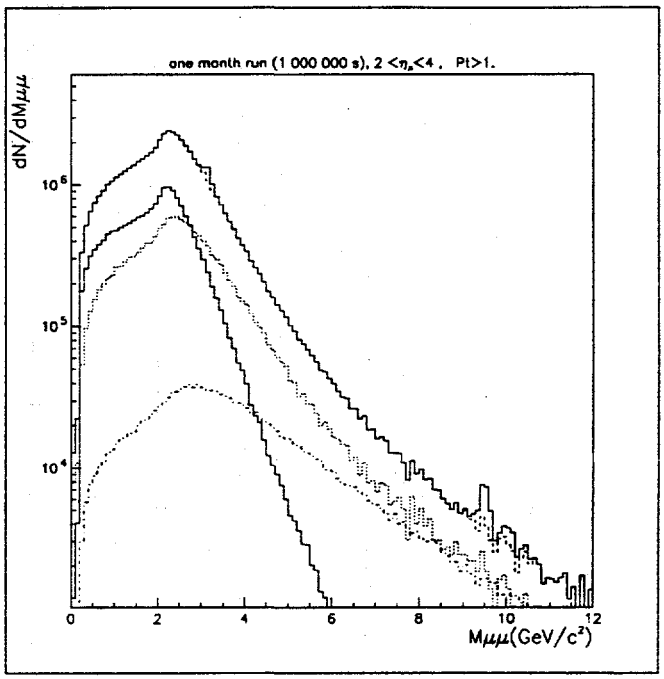

Figure 3. simulated mass spectrum for one month running, including $b\bar{b}$ and $c\bar{c}$ correlated and uncorrelated pairs (see text). solid line: total mass continuum or background from π and K decays; dotted line: muons pairs from c and $\bar{c}$; dot-dashed line: muons pairs from b and $\bar{b}$.

Effectively, it is observed (Figure 3) that the important production of muons from charm decay (0.5 per event), even higher than the production from π and k decays, yields to an important continuum in the J/ψ region, and the ratio signal/continuum is of the order of 5-10 % around the J/ψ peak. But due to the high statistic available (10^5) the statistical precision on J/ψ data point with continuum subtracted could stand between 1 and 10% in the same region. The figure 3 displays the three main componants of the continuum: combinatorial pairs produced by $c\bar{c}$, $b\bar{b}$ and π or K decays. In addition to these three components considered separately, combinations between them are also present, leading to the global mass continuum of the picture.

In the Υ mass region, the continuum originates directly from the decays of heavy flavours, thanks to the low production rate from π and K decays.

This high mass region has thus the specific interest to result mainly from the two observable we are seeking at : resonances which are the sensitive probes of the color screening effect and this continuum reference which originates from the same production mechanism.

5. Summary

There will be a unique detector at LHC dedicated to the search for quark gluon formation: the detector ALICE.

It should be of paramount interest to measure also the dimuon production in this detector, in order to study color screening effects in correlation with the other observables measured in Pb-Pb collisions, including the event by event selection.

Preliminary studies have shown that dimuon measurement in the forward region $2 < \eta < 4$ could allow such a correlated measurement for the Υ , Υ' , and also Υ ", and the high mass continuum originating from heavy flavours, which are the ideal reference at these energies. This measurement would also give access to J/ψ production.

Dimuon measurement in ALICE will be dedicated to heavy ion studies, and thus benefit of several advantages:

- flexibility : the absorber nature and position can be optimized, allowing minimization of pion and kaon decays background, securing the measurement of the high mass continuum component

- robustness : the mass resolution does not depend on reconstruction of muon trajectory upstream to the absorber

REFERENCES

1. H.Specht proceeding of Large Hadron collider Workshop, Aachen 4-9 October 1990, vol.2, CERN 90-10
2. T.Matsui and H.Satz, Phys.Lett. 178B (1986) 416.
3. C.Lourenco (NA38 collaboration) , proceeding of quark matter '93, Nuclear Physics A566 (1994) 77c
4. A,Mazzoni (Helios/3 collaboration) proceeding of quark matter '93, Nuclear Physics A566 (1994) 95c
5. F.Karsch proceeding of Large Hadron collider Workshop, Aachen 4-9 October 1990, vol.2, CERN 90-10
6. H.Satz Charmonium production versus open charm in nuclear collisions CERN-TH-7120/93
7. R.Stock, Event by event measurements in relativistic heavy ion physic, this workshop
8. H.Satz proceeding of quark matter '93, Nuclear Physics A566 (1994) 1c
9. L.Lyons, Progress in particles and nuclear physics vol7 (1981)
10. N.Craigie, Phys. Rep. 47 (1978) 515
11. P.Sonderegger proceeding of Large Hadron collider Workshop, Aachen 4-9 October 1990, vol.2, CERN 90-10
12. R.Gavai, D.Kharzeev, H.Satz, G.A.Schuler, K.Sridar, R.Vogt, to appear in *Hard Processes in Hadronic Interactions* H.Satz and X.N. Wang Editors, and Preprint CERN-TH.7526/94
13. H.Satz proceeding of Large Hadron collider Workshop, Aachen 4-9 October 1990, vol.1 p.188 , CERN 90-10
14. answers from ALICE to LHCC questions CERN/LHCC/94-15

15. Min Chen, L3H letter of intent, CERN/LHCC/93-15
and
Addendum on the measurement of the suppression of $\Upsilon + \Upsilon'$ in heavy ion collisions, L3P collaboration, CERN/LHCC 92-14
16. K.Geiger, proceeding of quark matter '93, Nuclear Physics A566 (1994) 263c
17. R.Gavai et al, Heavy quark production in pp collisions, GSI preprint GSI-94-76
18. M.Bourquin and M.Gaillard N.Phys B 114 (76) 224
19. C.Peterson et al., Phys. Rev. D 27 (1983) 105

Heavy ion physics at LHC with the Compact Muon Solenoid

M. Bedjidian, D. Contardo, R. Haroutunian, O. Drapier) [a]
V.I. Galkin, O. Kodolova, V.L. Korotkikh, I.P. Lokhtin, L.I. Sarycheva)[b]
R. Kvatadze, R. Shanidze)[c]

[a]Institut de Physique Nucléaire IN2P3-CNRS et Université Claude Bernard Lyon 1, 43 Bd du 11 Novembre 1918, F-69622 Villeurbanne Cedex, France

[b]Nuclear Physics Institute, Moscow State University, 119899 Moscow, Russia

[c]High Energy Physics Institute, Tbilisi State University, Georgia

The Compact Muon Solenoid was originally designed for the high luminosity p-p physics at LHC. We discuss its ability to do ion physics with hard probes and illustrate the performances with a simulation of the measurement of two acknowledged QGP signals :
- The Debye screening of the Υ family production.
- The jet quenching.

1. Motivation of the study

The Compact Muon Solenoid (CMS), is one of the two detectors proposed to achieve the primary goal of the LHC : the discovery of the Higgs boson(s). For this purpose, the detector is optimized for the pecise measurement of muons, photons, electrons and jets. It is a clear motivation to investigate its ability to measure the hard processes probing the formation of a Quark Gluon Plasma (QGP) in ion collisions.

It is the case of the heavy quark bounds states, long predicted to be suppressed in a QGP. In CMS they can be detected, via their muonic decay according to the principle adopted for the p-p physics.

The muon momenta are measured in the central tracker of the detector at a radius below 1.3 m of the interaction vertex. The muons are then filtered in the electromagnetic and hadronic calorimeters and trigger the data acquisition in the following muon chambers, up to a pseudo-rapidity of 2.6. This strategy has the advantage to provide a transverse momentum resolution of less than 1 % in the solenoidal magnetic field of 4 T. The drawback with heavy ions will be the huge background from the uncorrelated decays of pions and kaons. A different strategy is currently investigated by the ALICE collaboration, the hadrons absorber is located close to the interaction vertex and the muon momentum is measured in the following muon chambers at forward rapidities. In this case, the background will be reduced but the resolution of the different excited states of the resonances will be worsened.

The jet quenching is one other QGP signal that could be adressed using the CMS calorimeters. This aspect of the ion physics is not included in the ALICE goals.

In this paper we present simulations of the measurement of the Υ family states and of the jet reconstruction. All were performed with GEANT, using a full description of the CMS geometry and the map of the 4 T magnetic field. The overall view of CMS is shown in figure 1. A detailed description of the different sub-dectectors can be found in the technical proposal submited to the LHCC [1].

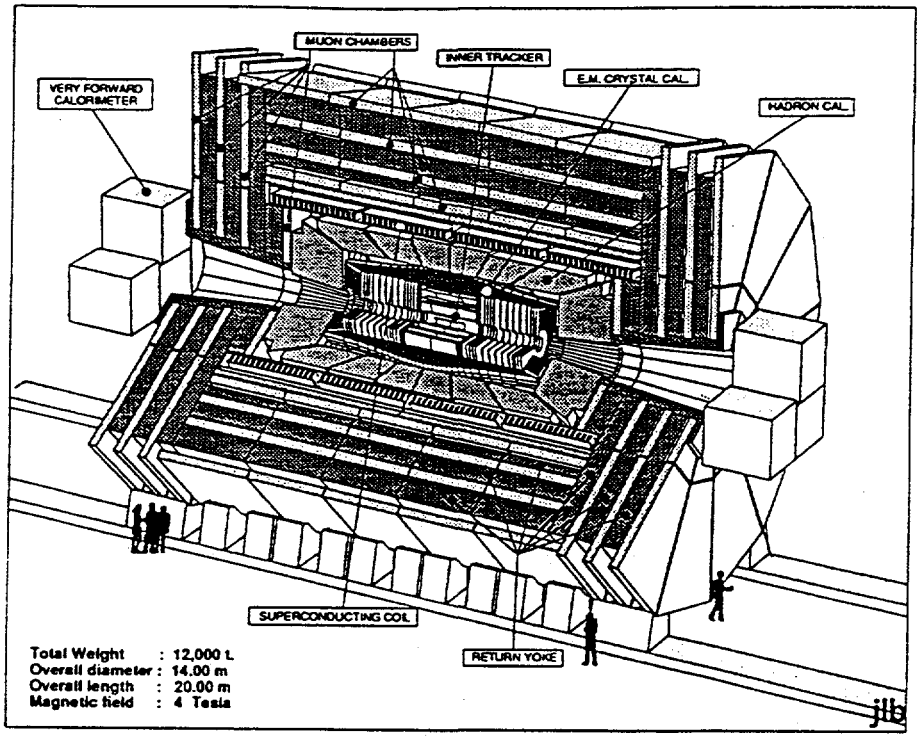

Figure 1. Three-dimensional view of the CMS detector.

2. Simulation of the Υ family measurement

2.1. Acceptance and resolution at the Υ mass

The acceptance at the Υ mass was estimated requiring that the decay muons reach at least one of the muon stations located in the absorber outside the coil of the CMS magnet. The resonances were generated with rapidity and transverse momentum distributions extrapolated from the data at lower center of mass energies [2]. These distributions are shown in figure 2 for the generated and accepted resonances. It can be seen that the acceptance covers the full transverse momentum range and extends up to a rapidity of 2.6. The natural acceptance of the CMS detector is 33 %. To optimize the signal to background ratio we have applyed a further cut on the individual muons with transverse momenta below 4 GeV/c, reducing the acceptance to 15 %.

A similar study was done at the J/ψ mass. In this case, the natural acceptance of the detector is 6 % limited to 1 % in the-barrel part. It is thus not excluded to measure the $c\bar{c}$ states which have a cross section about three orders of magnitude higher than the Υ states. The optimization of the trigger rate and of the signal to background ratio, that will probably be different than for the Υ resonances, has still to be investigated.

The resolution at the Υ mass was estimated assuming conservative spatial resolutions of the sub-detectors in the CMS central tracker and using only few points per track where the occupancy rate of the counters is small. The position of the vertex is known from the beam characteristics with transverse and longitudinal resolutions of respectively 200 μm and 5.3 cm. Two points were assumed in the Si-pixel layers, with a resolution of 20 μ in both directions, and three in the micro-strip gas chamber outer layers, with transverse and longitudinal resolutions of respectively 60 μm and 0.5 cm. Under these conditions, the mass resolution at the Υ mass will be 36 MeV/c^2 allowing a complete separation of the different excited states.

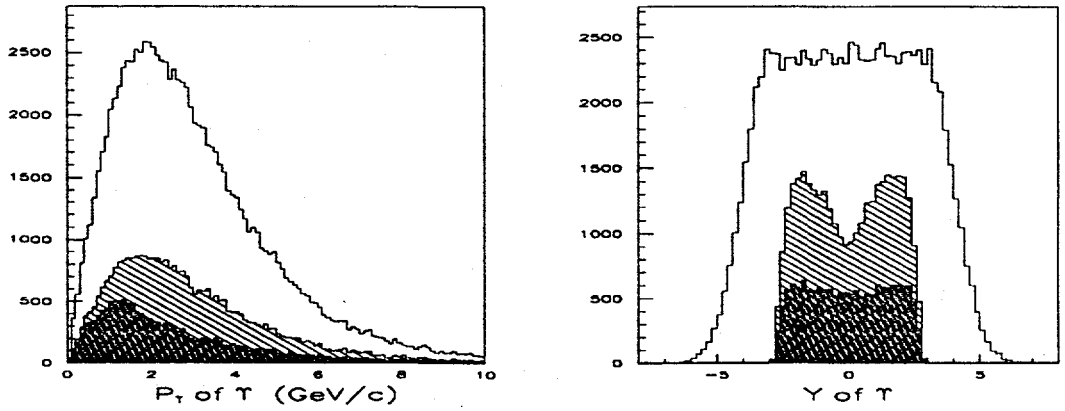

Figure 2. Generated transverse momentum and rapidity distributions at the Υ mass (full line). CMS natural acceptance (hatched area) and with $P_t^{\mu} > 4GeV/c$ (shaded area).

2.2. Reconstruction of the Υ decay muons

The full track reconstruction with the high multiplicities generated by ion collisions at LHC is a difficult task requiring a low occupancy rate of the detectors. On the other hand, it will be simplified in the present case where the goal of the reconstruction is limited to the matching of muon tracks, with transverse momenta above 4 GeV/c, in the muon stations and in the inner tracker detectors.

We have evaluated the occupancy rates in the CMS central tracker in the worst situation of central Pb-Pb collisions, with an upper estimation of 8000 charged plus 4500 neutral mesons (π+K) produced per unit rapidity. The secondary particle production was included in the simulation as well as the effect of the 4 T magnetic field and the specific characteristics of the sub-detectors. The first two layers of the tracker, close to the interaction vertex, are Si-pixels with a cell size of 0.125 x 0.125 mm^2. We found in this case a 1 % occupancy rate. The three following layers are made of Si-strip detectors with a cell size of 0.05 x 125 mm^2 for which the occupancy rate decreases from 40 % to 10 % with increasing radii. The rest of the detectors are micro-strip gas chambers (MSGC) organised in 7 (14) layers in the barrel (end caps) with cell sizes increasing from 0.2 x 125 to 250 mm^2 (0.2 x 50 to 90 mm^2) from the inner to outer radii. The occupancy rates for these detectors are shown in figure 3. It can be seen that they range from 13 % to 8 % in the 4 last layers of the barrel and from 5 % to 20 % at radii above 40 cm in the end caps.

A preliminary study of the muon reconstruction, in the barrel part of the detector, was performed using only two points in the muon stations and four in the last micro-strip gas chambers where the occupancy rates are the smallest. The spatial resolutions presented in the preceding section were included in the simulation. The reconstruction algorithm is based on a road technics : roads for the good tracks are defined from the impact positions in the detectors for true muon tracks (Υ accepted decay muons). The muon impacts are then mixed to those present in the central tracker and the tracks of combinatorial association of 6 impacts are submitted to a road test. With this algorithm, we identified 92 % of the muon tracks with 5 good hits and 5 % of false tracks. We thus expect an efficient muon reconstruction. It might be improved when including more points like for instance in the Si-pixel layers or in the Si-strip detector layer of lower occupancy rate.

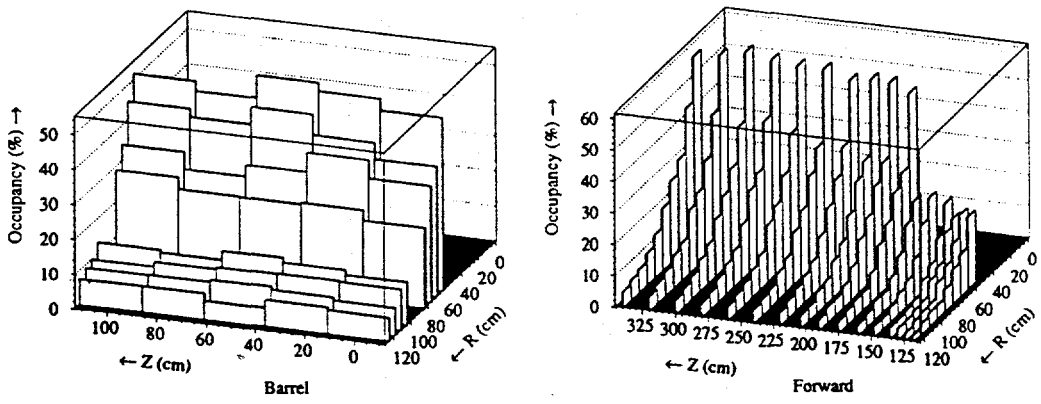

Figure 3. Occupancy rates in the CMS micro-strip gas chambers.

2.3. Signal to backround ratio

For this estimation, the cross section of the Υ states at LHC were extrapolated from the available data at lower center of mass energies. We used two assumptions for this extrapolation : a saturation of the cross section or a linear increase with the center of mass energy. The dependence of the cross section on the beam mass was assumed to follow a $A^{2\alpha}$ law, with $\alpha = 0.95$, as measured in the absence of QGP formation. The final values, obtained with the preceding assumptions, are listed in table 1 for various nuclei and in case of the Υ state. From the present knowledge, the ratio of the Υ' and Υ" to the Υ production should be respectively 0.3 and 0.1. It has to be noted that a recent measurement by the CDF collaboration [3], at 1.8 TeV, shows a cross section close to the linear extrapolation presented here.

The dimuon background consists mainly in uncorraleted muon pairs from pions, kaons, c and b quarks, decays. The simulations were done using the SHAKER distributions for the pions and kaons and the PYTHIA distributions for the $c\bar{c}$ and $b\bar{b}$ production. With the cross sections, $\sigma_{pp}^{c\bar{c}}$=1 mb and $\sigma_{pp}^{b\bar{b}}$=0.4 mb, we found that the background is dominated in this experiment by the pion and kaon decays. As mentioned in section 2.1, we optimized the signal to background ratio by selecting only the muons with a transverse momentum above 4 GeV/c.

In table 1, we present the statistics of Υ that will be measured in 15 days of integrated

luminosity at LHC and the corresponding signal to background ratio in a mass window of ±50 MeV around the Υ mass. These results are given for two sets of assumptions :

- A saturating cross section of the Υ and a multiplicity of 8000 charged particles per unit rapidity in central Pb-Pb collisions. This is a pessimistic case.

- A linear extrapolation of the Υ cross section and a multiplicity of 3000 charged particles per unit rapidity in central Pb-Pb collisions. This is an optimistic case.

We have reported the results for different ion species that can be accelarated at LHC, according to the expected beam luminosities. We assumed a multiplicity increasing with $A^{1.3}$ in the pessimistic case and with $A^{1.1}$ in the optimistic case. The simulated mass distributions with the statistics presented in table 1 are ploted in figure 3, in the case of Pb-Pb and Ca-Ca collisions, they show the expected measurement if none of the resonances are suppressed.

Table 1
Υ statistics and signal to background ratios, in 15 days of LHC integrated luminosity.

Beam	^{208}Pb	^{97}Nb	^{40}Ca	^{16}O
L ($cm^{-2}s^{-1}$)	10^{27}	9 10^{28}	2.5 10^{30}	3.2 10^{31}
σ (A-A) (b)	6.5	3.8	2.1	1.15
Pessimistic assumptions				
σ (Υ) (μb)	46	11	2	0.35
dNch/dy (y=0)	8000	3000	900	300
Υ in 15 days	6250	1.3 10^5	0.7 10^6	1.5 10^6
Signal/Background	0.07	0.19	0.76	2.1
Optimistic assumptions				
σ (Υ) (μb)	230	55	10	1.75
dNch/dy (y=0)	3000	1250	450	155
Υ in 15 days	32000	0.6 10^6	3.6 10^6	7.7 10^6
Signal/Background	2.3	6.0	14.1	27.0

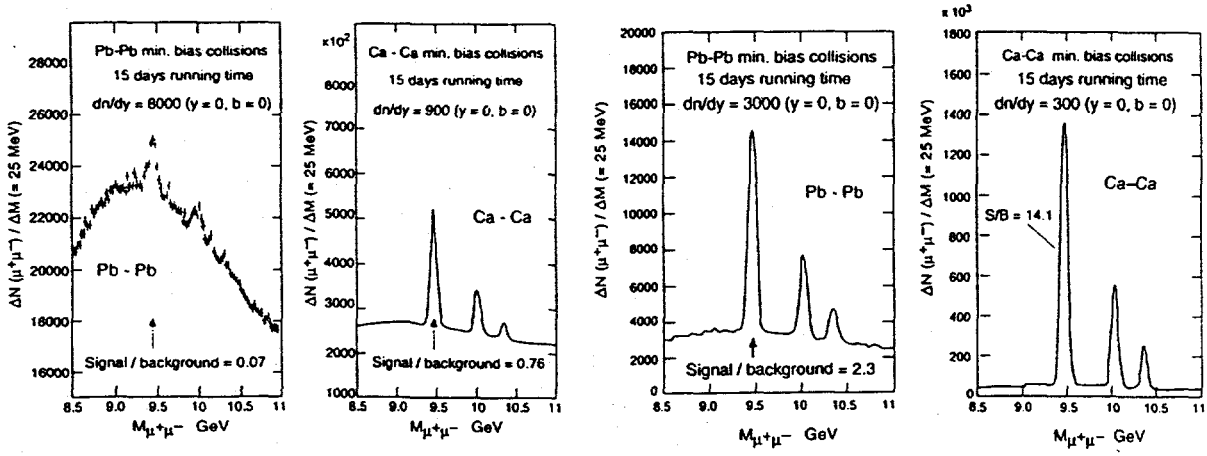

Figure 4. Simulated mass distributions with pessimistic and optimistic assumptions.

2.4. Sensitivity to the resonance suppression

The ultimate goal of the experiment will be to observe the suppression of the resonances due to the Debye screening in a QGP. It is expected that the critical temperature for the dissolution of the Υ is twice as large as the critical temperature of the phase transition while it is of the same order with the Υ' and Υ" excited states [4]. In other words, the excited states production should be strongly suppressed at LHC contrary to the Υ. The suppression of the different resonances can be measured, as a function of the enrgy density reach in the collisions, by comparing the production cross sections with increasing mass of the beams from proton to lead. To avoid the absolute normalization, we can study the production of the resonances relatively to a reference phenomena independent of the energy density reach in the collisions. This will allow to access the resonance suppression not only as a function of the incident beam mass but also as a function of the impact parameter of the collisions. Assuming that the Υ state can be used as a reference since it is not expected to be suppressed by the QGP formation, the suppression of the Υ' and Υ" resonances can be expressed by the double relative ratio of their production, with respect to the Υ, in p-p and A-A collisions :

$$S_{\Upsilon'} = (N_{\Upsilon'}/N_{\Upsilon})_{AA}/(N_{\Upsilon'}/N_{\Upsilon})_{pp} \quad (1)$$

The uncertainty on this ratio is an estimation of the sensitivity of the experiment to measure the suppression. It was evaluated assuming the same statistics for the p-p and A-A data as presented in table 1 for 15 days of integrated luminosity at LHC. With the pessimistic assumptions presented in the preceding section, we found that the CMS experiment should be able to measure, $S_{\Upsilon'(\Upsilon'')} \pm$ 16(50) % in Pb-Pb collisions and $S_{\Upsilon'(\Upsilon'')} \pm$ 1(3) % in Ca-Ca collisions. These values become respectively $S_{\Upsilon'(\Upsilon'')} \pm$ 2(4) % and $S_{\Upsilon'(\Upsilon'')} \pm$ 0.2(0.5) % with the optimistic assumptions.

The use of the Υ state as a reference has been criticized since only the direct production is expected to remain unchanged by the QGP formation. We are currently investigating the possibility to use the Z production in ion collisions as a reference to measure the suppression of the Υ states.

3. Jet reconstruction

As jets will be produced in hard processes occuring at the first stage of the ion collisions. They will propagate and strongly interact with the constituents of the dense matter formed in the collisions. It was suggested that the production rate of mono-jets or di-jets and the energy correlation in this later case will have a specific pattern if a QGP is formed [5]. We have studied the possibility to reconstruct the jets using the electromagnetic and hadronic calorimeters in CMS.

The jets were generated with PYTHIA and the p-p cross sections were extrapolated to the case of ion beams with a $A^{2\alpha}$ dependence, with α=0.9-1. At the nominal luminosity of the Pb-beam at LHC, 10^{27} $cm^{-2}s^{-1}$, the prodcution rate of jets with transverse momentum of 50 GeV, 100 GeV and 500 GeV should be respectively 15-45 Hz, 1-3 Hz and 2-6 10^{-3} Hz, allowing a sufficient statistics for a measurement in 15 days of integrated luminosity.

For the jet identification, we used the expected energy resolutions of the CMS calorimeters parametrized by the quadratic sum $\Delta E/E = a/\sqrt{E} \oplus b$, where the values of a and b

were respectively 2.0(68) % and 0.5(5.0) % for the electromagnetic (hadronic) calorimeter. The reconstruction algorithm was based on a cone-type jet finding where the parameters where adjusted to optimize the jet finding efficiency [6].

In the worst case of the central Pb-Pb collisions with a multiplicity of 8000 charged particles per unit rapidity, the jet E_t and direction (y,ϕ) are well reconstructed for E_t >50 GeV, but with a large contribution from false jets up to E_t=100 GeV. The jet efficiency, ϵ_1, is defined as the ratio of correctly reconstructed jets to the total number of generated jets. The misrecognition coefficient, ϵ_2, is the ratio of the number of false and generated jets. These parameters are listed in table 2, for different E_t values. It can be seen that the jets produced in Pb-Pb central collisions may be reliably reconstructed in the CMS detector for E_t >100 GeV. Further simulations are in progress to improve the recognition algorithm, using the information in the last layers of the central tracker. They are expected to reduce the E_t threshold on the jet measurement.

Table 2
Jet recognition efficiency and measurement resolutions in Pb-Pb central collisions.

E_t GeV	ϵ_1 (%)	ϵ_2 (%)	ΔE_t (GeV)	Δy	$\Delta\Phi$
50	0.85	0.57	3.8 ± 10	0.011 ± 0.04	0.001 ± 0.04
100	0.97	0.027	0.8 ± 12	0.004 ± 0.03	0.005 ± 0.03
500	0.99	0.004	1.0 ± 13	0.004 ± 0.02	0.003 ± 0.02

4. Conclusions

The ability of the CMS detector to trigger on low transverse momentum muons over a large rapidity range allows to measure the production of the Υ family states. It is not excluded that the J/ψ and ψ' can be measured at forward rapidities, but the signal to background ratio has to be studied in this case.

The high granularity and spatial resolution of the inner tracking device in the 4 T magnetic field should allow an efficient muon reconstruction and provide the necessary mass resolution to discriminate the different excited states. It will also help to keep the signal to background ratio at a tolerable level.

The electromagnetic and hadronic calorimeters can be used to measure the high momentum jets. The momentum cut will depend on the optimization of the jet recognition algorithm and on the final particle multiplicity of the ion collisions.

Although the measurement of global observables of the collisions was not yet simulated. The multiplicity should be measured with the Si-pixel detectors and the neutral energy with the electromagnetic calorimenter, both, up to $\eta = 2.6$. The charged energy will be measured in the hadronic calorimeters up to $\eta = 5$.

For all these reasons, the Compact Muon Solenoid proposed at LHC, in spite of design goals dictated by the requirements for the p-p physics, appears well suited to search for Quark Gluon Plasma signals with ion beams. It is a remarkable feature that the study of this physics can be done without additional cost to the detector.

REFERENCES

1. CMS Technical Proposal, CERN/LHCC 94-38 (1994).
2. M. Bedjidian et al., CMS TN/92-33 (1992).
3. V. Papadimitriou, private communication.
4. H. Satz, CERN 90-10, Vol. II, (1990) 1141.
5. M. Plumer, talk presented at this conference.
J. Pan and C. Gale, Phy. Rev. D50 (1994) 3235.
6. R. Kvatadze and R. Shanidze, CMS TN/94-270 (1994).

The ALICE Inner Tracking System: Design. Physics performance and R&D issues

P. Giubellino[a] for the ALICE Collaboration[b]

[a]INFN. Torino, Italy

[b]Athens. Bari. Beijing. Bergen, Birmingham. Calcutta. CERN. Cracow, Dubna, Frankfurt. Geneva. GSI. Heidelberg. IHEP. ITEP. Kosice, Legnaro. Lund, Marburg. Minsk. Messina. Moscow INR. Moscow Kurchatov. Munster, Novosibirsk. Oak Ridge. Orsay. Padua. Paris CdF. Prague. Rez. Rome. St. Petersburg, Utrecht. Turin. Warsaw, Wuhan. Zagreb

ALICE is a dedicated Heavy–Ion experiment proposed for the future LHC collider at CERN. The main goals of the ALICE Inner Tracking System are the reconstruction of secondary vertexes and the tracking and identification of low–p_t electrons; at the same time. it will provide a significant improvement of the momentum resolution at large p_t and the tracking and identification of low–p_t hadrons. The ITS will consist of five cilindrical layers. of radii from 7.5 to 50 cm. of high-resolution detectors. The unprecedented particle density foreseen, of up to 8000 particles per unit η. imposes the use of sophisticated, and often innovative, technologies for the detectors. the electronics and the support and cooling system. Therefore. extensive R&D programs are now being pursued on various aspects of the project. Here are presented the basic ideas for the design. a few examples of the expected performance. and a brief overview of the ongoing R&D.

1. INTRODUCTION AND SYSTEM OVERVIEW

The ALICE collaboration has proposed to build a dedicated detector to exploit the unique physics opportunities of ultra relativistic Heavy–Ion collisions at the LHC [1]. The experiment will study hadrons. electrons and photons of p_t up to 10 GeV/c in the central rapidity region, in order to detect the expected formation of a new phase of matter, the Quark–Gluon–Plasma. ALICE has been conceived as a general–purpose detector, in which hadrons. electrons and photons produced in the interaction can be measured and identified. The baseline design consists of a central detector covering the full azimuth, complemented by a multiplicity detector covering the forward rapidity region and a Zero Degree Calorimeter. The central detector will be embedded in a large magnet with a weak field. and will consist of a high–resolution Inner Tracking System, a cylindrical TPC, a Particle Identification Array and a single–arm electromagnetic calorimeter.

Given the very large multiplicities. the design of the tracking system has primarily been driven by the requirement for safe and robust track finding. It uses mostly three-dimensional hit information and dense tracking with many points in a weak magnetic

field of $\approx$ 0.2 T. The momentum cut-off should be as low as possible ($<$ 100 MeV/c), in order to study collective effects associated with large length scales. A low-p_t cut-off is also mandatory to reject the soft conversion and Dalitz background in the lepton-pair spectrum. At high momenta, the resolution has to be sufficient to measure leading particles of jets. In addition, the system has to be able to reconstruct hyperon decays.

In this scheme, the ITS provides the reconstruction of secondary vertexes, tracking and identification of low-momentum particles, down to a p_t of $\approx$ 20 MeV/c for electrons, and improvement of the momentum resolution. As shown in Fig. 1, it will consist of five cylindrical layers, covering the central rapidity region ($|\eta| \leq 0.9$) for vertices located within the length of the interaction region (2σ), i.e. 10.6 cm along the beam direction (z).

The general criteria of the design can be summarized as follows [1]): a) minimize the amount of material to limit multiple scattering: we limit the number of planes to five and their average thickness to 0.6% of X_0 each: b) position the outer planes so as to optimize the matching of the tracks with the TPC, taking into account the multiple scattering in the inner wall of the TPC, while mantaining the area, to a reasonable level; c) position the innermost layer as close to beam pipe as possible: d) define the radius of the beam pipe as a compromise between angular resolution and impact parameter resolution. We chose 6.5 cm, which satisfies both requirements. This way, the vacuum inside the beam pipe provides also a decay zone of the rigth dimensions for hyperons ($c\tau$ of order cm). Three to four layers will have analog readout for particle identification via dE/dx in the $1/\beta^2$ region, giving the ITS a stand-alone capability as a particle spectrometer for low-p_t tracks which do not reach the outer detectors because of decay, energy loss, or curling.

Considering the choice of technologies for the ITS, the requirements on speed are quite modest, since the minimum bias event rate will be of about 5KHz. This allows the use of fairly slow detectors and electronics and of heavily multiplexed readout. The radiation levels will be moderate, reaching a maximum of 16 krad/yr for the innermost layer. Since the resolution will be mostly limited by multiple scattering, also the required position resolution will not be critical on the scale of solid state detectors. On the opposite, the granularity, and therefore the two-track resolution, will have to be excellent.

The granularity required for the innermost planes can be achieved only with silicon micropattern detectors with two-dimensional readout, such as Silicon Pixel Detectors (SPDs) and Silicon Drift Detectors (SDDs). As a baseline design, we consider using SPDs for the innermost plane, and SDDs for the following ones. For the outer layers, at least one and possibly both could be equipped with gas or silicon micro-strip detectors. These detectors will have relatively short strips (50 mm), and a small stereo angle (30 mrad) between the two projections in order to avoid unacceptably large numbers of ghost hits.

The nominal parameters of each of the four detector types considered are indicated in Table 1, while in Table 2 are summarized the main parameters of the various layers.

2. PERFORMANCE

The ITS has been the object of extensive simulations both at the level of the overall performance and at the level of individual components. For example, the probability of matching the pulseheight on the two sides of double-sided silicon strip detectors in order to reduce the number of ghost hits [3] has been evaluated, and so has the impact of

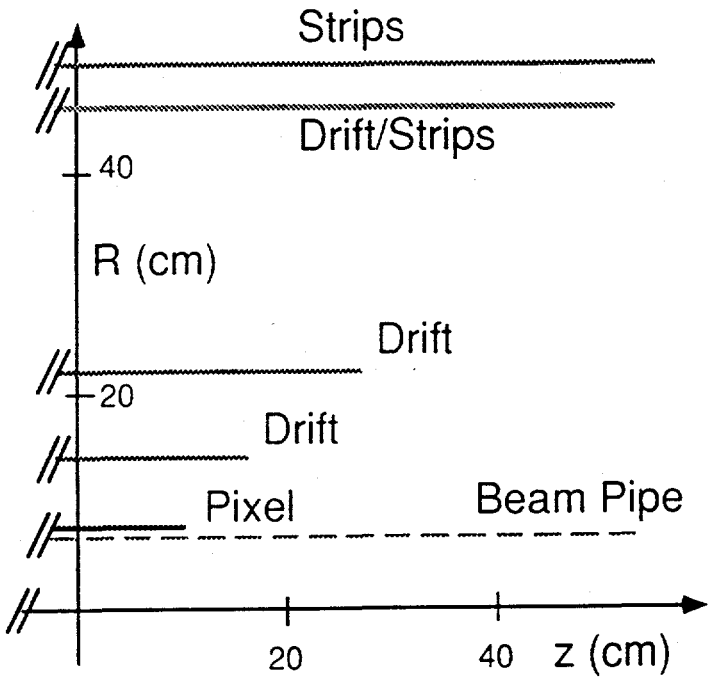

Figure 1. Transverse half-section of the Inner Tracking System

Table 1
Nominal parameters of the various detector types

Type	Spatial precision (μm)		Two-track resolution (μm)		Cell size (μm)	Module size (mm)	Channels per module
	$r\varphi$	z	$r\varphi$	z			
Pixel	22	78	150	540	75x270	4.8x69	16384
Drift	25	25	500	200	–	57x70	448
Si Strip	30	1000	200	7000	100x50000	75x50	2x750
MSGC	60	1000	800	12000	200x25000	100x50	2x1000

different algorithms on the resolution of SDDs [4]. The spatial resolution of the individual detectors has been simulated using the expected particle mix and momentum distribution, a detailed description of the detector performances and very conservative estimates for the performance of the electronics [2]. A few results are summarized in Table 3.

To give a feeling of the possibilities of the ITS as it is now conceived, we give here a few relevant plots from our overall detector performance simulations [1]. Tracks are first found in the TPC alone, with an efficiency of $\approx 93\%$, practically independent from p_t down to 100 MeV/c, with a negligible number of ghost tracks. Then, using the parameters from the TPC, we search for hits matching both in position and in angle in the outermost two layers of the ITS. The result, obtained for π, is shown in Fig. 2; for $p_t < 200$ MeV/c the efficiency drops below 90%. Including the inner layers in the search strategy, the matching efficiency improves substantially, remaining above 95% down to 100 MeV/c, with less than

Table 2
Physical parameters of layers

Layer	radius (cm)	Area (m^2)	Type	Detector modules	Electronic channels (k)	Barrel dissipated power (W)	Endplates dissipated power (W)
(1)	7.5	0.12	Pixel	400	6550	160	
(2)	14	0.34	Drift	96	45	75	430
(3)	22	0.75	Drift	192	90	150	860
(4a)	46	2.97	Drift	765	350	600	3400
(4b)	46	2.97	Si Strip	900	1440	1850	
(5a)	50	3.47	Si Strip	924	1400	1800	
(5b)	50	3.47	MSGC	700	1400	1800	
Tot		7.65			$\approx$ 9000	$\approx$2800 to $\approx$4000	$\approx$ 4700

Table 3
Selected simulation results for some detector types

Type	Spatial precision (σ in μm)		Average cluster size	
	$r\sigma$	z	$r\sigma$	z
Pixel	19	52	1.3 (pixels)	1.4 (pixels)
Drift	32	20	2.0 (anodes)	3.0 (FADC bins)
Si Strip	27	1100	1.3 (strips)	

5% ghost tracks. Finally, we consider the track finding of very low momenta using only the ITS. The main reason is the rejection of asymmetric Dalitz pairs, therefore we concentrate on electrons. The hits of tracks reconstructed earlier are removed, and we assume that the vertex position is known with a precision of 12.5 μm (the bunch size) in the transverse plane, and of 50 μm along the beam direction. The efficiency and relative number of ghost tracks are shown in Fig. 3 as a function of p_t. In Fig. 4 the momentum resolution for pions is shown as a function of momentum, obtained with the TPC alone and with the complete tracking system, from which the improvement introduced by the ITS for large momenta can be appreciated. The momentum resolution for electrons below 100 MeV/c, obtained with the ITS only, is $\approx$10%. Finally, the impact parameter precision using the full tracking system at 0.5 GeV/c is $\approx$200 μm for pions and $\approx$500 μm for protons. The result using the TPC only would be $\approx$1 cm for 0.5 GeV/c pions and therefore not sufficient for the reconstruction of hyperon decays.

The expected dE/dx resolution of silicon detectors has been simulated using as single detector response a modified Landau distribution which accurately describes the observed pulse-height distribution in 300 μm silicon detectors. The truncated mean using the two lowest out of four measurements is almost Gaussian with a σ of 10%. The result for tracks

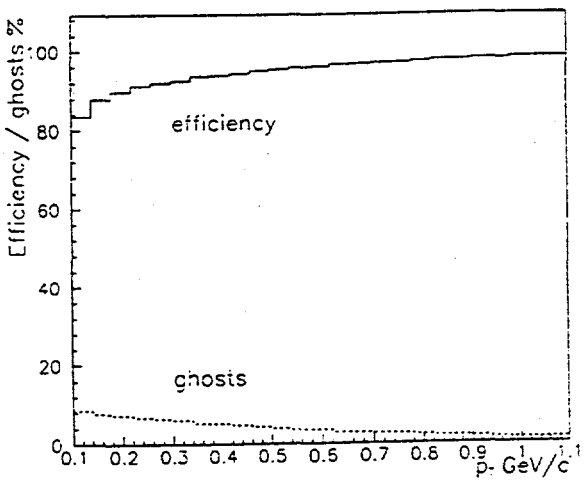

Figure 2. Efficiency of the connection and probability of incorrect matching between TPC and ITS as a function of p_t.

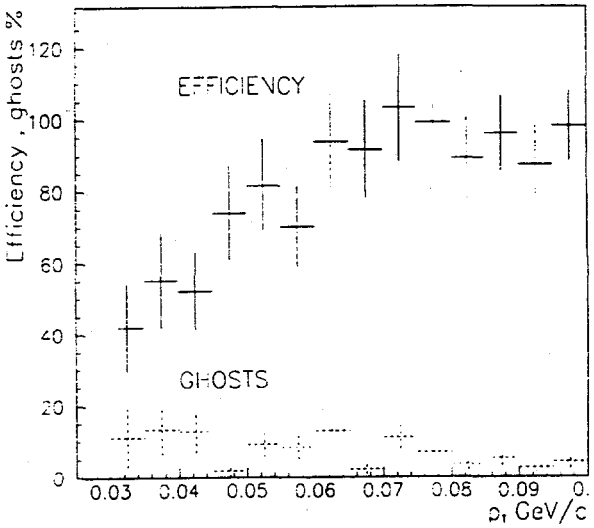

Figure 3. Efficiency of the track finding and relative ghosts yield as a function of p_t in the low momentum range.

with only three measurements are only slightly worse with a σ of 12%. The most probable energy loss in 300 μm Si is shown in Fig. 5. including density effects [1]. From this plot can be seen that the dE/dx measurement in the ITS will provide sufficient separation in the regions $p < 140$ MeV/c (e/π). $p < 520$ MeV/c (π/K). and $p < 1$ GeV/c (K/p).

3. DETECTOR R&D

3.1. Silicon Pixel Detectors

We have decided to use Silicon Pixel Detectors for the innermost plane mainly because of their optimum granularity. which will allow an occupancy below 0.5%. but also because of the simpler cooling as compared to SDD's and to provide and easily aligned reference plane for position calibration of the ITS. The small area of the first plane makes the cost tolerable. while the rapidly advancing R&D program assures its feasibility.

For the silicon pixels we follow an hybrid design with eight readout chips bump bonded to one detector, and with detecting elements of 270 μm $\times$ 75 μm. They will be assembled in ladders of four each. and the barrel will consist of 100 such ladders in a turbo assembly, since the size of the electronics will exceed the one of the detectors. We foresee to apply the same frontend architecture presently being used for the Omega-Ion experiment, which satisfies our requirements for the trigger scheme. the readout speed and the power consumption. In this scheme. the pixel information is stored as a digital bit. and read out sequentially on few lines. The results of the RD19/Omega-Ion development are indeed impressive [5,6]: a full four-plane telescope of 53 $\times$ 55 mm planes of pixel detectors has been succesfully built and operated. The pixel size is 75 μm $\times$ 500 μm. and the system of $\approx$300k sensitive elements has been functioning with about 2% dead pixels. In Fig. 6 is shown a photograph of one plane of the Omega-Ion setup. and in Fig. 7 one ladder assembled with the electronics.

The main developments which we still foresee are a reduction of about a factor two in the pixel size. which should be obtained by going from the 3 μm technology to the 1.2 μm

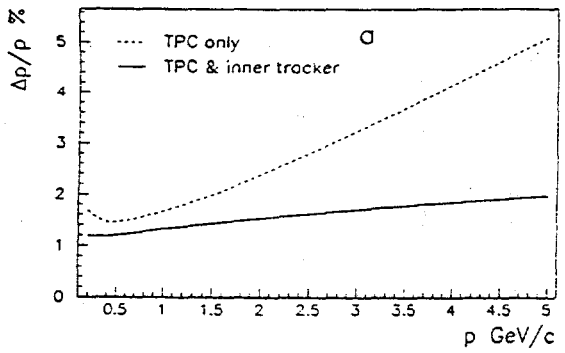

Figure 4. Momentum resolution as a function of momentum obtained by the TPC alone and by the TPC with the ITS.

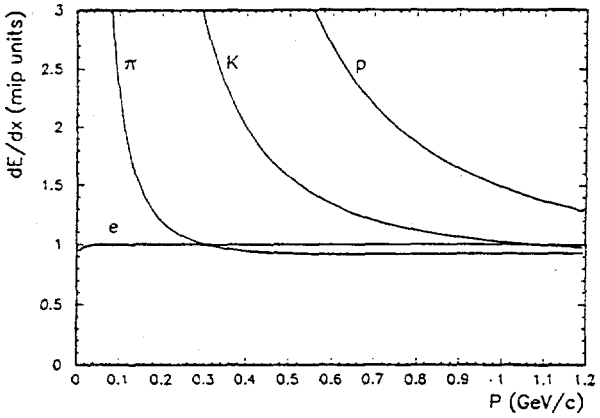

Figure 5. Most probable energy loss in 300 μm Silicon for e, π, K, p as a function of momentum, normalized to 1 at high p_t.

one, and, more important, the integration of the bus onto the chips themselves, in order to exclude the ceramic support. The latter does not pose principle problems, since there are no active elements in the fanouts. Finally, if mechanically stable, we would use 150 μm thick detectors, which have also succesfully been tested by RD19.

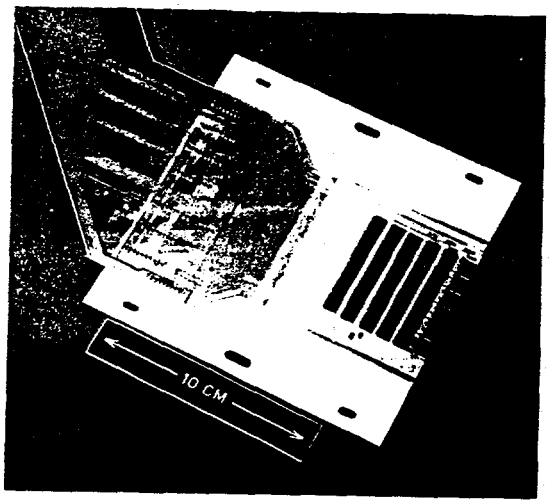

Figure 6. Photograph of one plane of the Omega–Ion pixel telescope

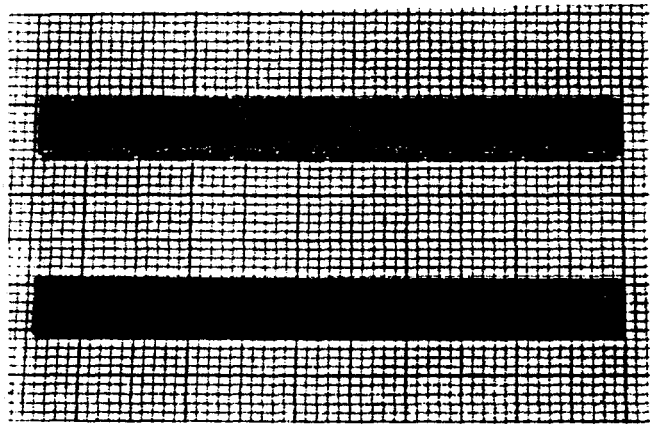

Figure 7. Photograph on one ladder assembled with the redout chips.

3.2. Silicon Drift Detectors

SDDs are ideally suited to this experiment, in which very high particle multiplicities are coupled with relatively low event rates: they exploit the measurement of the transport time of the charge deposited by a traversing particle to the collection electrodes to localize the impact point in one of the dimensions, thus enhancing resolution and multitrack capability at the expense of speed. In the NA45 experiment, a cylindrical SDD has

operated with track densities much larger than the ones foreseen for ALICE.

In a linear SDD a series of parallel strips on both surfaces of the high-resistivity silicon wafer, connected to a voltage divider, provides the electrostatic field which focuses the charges in the middle plane and forces them to drift parallel to the wafer surface to the collecting anodes. The small size of the anode, and hence its small capacitance ($\approx$ 50 fF), makes very low noise levels attainable. The coordinate perpendicular to the drift direction is measured by the position of the centroid of the collected charge. A space precision of better than 25 μm in both coordinates can be obtained for most of the detector surface. A two-track resolution of 150 μm is feasible by performing a waveform analysis, while 500 μm can be considered a worst-case figure.

Linear SDDs have been succesfully produced at both the BNL and the LBL labs in the USA, but for ALICE, given the large number of detectors needed, it is mandatory to establish industrial production. In a dedicated R&D effort (INFN DSI project) we are developing a detector design suitable for production by industry, which follows the philosphy of the ones developed for the UA6 [9] experiment at CERN and the STAR [8] experiment at RHIC. At the moment, a set of prototypes has been produced for DSI by CANBERRA, Belgium, trying a number of different designs and technological options. Following the tests on these prototypes, which are in progress now, we will define the choices for a detector of large area, i.e. as large as possible within a 4" wafer, optimized for ALICE. The optimization process will involve in particular a careful minimization of the guard areas. A photograph of one of the first prototypes produced by CANBERRA for our R&D is shown in Fig. 8. The sensitive area is split in two parts so that electrons drift in opposite directions in the two halves of the detector. The central electrode is the strip at the highest, negative, potential and the voltage is distributed to the electrodes by an integrated voltage divider. The anode pitch is 250 μm.

To establish the possibility of producing large numbers of SDDs, we have also studied the uniformity of the resistivity of Neutron Doped n-type high-resistivity silicon [7], from a large batch of 4–inch wafers which we also use for our prototypes. From our results, which included measurements both before and after several processing steps, we are confident that this material will be adequate for the production of large–area SDDs.

For the readout, we foresee at present that each anode pad will be wire-bonded to a low-noise preamplifier-shaper with Gaussian shaping, followed by a Switched Capacitor Array (SCA) [8]. We have developed within DSI a 32–channel frontend chip in bipolar technology [10] (OLA). The chip has been succesfully produced and tested, and is described in detail in [10]. Let us recall here that the circuit has a peaking time of $\approx$60 ns, the noise is below 300 electrons at zero input capacitance and the power consumption is 2 mW/channel, mostly due to the output driver. The on–detector readout boards and the low–mass interconnections, e.g. kapton ribbon cables with dense Al traces [11] are critical for our design, and prototypes are being developed.

3.3. Strip Detectors

Double–sided silicon strip detectors can be considered well understood, since a large system is in operation [12] and more are under construction. Therefore, our development effort is concentrated on the production of very simple detectors, which, thanks to the limited number of processing steps involved, could be fabricated at low cost and with good

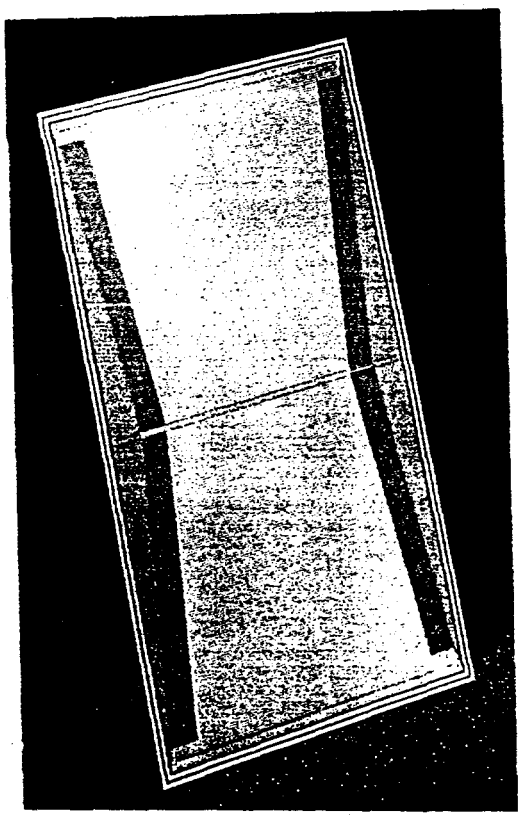

Figure 8. Photograph of one of the prototypes produced by CANBERRA for the DSI R&D project

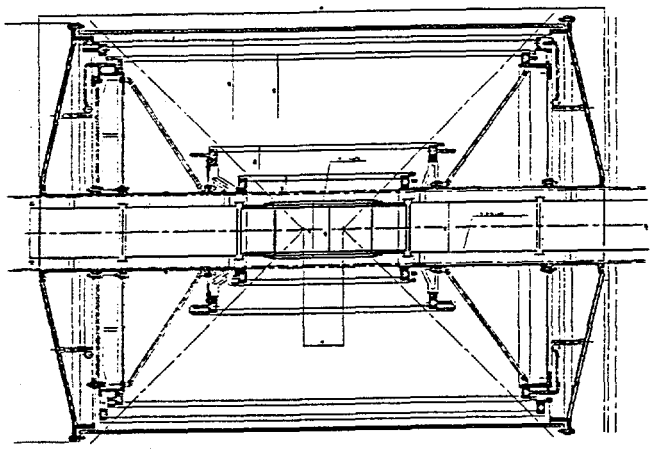

Figure 9. Side view of the mechanical support of the ITS. The independent 1st layer is situated directly on the central part of the beam pipe

reliability. A specific effort in this direction is being pursued by the Ukrainian groups of the collaboration. A first set of prototypes ha been designed and is now in production.

For the Microstrip Gas Chamber, the R&D effort is carried on within the RD28 collaboration. The development specific to ALICE is centered on the assembly and readout problems linked to our setup, in which double-sided readout with a small stereo angle is foreseen. We are exploring both a single-gap solution and a double-gap (i.e. two MSGC's back to back) one. The efficiency of MSGCs for inclined tracks, essential to reconstruct low-momentum particles, has been specifically studied, with encouraging results.

For the silicon strip and gas microstrip detectors we have done a conceptual study of a frontend chip based on BiCMOS technology. This choice would allow an optimized preamplifier to be integrated together with a storage cell, a multiplexer and the ADC, making best use of the low rate environment, which does not require a pipeline, and minimizing the interconnections (one output line per detector). A prototype version of this chip is now being designed.

4. MECHANICS AND COOLING

Since the minimization of the material thickness is an absolute priority, the support and cooling system is the object of a specific, extensive development program [13]. We

are studying a support structure in which the material is concentrated in the conical endplates, covering a minimum solid angle, and the detectors are organized in ladders, parallel to the beam direction and held by linear structures (ribs). At this stage we are studying three possible options, which arise mainly from different assembly schemes: a) rigid end-caps and outer honeycomb cylinder that form a space structure to support Si ladders; b) clamshell design; c) five relatively independent cylinder detectors supported by the cone end-caps and the outer honeycomb carbon fiber cylinder, (shown in Fig. 9). We will use high modulus Carbon Fiber Composites both for the space-frame Si ladders support and for the general support of the Tracker, because of their high mechanical properties and very low CTE that can be matched with that of Silicon by using additives.

4.1. Cooling

The cooling scheme determines the overall mechanical construction and is a key point to the design of the ITS. Different schemes (gaseous, liquid, evaporative) have been studied [14] and two options were selected for further development:

– localized, evaporative cooling in a closed system under atmospheric pressure for the Si-drift and Si-strip (or MSGCs) detectors, that is expected to provide uniform temperature fields (within 3–4 °C in the detector volume) and a thermostabilization of the whole ITS of the order of 0.1 °C at ambient temperature. Such scheme should also allow minimal stresses at turn-on and switch-off and optimize the total amount of material. As a coolant, we favour the use of C3F7I which has boiling temperature of 25-20 °C under 1 bar pressure. The total amount of condensed coolant in the volume of the ITS can be estimated to be 0.5-1.0 kg. Tests of a 1 meter ladder prototype with a 3 mm a freon cooling artery have confirmed our calculations, giving a temperature gradient along the ladder within 0.8 °C for up to 25 W power. The main problems now under study are the efficient heat drain from the front-end electronics to the cooling arteries and the control of the local liquid freon supply. A prototype system using separated phases and allowing a very thin device is now under test [14]

– uniform gas cooling of the first layer. In the first layer, composed of pixel detectors, the heat will be produced uniformly with a density of 0.13 - 0.17 W/cm^2. Since the temperature gradients for pixels are limited only by alignement and mechanical stability, gas cooling of this layer is possible, using the cylinder gap (1.5 cm) between the first layer and the beam pipe as channel for the gas flow.

4.2. The ladders

The ladder design has evolved significantly during the R&D phase. The first prototype was a linear supporting structure formed by a carbon fiber semicylinder shell (diameter 5 mm,thickness 0.4 mm), housing the 100 μm Al pipe of 3 mm in diameter that serve as cooling channel and as a power bus 10. The thermoconductive Al pipe helps to provide a uniform temperature along the line, avoiding the formation of hot spots.

Afterwards, we have investigated several alternative designs. One of them, shown in Fig. 11, is based on lateral blade ribs and a central cooling artery; super thermoconductive graphite fibers are used for the local heat drain from the electronics to the cooling arteries. The latest prototype, which we consider most promising at the time, is a carbon-fiber ladder support structure which, still respecting the limits on the total amount of material, should show 20 μm sagging over 1 m length. A 1.1 m monolithic prototype of this design

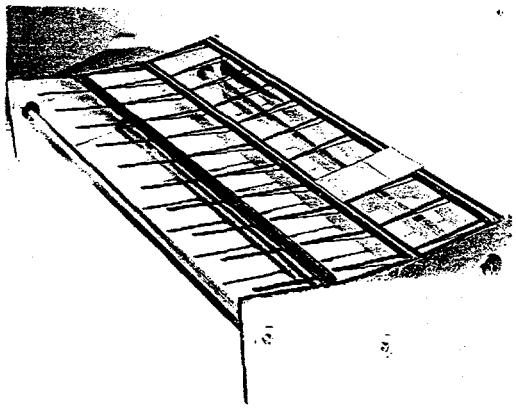

Figure 10. Photo of the 1st 0.5 m carbon fiber ladder prototypes

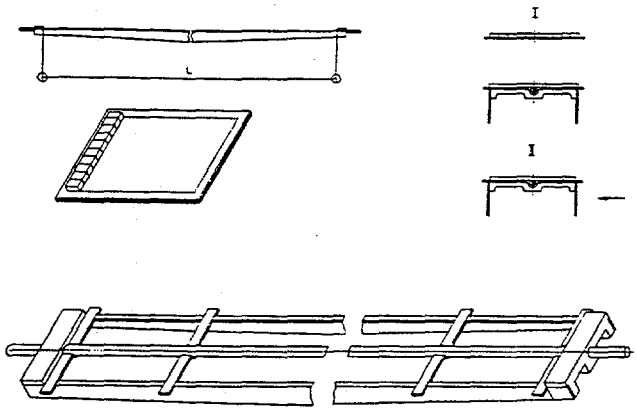

Figure 11. Ladder design with central cooling artery and blade ribs

has been manufactured in carbon fiber and is now under test.

The exact amount of material in each layer will be fixed only after the finalization of the design, but we have developed estimates of material for a realistic case, which has been calculated to provide enough mechanical precision and satisfy the cooling requirements; the result is about 0.27% of X_0 per layer, of which about half due to the coolant fluid, in addition to the detector modules, which are on average 0.33%, giving a total of 3% of X_0 for the ITS with five layers.

REFERENCES

1. N.Antoniou et al., CERN/LHCC/93-16.LHCC/I 4 . 1 March 1993
2. B.Batyunya and A.Zinchenko, ALICE/94-31. November 1994
3. M.Monteno, ALICE/94-13, June 1994
4. M.Kozlowski et al, ALICE/94-10, May 1994
5. E.H.M. Heijne at al, CERN/ECP 94-1, 10 March 1994
6. F. Antinori et al, proceedings of Quark Matter 1995 conference.
7. S. Beolé et al, proc. of the 6th Pisa Meeting on Frontier Detectors for Frontier Physics, 1994, to be published in Nucl. Instr. and Meth.
8. STAR collaboration, Conceptual Design Report for the Solenoidal Tracker At RHIC.
9. A. Vacchi et al, Nucl. Instr. and Meth. A306 (1991) 187.
10. W.Dabrowski et al. proc. of the International Conference on Advanced Technology and Particle Physics, Como, Oct. 1994, to appear in Nucl. Phys. B, proc. suppl.
11. V. Bortchev et al., ALICE/94-28
12. G. Batignani et al., NIM A326 (1993) 183-188.
13. G.A. Feofilov et al., proceedings of the International workshop on Advanced Materials for High Precision Detectors, Archamps 19 94. CERN 94/07.
14. O.Godisov et al., proceedings of the WELDEC Workshop, Lausanne, Oct.1994

Particle Identification Using Time-Of-Flight Technology for the ALICE Experiment

H.R. Schmidt, ALICE-Collaboration
GSI Darmstadt

The large multiplicities expected for LHC Pb+Pb collisions require new developments in particle identification techniques. Presently, Pestov Spark Counters, low pressure Parallel Plate Chambers and scintillators with photo multiplier readout are under consideration.

1. INTRODUCTION

The particle identification (PID) capabilities (>2σ mass separation) of the Inner Tracker and the TPC of the ALICE experiment are limited to the $1/\beta^2$ regime, i.e. to momenta $p_{\pi,K} <$ 0.8 GeV/c (Fig. 1). In order to extend the PID to higher momenta it is necessary to supplement the dE/dx measurements by high resolution time-of-flight (TOF) or velocity measurements. This will allow to measure inclusive particle spectra or particle ratios up to 4 GeV/c (2-3σ mass separation) and event-by-event observables as well as high p_t-phenomena up to 3 GeV/c (3-4σ mass separation). Hereby a TOF resolution σ≈100 ps is assumed, which yields the combined mass separation of the TPC and TOF as shown in Fig. 2.

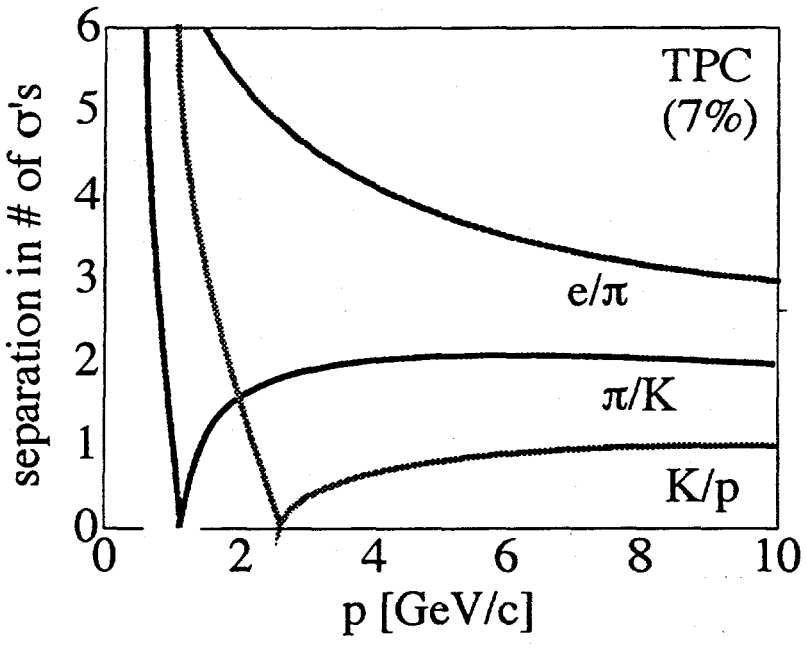

Fig. 1 Particle identification capability of a TPC with 7% dE/dx resolution.

The requirements to the detector are dominated by the large multiplicity of charged particles expected in the acceptance ($|\eta|<1$) of the TOF barrel, i.e. up to 12000 charged particles ($dN_{ch}/dy=8000$). This gives a particle density of more then 100 particles/m^2 at a barrel radius of 3 m, and hence a cell size of $\approx$ 10 cm^2 for a double hit probability of 5%.

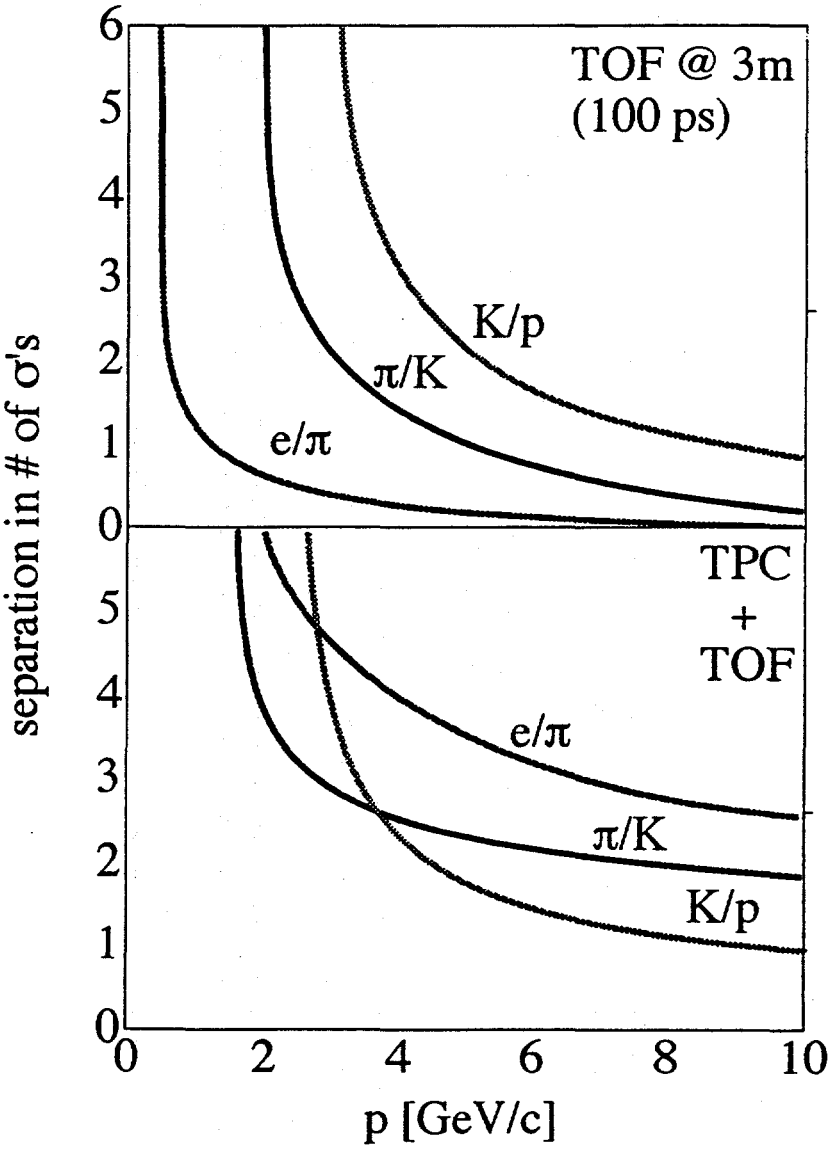

Fig.2 Particle identification of the TOF counters alone (top) and in combination with the TPC of Fig. 1 (bottom)

Several TOF techniques have been devised: the Pestov Spark Counter as base line option, Parallel Plate Chambers (PPC) and conventional scintillator with photo multiplier readout. The pro's and con's of these options are summarized in Table 1.

Table 1

		
Pestov Spark Counter		
GSI Darmstadt BINP Novosibirsk JINR Dubna MEPHI Moscow	• best time resolution • very good 2-dim. position resolution • no preamplifier • suppressed response to background radiation • potentially cheap production	• new technology • limited lifetime • limited count rate capability • gaseous counter • new electronics needed
Scintillator with photo multiplier readout		
INFN Catania University of Athens JINR Dubna	• known technology, robust • good time resolution • easy handling production	• expensive (PMT)
Parallel Plate Chambers		
ITEP Moscow	• relative simple design • cheap production	• bad time resolution • low efficiency • gaseous counter • needs preamplifier

2. SCINTILLATOR WITH PHOTO MULTIPLIER READOUT

For this option the technology is well proven. However, the large number of cells requires a substantial reduction of the price of PMT's. In addition, the tubes have to be of the "fine-mesh" type since they will be operated in a magnetic field. A collaboration between the University of Catania and the JINR Dubna has been formed with the goal to develop the mass production technology for fine-mesh tubes in Russia.
Alternatively, the properties of (commercially available) multi-anode photo multipliers are investigated. Here the main limitation comes presently from the pixel sizes (<1 cm^2), which limits the effective thickness of the scintillator and hence the primary photon yield severely.

3. PARALLEL PLATE CHAMBERS

A Parallel Plate Chamber (PPC) is a single gap gaseous detector with planar electrodes working in the avalanche mode. It consists of two planar metallized electrodes made of ceramic or plastic and kept at a fixed distance (0.5 - 2 mm) by spacers (Fig. 3). The working surface is of size from 30 x 30 mm^2 up to 60 x 60 mm^2, while the detector thickness is about 3 mm. A high uniform electric field (4 - 6 kV/mm) applied between two flat and parallel electrodes yields immediate Townsend amplification of the primary ionization. The motion of electrons in the avalanche induces a very fast (with a risetime about 1 nsec) signal on the electrodes. The gas gain up to the order of 10^4 can be obtained without sparking.

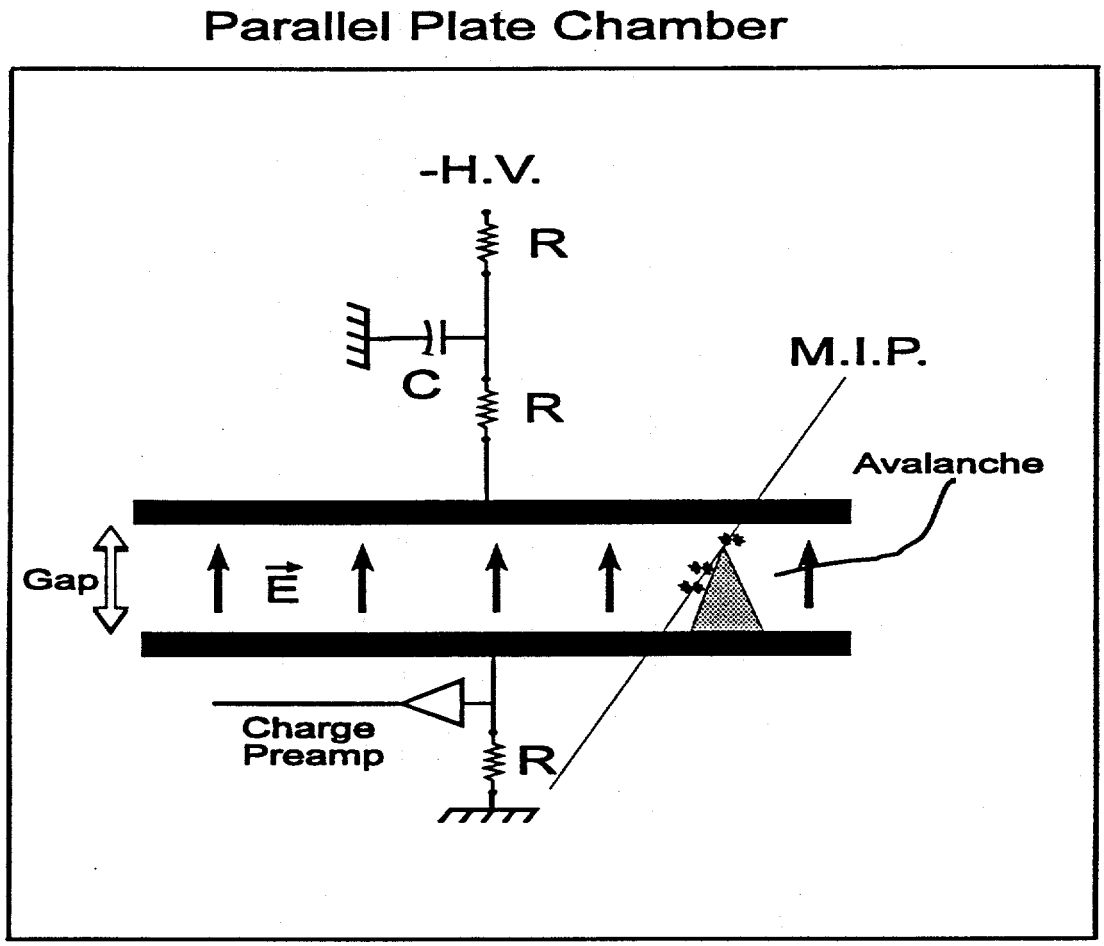

Fig. 3 **Sketch of a PPC and of it's HV and readout circuits**

The performance of PPC's has been evaluated in test beam setup at ITEP. After subtraction of the contribution of the trigger counters an intrinsic resolution of 190 ps (Fig. 4) is extracted. The efficiency of the counter is larger than 65%. The efficiency and the timing resolution of a PPC can be improved by using a double gap version. In this case the PPC will have two gas gaps. The central electrode is produced from thin mylar foil and the high voltage is applied to the two outer electrodes. The preamplifier is connected to the inner electrode.

The overall performance of the TOF system based on PPC could be enhanced by using several layers of PPC's. The final choice would require a compromise between the desired timing resolution and the thickness and complexity of a multi-layer TOF-barrel.

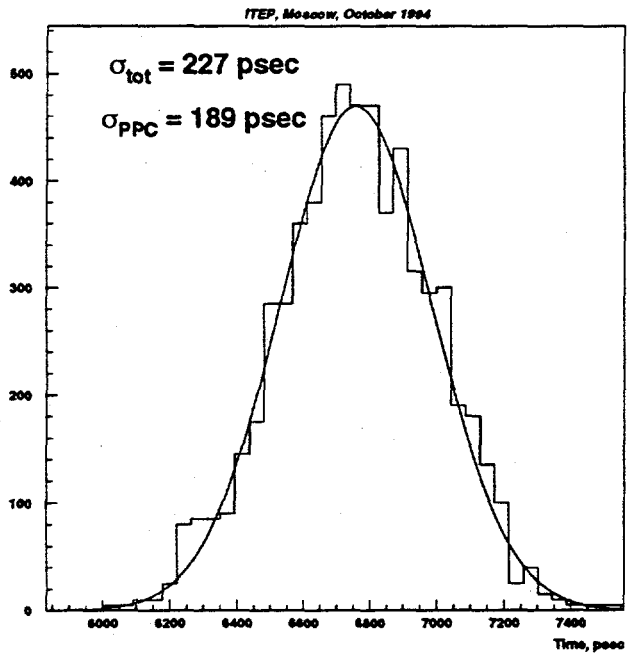

Fig. 4 Time resolution obtained with a PPC

4. PESTOV SPARK COUNTERS

A schematic layout of the Pestov Spark Counter is shown in Fig. 5. This detector is a gaseous parallel plate counter working in the streamer mode. The spark gap is only 100 μm and the working gas is Ar at a pressure of 12 bars. The major feature of the counter is the use of a special, highly resistive glass ($\rho \approx 5 \cdot 10^9 \Omega$cm) as anode which, together which the admixture of several quencher gases, keeps the discharge after a spark local.

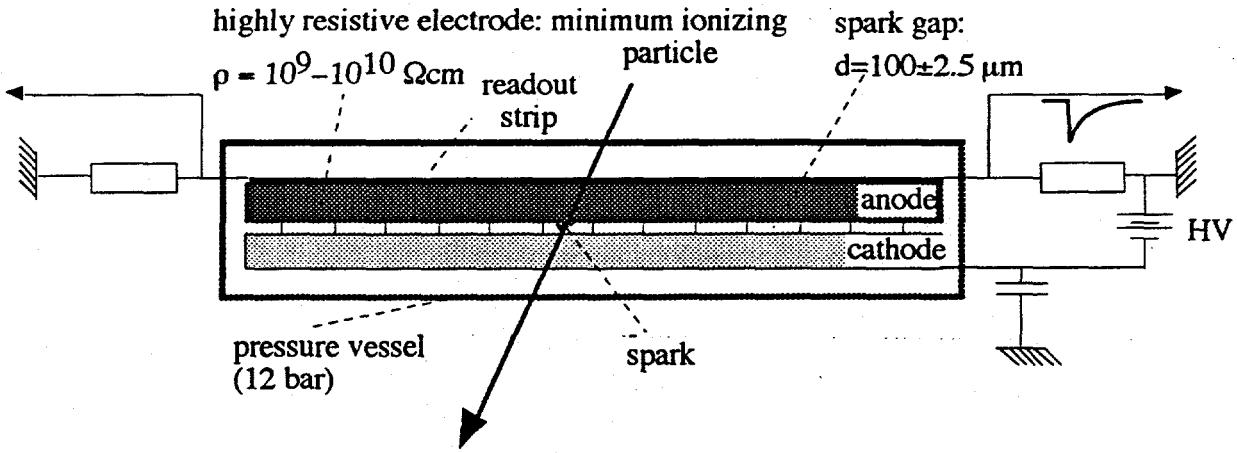

Fig. 5 Schematic layout of the Pestov Spark counter.

Prototype studies of this counter type at Novosibirsk [1] have shown that a time resolution of up to 25 ps, an efficiency close to 100%, a position resolution better then 500 μm and a rate capability of 20 kHz/cm^2 can be reached.

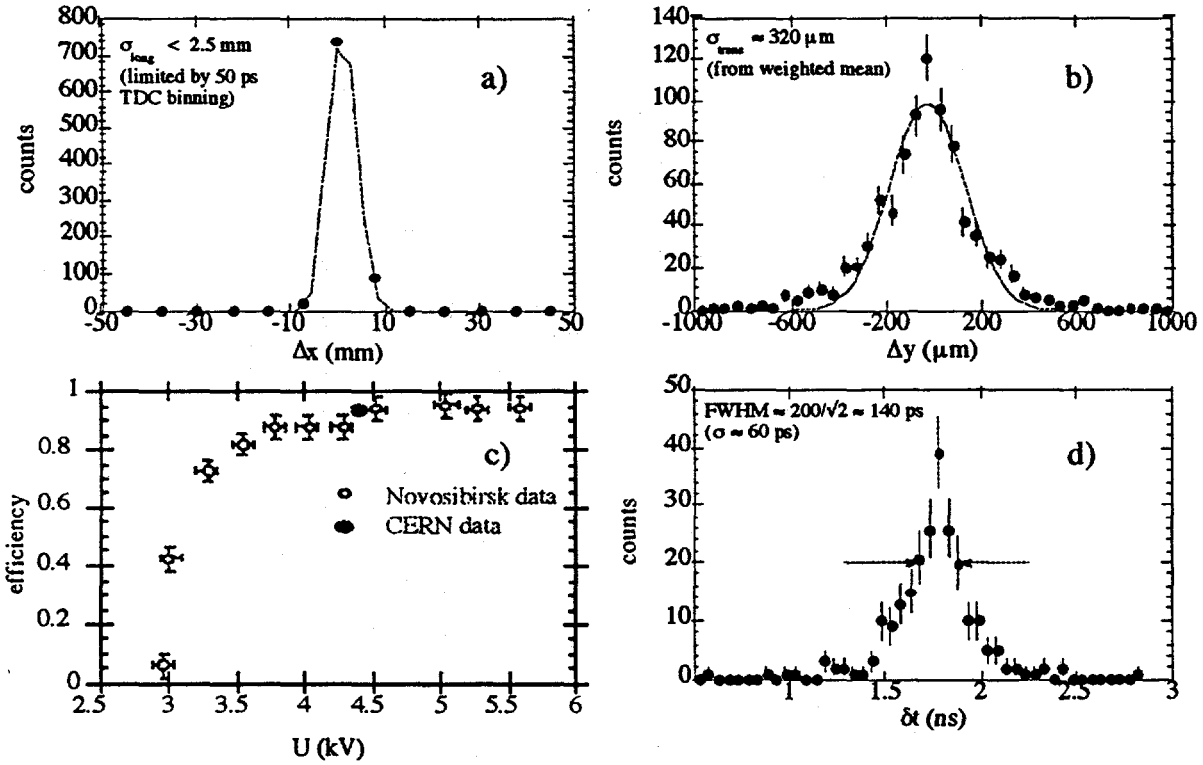

Fig. 6 a) Longitudinal position resolution from left-right time difference; b) transverse position resolution from weighted mean over three strips; c) absolute efficiency obtained at CERN (closed circle) from measuring two counters in coincidenc in comparison with earlier results from Novosibirsk (open circles); d) intrinsic time resolution from two counters in start-stop mode.

Basically, this performance has been reproduced by counters build at GSI Darmstadt in collaboration with BINP Novosibirsk. Figs. 6 shows the performance in terms of efficiency (c) position (a,b) and time resolution (d) obtained in a CERN test run. However, the time resolution in these test was limited to $\sigma \approx 60$ ps, mainly because the standard leading edge discriminators used did not match the characteristics of the pulses from the counter.

The major task of R&D work to be carried out is to develop spark counters (and establish their performance in terms of time and position resolution, stability of operation and lifetime) whose components are suitable for mass production in industry. This task includes in particular the development of:

- mass production techniques of semi-conductive glass anodes with a bulk resistivity in the range of ($\rho \approx 5 \cdot 10^9 \Omega$cm);
- metallic (or metallized) cathodes free of any surface defects;
- miniature spacers to maintain the spark gap of 100 μm with a precision of better then 3% at a minimal efficiency loss due to dead area;
- means of signal transportation from the location of the spark to a the discriminator with minimal loss of timing resolution;

- a discriminator with close to zero time walk for fast pulses (≈300 ps rise time);
- a time-to-amplitude converter chip.

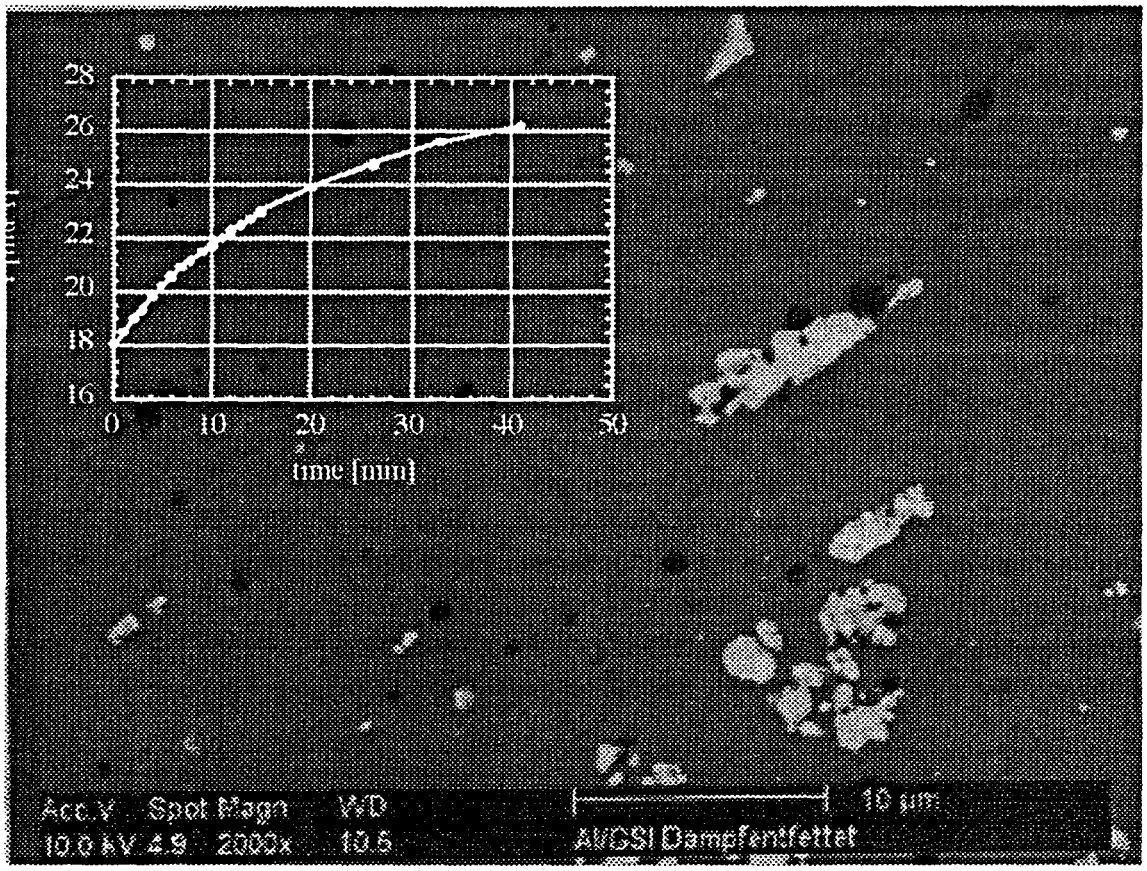

Fig. 7 Electron microscope picture of the surface of diamond polished bulk aluminum. The insert shows the time dependence of the background rate of a counter equipped with this cathode.

4.1. Glass

An R&D effort has be initiated at the SCHOTT Werke, Mainz. The difficulty to produce this type of iron-oxide glass is to control the redox and crystallization processes which are responsible for the final physical properties and, most important, the resistivity of the glass. First test meltings at SCHOTT have shown that most of the relevant physical properties of the glass are at hand and the prospects for a controlled adjustment of the resistivity to the proper value are promising.

4.2. Cathode

Previous experience with the counters build at GSI and CERN has shown that vacuum evaporation onto float glass can, -in principle-, produce cathodes of sufficient quality. However, the evaporation must proceed via diffusion and, in order to obtain zero pin hole density, two layers of copper have to be evaporated onto a chromium layer applied first for

better sticking. Thus, in order to circumvent this time consuming procedure, alternative methods of cathode production are presently investigated. Surface of high enough quality are, -in principle -, manufactured by diamond polishing. Counters equipped and tested with bulk aluminum cathodes have shown a rather high background rate (20 Hz/cm^2), depending on time span of operation and operating voltage. Electron microscope pictures of the cathode used show a large density ($\approx 10^6$/cm^2) of microscopic ($\approx \mu$m) defects in the aluminum as shown in Fig. 7. Also shown as insert is the time dependence of the background rate. These types of defects, presumably originating from the aluminum production process were found in all types of commercially available aluminum alloys investigated.

4.3. Electrostatic Properties

To minimize field irregularities in the vicinity of spacer the geometry has to be optimized with respect to its electromagnetic properties. For that purpose the program MAFIA [2] is used. MAFIA is an interactive program package for the computation of electromagnetic fields. It is based directly on the fundamental equations of electromagnetic fields, the Maxwell equations. Basic to the simulation is the theory of discrete Maxwell grid equations, the Finite Integration Technique (FIT). This self-contained theory allows the formulation in form of algebraic matrix equations. The matrices fulfill the same formal relations as the differential operators in the basic field equations. The vector solutions on the 3-dimensional grid possess the same physical properties as the electromagnetic fields.

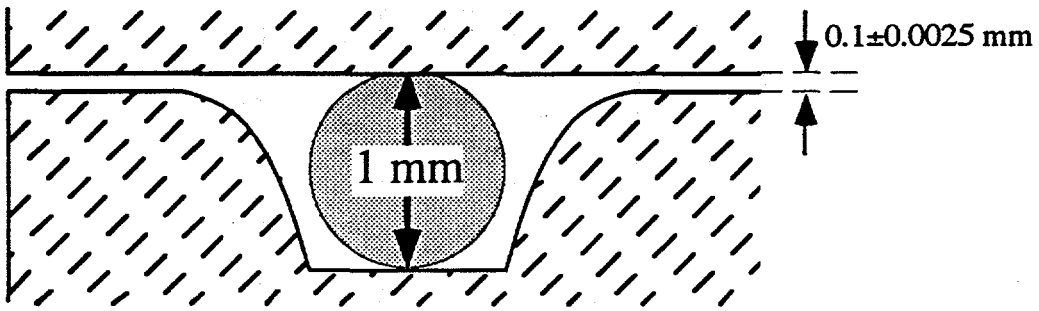

Fig. 8 Spacer design to maintain a 100 μm gap between the electrodes.

As the counter is operated close to a twofold overvoltage (6□MV/cm), any geometric irregularities (spacers, edges) have to be optimized carefully for minimal field distortions, which would lead to spontaneous discharges. To realize spacers, which maintain the spark gap of 100 μm under an electrostatic pressure of 1.5□N/cm^2, it is proposed to drill a hollow in the anode and use glass marbles ($\varepsilon \approx 2.5$) as spacers, as shown in Fig. 8. The curvature in the picture can be parametrized as $f(x) = x^n$.

The computation time depends on the number of grid-points, but doesn't exceed a few seconds. For detailed analysis 1-dimensional histograms, which show the field strength as a function of a coordinate, are shown in Fig.9. The strength of the electric field in vertical direction is plotted both along the flat and the shaped electrode. The calculations are done for a curvature of $f(x)=x^n$, n=2,4. It is clearly visible that in the first an increase of about 5% in

the electric field in the region near the bending is obtained. The other (n=4) geometry yields values of less than 1%. For the field close to the lower anode different aspects become important. Going on the anode surface towards the center axis of the hollow, the fields decreases, since the distance to the cathode increases. But close to the point, where the marble touches the anode, the field is increased, due to focusing effects by the marble. Very close to the center the field drops to a low value again. Here the computational accuracy is reduced, since it is difficult to produce a grid with finite cell size, which includes spheres and rectangular objects at the same time. However the results obtained by MAFIA are in very good agreement with the ones from the reference [3].

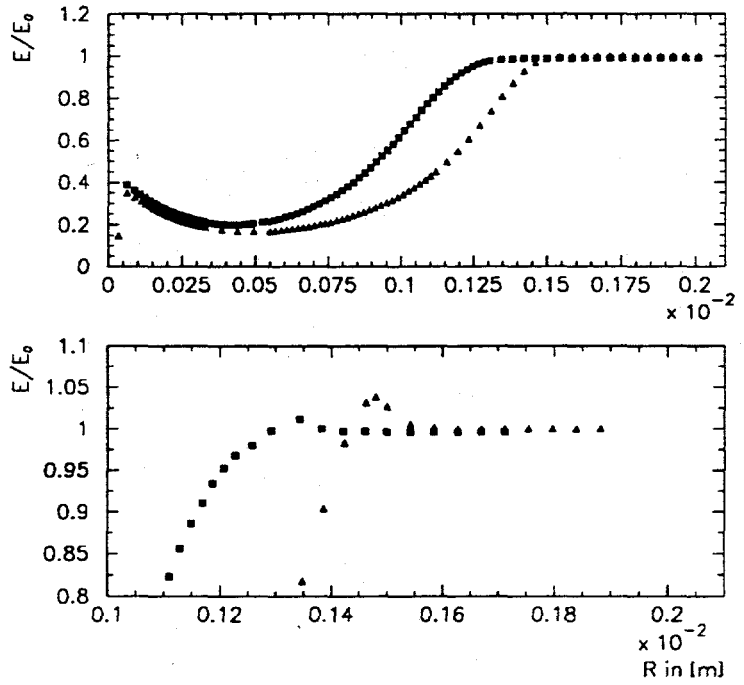

Fig. 9 Electric field strength along the flat (top) and along the shaped electrode (bottom). The triangles and squares correspond to $f(x)=x^n$, with n= 2 and 4, respectively.

4.4. Electronics

4.4.1. Double Threshold Discriminator

Both the large multiplicities expected for central Pb+Pb collisions as well as the pulse characteristics of the spark counter require the development of a specific discriminator. As for the first point, the discriminator design must be suitable for VLSI. Unfortunately, leading edge discriminators (LED) based on tunnel diodes, which have been successfully used for earlier spark counter work, cannot be integrated. As for the second point, the test of standard LED's (GSI 8001, LeCroy 623 and LeCroy 620) with spark counter pulses as well as with generator pulses yielded an electronic resolution of only 70 ps, not matching the intrinsic resolution of the counter of up to 25 ps. It should be noted that the pulses from the spark counter feature an amplitude rise time below 300 ps and an irregular falling slope. For this

reason neither standard slewing corrections of the time walk based on an amplitude measurement nor constant fraction discriminator techniques are appropriate. A solution has been proposed [4] based on the simultaneous measurement of two different thresholds for each pulse as already used for the MARK III detector at SLAC. This allows for offline extrapolations to the start of each pulse, taking the input-to-output voltage transfer curve of the LED into account. Differently from the SLAC approach, the present double-threshold discriminator (DTC) design realizes the above concept in one unit, i.e. the walk correction is performed by hardware circuits. The working principle of the DTC is shown in the block diagram of Fig. 10.

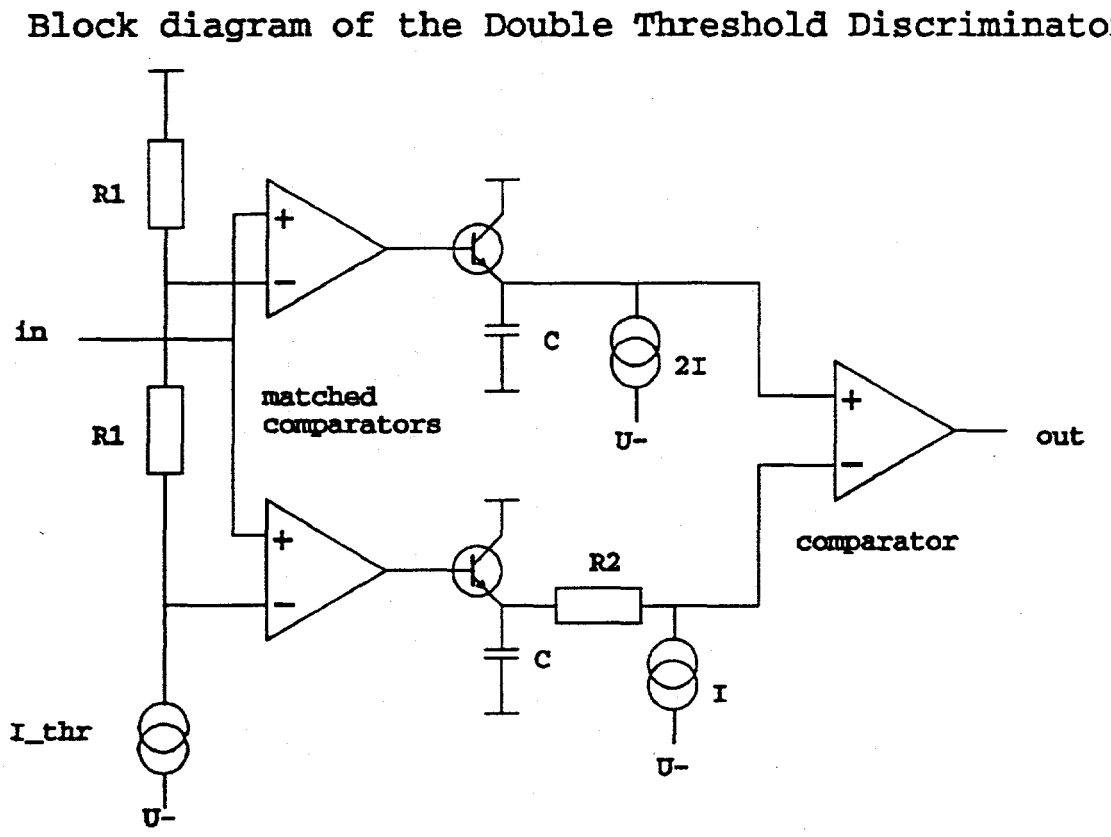

Fig. 10 Schematic layout of the double threshold discriminator described in the text.

Two input comparators with different thresholds have current outputs connected to integrated capacities C1 and C2. The potential difference from the capacities is applied to the input of at third comparator. The proper choice of resistors and capacitors yields the correct timing of the output pulse irrespective of the input rise time. A prototype circuit has been developed and tested at GSI and the dependence of the output pulse timing on the input rise time has been determined. A systematic deviation from constant timing of only 6ps RMS has been obtained.

4.4.2. Time-to-Amplitude Converter

Several groups have proposed digital TDC's or TAC's based on CMOS ns-gate arrays [5]. Common to all approaches is the necessity to interpolate between the time steps of the gates to reach sub-nanosecond resolution. At GSI a prototype TAC has been build and tested, where an analog electronics solution is used to do the interpolation. A schematic block diagram of the circuit can be found in Fig. 11.

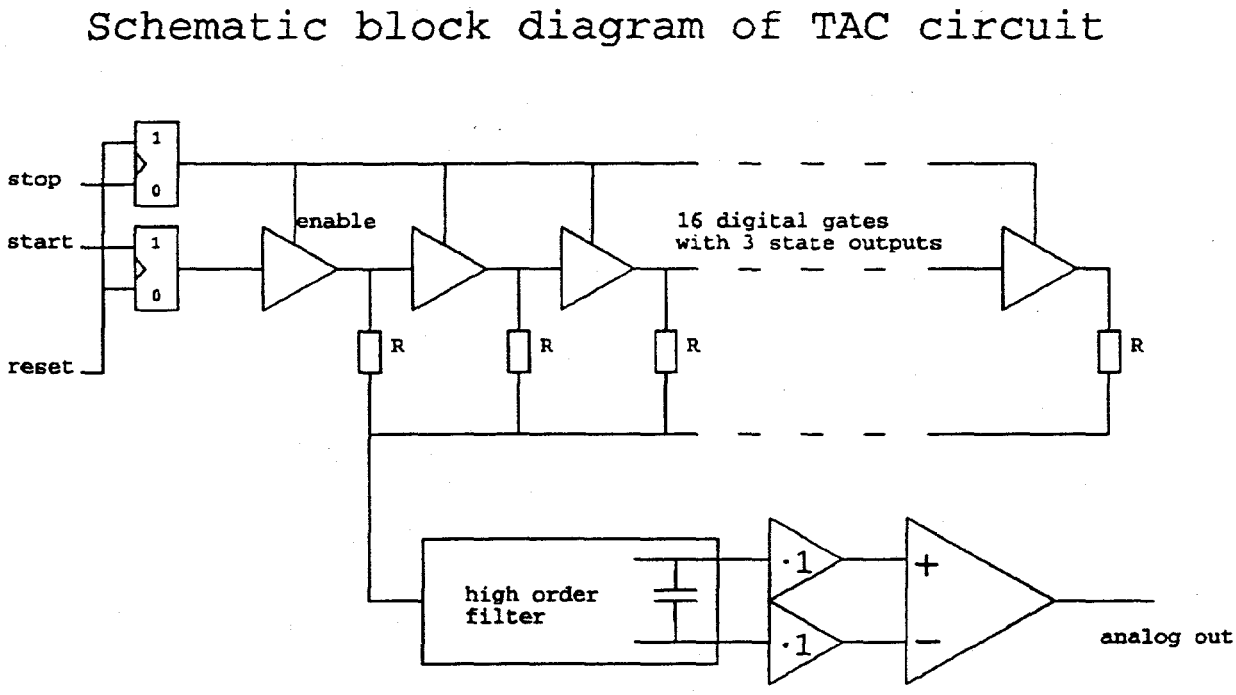

Fig. 11 Schematic layout of the TAC described in the text.

A start signal is used to set a flip-flop. The output of this flip-flop is connected to the input of a chain consisting of 16 digital buffers. In this chain every input port is connected to the output of the previous buffer. In this way a rising edge at the first buffer propagates through the chain with a velocity determined by the delay of the buffers. Separated by these delays the outputs change state from low to high. All outputs are connected via equal resistors to a common node. At this node the average output voltage of the buffers is obtained. It has the shape of a step function. This point is also connected to the input of an high order analog filter of adapted impedance. The filter is used to remove from the step function the components that create the single steps. The remaining curve increases linearly. It is obtained on a capacitor at the filter output. When the stop signal is given, the gates of the chain are set to their high impedance state. Also the capacitor at the filter output is disconnected and the charge is conserved. The voltage is read by an ADC and converted with an accuracy of 10□bit. To reset the whole circuit the flip-flops in the inputs for start and stop are reset. The whole circuit returns then to the initial state after a very short time and an output voltage of 0V is

reached very precisely. Measurements have been performed on several prototypes of the TAC. The accuracy can be determined here to be 70□ps RMS in the full range of 26□ns.

REFERENCES

[1] Yu.N. Pestov, Nim A265 (1988) 150.

[2] T. Weiland, Particle Acc. Vol.15(1984), pp.245-291

[3] Yu.N. Pestov and M.A. Tiunov, BUDKERINP 94-77.

[4] Yu. N. Pestov et al., preprint BNIP 94-31 (1994)

[5] J.F. Genat, Proc. of the 1st Annual Conference on Electronics for Future Colliders, Le Croy Corp., (1991)231; J. Christiansen et al., Nucl. Science Sym. (1993) 625

Is There a Role for Fixed Target Heavy Ion Physics Beyond RHIC Startup?

J. Sandweiss[a]

[a]Yale University
New Haven, CT

The interesting and important physics opportunities provided by AGS and CERN fixed target facilities will be far from exhausted by the time of RHIC turn on. Given the need for the AGS to provide heavy ion beams for injection into RHIC, the cost effectiveness of fixed target experimentation with AGS beams will be high. Examples of the physics are given.

1. GENERAL CONSIDERATIONS

The decision to continue fixed target experimentation with heavy ion beams at CERN and especially at the AGS should be based on physics considerations. We note that because the AGS will need to operate as the injector to RHIC, and may well need to provide test beams for ongoing development of RHIC detectors, the cost of a fixed target program will be incremental. Of course, the costs will not be entirely negligible, but the cost effectiveness of the fixed target program can be high.

While the importance of RHIC to heavy ion physics is clearly primary, it is also true that many unique and important aspects of the subject can only be addressed with the fixed target program. Thus we argue that such a program should be part of the planning for the future of high energy heavy ion physics. Fixed target experiments to be performed should be carefully selected and should represent research that is unique to the fixed target regime. We shall illustrate below a number of such areas of research. It will be clear that even the topics mentioned cannot be fully exploited before RHIC start up.

2. COMPARISON OF RHIC AND FIXED TARGET REGIMES

The importance of RHIC, of course, derives from the high energy of the collisions and the likely possibility that a high temperature, baryon free, central region will be produced. However, some aspects of heavy ion physics do not require these conditions (some, indeed, are precluded by them). In addition, the low luminosity of RHIC relative to fixed target conditions (600 interactions/s versus 2×10^7 interactions/s) precludes a variety of sensitive studies.

The study of the baryon rich region offers the highest density nuclear systems and even at fixed target energies may have sufficient excitation to produce a (baryon rich) QGP. Clearly this is a subject of considerable interest.

Fixed target energies are well above strange particle threshold and also produce baryon rich systems. They are thus the favored region for searching for strange quark matter, for multi strange hypernuclei, and for the double hyperon chiral solitons predicted from some variations of the Skyrme model. In all of these searches and studies the substantially greater luminosity of the fixed target experiments is crucial. Without it, significant sensitivities cannot be achieved.

Finally, some recent theories have proposed [1], [2] that a (baryon rich) QGP is made, but infrequently, at fixed target energies. Thus it is, in principle, possible to identify two distinct categories of events, and thus to directly illustrate that there are two distinct phases. This may actually turn out to be difficult at RHIC since every central event may make a QGP!

3. SOME EXAMPLES OF FIXED TARGET PHYSICS

In this section, we examine several topics which from today's perspective appear to be important and interesting and which require fixed target experiments.

3.1. Studies of the High Density Baryon Rich Regime

While the current program has provided considerable information on the high density, baryon rich regime, many interesting aspects will be left unfinished by the time of RHIC turn on. An example of such studies is the study of leptons and photons produced in central Au-Au or Pb-Pb collisions at the fixed target energies. Such studies, among other goals, would allow the measurement of mass shifts of vector mesons (phi and omega) due to effects of the dense medium. There are at present no experiments planned for the AGS which provides the most dense baryon rich environment. Given the complexity of such experiments and the time needed to design and mount them, none will be done if there is no possibility of operating the AGS fixed target program after RHIC start up.

3.2. Searches for Strangelets with Lifetimes <50 ns

Experiments currently underway at CERN and the AGS are searching for strange quark matter states (strangelets) with good sensitivity, approaching 10^{-11} (in AGS E-864) but are restricted to lifetimes of the order of 50 ns (or larger). Although there is reason to believe that if strangelets exist, at least some of them will have lifetimes of this order, this expectation is based on a number of assumptions. It could well be that the systematics of strangelets (if they exist) is such that they will have lifetimes of the order of hyperfragments, i.e. in the 10^{-10} second range.

The strangelets discussed here are those which are stable against the strong interaction but decay via the weak interaction. The 10^{-10} second lifetime range would be expected for the two body weak neutron decay. To amplify the statement above, the weak neutron decay is possible for strangelets that are "strangeness rich" and we would expect that not all strangelets are produced as strangeness rich. However, it may be that the production mechanism does actually make all the strangelets as strangeness rich, in which case, the current experiments would fail to detect them. An example of a production process which would do this is as follows. The collisions could produce a baryon rich QGP which ends up as a strangelet via the strangelet distillation mechanism proposed by the Frankfurt group [3]. This mechanism could well end up with strangeness rich (and negatively charged)

strangelets.

Given the importance of determining whether or not strange quark matter exists, an experiment sensitive to the shorter lifetimes would be important. As will be noted such an experiment could also carry out interesting searches for small strangelets which decay by the strong interaction but which are "metastable" due the strong interaction dynamics. Finally, such an experiment would also allow studies of multistrange hyperfragments.

3.3. Strangelet Like States that Decay by (Suppressed) Strong Interactions

As has been pointed out by Gilson and Jaffe [4], strange quark matter states of low mass may well exist which are not be stable against strong decay, but which have "long" lifetime because the strong decay is inhibited by several suppression factors.

Essentially, due to shell effects, decay via single baryon emission is energetically forbidden. Thus, the strangelet must decay by "fissioning into several Λ hyperons and a nucleus, or dissolving into Λ hyperons and neutrons". Suppression results because substantial quark rearrangement is needed. It is difficult to accurately estimate the suppression but it could be substantial. The situation is crudely analogous to alpha decay of a nucleus which is a strong interaction process but which may have lifetimes usually characteristic of weak decays.

The most striking aspect of this situation is the observation that there are a large set of parameters which predict these quasi-stable strangelets. The range of parameters is much larger than those which predict the the states which are completely stable against strong decay.

Again, these states could be searched for in a short lifetime experiment such as that mentioned in the previous section.

3.4. Multiply Strange Hyperfragments

Recently it has been suggested that properly configured hyperfragments would be stable against strong decay [5] and estimates of their production rates in heavy ion collisions have been carried out [6]. The basic idea is that if the hyperfragment contains the right "mix" of Λ^0 and Ξ hyperons, the strong decay caused by (for example) $\Xi^0 + N \rightarrow \Lambda + \Lambda$ is Pauli blocked by the Λ's already present. It is possible that states of arbitrary strangeness and large baryon number can exist.

From the estimates of [6] it appears that the heaviest state which could be detected would be ${}_{\Xi^0\Lambda\Lambda}{}^{7}He$ made in $\simeq 2 \times 10^{-7}$ of central Au-Au collisions.

These states are important to study for a number of reasons.

1. They constitute a "new" nuclear physics with four distinct particles (rather than two). Many new configurations will be permitted with interesting new sytematics.

2. Every such multiply strange hyperfragment which is identified eliminates the existence of a strangelet with the same strangeness (S) and baryon number (A) since the hyperfragment could decay by the strong interaction into the strangelet and a "weak" lifetime would not be observed. As it happens, there is considerable overlap in S and A between the possible light strangelets and the multiply strange hyperfragments.

3. The study of the systematics of the multiply strange hyperfragments could shed light on the possible existence of true strange quark matter.

3.5. Searches for Baryon Rich QGP, Infrequently Produced

Recently, theoretical calculations [1], [2] have made plausible arguments that in central Au-Au collisions at AGS and CERN energies a QGP is occasionally produced. Essentially, these calculations point out that in such a central collision the thermodynamic state produced is one for which the equilibrium configuration would be a (baryon rich) QGP. However, the duration of this situation is limited by the finite time of the collision and as a result there usually is insufficient time to nucleate a "bubble" of the plasma phase before the collision is over. However, as nucleation is a fluctuation phenomenon, it occasionally does happen that a bubble of the new phase is nucleated in the collision. When this happens, the bubble grows rapidly on the time scale of the collision and a substantial fraction of the collision volume undergoes a phase transition. Of course, as the collision proceeds the QGP cools, converts back to a hadronic system and finally the collision products "freeze out" into the final hadrons which are detected by the experimental apparatus.

The experimental problem is then one of detecting these rare but distinctive events. With the advent of modern techniques, there are now several promising approaches to doing so. We discuss, as an example, one such approach.

When a QGP is produced one almost certain consequence is the production of significantly greater entropy. Furthermore, as the collision proceeds through its various stages, the entropy never decreases. Thus, one class of signals focuses on aspects of the collision which are measures of the entropy produced in the collision. The largest effect of the increased entropy is increased pion multiplicity. In addition, one would expect some of the entropy increase to result in an expanded freeze out volume. The coalescence rate of formation of nuclei from the expanding fireball is sensitive to the density of baryons during freeze out. If the freeze out radius increases, the density of baryon decreases and the yield of coalesced nuclei will decrease. The larger the baryon number of the coalescence product, the more the rate will decrease.

Unfortunately, only the pion multiplicity can be measured on an event by event basis. However, with sufficient events, it is possible to deal with large sets of events all with very similar pion multiplicities. We call these sets "super events". For each super event we can measure the yield of coalesced nuclear states. We can thus study the two dimensional distribution in the two dimensional scatter plot of pion multiplicity versus the yield of coalesced deuterons (for example). If a subset of the events arise from QGP production, one would expect to see a "hot" spot on the scatter plot corresponding to high pion multiplicity and low coalescence yield. This can be done (with a sufficiently high rate experiment) with deuterons, tritons, alpha particles, etc. In addition the same super event approach will allow the search for hot spots in the scatter plot of pion multiplicity and antiproton yield.

Experiments whish are capable of such studies are just now coming on line. One very striking aspect of such studies is that they offer the possibility of establishing the existence of two distinct classes of events in the same family of collisions. If one of these classes would show the characteristics expected of a QGP, this would amount to convincing evidence that a QGP really exists. This demonstration may not be easy at RHIC in that

every central collision may produce a QGP and one will not be able to demonstrate in a straightforward manner the existence of two distinct phases. To show this they really have to coexist , as they might well do at fixed target energies.

3.6. Search for the Strangeness Distillation Mechanism

If it turns out that QGP production can be established as occurring in a subset of fixed target events, one can envision experiments that search for the phenomenon of strangelet distillation [3]. This can be done whether or not strangelets exist. If strangelets do not exist the distillation mechanism will produce a multi strange hyperon system. If an experiment with a high acceptance for hyperons were mounted one could look for hyperon bursts associated with the hot spots in the pion multiplicity coalescence yield scatter plots. The phenomenon of strangeness distillation requires a baryon rich QGP. Furthermore, determining whether or not it exists is a fundamental measurement in high energy heavy ion physics. As an example, we note that its existence is a strong clue that the hadron to QGP phase transition is first order.

4. CONCLUSIONS

In the previous sections we have tried to indicate that even from today's perspective there is a rich and fundamental program of physics with high energy heavy ion beams with fixed target geometry.

The examples given do not aim at constituting a complete list. Also, they have been chosen to be of interest now without assuming too much about future discoveries. Before concluding, we should remember that if a number of experiments currently underway should give positive results, it will be very important to move ahead with follow up experiments. Thus, if an H is found we will want precise measurements of its mass and lifetime and knowledge of its interactions with ordinary nuclei, etc. Likewise if strangelets are found, many questions will be most pressing. However, as has been noted above, at this time we can perceive an important and highly cost effective program deriving from fundamental questions now before us.

REFERENCES

1. K. Werner Phys. Rev. Lett. 73,1594 (1994)
2. "Nucleation of Quark-Gluon Plasma from Hadronic Matter", J. Kapusta, A. Vischer, and R. Venugopalan, Univ. of Minn. preprint 94/5-T
3. C. Greiner, P. Koch, and H. Stocker, Phys. Rev. Lett. 58,1825 (1987)
4. E.P. Gilson and R.L.Jaffe, Phys. Rev. Lett. 71,332 (1993)
5. J. Schaffner, C.B. Dover, A. Gal, C. Greiner, and H. Stocker, Phys. Rev. Lett. 71, 1328 (1993)
6. A.J. Baltz, C.B. Dover, S.H. Kahana, Y. Pang, T.J. Schlegel, and E. Schnedermann, Phys. Lett. B 325, 7, (1994)

QM95 Workshop on Physics With the Collider Detectors at RHIC and LHC

8 January, 1995
Monterery, California

T. Hallman and J. Thomas, Chairpersons

Introduction and Welcome , DeAnza III (9:00 am)

9:10	Event by Event Measurements in Relativistic Heavy Ion Physics	R. Stock (Frankfurt)
9:40	Is There a Role for Fixed-Target Heavy Ion Physics Beyond RHIC Startup?	J. Sandweiss (Yale)

10:10 Coffee

Parallel Session 1 (Morning), DeAnza III

10:30	The Measurement of Hadronic Observables With The Solenoidal Tracker At RHIC (STAR)	R. Bellwied (WSU)
11:00	PHOBOS Physics Capabilities	M. Baker (MIT)
11:30	Mid-Rapidity Measurements With the BRAHMS Spectrometer	D. Beavis (BNL)
12:00	An Update on the RHIC Construction Project	S. Ozaki (BNL)

Parrallel Session 2 (Morning), DeAnza II

10:30	Electron Measurement at PHENIX	Y. Akiba (INS, Tokyo)
11:00	Particle Identification Using Time of Flight Technology in ALICE	H. R. Schmidt (GSI)
11:30	Vector Meson and Heavy Quark Measurements With PHENIX/Muon	P. McGaughey (LANL)
12:00	Studies for Di-Muon Measurement in ALICE	D. Jouan (IPN, Orsay)

12:30 Lunch

Parallel Session 1 (Afternoon), DeAnza III

14:00	Direct Photon Physics With PHENIX	S. White (BNL)
14:30	Photon Spectrometer (PHOS) of the Heavy Ion Experiment (ALICE) at LHC	V. Manko (Kurchatov)
15:00	Studying High Density Nuclear Matter in STAR Using Hard Scattering of Partons as a Probe	W. Christie (BNL)
15:30	Hadron Distributions at Higher Rapidity Using the BRAHMS Forward Spectrometer	B. Moskowitz (BNL)
16:00	Study of Muon Pair Production in Ion Collisions at LHC With the Compact Muon Solenoid (CMS)	D. Contardo (IPN, Lyon)

Parallel Session 2 (Afternoon), DeAnza II

14:00	HBT Measurements With PHOBOS at RHIC: Capabilities and Limitations	G. Roland (MIT)
14:30	HBT in STAR/PHENIX/ALICE	W. Zajc (Columbia)
15:00	The ALICE Inner Tracking System: Design, Physics Performance, and R&D Issues	P. Giubellino (INFN, Turin)
15:30	Measurements of Strangeness Production in the STAR Experiment at RHIC	K. Wilson (WSU)
16:00	Strangeness Production in ALICE	K. Safarik (CERN)

16:20 Coffee

Plenary Session, DeAnza III

16:50	Concepts of Event by Event Analysis	H. Strobele (Frankfurt)
17:10	Comments on Physics With the Collider Detectors at RHIC and LHC	H. Gutbrod (GSI)
17:40	Comments on Physics With the Collider Detectors at RHIC and LHC	W. Willis (Columbia)
18:10	Adjourn	